Progress in Particle and Nuclear Physics 132 (2023) 104031

Contents lists available at ScienceDirect

Progress in Particle and Nuclear Physics

journal homepage: www.elsevier.com/locate/ppnp

Review

Calorimetric low temperature detectors for heavy ion physics and their application in nuclear and atomic physics

Peter Egelhof [a,b,*], Saskia Kraft-Bermuth [c,*]

[a] GSI Helmholtzzentrum für Schwerionenforschung, D-64291 Darmstadt, Germany
[b] Johannes Gutenberg-Universität, Institut für Physik, D-55128 Mainz, Germany
[c] Technische Hochschule Mittelhessen, D-35390 Giessen, Germany

ARTICLE INFO

Article history:
Available online 20 March 2023

Keywords:
Calorimetric low temperature detectors
Heavy ion physics
Atomic and nuclear physics
Electronic energy loss
Nuclear fission
Lamb shift measurements

ABSTRACT

The concept of a relatively new type of energy sensitive detectors, namely calorimetric low temperature detectors, which measure the temperature rise of an absorber due to the impact of an energetic particle or photon, is displayed, and its basic properties and its advantage over conventional detector schemes is discussed. Due to the low operating temperature, the impact of a microscopic particle or photon affects the properties of a macroscopic piece of matter (absorber) and therefore allows to measure the incident energy with high sensitivity and with high resolution. The present article will focus on the application of such detectors in the field of heavy ion physics, and it will be demonstrated that this type of detector bears a large potential as a powerful tool for many fields of nuclear and atomic heavy ion physics.

The design and construction of calorimetric low temperature detectors for the detection of heavy ions in the energy range of $0.05-360$ MeV/u, operated at temperatures around $1-2$ K, and of hard x-rays in the energy range of $50-100$ keV, operated at temperatures of $50-100$ mK, is displayed and examples of the performance are presented.

The excellent energy resolution of the order of $\Delta E/E = 1-5\times10^{-3}$ for various ion species, ranging from ^{4}He to ^{238}U, and the linearity of the energy response without any indication of pulse height defects, and the obtained mass resolution down to $\Delta m = 1.3$ amu for heaviest ions like ^{238}U, which represent a considerable improvement as compared to conventional heavy ion detectors based on ionization, have already allowed for various first applications in nuclear heavy ion physics. As prominent examples, the precise determination of isotopic yield distributions of fission fragments from thermal neutron induced fission of ^{238}U and ^{239,241}Pu, the precise determination of electronic stopping powers of various ions in various absorbers down to energies far below the Bragg peak, and the trace analysis of rare isotopes in accelerator mass spectroscopy, will be discussed. Future perspectives for further applications for high resolution nuclear spectroscopy, and the direct in-flight mass identification of heavy ions for the identification of superheavy elements and of reaction products from reactions with radioactive beams in inverse kinematics, and others, are also displayed.

Concerning the field of atomic physics, where energy resolutions down to $\Delta E = 22$ eV for 60 keV x-rays have been obtained, the application of calorimetric low temperature detectors for Lamb shift measurements on hydrogen-like heavy ions, and various other applications, will be discussed.

* Corresponding authors.
E-mail addresses: p.egelhof@gsi.de (P. Egelhof), saskia.kraft-bermuth@mni.thm.de (S. Kraft-Bermuth).

https://doi.org/10.1016/j.ppnp.2023.104031

Contents

1. Introduction

The success and the progress of experimental physics and the quality of experimentally determined results generally depend on the performance of the available detection systems with respect to important properties like energy resolution, detection threshold, detection efficiency, granularity, etc. Consequently the search for, and the development of, improved detection techniques is always a basic part of research activities in all disciplines of experimental physics. When focusing on atomic, nuclear, particle and astrophysics, energy sensitive detectors for radiation – covering photons from the infrared to visible light via x-rays to hard $\gamma-$rays, and particles, such as $\alpha-$, $\beta-$radiation, light and heavy ions and various exotic particles in a wide range of energies, with high energy resolving power, and a large dynamic range – are of particular importance.

However, many of the conventional techniques for the energy sensitive detection of radiation have already reached their principle limitation in energy resolution, detection threshold, and other properties. For example, detectors which operate on a charge collection principle following ionization processes in matter, such as ionization chambers or semiconductor detectors, or based on photon counting from scintillation light, such as scintillation detectors, etc. have physical limitations due to statistical fluctuations of the number of charge carriers or photo electrons involved in an event, which is determined by the energy gap for the creation of the secondary particles or photons to be detected (about $10-30$ eV for a gaseous ionization detector, about 5 eV for a scintillation detector, and of the order of about $0.7-1$ eV for a semiconductor detector [1,2]). Moreover, the resolving power is often limited due to incomplete energy detection which appears due to direct phonon excitation, i.e. heat production, as well as charge recombination, due to short lifetimes because of radiation damage, or limited detection efficiency (for example, small effective solid angles of high resolution magnet spectrometers or of crystal spectrometers for x-rays).

On the other hand, the need for more sensitive and versatile instruments for a large number of experiments in astrophysics, nuclear and particle physics was the driving force for the development of alternative detection concepts. Whereas most of the standard methods for detection of radiation are based on ionization, the rapid development of low temperature physics and techniques has allowed for the investigation of a novel detection concept for radiation, which is independent on ionization processes, namely the concept of thermal detectors. In contrast to ionization detectors, where the amount of electron–ion pairs, created by the impact of a photon or particle into an absorber, is detected, the basic concept of thermal detectors is focused on the variation of the thermal properties of an absorber due to the impact of radiation. This concept, which is essentially different from that of conventional detectors, opens completely new and promising perspectives for radiation detectors. In order to allow for a measurable change of the properties of a macroscopic piece of matter (i.e. the absorber) due to the impact of a microscopic particle, and to optimize the sensitivity, such detectors take advantage of the drastic drop of the heat capacity of solids at low temperatures due to the Debye law. Consequently, such detectors are operated at low temperature and are therefore called *low temperature detectors*. It is obvious that for the design and the optimization of such detectors the basic understanding of the solid state properties of the detector constituents, in particular at low temperatures, is essential.

Within the last 2–3 decades, a large variety of different detection concepts for low temperature detectors has been investigated by numerous research groups all over the world for various applications in different fields of physics. In many cases already excellent results have been reported. For a detailed overview on the field, including the different detection concepts, the physics motivations, and the historical development, the reader may be referred to the following review articles: [3–26]. The present article will focus on the concept of **C**alorimetric **L**ow **T**emperature **D**etector**s**, in the following called *CLTDs*, and on their applications in heavy ion based nuclear and atomic physics. Calorimetric detectors

– often also called *microcalorimeters* – determine the kinetic energy of an incident particle or photon by measuring the resulting temperature increase in an absorbing medium with low heat capacity after the deposited energy is thermalized (i.e. converted to heat). After the temperature rise is read out by a thermometer, which is thermally coupled to the absorber, the incident heat is transferred to a heat sink, enabling the detector to return to its base temperature and making it ready for the detection of the next incident particle. This distinguishes the present concept of single particle detectors from that of a bolometer which detects an integrated flux of particles or photons.

The potential advantages of this detector concept over conventional detectors based on charge collection after ionization (solid state Si or gaseous detectors) are:

- the smaller energy content of the detected quanta (i.e. phonons), the excitation energy of a thermal phonon being of the order of only $\leq 10^{-4} - 10^{-3}$ eV [27], to be compared to the energy gap of conventional detectors of about one to several eV (see above),
- the more complete energy detection (almost the whole kinetic energy deposited by the incident particle or photon is converted into heat after the decay of initial electronic excitations) with the absence of any pulse height defect due to charge recombination,
- the possibility to omit any entrance window or dead layer.

This reduces considerably the fluctuations in the detected amount of energy, and therefore can lead to substantial improvements concerning the basic detector properties as for example the energy resolution, the linearity of the energy response function, the detection threshold, etc.

Other potential advantages are

- the reduced noise power at low temperatures,
- the capability to detect weakly- or non-ionizing particles,
- the higher flexibility in the choice of the absorber material, to be optimized with respect to radiation hardness, detection efficiency and other criteria like the capability of embedding the radiation source (α, β, or γ) to be studied within the detector.

Historically, the application of bolometric or calorimetric detection techniques, measuring the deposited energy of radiation in an absorber after its conversion to heat, is already an old concept in various fields of physics, dating back to the 19th century. In 1881, the American astronomer S. P. Langley invented a bolometer with which he was able to measure the energy flow of the sun in the far infrared region of the spectrum [28]. Already in the early days of nuclear physics, when radioactivity was discovered, P. Curie and A. Laborde demonstrated in 1903 that the radioactive decay of radium leads to a remarkable production of heat in a calorimetric device [29].

However, as these investigations were performed at room temperature, the sensitivity was limited by the relatively large heat capacity of the absorber, and therefore allowed only to detect the integrated energy produced by a large number of decay events. The observation of F. Simon a few years later in 1935 that calorimetric detectors, operated at low temperature, could have a considerably enhanced sensitivity [30] marked an important milestone in the calorimetric detection of individual particles. In 1939, the idea to improve the sensitivity of radiation detectors at low temperatures was brought up independently by A. Goetz [31]. Since then, many advances have been made in the development of low temperature detectors. In the following years, first successful steps have been undertaken on the detection of single α-particles using various kinds of low temperature detectors [32–40]. It happened also in this time-interval of the 70ties and 80ties of the last century, that some of the pioneers of the field, T. O. Niinikoski, E. Fiorini, D. McCammon, S. H. Moseley, B. Cabrera, B. Sadoulet, F. von Feilitzsch, and their co-workers, explored several possibilities of applications of low temperature detectors for astrophysics, particle physics, and other fields [41–47], see also [48] (for a more complete overview on the history of low temperature detectors see also [3]). A few years later, D. McCammon et al. [49,50] published an impressive result obtained with a calorimetric detector, the energy resolution of $\Delta E = 7.3$ eV for 6 keV x-rays (to be compared to the resolution of a semiconductor detector of around $110 - 120$ eV [4,17]), staying for many years the best result concerning the resolution power of a calorimetric low temperature detector. Principle limitations of CLTDs concerning their energy resolution were discussed already in 1984 for the detection of x-rays [37,51,52], and in 1985/86 for the detection of light and heavy ions [53,54].

Based on all these interesting proposals and developments a first workshop on low temperature detectors (LTD1) was held in 1987 [48] at the Ringberg Castle near Munich, Germany with 43 participants. Various ideas and phenomena were discussed about low temperature detection of particles and photons. This workshop can be considered as the starting point of a rapidly growing field of physics research. Due to its success and the big interest further subsequent biannual international workshops – namely LTD2–19 – have been organized over the years, the last, LTD19, being held at NIST, Gaithersburg, USA, in 2021 [55]. Already the LTD18 counted more than 400 participants from 17 countries, and a still growing community of physicists and technicians all over the world is meanwhile established. Much of the original work can be found, and the progress of many developments can be followed in the Proceedings of these workshops (the latest being the Proceedings of the LTD17 [56], LTD18 [57] and LTD19 [55]). A compilation of the references concerning the Proceedings of LTD1-16 can be found in [4].

Many of the ideas discussed already in 1987 and before have meanwhile been demonstrated to work, and a large variety of detection concepts for low temperature detectors with fascinating capabilities has been investigated over the

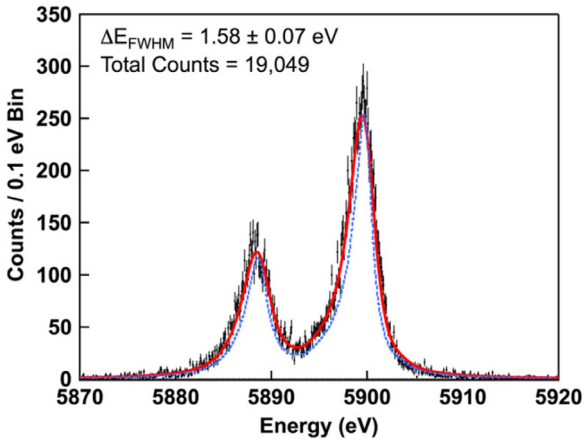

Fig. 1.1. Energy spectrum obtained with a CLTD consisting of a Mo/Au transition edge sensor on an Au absorber [123] for 5.895 keV Mn-Kα x-rays from a ^{55}Fe source. The blue line represents the natural line shape of the group of Kα lines. The energy resolution ΔE(FWHM) = 1.58(7) eV represents the up to date best resolving power obtained with a CLTD.
Source: Figure reprinted from [19] with kind permission of IOP Publishing.

years by numerous research groups all over the world for many applications in different fields of physics, and impressive progress on the technical developments, and excellent results have been reported, and have been used to explore new frontiers in physics. Whereas many detection concepts for the investigation of fundamental problems in astronomy, nuclear physics, atomic physics, astrophysics, particle physics, and weak interactions and cosmology were or are presently applied in various experiments, some are still under development for future investigations. For an overview, the reader may be referred to some reviews on this subject [3–26,58–60]. A few examples, which range from fundamental research to applications in life sciences, material analysis and industrial quality control, without the claim to be complete, are:

- microwave, infrared, x-ray and $\gamma-$ray astronomy and astrophysics, including rocket and satellite missions, which all profit from the excellent energy resolution and the large dynamic range of CLTDs. In this field, excellent results were already obtained, and very promising projects have been started [4,18,20,21,61–73].
- the search for dark matter (i.e. particles like **W**eakly **I**nteracting **M**assive **P**article**s** (WIMPs) or other exotic dark matter candidates) in the universe. These research projects profit from the low detection threshold and the almost complete energy detection of CLTDs, leading to a high sensitivity to the impact of weakly ionizing or non-ionizing particles. In this field, several big collaborations all over the world are involved [4,6,11,12,46,48,74–83].
- the direct detection of low energy solar or galactic neutrinos [3,6,11,12,44,48,84], which profit from the same advantages of CLTDs as discussed in the previous topic.
- neutrino mass experiments including the search for the neutrino-less double beta-decay and beta-endpoint measurements, which both profit from the excellent energy resolution and the flexibility in the absorber material, allowing for the absorber material to be identical with the $\beta-$source. Besides the high efficiency of this method, it also enables to exclude systematic uncertainties due to final state interactions. Also here several large collaborations word wide are involved [3,4,6,7,11,42,85–102].
- atomic and nuclear physics. This topic, including in particular heavy ion physics, represents the main topic of this review article, and will be accordingly discussed in more detail below in Sections 4–6 of the present article. It profits from the high energy resolution and energy linearity of CLTDs, and also (in the case of decay spectroscopy like $\alpha-$decay or x-ray spectroscopy) from the large detection efficiency and from the flexibility in the absorber material.
- applied physics and life sciences, including condensed matter research like x-ray microanalysis and ion-material analysis, radiopurity investigations, as well as forensic and environmental monitoring through $\alpha-$spectroscopy (without dead layers and energy degradation in the source), mass-spectrometry of bio-molecules (MALDI within the Human Genome project), and others. These investigations profit mainly from the high energy resolution and the high detection efficiency of CLTDs, in particular for very slow incident particles. For details, the reader may be referred to [4,19,26,54,103–122],and [22, and references therein].

In order to demonstrate the power of the concept of LTDs concerning the spectral energy resolution, we refer to the presently, to our knowledge, best result so far obtained with a CLTD by S. J. Smith et al. [123] with ΔE(FWHM) = 1.58 ± 0.07 eV for 5.9 keV x-rays. This result (see Fig. 1.1), which was obtained with a $35 \times 39\,\mu m^2$ Mo/Au transition-edge sensor on a 4.5 μm thick Au absorber, and which corresponds to a resolving power of $E/\Delta E = 3700 \pm 170$, is substantially superior as compared to the theoretically best value $\Delta E \approx 110 - 120$ eV which can be obtained with a conventional semiconductor detector under similar conditions [4,17].

On the other hand, one should be also aware that CLTDs have, due to their detection principle, some drawbacks concerning their performance, namely the maximum active detector volume (limited by the heat capacity), and the rate capability, that means the maximum count rate that the detector can sustain (limited by the thermalization time and by the coupling to the heat sink, leading to relatively large signal decay times, in particular for very low temperatures). Dependent on the demands of the individual experimental applications, these limitations can be partly overcome by compromises on the active detector volume and the sensitivity, and/or by constructing large arrays of individual detector pixels (for details see Section 3.2.4).

The present review article is intended to focus on CLTDs for heavy ion physics, including their design, construction, performance, and their application in various nuclear physics and atomic physics experiments. The detector design will concentrate on composite calorimetric detectors with three different readout schemes, namely semiconductor thermistors, superconducting transition-edge sensors and magnetic sensors. The corresponding heavy ion research projects were, and still are, motivated by the excellent research opportunities provided by various heavy ion facilities all over the world, already existing or under construction or planned for the future. These include not only big heavy ion facilities, like for example GSI, Germany [124], GANIL, France [125], Argonne National Laboratory, USA [126], RIKEN, Japan [127], and FAIR, Germany [128–130], FRIB, USA [131], HIAF, China [132], RAON, South Korea [133], but also smaller, very specialized and dedicated facilities, as for example **A**ccelerator **M**ass **S**pectrometry (AMS) facilities (at Vienna, Austria, Cologne, Germany, Florence, Italy, Caserta, Italy, Canberra, Australia, Sevilla, Spain, as well as Zurich, Switzerland [134–141]), and research facilities at Jyväskylä, Finland [142], MPI Heidelberg, Germany [143], LLNL Livermore, USA [144], ILL Grenoble, France [145], and many others. In particular, the availability of well performing dedicated separators providing, among others, high quality and high intensity radioactive beams, reaching far outside the valley of stability in the chart of nuclides, high intensity fission fragments from neutron induced fission at high flux reactors, highly effective production of well separated very rare species like superheavy elements, very rare isotopes, important for trace analysis, etc., as well as stored and cooled stable and radioactive heavy ion beams with excellent beam quality, and of highly charged heavy ions, opens a playground for various applications of CLTDs in atomic, nuclear and applied heavy ion physics.

The conditions for the application of CLTDs in heavy ion physics with respect to the total energy deposited in the detector, reaching in some cases values of up to several GeV, and the amount of energy per detector volume deposited in the absorber, are in the most cases by orders of magnitude different as compared to the conditions for many applications in other fields of physics, as discussed above. It will be demonstrated in the present review article that CLTDs provide, due to their detection principle, also in the field of heavy ion physics excellent performance with respect to energy resolution, energy linearity, detection efficiency, and radiation hardness (i.e. resistivity against radiation damage), not reached by conventional ionization detectors operating on the charge collection principle. The latter are limited by the incomplete energy detection due to the high ionization densities produced by heavy ions in matter, leading to charge recombination, and/or due to inactive entrance windows, dead layers, etc. High-resolution magnet spectrometers for heavy ions, or crystal spectrometers for x-rays, are capable of achieving comparable or even better energy resolution, but on the cost of small dynamic range and limited solid angle and thus limited detection efficiency, and, for the case of magnet spectrometers, charge state ambiguities, in particular for slow heavy ions.

The proposal to apply CLTDs for the energy sensitive detection of heavy ions dates back to the late eighties of the last century, and was initiated at that time by K. W. Shepard [146] and W. Henning [147], whereas a few years later the application of CLTDs for Lamb shift measurements on hydrogen-like heavy ions was proposed [148]. Consequently, a research project was started in 1988 at the University Mainz, Germany, and at the GSI, Darmstadt, Germany [149–151] with the aim to study the response of CLTDs to the impact of energetic heavy ions in the energy range of about 0.05 MeV/u up to several hundred MeV/u, and to develop heavy ion detectors, and later also x-ray detectors for hard x-rays, with high energy resolution. After several years of trial and error in the development and construction of appropriate detectors, first excellent results on the performance of such detectors concerning energy resolution and energy linearity for a wide range of ions (^{4}He…^{238}U) and energies (0.05–360 MeV/u) were obtained [152–155]. Depending on the individual experimental conditions, relative energy resolutions of the order of $\Delta E/E = 1 - 5 \times 10^{-3}$ have been obtained even for the heaviest ions. In contrast, conventional heavy ion detectors, operating on a charge collection principle, provide relative energy resolutions of $\Delta E/E \geq 1 - 5 \times 10^{-2}$ for heavy ions, becoming substantially worse for low energies and very heavy ions [54,156]. For the detection of hard x-rays, energy resolutions of the order of 70 eV, down to 46 eV, for 59.6 keV x-rays were obtained [157,158], to be compared to a theoretical limit of 380 eV for conventional semiconductor detectors under these conditions.

Having these promising results in mind, a large potential for present and future applications was discovered (for an overview, the reader may be referred to a couple of review articles [15,23,24,59,158]). It was shown that CLTDs may become powerful tools for heavy ion physics, as several successful applications in various areas of experimental heavy ion research were started and have already provided first results which will be discussed in the present review. These include

- the investigation of precise isotopic yield distributions of fission fragments [159–161] with the aim of a better understanding of the fission process and to obtain important information for nuclear structure, reactor and neutrino physics,
- the investigation of the interaction of heavy ions with matter, namely the precise determination of electronic stopping powers of heavy ions in matter [155,162],

- **A**ccelerator **M**ass **S**pectrometry (AMS) [163] investigations for trace analysis [154,164,165],
- the application in Lamb shift experiments on hydrogen-like heavy ions [24,158,166–169], which allow an unambiguous test of bound-state QED in the unperturbative regime of extremely strong Coulomb fields.

These developments were and are still continued at the Justus-Liebig-University, Giessen, Germany and the TH Mittelhessen University of Applied Sciences, Giessen, Germany, in close cooperation with GSI and FAIR. Over the years, several research activities concerning the application of CLTDs in heavy ion physics were also started in several laboratories all over the world, such as for example (without the claim to be complete) at LLNL Livermore, USA, in cooperation with the Goddard Space Flight Center of NASA, USA [71,105,112,170–175], the Harvard Smithsonian Center for Astrophysics, Cambridge, USA [176], the National Institute of Standards and Technology (NIST), Boulder, USA [26,110,113], the Los Alamos National Laboratory, USA [22,111], the University of Milano-Bicocca, Italy [40,103,120], the University of Heidelberg, Germany [24,112], the University of Jena, Germany [177] and the CEA Saclay and the University of Orsay, France [107].

Concerning the future perspectives for the application of CLTDs in heavy ion physics, which will also be discussed in detail in the present review article, we are convinced that CLTDs will become powerful tools in heavy ion physics as they bear a large potential for various applications in basic and applied heavy ion research, such as nuclear structure and astrophysics, atomic physics, the physics of symmetries and basic interactions, and the interaction of heavy ions with matter. They include:

- high resolution nuclear spectroscopy,
- applications in nuclear structure and astrophysics such as the exploration of the limits of nuclear stability, where an event-by event direct in-flight mass identification via the combined energy/time-of-flight detection may be applied for the identification of superheavy elements, or the identification of beam-like reaction products in direct reaction experiments, or in-flight γ-spectroscopy with radioactive beams in inverse kinematics,
- further applications in the identification of fission fragments and the determination of isotopic yield distributions, in particular for heavy fragments, for providing important information for nuclear structure, reactor and neutrino physics,
- applications in AMS trace analysis experiments improving the sensitivity, the identification of rare isotopes and the background suppression,
- high resolution x-ray spectroscopy on highly charged heavy ions in flight or at rest for atomic physics, in particular for sensitive tests of the QED in ultra-high electromagnetic fields.
- investigations in applied physics such as heavy ion channeling experiments in single crystals, as well as further experiments on stopping powers of heavy ions in matter, decay energy spectroscopy, and life sciences,

The present review is organized in the following way: After a description of the operation principle and the basic properties of CLTDs, including the potential advantage over conventional detection schemes in Section 2, the design, construction and performance of CLTDs for the detection of heavy ions is discussed in Section 3. A review on various applications of CLTDs in heavy ion physics, including the investigation of isotopic yield distributions of fission fragments, the precise determination of electronic stopping powers, and first applications in AMS is presented in Section 4, followed by an overview on perspectives for future applications in Section 5. In Section 6 the design, construction and performance of CLTDs for the detection of hard x-rays and their application in atomic physics experiments with highly charged heavy ions is described. Finally conclusions and an outlook are presented in Section 7.

2. Detection principle and basic properties of CLTDs

In this section the detection principle of calorimetric low temperature detectors (CLTDs) and their properties will be discussed. For various applications in different fields of physics quite a number of different detection and readout schemes are used, dependent on the individual experimental conditions. For an overview see [3,4,12,13,15,17,24,178–182].

In the present review we will restrict ourselves to the case of composite calorimeters, that means that, in contrast to so called monolithic calorimeters where thermometer and absorber are identical, the absorber and the thermometer are separated, and to a readout scheme of the thermal signal which is based on the resistance change of a temperature dependent resistor. For the case of x-ray detection the alternative readout scheme of a magnetic calorimeter which is based on the readout of a change of magnetization of a paramagnetic sensor is also used. This scheme will be discussed in Section 6.3.2.

2.1. Thermal particle detection

Calorimetric low temperature detectors are thermal detectors, this means that their detection principle is based on the measurement of the temperature increase of a piece of matter – in the following called *absorber* – after the energy which is deposited by an incident particle or photon is converted into heat (i.e. thermal phonons). A schematic view of the detection scheme of a composite CLTD is displayed in Fig. 2.1. The detector consists of three basic components: an absorber, characterized by its heat capacity C, a thermometer, characterized by the temperature dependence of the

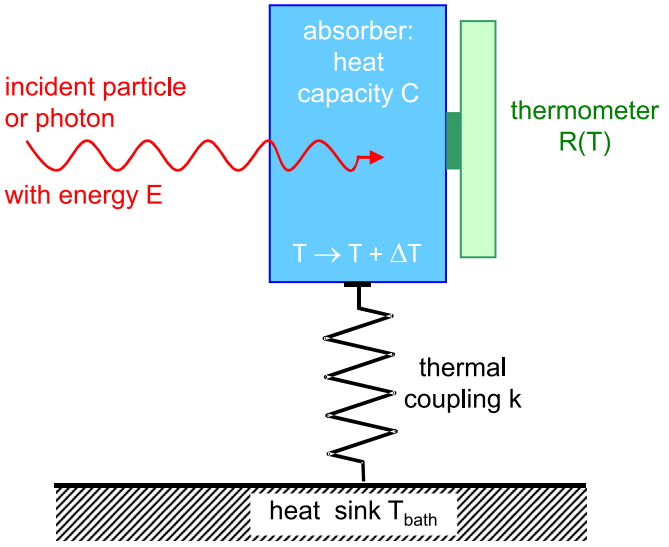

Fig. 2.1. Schematic view of the detection principle of a composite calorimetric low temperature detector: The detector consists of an absorber with heat capacity C, a thermometer with its temperature-dependent resistance $R(T)$, and a thermal link k to a heat sink at bath temperature T_{bath}.

resistor $R(T)$, and a thermal link to a heat sink at bath temperature T_{bath}, characterized by the thermal coupling k to the absorber.

The impact of a particle or a photon leads primarily to atomic and solid state excitations, namely to ionization and the production of high energetic ballistic phonons in the absorber [1,2,54,183]. The process of slowing down of an energetic ionizing particle, like a heavy ion, to rest is dominated by the interaction of the ion with electrons of the bulk material, leading to the creation of electron–hole pairs (electronic energy loss) [1,2,183,184], and, in particular for slow ions, to the interaction with nuclei of the bulk material leading to lattice vibrations or recoil ions from Rutherford scattering (nuclear energy loss) [1,2,183,184]. The interaction of photons like x-rays or $\gamma-$rays with the absorber material leads to the production of electrons (photo effect), which also create electron–ion pairs through inelastic electron scattering [1,2], and solid state excitations in the bulk material. In a second step, after the recombination of the electron–ion pairs, the deexcitation of excited electronic states, and the decay of high-energetic phonons to thermal phonons, the majority of the deposited energy is converted to heat (thermal phonons). The absorber reaches thermal equilibrium after a typical thermalization time of the order of 10^{-8} s (for details see [54,183,185–187]). The corresponding temperature increase ΔT of the absorber allows now to determine the amount of the deposited energy with a suitable thermometer, which should be strongly thermally coupled to the absorber. The thermometer – in the present case a temperature dependent resistor – responds to the increased temperature by a change of resistance of a properly biased thermistor. It is measured by passing a constant current I through the thermistor and observing a corresponding voltage change. Finally the deposited heat is transferred to a heat sink, and the absorber temperature returns back to its base operation temperature T_{base}, making the system ready for the detection of the next incoming particle.

The amplitude of the observed thermal signal is for the ideal case, assuming that the deposited energy E of the particle or the photon is fully thermalized, given by

$$\Delta T = \frac{E}{C} \tag{2.1}$$

ΔT is proportional to the incident energy and inversely proportional to the heat capacity $C = c\,m$ of the absorber, c denoting the specific heat, and m the mass of the detector. Since the specific heat of solids generally decreases with temperature (see next section) calorimetric detectors need to be operated at low temperatures to allow for a sufficiently high sensitivity with an appreciable temperature increase ΔT. In addition, the absorber volumes are kept as small as possible. Therefore CLTDs are also often called *microcalorimeters*.

The time development of the thermal signal is schematically displayed in Fig. 2.2. It is, under the assumption that the rise-time τ_{rise} of the signal is negligibly small as compared to the fall-time τ_{fall}, given by:

$$T(t) = T_{base} + \frac{E}{C}\,\exp\left(-\frac{t}{\tau_{fall}}\right) \tag{2.2}$$

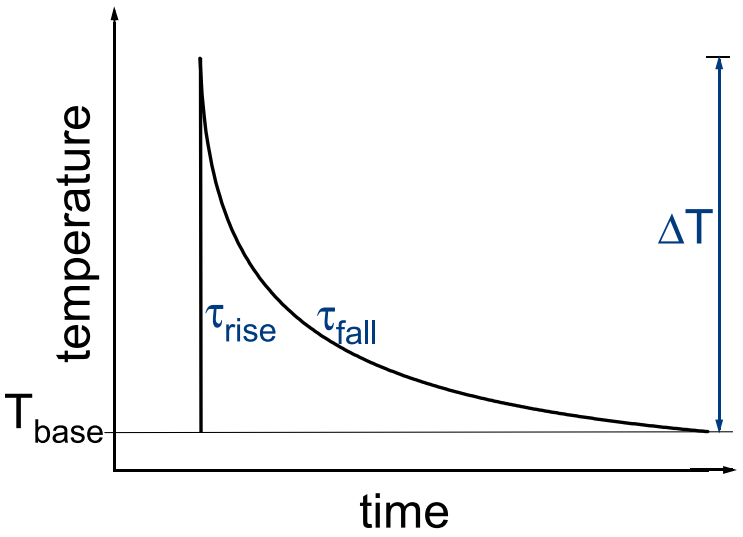

Fig. 2.2. Schematic view of the time dependence of the thermal signal.

Here, T_{base} denotes the operating temperature of the detector. The dynamic behavior of the CLTD is determined by an exponential decay of the thermal signal with a thermal time constant τ_{fall}, which is in first approximation (for details see Section 2.3) given by :

$$\tau_{fall} = \frac{C}{k} \tag{2.3}$$

Thus the fall time, which determines the maximum acceptable count rate (i.e. rate capability) is limited by the heat capacity C and the constraint that the thermal coupling to the heat sink (defined by k) needs to be sufficiently weak in order to avoid that heat will escape from the absorber to the heat sink before thermal equilibrium is reached, and that the full energy signal can be detected. Typical values for τ_{fall}, which depend on the individual experimental conditions and requirements, like absorber volume, absorber material, etc., are in the range of about 100 µs up to 10 ms or more. A lower limit for the rise time τ_{rise} of the thermal signal is given by the thermalization time, but in most practical cases the rise time is determined by the time constants of the electronic readout circuit, and is in the range of about $1 - 10$ µs.

2.2. Optimization of the sensitivity

The application of a composite calorimeter enables to optimize all three basic components of the device individually:

2.2.1. The absorber

The most efficient strategy to optimize the sensitivity of a calorimetric detector is based on the temperature dependence of the heat capacity $C = m\,c$ of the absorber. The specific heat c of a solid is determined by contributions of lattice vibrations (phonons) c_l and of the conduction electrons c_e [27]. Applying the Debye law for the contribution of the lattice [27], we receive for a normal conducting material:

$$c = c_l + c_e = \alpha_c \left(\frac{T}{\Theta_D}\right)^3 + \beta_c\, T \tag{2.4}$$

where Θ_D is the Debye temperature, α_c is given by $\alpha_c = 1944\,\mathrm{J\,mol^{-1}\,K^{-1}}$, and β_c is a material-dependent constant. Having in mind that for normal conducting metals the contribution of the conduction electrons with its linear T-dependence dominates the heat capacity for low temperatures (below temperatures around typically $1 - 10$ K), lowest heat capacities are obtained for dielectric materials with high Debye temperatures, for which the contribution of the conduction electrons vanishes.

For the special case of superconducting materials we obtain for the contribution of the electrons [188]:

$$c_e = \frac{a}{T^{3/2}} \exp\left(-b\frac{T_C}{T}\right) \tag{2.5}$$

which reflects the number of thermally excited electrons across the energy gap of the superconductor. a and b are material constants. Here we obtain for temperatures below the critical temperature T_C that the contribution of the electrons

Table 2.1
As an illustrative example, the temperature dependence of the heat capacity C and the temperature increase ΔT due to the impact of a 1 MeV α-particle on a sapphire absorber with a volume of 1 mm^3 is displayed. In the last column, the theoretical limit ΔE_{theo} for an ideal calorimeter, calculated according to Eq. (2.26) with $\xi = 2$, is displayed. Note that the theoretical limit for the energy resolution of a semiconductor detector is about 7.5 keV [193].

T [K]	C [J/K]	ΔT [mK]	ΔE_{theo}
300	9×10^{-3}	9×10^{-8}	3.2 GeV
10	4×10^{-7}	2×10^{-3}	700 keV
1	4×10^{-10}	2	2.2 keV
0.1	4×10^{-13}	2000	7 eV

Table 2.2
As a second illustrative example, the temperature dependence of the heat capacity C and the temperature increase ΔT due to the impact of mono-energetic x-rays with an energy of 50 keV on a tin absorber with an area of 1 mm^2 and a thickness of 50 μm is displayed. In the last column, the theoretical limit ΔE_{theo} for an ideal calorimeter, calculated according to Eq. (2.26) with $\xi = 2$, is displayed. Note that the theoretical limit for a semiconductor detector is about 350 eV.

T [K]	C [J/K]	ΔT [mK]	ΔE_{theo}
300	8×10^{-5}	1×10^{-7}	295 MeV
1	9×10^{-10}	1.1×10^{-2}	3.3 keV
0.1	7.5×10^{-13}	10.7	9 eV
0.05	9.3×10^{-14}	85.9	2 eV

decreases exponentially with the temperature, and therefore, the contribution of the lattice c_l dominates for very low temperatures similar to the case of dielectric materials.

The most important constraints for optimizing the absorber material are:

- The absorber material should be a dielectric material, or a superconductor operated below the critical temperature, with a high Debye temperature.
- The absorber material should provide fast and complete thermalization of the incident energy. In particular, the choice of an absorber material which maximizes the amount of the absorbed energy transferred to heat within the time window of the readout system is one of the challenges of the detector technology for CLTDs. It is this issue which determines, among others, the practical limitation of the energy resolution. Therefore, any loss processes due to lattice defects, Frenkel pairs, or metastable electronic states, etc., where a part of the incident energy may be trapped, should be avoided or minimized (for details see Section 2.4.2 and [53,54]).
- The absorber material should be radiation hard, that means it should not be much affected by radiation damage. This is in particular important for the detection of heavy ions.
- The absorber material should be optimized with respect to the absorption efficiency. This concerns the chance for the escape of secondarily produced radiation (electrons, or photons) out of the absorber volume, as well as the absorption efficiency (photo-peak efficiency) for the detection of x-rays. In addition, the absorber volume should be sufficiently large to ensure that incident ions are slowed down to rest within the absorber.

In practice, some absorber materials, such as for example sapphire for the detection of heavy ions, mercury-tellurite (HgTe or HgCdTe) for the detection of low energetic x-rays [49,50,170,189], and Sn, Pb or Au for the detection of hard x-rays [157,173,190–192], [24, and references therein] have already shown very good performance.

In order to demonstrate the dependence of the sensitivity of a CLTD on the absorber temperature, the temperature dependence of the heat capacity C and of the temperature increase ΔT are listed in Tables 2.1 and 2.2 for two individual examples, namely for the impact of a 1 MeV particle on a sapphire absorber with a volume of 1 mm^3 (Table 2.1), and for the impact of a 50 keV x-ray on a tin absorber with a thickness of 50 μm and an area of 1 mm^2 (Table 2.2). In addition, the theoretical limit of the energy resolution ΔE_{theo}, according to Eq. (2.26) under the assumption of an ideal CLTD, which is determined by the thermodynamical fluctuations (i.e. quantum statistics) and Johnson noise [50,51,178], (for details see Section 2.4.1) is listed in both tables. It is obvious from both tables that for sufficiently low temperatures the impact of a microscopic particle or photon affects the properties of a macroscopic piece of matter (i.e. absorber), and, therefore, allows to measure the incident energy with high sensitivity and very good energy resolution.

2.2.2. The thermometer

As thermometers for reading out the temperature increase ΔT of a CLTD, thermistors are most commonly used. For such thermistors, the change of the temperature of the absorber is converted to a change of its resistance R. When biasing the thermistor with a constant current, the change of its resistance leads to a voltage pulse which is finally read out by well adjusted readout electronics (see also Section 3.3). For optimizing the sensitivity of the thermistor a high dR/dT is

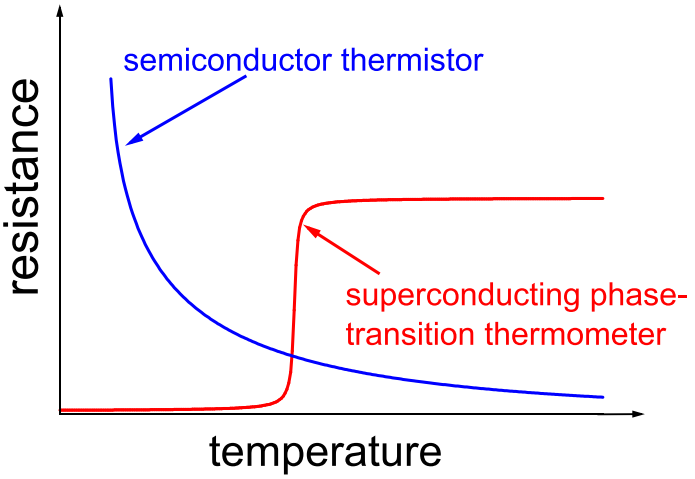

Fig. 2.3. The typical temperature dependence of the resistance R of a semiconductor thermistor and of a superconducting phase-transition thermometer is schematically displayed for comparison.

required. As parameter for the sensitivity of a thermistor the dimensionless quantity

$$\alpha = \frac{d \log R(T)}{d \log T} = \frac{T}{R}\frac{dR}{dT} \tag{2.6}$$

is commonly used[1] [178]. Besides the requirement of a high value of α, a good thermal contact between thermometer and absorber is necessary for a proper operation of the CLTD.

In the following, two types of thermistors, both having advantages and disadvantages, namely semiconductor thermistors and superconducting phase-transition thermometers, also called **T**ransition-**E**dge **S**ensors (TES), will be discussed. The typical dependence of the resistance R as a function of the temperature T is displayed schematically in Fig. 2.3 for both cases.

The semiconductor thermistor consists of a small piece of a semiconductor material (here Si or Ge are most frequently used) which is heavily doped and compensated, and which is typically connected to the absorber by a glue with good thermal conductivity (for a detailed discussion see [12,179]). For providing a proper doping of the thermistor with donors and acceptors, ion implantation or **N**eutron **T**ransmutation **D**oping (NTD), performed with thermal neutrons from reactors [12,179], is frequently used. The impurity concentrations are chosen to be slightly below the metal–insulator transition [12,179]. An important requirement for the fabrication of thermistors is to achieve a good and reproducible doping homogeneity.

For low temperatures such thermistors provide a steep rise of the resistance with decreasing temperature due to the mechanism of *phonon assisted hopping conductivity*, also called *variable range hopping conductivity* [179,194–196]. For Si or Ge thermistors a typical $T-$dependence of the resistance

$$R(T) = R_0 \exp\left(\left(\frac{T_0}{T}\right)^{1/2}\right) \tag{2.7}$$

is observed for temperatures between 10 mK and 4 K. R_0 and T_0 are determined by the material properties of the semiconductor and by the doping density [179,194]. In Fig. 2.4, an example for the $R(T)$ characteristics of a germanium thermistor consisting of a $3 \times 1 \times 0.5\,\mathrm{mm}^3$ germanium crystal, heavily doped and compensated with indium (2×10^{17} atoms/cm^3) and antimony (1×10^{17} atoms/cm^3), for which a resistance of $R = 200\,\mathrm{k\Omega}$, a $dR/dT = -0.48\,\mathrm{M\Omega/K}$, and an $\alpha = -3.3$ is obtained at $T = 1.7\,\mathrm{K}$, is displayed [164]. The $R(T)$ characteristics is well described by Eq. (2.7) with values of $R_0 = (69 \pm 1)\,\Omega$ and of $T_0 = (106 \pm 2)\,\mathrm{K}$.

A superconducting phase-transition thermometer consists typically of a film or strip of superconducting material which can be evaporated or glued on the absorber. For a detailed discussion see [17,180]. Typical superconducting materials used are Al, Ti, Mo, W, Ir or others [4,180]. As illustrated in Fig. 2.5 (left-hand side), the thermometer is operated at a temperature below or around the transition temperature T_C in the narrow transition region between the superconducting and the normal conducting state, where its resistance changes between zero and the value R_N for normal conductivity. In the temperature range within 25%–75% of R_N, an approximately linear behavior with $dR/dT \approx$ const. (exactly constant in the ideal case) needs to be obtained for a linear energy response of the detector, and a small transition width δT is required

[1] log in this case denotes the *natural logarithm* to base e. We follow the notation used in [178].

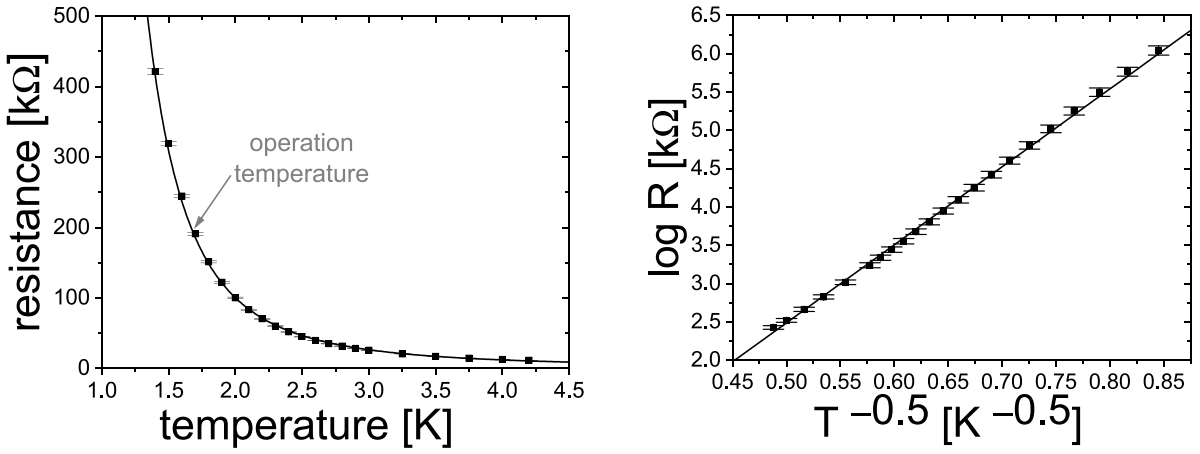

Fig. 2.4. $R(T)$ characteristics of a Germanium thermistor used for the present investigations [15,164]. The data set is displayed in a linear (left -and side) and a logarithmic scale (right-hand side). The solid lines represent a fit to the data using Eq. (2.7) (Please note that log denotes the *natural logarithm*. For details see text).

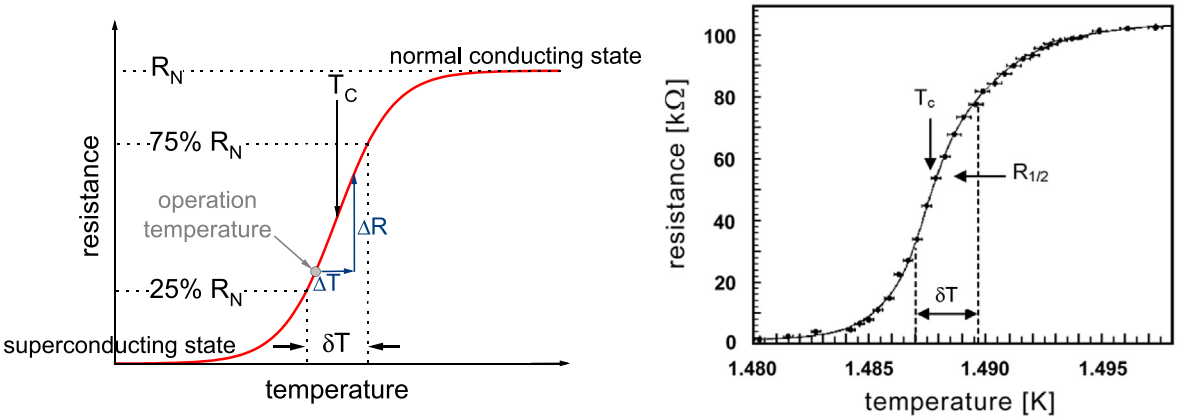

Fig. 2.5. left-hand side: The $R(T)$ characteristics of a superconducting phase-transition thermometer in the region of the phase transition between the superconducting and the normal conducting state is schematically displayed. At the operating temperature, usually chosen in the linear region of the transition below the transition temperature T_C, a temperature increase ΔT due to the impact of a particle or a photon induces a resistance change ΔR. δT denotes the transition width. right-hand side: $R(T)$ characteristics of an Al phase-transition thermometer used for the present investigations (for details see text).
Source: Figure reprinted from [15] with kind permission of Springer.

for a high sensitivity. For proper operation, care has to be taken that the amplitude ΔT of the temperature increase does not overshoot the transition region. This can be realized for an energy range of the incident particle or photon, defined by the experimental requirements, by a proper choice of the absorber volume and with that of the heat capacity of the absorber.

In Fig. 2.5 on the right-hand side, an example of a typical $R(T)$ characteristics of a superconducting phase-transition thermometer, used for the present investigations, is displayed. The sensor consists of a 10 nm thick Al film, patterned in a meander-like structure in order to match its resistance to conventional readout electronics. The Al meander structure has 51 strips of 10 µm width and 1 mm length each, and is evaporated by photolithographic techniques on a sapphire absorber (see also Section 3.2.3.1). At a transition temperature of $T_C = 1.488$ K, a transition width of $\delta T = 2.9$ mK, a resistance of $R(T_C) = 52$ kΩ, and a $dR/dT = 21$ MΩ/K, leading to a sensitivity of $\alpha(T_C) = 601$, is obtained [15].

In practice, the challenge in detector technology is to produce samples with reproducible homogeneous transition curves and transition temperatures. Furthermore, such detectors require a very good temperature stabilization. For the case of detector arrays, even small variations of T_C for different detector samples may, due to the small temperature window for proper operation, make it impossible to operate them all at the same bath temperature, and can lead to the need of individual temperature adjustment by heaters on the individual detector pixels (see also Section 3.2.4 and Section 3.5.2).

Comparing finally the two thermometer concepts discussed, we find for both types advantages and disadvantages. Semiconductor thermistors have a negative slope of the $R(T)$—curve, and provide a much higher dynamic range of the

incident energy, at the cost of sensitivity – typical values for α are -3 to -10 [4] – and energy linearity. Superconducting phase-transition thermometers have a positive slope of the $R(T)$−curve, and provide very high sensitivity of the order of $\alpha \sim 600 - 1000$ [4], and very good energy linearity because of the linear $R(T)$ characteristics in the operating window, at the cost of the dynamic range for the incident energy due to the narrow transition region.

2.2.3. The thermal link to the heat sink

The heat sink of the detector system (see Fig. 2.1) is in the most cases realized by a block of metal – copper is a convenient material – which has a good thermal contact to the cold bath of the cryostat. The thermal link of the CLTD to the heat sink can be realized by a metal wire or metal strip, which connects thermally the absorber with the heat sink. The thermal coupling constant k, which defines, besides the heat capacity C of the absorber, the thermal time constant τ_{fall} of the CLTD (see Eq. (2.3)), is determined by the geometry of the wire or strip (length l and cross section A) and its specific thermal conductivity λ:

$$k = \lambda \frac{A}{l} \tag{2.8}$$

For optimizing the thermal link several constraints have to be taken into account:

- the thermal link must be sufficiently strong to transport the steady flow of heat which hits the CLTD from its environment. This is particularly important for CLTDs housed in cryostats which have a window-less connection to a beamline transporting the incident particles to be detected (for details see Section 3.4).
- the maximum count rate to be accepted by the CLTD increases linearly with the strength of the thermal coupling contact.
- the thermal link must be kept sufficiently weak in order to avoid that the heat deposited in the absorber from the incident particle or x-ray will partly escape to the cold bath before thermal equilibrium is reached and the full energy signal to be measured can be read out. Thus, a degradation of the energy resolution is avoided.

Therefore, for each application a compromise needs to be made, concerning the heat capacity of the absorber, the total energy to be detected, the operating temperature, the necessary rate capability, etc., dependent on the individual experimental conditions.

Before concluding this section it should be pointed out that for a successful design and realization of CLTDs, a detailed understanding of the solid state and thermal properties of the materials used for the detector components – in particular at low temperatures –, and of the detailed thermalization processes of the incident energy in the absorber material are essential.

2.3. The thermal signal

As described in Section 2.1, the creation of a thermal signal by a CLTD happens in two steps. Firstly, the energy of an incoming particle is converted into heat in the absorber. Secondly, the heat induces a resistance change in the thermometer which is detected as the change of a voltage while a constant current is applied.

2.3.1. Thermalization of the incident energy

When a heavy ion hits the absorber, its energy is transferred to the lattice by different processes which strongly depend on the ion energy. Fig. 2.6 gives an overview on the different processes.

Depending on the kinetic energy of the ion, two energy loss processes can occur:

- The incident ion interacts with the electrons of the solid (in this case the absorber), causing excitation or ionization. This process is referred to as *electronic energy loss* or *electronic stopping power* S_{el}.
- In particular at low ion energies, at the end of the track of the incoming ion, Rutherford scattering of the ion on the absorber nuclei occurs. This results in the creation of phonons or in the displacement of target atoms within the lattice. This process is referred to as *nuclear energy loss* or *nuclear stopping power* S_n.

For energetic heavy ions, the electronic stopping power is usually the dominant process of the energy transfer. The nuclear energy loss becomes dominant only after slowing down of the incoming ion or for ions with low incident energy.

After the incident ion is stopped to rest, the excited or ionized atoms deexcite or recombine with electrons after a certain time. The excitation energy is transferred to the lattice in the form of lattice vibrations, i.e. phonons. However, along the ion trajectory, the ionization density of the target can become very large. The freely moving electrons leave the proximate volume of the trajectory very fast. The remaining positive atomic cores repel each other. This mechanism can also create phonons. If the ionization density becomes too large, atomic cores may even be displaced from their lattice and form so-called *Frenkel pairs*. Such Frenkel pairs can be very long-lived and trap phonons, creating one of the potential loss processes which may impede the energy detection.

Elastic scattering of ions on the target atoms creates phonons directly, because the target atoms are slightly displaced from their original lattice position. However, also nuclear energy loss can create *Frenkel pairs* if the transferred energy is large enough. In addition, other processes like the creation of photons (Cherenkow light), sputtering, bremsstrahlung or

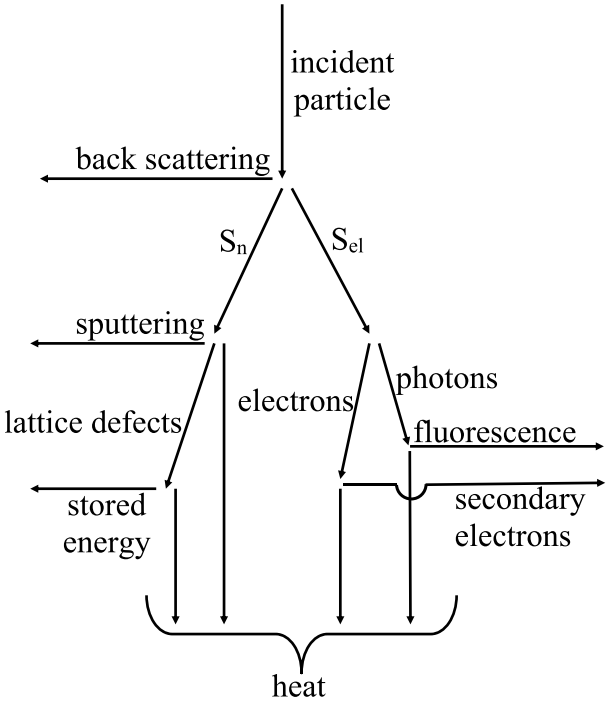

Fig. 2.6. Schematic overview on the energy flow in the absorber of a CLTD after the impact of an ion. S_n and S_{el} denote the nuclear energy loss, and the electronic energy loss, respectively. Processes which are indicated by side arrows do not contribute to the thermal signal.
Source: Adapted from [54].

the reaction of ions with target nuclei may occur, but they are only relevant at very low (sputtering) or very high ion energies. In the worst case, these processes have to be taken into account as losses of the thermal signal.

As described above, electronic and nuclear energy loss create energetic secondary particles, i.e. free electrons and/or excited atomic cores. These secondary particles deexcite or recombine, thereby transferring part of their energy to the lattice. However, they can also excite or ionize other target atoms and create a cascade of secondary particles until the energy has become too low for further excitation. These cascade particles again recombine or deexcite and create phonons [2,197]. After a certain time, almost the full kinetic energy of the incoming ion has been transferred to phonons in the absorber. These initial phonons are acoustic or high-energy phonons. When scattering on other phonons, on Frenkel pairs or at the surfaces of the solid, these high-energy phonons decay into thermal phonons within about 10^{-11} s [187]. For thermal phonons, the mean free path is determined by the dimensions of the crystal, because they only scatter on the crystal surfaces. After a thermalization time, the thermal phonons have traveled through the whole crystal. The absorber is then in thermal equilibrium and the temperature rise can be read out as the corresponding voltage signal.

2.3.2. The equation of heat and its solution for small temperature signals

The transfer of the ion energy to the lattice is the sum of many microscopic interactions in the absorber which can only be described by Monte Carlo simulations. To describe the temperature signal as a function of time, it is necessary to move from microscopic interactions to the macroscopic quantity *heat*. Die change of the quantity of heat $dQ(t)/dt$ in the detector is defined by the power $P_{in}(t)$ that is transferred *to the detector* and the power $P_{out}(t)$ that is removed *from the detector* via the thermal coupling:

$$\frac{dQ(t)}{dt} \equiv C(T(t))\frac{d}{dt}T(t) + T(t)\frac{d}{dt}C(T(t)) = P_{in}(t) - P_{out}(t) \tag{2.9}$$

The heat which is removed from the detector via the thermal coupling is given by

$$P_{out} = \int_{T_{bath}}^{T(t)} k(T')dT' \tag{2.10}$$

where T_{bath} is the temperature of the heat bath as described in Section 2.1. $T(t)$ is the temperature of the detector as a function of time. The power $P_{in}(t)$ that is transferred to the detector has several components:

- The energy that is introduced by the incoming particle or x-ray can be described in good approximation by a Delta function if the thermalization time is short compared to the thermal time constant τ_{fall}:

$$P_E = \epsilon\, E\, \delta(t) \tag{2.11}$$

  The factor ϵ takes into account that a part of the incident energy may not have been transferred to the phonon system (see Fig. 2.6).
- As a current I is applied to a resistor, Joule heating P_J has to be taken into account:

$$P_J = R(T) \cdot I^2 \tag{2.12}$$

- In addition, heat is introduced from the environment, e.g. from "hot" surfaces or apertures (black bodies) surrounding the detector. While this contribution P_H may vary over time, it can be considered to be constant within the time scale of a single temperature signal.

Taking into account all these contributions, the thermal balance of the detector can be described by the equation

$$C(T)\frac{dT(t)}{dt} + T(t)\frac{d}{dt}C(T(t)) = \epsilon \cdot E \cdot \delta(t) + R(T) \cdot I^2 + P_H - \int_{T_{bath}}^{T(t)} k(T')dT' \tag{2.13}$$

Without incoming ions, Joule heating and thermal radiation from the environment are in equilibrium with the power that is removed from the detector:

$$R(T_{base}) \cdot I^2 + P_H - \int_{T_{bath}}^{T_{base}} k(T')dT' = 0 \tag{2.14}$$

T_{base} is the equilibrium or operation temperature of the detector. When a particle or an x-ray photon hits the absorber, it creates a temperature change ΔT. If $\Delta \mathrm{T} \ll T_{base}$ is fulfilled, $C(T)$, $k(T)$ and dR/dT can be considered to be constant as $C(T_{base}) \equiv C$, $k(T_{base}) \equiv k$, $dR/dT(T_{base}) \equiv dR/dT$. We can then linearize equation (2.13) and obtain:

$$C\,\frac{d}{dt}\Delta\mathrm{T}(t) = \epsilon \cdot E \cdot \delta(t) + \frac{dR}{dT} \cdot I^2 \cdot \Delta\mathrm{T}(t) - k \cdot \Delta\mathrm{T}(t) \tag{2.15}$$

With the ansatz $\Delta\mathrm{T}(t) = A \cdot \exp(-t/\tau_{eff})$ we obtain the solution for small temperature signals ($\Delta\mathrm{T} \ll T_{base}$)

$$\Delta\mathrm{T}(t) = \frac{\epsilon \cdot E}{C} \cdot \exp\left(-\frac{t}{\tau_{eff}}\right) \text{ with } \tau_{eff} = \frac{C}{k - \frac{dR}{dT} \cdot I^2} \tag{2.16}$$

It has to be stressed that this solution is only valid under the assumption of $\Delta\mathrm{T} \ll T_{base}$. If the temperature change ΔT is of the same order of magnitude as the operating temperature T_{base}, which is often the case for x-ray detectors, the temperature dependence of $C(T)$ and $k(T)$ has to be taken into account explicitly. Analytic solutions for the temperature signal are obtained by numerically solving Eq. (2.13) in that case.

The time constant τ_{eff} differs from the time constant $\tau_{fall} = E/C$ presented as a first approximation in Section 2.1. The term $\frac{dR}{dT} \cdot I^2$ is usually referred to as *electrothermal feedback* [178]. If the detector warms up during particle detection, the Joule heating changes due to the change in the thermistor resistance. If the sensitivity α (defined in Eq. (2.6)) is negative – as it is the case for semiconductor thermistors –, the Joule heating will decrease and the detector cools down faster. If α is positive – as for a TES –, Joule heating will increase and the cooling down back to the operating temperature is slowed down. In this case, the electrothermal feedback term may even become larger than the thermal coupling k, which will result in a negative effective time constant. That means that the detector will not cool down to the base temperature any more. Rather, its temperature will continue to increase and it will become unstable. In particular for transition-edge sensors which have a positive α, the electrothermal feedback, therefore, limits the applicable measurement current [178].

2.3.3. Readout of the thermal signal

Fig. 2.7 displays the readout scheme for a current-biased CLTD [164,184]. To keep the current constant when the resistance changes, the temperature-dependent resistance $R(T)$ is in series with a load resistance $R_L \gg R(T)$. The temperature signal ΔT causes a change of the resistance $\Delta\mathrm{R}(T)$. This resistance change is read out as a voltage signal $U(T) = \Delta\mathrm{R}(T)I$.

The transfer function of the readout scheme displayed in Fig. 2.7 corresponds to a low pass filter with the time constant

$$\tau_{el} = \frac{R_L R(T) C_S}{(\mathrm{R(T)} + R_L)} \approx C_S \cdot R(T) \text{ for } R_L \gg R(T) \tag{2.17}$$

C_S is the stray capacitance of the detector and the readout cables. In the usual case of $\tau_{el} \ll \tau_{eff}$, the thermal decay time of the voltage signal will not be affected by the stray capacity. The rise time of the voltage signal, however, is determined by the electronic time constant τ_{el}, because τ_{el} is much longer than the actual thermalization time (see Section 2.2).

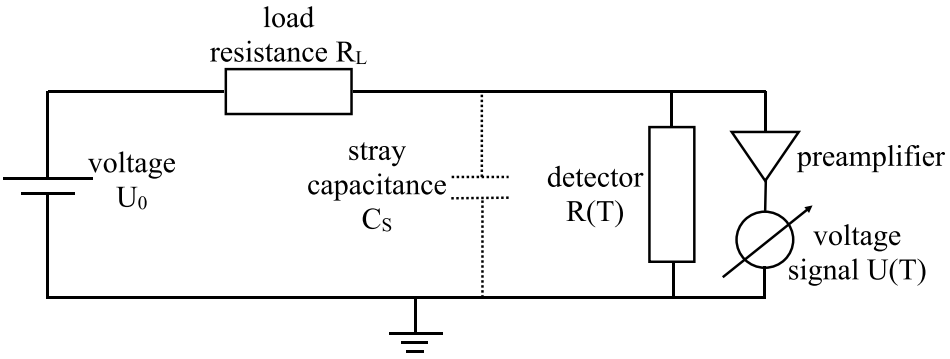

Fig. 2.7. Readout scheme for a current-biased CLTD: The temperature-dependent resistance $R(T)$ is biased with a constant current I in series with a load resistance R_L. As long as $R_L \gg R(T)$, the current does not change if $R(T)$ varies. The resistance change $\Delta R(T)$ is read out directly as a voltage signal $U(T)$ [164,184].

If the resistance change ΔR is small against the resistance of the thermistor at the operating temperature, the voltage signal is described by

$$\Delta \mathrm{U}(t) = U_{max} \cdot \left[\exp\left(-\frac{t}{\tau_{eff}}\right) - \exp\left(-\frac{t}{\tau_{el}}\right) \right] \tag{2.18}$$

$$\text{with } U_{max} = \frac{\epsilon \cdot E}{C} \cdot \frac{dR}{dT} \cdot I \tag{2.19}$$

If $\tau_{el} \ll \tau_{eff}$ is no longer fulfilled, the voltage amplitude U_{max} decreases. Therefore, the stray capacities have to be kept sufficiently small. But also the resistance $R(T_{base})$ has to be kept small enough so that the condition $\tau_{el} \ll \tau_{eff}$ is not jeopardized. Otherwise, a larger resistance may result in a smaller voltage signal even if the same measurement current is applied (for more details see [164,184]).

2.4. Energy resolution

An important property that characterizes any energy detector is its energy resolution. As the energy transfer to either charge or light or – in the case of CLTDs – heat is governed by statistical processes, the response of an energy detector to the detection of an ensemble of mono-energetic particles with energy E_0 is given by a Gaussian distribution:

$$p(E) = \frac{1}{\sqrt{2\pi}\,\sigma} \exp\left(-\frac{(E-E_0)^2}{2\sigma^2}\right) \tag{2.20}$$

$p(E)$ thereby describes the probability distribution to detect a particle of energy E_0 in an energy interval $E_0 + dE$. σ is the standard deviation of the energy. More commonly, energy detectors are characterized by the **F**ull **W**idth at **H**alf **M**aximum (FWHM) of the distribution, also referred to the *energy resolution* ΔE of a detector. It is given by

$$\Delta E = 2\ln(2)\,\sigma \approx 2.35\,\sigma \tag{2.21}$$

The energy resolution is determined by a sum of different contributions which can roughly be divided into two categories: *Baseline noise* describes all noise sources which are independent of the particle detection process. The conversion of the particle energy into phonons, on the other hand, may be impeded by loss processes which are again subject to statistical fluctuations and, therefore, contribute to the energy resolution. In the following discussion, we will summarize these contributions as *conversion noise*.

D. McCammon has given an excellent discussion of the different contributions to the energy resolution of CLTDs in [178]. For the sake of completeness, we will summarize the main arguments of this discussion concerning resistance thermometers in Section 2.4.1. Section 2.4.2 will focus on the specific details for the detection of heavy ions, in particular regarding the conversion of the ion energy into phonons. In Section 2.4.3, the theoretical limit of the energy resolution of a CLTD will be discussed.

2.4.1. Baseline noise due to thermal and electronic noise sources

2.4.1.1. Noise due to thermodynamic fluctuations (phonon noise)

A CLTD is fundamentally a heat capacity C coupled to a heat sink at temperature T_{bath} by a finite thermal conductivity k (see Fig. 2.1). Even in equilibrium, phonons are exchanged constantly between the absorber and the heat sink. The fluctuation in the energy content of the detector is given by fundamental thermodynamics as

$$\left\langle \Delta U^2 \right\rangle = k_B T_{bath}^2 C \tag{2.22}$$

where k_B is the Boltzmann constant. Taking into account the thermal conductivity as well as the electrothermal feedback, this equation is modified to

$$\langle \Delta U^2 \rangle = k_B T_{bath}^2 \, k\tau_{eff} \tag{2.23}$$

This equation assumes that detector and heat bath are in total thermal equilibrium with $T_{base} = T_{bath}$. However, due to the finite thermal coupling the real detector temperature will always be somewhat higher than T_{bath}. To take this into account, J. C. Mather has derived an *effective thermal coupling constant* $k^\star$ [198] with specific correction terms for insulators, metals and superconductors.

2.4.1.2. Johnson noise of thermometer and load resistor

When a current is flowing through a resistance, heat dissipation is unavoidable. The thermal fluctuations of the charge carriers create small voltage changes which are referred to as *Johnson noise*. This type of noise is always present in a resistance thermometer and contributes to the overall energy resolution. Following D. McCammons derivation [178], the spectral density function can be written as

$$e_{J,therm} = \frac{R_L}{R_L + R(T)} \, \frac{\sqrt{4k_B T \, R(T)}}{1 - \beta A} \tag{2.24}$$

The term βA takes into account the electrothermal feedback. For positive electrothermal feedback (positive α) as in transition-edge sensors, this factor may considerably enhance the Johnson noise [198]. Expression (2.24) illustrates that Johnson noise can be minimized if the load resistance R_L is kept large compared to the thermistor resistance $R(T)$. In that case, Eq. (2.24) is simplified to

$$e_{J,therm} \approx \frac{\sqrt{4k_B T \, R(T)}}{1 - \beta A} \tag{2.25}$$

One advantage of low temperature detectors is that the low operating temperatures generally lead to low values of the Johnson noise term.

Phonon noise and Johnson noise are present in every type of resistance thermometer. Therefore, it is common to summarize these contributions in one formula and write for the intrinsic energy resolution of a CLTD [50,51,178]:

$$\Delta E_{int} = 2.35 \, \xi \, \sqrt{k_B T^2 mc} \,, \quad 1 < \xi < 3 \tag{2.26}$$

m is the total mass of the detector, c is its specific heat capacity. The factor ξ takes into account the contribution to the heat capacity of conducting electrons, as well as the effective thermal coupling constant $k^\star$.

The thermal movement of the atoms in the thermistor leads to statistical fluctuations of the resistance which cause statistical fluctuations of the current flowing through the thermistor. The noise spectral density is proportional to $1/f$ [178]. Therefore, this contribution is often referred to as $1/f$ *noise*.

2.4.1.3. Amplifier noise

Preamplifiers and amplifiers may also contribute to the overall electronic noise. Following the discussion in [178], their noise can be described as a quadratic sum of voltage noise and current noise:

$$(\Delta U)^2 = (\Delta U_A)^2 + \frac{R_L}{R_L + R(T)} \, \frac{(\Delta I_A)^2}{1 - \beta A} \tag{2.27}$$

This term is minimized if the condition $R_L \gg R(T)$ is fulfilled which is also demanded by the minimization of the Johnson noise. In addition, care has to be taken to choose amplifiers which are optimally adapted to the thermistors, in particular regarding the input impedance. Generally, it is possible to make the amplifier noise sufficiently small so that it is negligible as compared to the other noise sources [178].

2.4.1.4. Photon noise

The detector exchanges energy with its environment not only via the thermal link to the heat sink. Thermal radiation from the environment of the detector may also introduce heat into the absorber. The fluctuations of the thermal radiation present an additional source of thermal fluctuations. Its spectral density function is independent of the frequency and, according to the Stefan-Boltzmann-law, given by

$$e_{SB} = \sqrt{4\sigma_{SB} \, k_B T_{en}^5}, \quad \sigma_{SB} = \text{Stefan-Boltzmann constant} \tag{2.28}$$

It has to be emphasized that T_{en} in this equation refers to the temperature of the heat radiating surfaces surrounding the detector, not to the operating temperature of the detector. Taking into account absorption and emission coefficients of the absorber, as well as the solid angle of the heat radiation hitting the detector, this translates into a contribution to the energy resolution of [199]

$$\Delta \mathrm{E}_{photon} = 2.35 \sqrt{\tau_{eff} \cdot \frac{\Omega}{\pi} \cdot a(\lambda)\epsilon(\lambda) \, A_D \cdot 8\sigma_{SB} k_B T_{en}^5} \tag{2.29}$$

where A_D is the active detector surface and Ω the solid angle. The factors $a(\lambda)$ and $\epsilon(\lambda)$ take into account the absorption and emission coefficient of the detector surface. In particular for the detection of heavy ions, apertures towards a beamline or target cannot be completely omitted because heavy ions have only a short range in matter and will be hindered to reach the detector if thin foils at low temperatures are introduced. Therefore, heat radiation from room temperature sources can introduce a considerable amount of heat to heavy ion CLTDs. To minimize this contribution, the detectors are generally surrounded by several thermal shields. Apertures are kept as small as reasonably possible by experimental demands. If feasible, i.e. for higher ion energies, cooled entrance windows made of ultra-thin foils are applied (see Sections 3 and 4 for a more detailed discussion).

2.4.1.5. Summary

As described by Eq. (2.26), phonon and Johnson noise may be combined and can be estimated if the heat capacity and the operating temperature of the detector are known. Examples are given in Tables 2.1 and 2.2. As quoted in Table 2.1, for a sapphire absorber with a volume of 1 mm^3 an energy resolution of 2.2 keV can be estimated for an $\alpha-$particle with an energy of 1 MeV at an operating temperature of 1 K. The contribution of photon noise and amplifier noise have to be added quadratically to this contribution. However, as discussed above, the amplifier noise can usually be neglected as compared to the other noise sources. The photon noise depends very strongly on the experimental conditions and may, therefore, contribute considerably to the overall noise budget.

2.4.2. Conversion noise

Conversion noise or thermalization noise summarizes all noise sources which are connected to the process of transferring the kinetic energy incident on a CLTD to a temperature signal. In Section 2.1 and Section 2.3.1, the processes which govern the energy deposition of a heavy ion or an x-ray in the absorber have been discussed in detail. All of these processes are subject to statistical fluctuations which contribute to the energy FWHM. In addition, losses of the deposited energy as well as losses of phonons, which do not contribute to the thermal signal, may occur. The statistical fluctuations of these losses may also increase the energy resolution of the detector.

2.4.2.1. Quantum fluctuations (statistics of the detected quanta)

In the case of an ideal CLTD, all kinetic energy incident on the detector is used to create phonons. For a phonon at a temperature T, the energy is given by

$$E = k_B T \tag{2.30}$$

The number of created phonons is therefore given by the simple relation

$$N = \frac{E_{kin}}{k_B T} \tag{2.31}$$

As the creation of phonons is a statistical process, the ultimate limit in energy resolution is given by the statistical fluctuations of their number, i.e.

$$\Delta E_{qf} = 2.35\sqrt{N} k_B T = 2.35\sqrt{E_{kin}\, k_B T} \tag{2.32}$$

However, for heavy ions with a kinetic energy of the order of MeV, the number of phonons is very large (of the order of 10^9). As a consequence, the contribution of quantum fluctuations to the energy resolution is relatively small. Examples are given in Table 2.3 in Section 2.4.3. The contribution to the energy resolution is, for example, $\Delta E_{qf} = 62$ eV for α-particles with an energy of 5.5 MeV, $\Delta E_{qf} = 133$ eV for uranium ions with an energy of 18 MeV, and $\Delta E_{qf} = 845$ eV for uranium ions with an energy of 1 GeV. For 50 keV x-rays, an energy resolution of $\Delta E_{qf} = 38$ meV can be calculated from the values given in Table 2.2.

2.4.2.2. Statistics of energy loss processes

In a real CLTD, the incident energy may not be transferred to 100% to heat and may not fully contribute to the temperature signal. Different loss processes may occur which lead to a fluctuation in the detected amount of energy. The statistics of these fluctuations lead to an additional contribution to the energy resolution. For semiconductor detectors, the most pronounced effect is the reduction of the detected energy due to recombination of the electrons and holes. When the created charge density is very high – which is often the case for the detection of heavy ions – the electrons and ions recombine before the electrons reach the electrode and contribute to the energy signal. This so-called pulse-height-defect (see also Section 2.5) leads to a decrease in the energy signal, but also to a decrease in energy resolution because the number of the detected electrons fluctuates. For CLTDs, this effect is expected to be negligible because after recombination the excitation energy is transferred to heat and, accordingly, it is detected. However, there are other loss processes which may play a role in CLTDs (see also Fig. 2.6). H. H. Andersen [53,54] has given a detailed discussion of energy loss processes of various ions in a diamond absorber and their influence on the energy resolution of a CLTD. His results are summarized in Fig. 2.8. In the doubly logarithmic scale, the FWHM decreases almost linearly with temperature if only thermodynamic fluctuations are taken into account. However, the different contributions of internal electrons, fluorescence, as well as Frenkel pairs lead to an increase in the FWHM which is independent of the detector volume and leads to the different horizontal lines in Fig. 2.8.

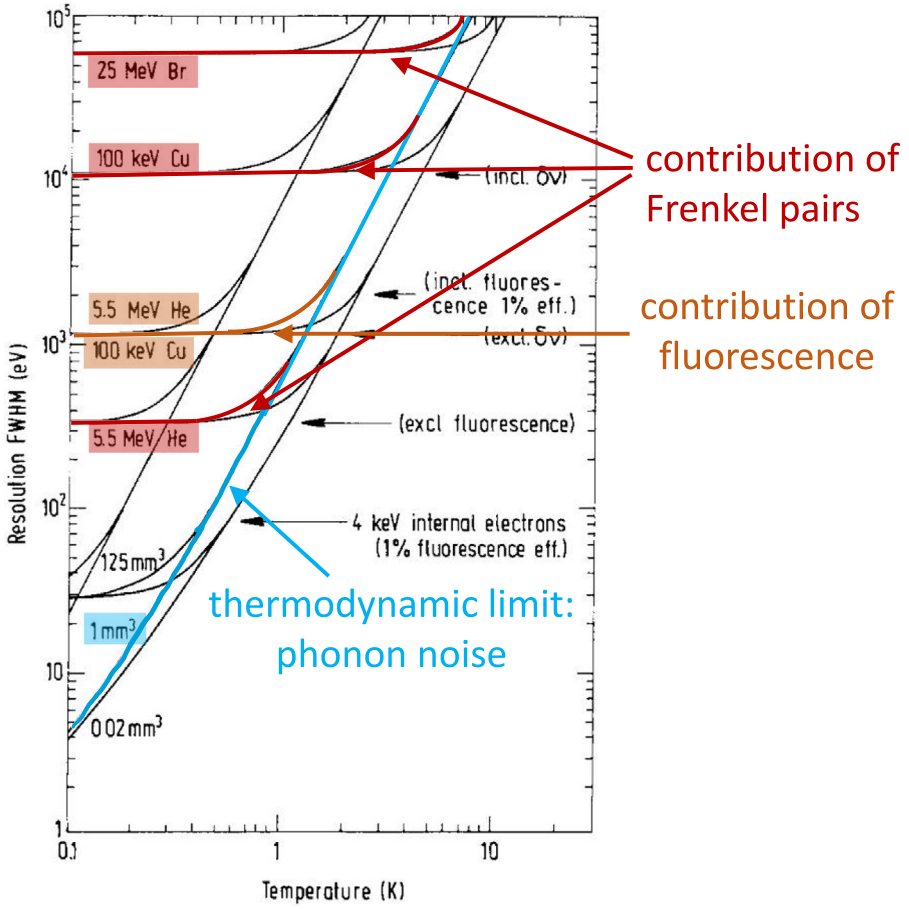

Fig. 2.8. Theoretical predictions for the energy resolution for the detection of various ions in a CLTD with a diamond absorber of different volumes. The calculation for the absorber volume of 1 mm^3 is highlighted. The blue line describes the thermodynamic limit from fluctuations in the number of phonons (Eq. (2.32)). The contribution from the creation of Frenkel pairs (marked in red) is dominant for the heavy ions Br and Cu and limits the relative energy resolution to $\Delta E/E = 2 \times 10^{-3}$ for 25 MeV Br ions and to $\Delta E/E = 11\%$ for 100 keV Cu ions. For the light ion He, the contribution from losses by fluorescence (marked in dark orange), i.e. photons, is more significant. It limits the relative energy resolution to $\Delta E/E = 2 \times 10^{-4}$. *Source:* Figure adapted from [54].

Creation of Frenkel pairs

As was described in Section 2.3.1, electronic as well as nuclear energy loss can result in a permanent displacement of absorber atoms from their lattice position. Such *Frenkel pairs* [54,200] can be very long-lived for the low operating temperatures of CLTDs. The displacement energy is then stored in the lattice and not converted into phonons. Accordingly, Frenkel pairs act as *phonon traps*. The trapped phonons do not contribute to the temperature signal. This has two consequences: On the one hand, the temperature signal will be reduced and may no longer be proportional to the kinetic energy of the detected ion. On the other hand, the quantum fluctuations of the loss process will contribute to the energy resolution of the detector according to

$$\Delta E_{FP,n} = 2.35\sqrt{0.42\,\frac{\delta E_n}{E_d}}\,Q_{FP} \tag{2.33}$$

$$\Delta E_{FP,el} = 2.35\sqrt{0.17\,\frac{\delta E_{el}}{E_d}}\,Q_{FP} \tag{2.34}$$

δE_n and δE_{el} denote the integral of the nuclear and electronic stopping power along the ion path. Q_{FP} is the amount of heat trapped by one Frenkel pair, and E_d is the displacement energy [54,201]. According to H. H. Andersen [54], there is no coupling between the electronic and the nuclear stopping channels. Therefore, both contributions have to be weighted with the relative contribution of nuclear and electronic energy deposition and have to be added quadratically. The relative contributions depend on the nuclear charge and mass of the incident ion and of the target material, as well as on the ion energy.

Table 2.3
Calculated values for the different contributions to the conversion noise of a CLTD after the impact of an ion: E_d is the displacement energy of the lattice, Q_{FP} is the energy necessary to create a Frenkel pair. δE_n and δE_{el} are the deposited nuclear and electronic energy contributions integrated over the ion path. $\Delta E_{FP,n}$ and $\Delta E_{FP,el}$ describe the contributions to the FWHM energy resolution by the creation of Frenkel pairs, ΔE_{fl} the contribution of fluorescence and $\Delta E_{(FP)^2}$ the fluctuations between nuclear and electronic energy loss. ΔE_{CN} is the squared sum of all contributions to the conversion noise. For comparison, the last column displays the FWHM expected from quantum fluctuations according to Eq. (2.32). All calculations were performed for an operating temperature $T_{base} = 1.5$ K and an absorber volume $V = 1\,\text{mm}^3$.

Absorber	Ion	δE_n [MeV]	δE_{el} [MeV]	$\Delta E_{FP,n}$ [keV]	$\Delta E_{FP,el}$ [keV]	ΔE_{fl} [keV]	$\Delta E_{(FP)^2}$ [keV]	ΔE_{CN} [keV]	ΔE_{qf} [keV]
Diamond	$E_d = 28$ eV		$Q_{FP} = 12$ eV						
	5.5 MeV α[a]	0.006	–	0.3	–	1.0	0.4	1.1	0.062
	25 MeV Br[a]	1.1	–	3.6	–	2.2	52	52	0.133
Sapphire	$E_d = 16$ eV		$Q_{FP} = 9$ eV						
	5.5 MeV α[b]	0.011	5.48	0.4	5.1	1.4	0.1	5.2	0.062
	18 MeV U[b]	8.69	9.30	9.3	6.7	2.4	429	429	0.133

[a]Calculation of H. H. Andersen taken from [54].
[b]Present work [164].

Additional energy loss processes

A certain fraction of the incoming ions may be backscattered from the surface of the absorber or cause sputtering of absorber ions. However, the sputtering cross section is strongly dependent on the energy. Therefore, only heavy ions at energies below 1 MeV may cause considerable sputtering yields which may then deteriorate the detector performance. If the detection of such low ion energies is intended, a careful determination of sputtering yields is needed [54] (see Fig. 2.6).

When electronic energy loss is dominant, the creation of fluorescence photons has to be considered. When ions and electrons which have been created by electronic stopping processes recombine, they can transfer their recombination energy also into the creation of photons. While most of these photons will remain in the absorber (dependent on the absorber volume) and therefore will contribute to the temperature signal, a small amount of photons may escape from the absorber and cause a loss in the detected energy. For diamond absorbers, H. H. Andersen [54] estimates this contribution to be around 1% of the particle energy, because diamond is a very efficient scintillator (see Fig. 2.8). As will be discussed in Section 3, sapphire is used as absorber material for most of the present investigations. Sapphire scintillates only at very low temperatures well below 1 K [202], so an upper limit of 1% probably overestimates this contribution.

As an alternative to fluorescence photons, the recombination energy can also be used to create $\delta-$electrons. However, according to H. H. Andersen [54] this mechanism is negligible in insulators. Electrons which have been created by electronic energy loss can also be trapped in metastable states. If the life time of these states is long compared to the thermalization time, the trapped electrons do not recombine in time to contribute to the temperature signal. The life time and the number of such states depends strongly on the absorber material. For single crystals like diamond or sapphire, their density is relatively small. However, in heavily doped semiconductor thermistors they may cause significant losses of the deposited energy [203,204].

Radiation damage

Radiation damage may occur in CLTDs after the detector was irradiated with a critical dose which depends on the absorber material, as well as on the nuclear charge and the energy of the incident ions. If the number of Frenkel pairs becomes too large, the crystal lattice of the absorber may suffer permanent damage. In particular for heavy ions, the defect density along the track can become considerable, creating so-called *thermal spikes* [201,205]. Within these spikes, the crystal locally melts. Due to the high density of charges, the displaced atoms are driven out of the melted volume (*Coulomb explosion*) [205], leaving behind a permanently amorphous *ion track*. In this amorphous region, the Debye law for the heat capacity no longer holds. The heat capacity can become considerably larger than in the crystalline regions. Thus, ion tracks may severely decrease the temperature signal. In addition, they may hinder the thermalization process because the mean free path of phonons in such amorphous regions is much smaller than in a crystal [27].

Excess noise

In addition to the contributions discussed above, D. McCammon et al. have observed additional noise contributions in semiconductor thermistors. They call them *excess noise*. Different mechanisms have been proposed for this noise contribution:

- D. Liu et al. contributed part of it to the limited coupling between the electron and the phonon system in a thermistor. This limited coupling between the two thermal systems leads to a fluctuation in the energy content between electrons and phonons, thus causing fluctuations in the temperature signal [206].
- In [179], D. McCammon discusses a second possible mechanism which is related to two-dimensional effects in the electron gas. This effect is more pronounced for silicon thermistors because the doped layer in these thermistors is relatively thin.
- D. McCammon discusses also a potential local dependence of the energy response function [178]. This aspect will be further elaborated in Section 3.6.2.1.

Table 2.4
Example for the different noise contributions in two detectors with an Al TES and a germanium thermistor [164]. All values were calculated for an operating temperature of $T_{base} = 1.5$ K and are given in keV. The conversion noise for a 5.5 MeV α-particle was scaled with the volume of the sapphire absorber to $\Delta E_{CN} = 5.5$ keV.

	Johnson noise	Amplifier noise	Phonon noise	Photon noise	Sum including ΔE_{CN}
Al TES	5	5	7	2	11
Ge	40	19	8	2	45

As all the contributions discussed in Section 2.4 are considered independent of each other, they have to be added quadratically in order to get a full estimate on the expected energy resolution.

2.4.3. Theoretical limit of the energy resolution of a CLTD

Table 2.1 in Section 2.2 illustrates the dependence of the energy resolution on the operating temperature and the Johnson noise for the example of an α-particle in a sapphire absorber with a volume of 1 mm^3, taking into account only the thermodynamic fluctuations. In particular, the value of $\Delta E_{theo} = 2.2$ keV at 1 K – which is independent of the energy of the α-particle and only dependent on the operating temperature – may be compared to the results of Table 2.3, where the contribution of the conversion noise is estimated to be 5.2 keV. Eq. (2.26) does not take into account either the nature of the detected particles or details of the energy deposition process. However, it represents a lower limit for the energy resolution that can be obtained. Compared to that value, the contribution from quantum fluctuations ΔE_{qf} as shown in Table 2.3 can be neglected.

In Table 2.4, the conversion noise is compared to the other noise contributions for two detectors which were used in part of the present investigations [164]. The detectors are described in detail in Sections 3.2.2.1 and 3.2.3.1. The point has to be stressed that these noise contributions strongly depend on the thermistor type, operating temperature and specific experimental conditions, and may vary accordingly. For the germanium thermistor which operates with a resistance of $\sim$200 kΩ, the Johnson noise is clearly the dominating factor, while for the TES with an operating resistance of $\sim$50 kΩ, all contributions are of the same order of magnitude. The energy resolution for α-particles was in all cases above this theoretically estimated limit, indicating that other limits on the energy resolution are present. Further details of the detector performance and additional noise sources will be presented in Section 3.

2.5. Potential advantages over conventional detection schemes

Due to their operation principle CLTDs provide potential advantages over conventional ionization detectors, such as semiconductor detectors or ionization chambers, etc. Whereas the following discussion is valid for many kinds of CLTDs for various applications, a special emphasis is given to detection schemes for heavy ion physics, namely detectors for energetic heavy ions and hard x-rays. Potential advantages of CLTDs with respect to basic detector properties are:

- the smaller energy gap ω for the creation of an elementary excitation, leading to a better counting statistics of the detected quanta. Whereas the energy gap ω for producing an electron–ion pair or a photo electron in a conventional ionization detector based on charge collection is of the order of one to tens of eV (about 0.7–1 eV for a semiconductor detector and about 10–30 eV for a gaseous ionization detector [1,2]), the excitation energy of thermal phonons is of the order of $\omega \leq 10^{-4} - 10^{-3}$ eV [1]. This results in much lower statistical fluctuations, decreasing with $\sqrt{\omega}$ (see Section 2.4.2.1), and therefore in a potentially better energy resolution and a lower energy threshold. It should be noted, however, that – in contrast to the case of x-rays – for the relatively large incident energies of energetic heavy ions this effect is of minor importance as compared to other limiting factors, except for the lowest total energies of $E \leq 10$ MeV;
- the more complete energy detection leading to considerably smaller statistical fluctuations of the loss processes, and to a better energy linearity, as compared to detectors based on charge collection. Whereas in CLTDs the majority of the incident energy (at least more then 95%) is converted into heat (within a relatively short thermalization time of $\ll 1\,\mu$s) after the decay of the initial electronic excitations (see Section 2.4.2, Table 2.3 and [54]), considerable losses in the ionization signal up to 60%–80% may appear for ionization detectors due to direct phonon creation and charge recombination. The latter effect is particularly dominating for the impact of very heavy ions in matter due to the creation of extremely high charge densities. Besides the deficit of the detected energy, this effect results also in a substantial pulse height defect [154,207–210], which is dependent on energy, mass and nuclear charge of the incident ion. For example, this defect for different ion species can be as high as about 60% when comparing the signals created by a carbon ion to those of an uranium ion at the same energy (see Section 3.6.2 and Fig. 3.21). Therefore, besides statistical fluctuations of the loss processes, affecting the limit in energy resolution, the pulse height defect affects substantially the linearity of the energy response. Therefore CLTDs provide an energy measurement which is usually independent of energy, mass and nuclear charge of the incident ion.

- the ability to efficiently detect weakly or non-ionizing particles, which is also due to the almost complete energy detection of CLTDs. This effect is important, for example, for the detection of very slow ions for which the stopping power is dominated by nuclear stopping, or for the search for dark matter (see Section 1).
- the lower detection threshold due the fact that CLTDs can be constructed without any dead layers and, in some cases, also without entrance windows, which are unavoidable in conventional ionization detectors and therefore result there, especially for very slow heavy ions, in limitations in detection efficiency, energy resolution due to energy loss straggling effects, and energy linearity due to the Z-dependent energy loss in the inactive detector components;
- the flexibility in the choice of the absorber material. As compared to conventional ionization detectors, a much wider variety of materials is expected to fulfill the conditions for absorber materials of calorimetric detectors (see Section 2.2). The absorber material may therefore be optimized with respect to radiation hardness (important for heavy ion detection), and detection efficiency, for example to optimize the photopeak efficiency for x-rays. The short lifetimes caused by radiation damage, mainly due to lattice damage by nuclear stopping, is one of the limitations of semiconductor detectors when detecting high count rates of very heavy ions. Other criteria, for which the choice of the absorber material is important, are defined by the individual experimental demands, such as for example applications where the radiation source is identical with the absorber material (see Section 1);
- the smaller noise power at low temperatures. Several contributions to the thermal and electronic noise are decreasing with temperature, and are therefore reduced due to the low operating temperatures of CLTDs (see Section 2.4.1).

Finally the performance of CLTDs is compared with some other conventional detection techniques, which are not operating on charge collection:

- Magnet spectrometers provide similar or even higher energy resolution, but they are, in particular for higher incident ion energies, relatively big devices, not easy to handle, and are limited by relatively small solid angle acceptance and a narrow dynamic range. Moreover they are limited, in particular for the detection of slow heavy ions, by charge state ambiguities.
- Dispersive detection techniques, such as crystal spectrometers [172,211], which are frequently used for high resolution detection of x-rays, provide very good or even better energy resolution, but on the cost of dynamic range and detection efficiency due to the very limited solid angle acceptance.

3. CLTDs for the energy-sensitive detection of energetic heavy ions

3.1. Experimental conditions and specific requirements for the detection of energetic heavy ions

The research project for the design, development and construction of CLTDs for the energy-sensitive detection of energetic heavy ions was motivated by the rapid development of heavy ion physics in numerous research facilities, already existing or under construction or being planned, world wide [124–134,136–145]. These research facilities already provide, or will provide, excellent conditions for various experimental research projects of high interest, and have already attracted a world-wide growing community of researchers. One prominent example is the GSI/FAIR facility at Darmstadt, Germany [124,128–130].

Heavy ion beams of highest intensity and quality, and well performing separators providing, among others, high intensity secondary radioactive beams, reaching far outside the valley of stability in the chart of nuclides, high intensity beams of fission fragments, and highly effective production of very rare species like superheavy elements, are or will be soon available. They have therefore a large potential for addressing a wide spectrum of many important questions in nuclear physics, nuclear astrophysics, applied heavy ion physics, and many more [124–131,212] which will address, among others, the exploration of the limits of nuclear stability (dripline nuclei, superheavy elements), the exploration of astrophysical scenarios (element synthesis in the universe, supernova evolution, s-, r-, rp-processes, etc.), the isospin dependence of nuclear structure, as well as new modes of collective excitations (access to the nuclear equation of state), the dynamics of nuclear fission processes, and the interaction of heavy ions with matter.

Therefore, heavy ion detectors with highest energy resolution and/or highest detection efficiency, good energy-pulse height linearity, low detection threshold, and radiation hardness are required:

- for high-resolution nuclear spectroscopy with cooled heavy ion beams available from storage rings;
- for mass identification via combined energy/time-of-flight detection for reaction products in direct reaction- and γ-spectroscopy experiments with radioactive beams. Such experiments, performed in inverse kinematics, require an event by event identification of the beam-like reaction products;
- for a unique background-free and highly efficient mass determination – again via combined energy/time-of-flight techniques – for the identification of superheavy elements;
- for a highly efficient and background-free identification of rare isotopes in accelerator mass spectrometry [163] via a high-resolution total energy measurement. Hereby, high detection efficiency for very slow heavy ions ($E \leq 0.1\,\mathrm{MeV/u}$) is also very important;
- for an identification of fission isotopes from neutron induced fission;
- for a precise determination of stopping powers of heavy ions in matter.

Table 3.1
Range of various heavy ions in sapphire for energies between 0.1 and 500 MeV/u, calculated using the program SRIM [213].

Energy	Range in μm for			
in MeV/u	^{20}Ne	^{40}Ar	^{132}Xe	^{238}U
0.1	1.4	1.6	2.7	2.7
1	6	7	10	12
10	94	72	57	62
100	4760	2980	1230	945
500	70 800	43 800	15 900	8080

When designing cryogenic detectors for energetic heavy ions, it has to be realized that the conditions and detector parameters with respect to absorber size, incident energy, energy resolution, amount of radiation damage, etc., are different by orders of magnitude from those of most other applications of such detectors (see Section 1). The typical incident kinetic energies of the heavy ions to be detected in the various applications range from energies well below the Coulomb barrier ($E \leq 0.05 - 1$ MeV/u) via energies around the Coulomb barrier ($E \approx 3 - 10$ MeV/u) up to relativistic energies ($E \geq 100 - 2000$ MeV/u), thus corresponding to total energies of $E \approx 10 - 20$ MeV up to some hundred GeV. Despite the relatively large total energies, the high specific energy loss of heavy ions in matter leads to comparably small ranges (2 μm − 15 mm in most cases, except for light relativistic ions, see also Table 3.1), thus allowing relatively small absorber volumes. If quantitatively compared to the detection of photons, electrons or protons and light ions, etc., it turns out that, due to the characteristic energy loss processes, the energy deposit per range in matter is for heavy ions by orders of magnitude higher. This specific feature makes CLTDs, which reach their highest sensitivities for small absorber sizes, attractive for the detection of heavy ions. Due to the relatively high incident energies, already operating temperatures around 1.5 K will allow sufficient sensitivity of calorimetric detectors for heavy ions, thus reducing the demands on low temperature technology.

Concerning the energy resolution power required a relative resolution of $\Delta E/E$ of the order of one to a few times 10^{-3} would, as compared to conventional heavy ion detectors, be already a big step forward for various applications in heavy ion physics.

3.2. Detector design and detector characterization

3.2.1. Sapphire absorbers

As described in Section 3.1, the short ranges of heavy ions in matter favor small absorber sizes for CLTDs. Following the discussion in Section 2.2, a high temperature signal is obtained by realizing a small absorber heat capacity and a high sensitivity of the thermistor. On the other hand, the active detector area cannot be made arbitrarily small. Therefore, a material with low specific heat capacity is mandatory. As the detection of heavy ions does not demand for any specific properties of the absorber (except radiation hardness and a fast and complete thermalization), an insulator with a high Debye temperature is an obvious choice. According to H. H. Andersen, diamond is the ideal absorber from the heat capacity point of view, because its Debye temperature is exceptionally high [54]. In addition, it is the hardest material available and shows exceptional resistance against radiation damage by heavy ions [214]. However, it is also a very expensive material, hard to machine and difficult to grow to large crystals. A close choice is sapphire (single crystal Al_2O_3) with a Debye temperature of around 1000 K. Because it is widely used in laser physics, large single crystals of excellent crystal quality are available at a reasonable cost. It can be machined into a wide variety of geometries, including thin wafers which can be used as substrates for photolithography. Its heat conductivity, which is exceptionally large for an insulating material, is a further advantage [215]. B. Canut et al. have investigated the susceptibility of sapphire to radiation damage caused by swift heavy ions [216]. While small damage effects have been observed, the effect was much smaller than in quartz or conducting oxides.

The impact of α-particles on a single crystal of sapphire has been investigated by K. W. Shepard et al. already in 1975 [35]. They used a superconducting aluminum film as a resistance thermometer, even though no energy-sensitive particle detection was intended. Following these investigations, sapphire absorbers with superconducting aluminum transition-edge sensors are one type of CLTDs which have been developed for heavy ion detection. These detectors are described in detail in Section 3.2.3. To overcome the limited dynamic range of transition-edge sensors, composite detectors consisting of a sapphire absorber and a semiconductor thermistor were also investigated. These detectors are discussed in Section 3.2.2.

3.2.2. CLTDs based on semiconductor thermistors

3.2.2.1. Detector design

As is described in Section 2.2, semiconductor thermistors consist of silicon or germanium which is heavily compensated doped to achieve a conductivity slightly below the metal–insulator transition [12,179]. In this case, the temperature dependence of the resistance below 4 K is given by Eq. (2.7) (see also Fig. 2.4). For the present investigations, germanium

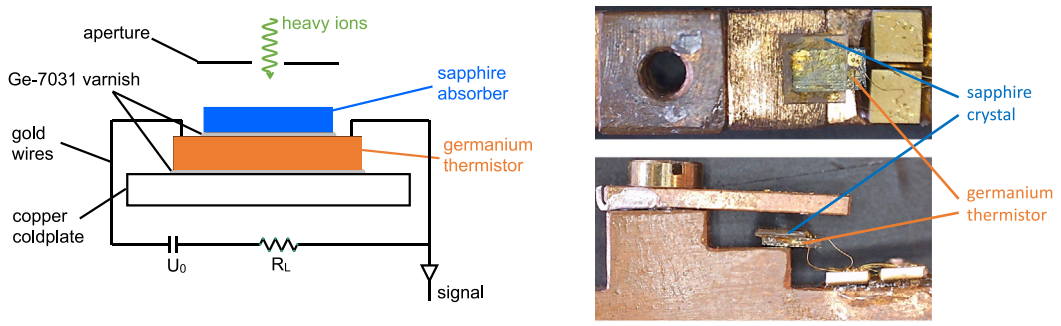

Fig. 3.1. On the left-hand side, a schematics of the composite CLTD with a germanium thermistor and a sapphire absorber is displayed (adapted from [15]). The germanium thermistor is glued on the copper cold plate by means of GE7031 varnish [217]. The sapphire absorber, in turn, is glued onto the germanium thermistor with GE7031. On the right-hand side, photos of the detector are shown. To make sure that only the sapphire absorber is hit by the ions, an aperture with a diameter of 0.5 mm was mounted in front of the CLTD.

thermistors were chosen. These had been produced by the *Chemical and Metallurgical Division of Sylvania Electric Products Inc.*.[2] The doping concentration was chosen sufficiently high to provide a high value of α in the intended range of operating temperatures around 1.5 K. The germanium crystals were doped with $2 \times 10^{17}\,\mathrm{cm}^{-3}$ of indium and $1 \times 10^{17}\,\mathrm{cm}^{-3}$ of antimony by conventional ion implantation. The original crystals of $6 \times 3 \times 0.5\,\mathrm{mm}^3$ were cut into pieces of $0.5 \times 0.5 \times 0.5\,\mathrm{mm}^3$ and $1 \times 0.5 \times 0.5\,\mathrm{mm}^3$.

In addition to the electronic noise sources discussed in Section 2.4, *Schottky noise* can provide a considerable contribution to the overall noise budget if the contact resistance between the thermistor and the readout cables is large. If a semiconductor is contacted to a metal, the free electrons from the metal will travel into the semiconductor and create a depletion layer [27]. The resulting *Schottky barrier* prevents charge carriers from the semiconductor from traveling into the metal, thus effectively suppressing conduction. To minimize this effect, the contact surfaces of the germanium crystals contain a layer with increased doping concentration of boron doping and are covered with a contact layer of palladium and gold. Electronic contacts are realized by ultrasonic bonding of gold wires with a diameter of 25 μm.

In early investigations a monolithic germanium CLTD was used. That means that the germanium crystal was chosen as absorber and thermistor at the same time. However, tests with heavy ions showed that germanium was not a suitable absorber material. Using the germanium crystals directly for the detection of heavy ions did not yield satisfactory results [151,217]. The spectra showed a complex multi-peak structure which was dependent on operating temperature and position of the ion impact. These structures were interpreted as effects of inhomogeneities in the doping concentration, of inhomogeneous thermalization and of energy loss processes.

Consequently, a composite detector with sapphire absorber(s) was realized for a germanium crystal from the first production badge [152,217]. The sapphire absorber had a thickness of 0.3 mm and lateral dimensions of about $1.8 \times 1.9\,\mathrm{mm}^2$. It was glued onto the germanium thermistor by means of the low-temperature epoxy GE7031.[3] This epoxy provides high thermal conductivity at low temperatures. In addition, it maintains its mechanical flexibility, thus mediating between the different thermal expansion coefficients of sapphire and germanium. The schematic setup and photos are displayed in Fig. 3.1. For the first prototypes, the detectors were glued on the copper holders by means of GE7031 varnish. However, it was discovered that this coupling was too strong and led to a loss in signal amplitude of the thermal signal and bad energy resolution [217,218]. Therefore, in the later design the thermal coupling between thermistor and heat sink was realized by the wires which also provide electrical contact.

The electrical contact of the germanium thermistor is realized by means of so-called *ultrasonic ball bonding*. The concept is displayed in Fig. 3.2. A gold wire of typically 25 μm in diameter is formed into a ball, pressed onto a gold contact surface and fixed there by a pulse of ultrasonic power. Then the bond tip is moved to the gold contact pad, where the gold wire is again fixed by pressure and ultrasonic power. With this technique, small yet mechanically quite stress-resistant connections are realized which are strong enough to hold the small sapphire crystal without further support.

To provide the connection to the preamplifiers at room temperature, the gold coated pins for electrical contact are soldered to wires of phosphor bronze. Phosphor bronze is an alloy with low thermal conductivity, thus minimizing the introduction of heat load from room temperature to the detectors. To further reduce this heat load, the wires are thermally anchored by wrapping them around copper cylinders which in turn are screwed to the different temperature stages at 77 K and 1.2 K. Again Ge7031 is applied for additional thermal contact.

For a later experiment at high ion energies, an additional sapphire absorber with a thickness of 6 mm and a diameter of 3 mm was glued onto the first sapphire absorber. Fig. 3.3 shows this composite detector on the left-hand side. The

[2] Today: *Osram Sylvania Inc.*, Wilmington (DEL), USA.

[3] Cryophysics GmbH, Dolivostraße 9, 64293 Darmstadt, Germany.

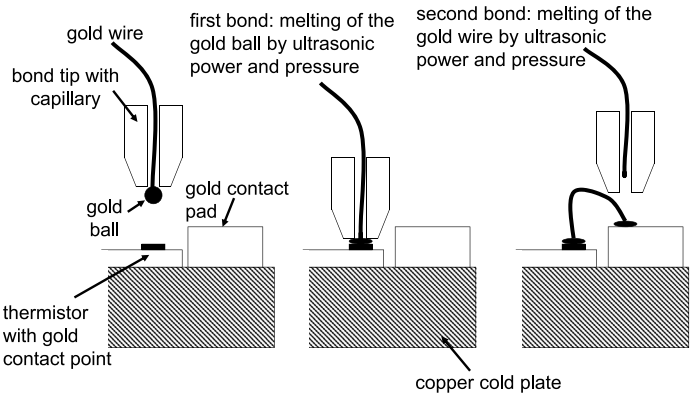

Fig. 3.2. This schematics displays the steps of ultrasonic ball bonding.

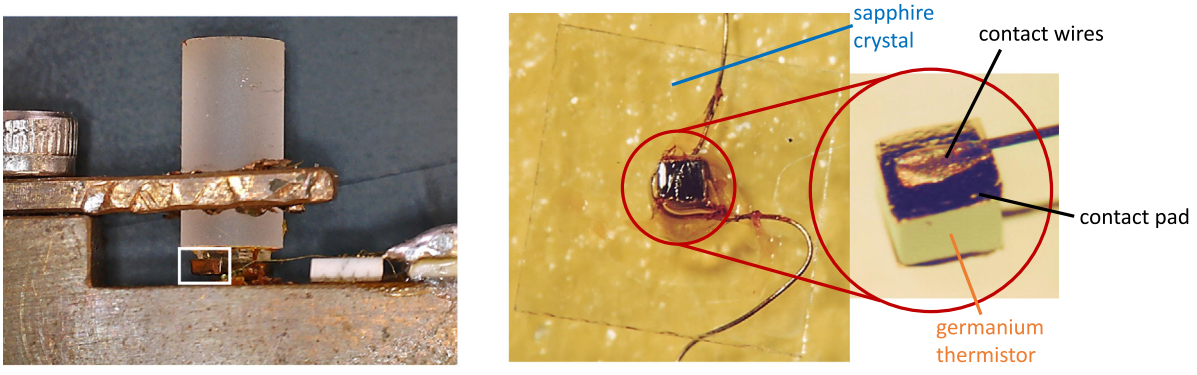

Fig. 3.3. On the left-hand side, this figure shows a photo of a composite CLTD consisting of a large sapphire absorber, which was added to account for the larger range of high energetic heavy ions, and a germanium thermistor (denoted by the white square). On the right-hand side, a germanium thermistor glued onto a thin sapphire absorber made for low ion energies is displayed [164].

large cylindrical crystal is held by thin tips of stainless steel and a small drop of GE7031 varnish to maintain mechanical stability.

In the second production badge, it was tried to further reduce the Schottky barrier by applying boron doping. The germanium crystals were doped on opposite surfaces by the *Haller-Beeman Assoc. Inc.*[4] to a boron concentration of 2×10^{19} cm^{-3}. The thickness of the doped layer is around 0.13 µm [164]. Afterwards, the surfaces were covered with 20 nm of palladium for better adhesion and then with 400 nm of gold. An annealing step at 300 °C was applied to anneal defects caused by the implantation process. Copper wires with a diameter of 50 µm were glued onto the gold contacts by means of the epoxy *Epo-Tek H20E*.[5] Fig. 3.3 shows an example on the right-hand side. The target of the second production badge were ions in an energy range below 1 MeV/u. Accordingly, a germanium crystal with a dimension of $0.5 \times 0.5 \times 0.5$ mm^3 was glued on a sapphire absorber with a thickness of only 50 µm and an area of 3×3 mm^2.

3.2.2.2. Detector characterization

R(T) curves

$R(T)$ curves were the first characterization step to investigate if the expected values for R_0 and T_0 had been realized and if the expected exponential Mott behavior was observed. An example for a detector of the second production badge is displayed in Fig. 2.4 in Section 2.2. Both CLTDs follow the expected Mott behavior perfectly well. The solid lines represent fits to the data with Eq. (2.7). The values of R_0 and T_0 are $(69 \pm 1)\,\Omega$, and (106 ± 2) K, respectively. At an operating temperature of 1.7 K, this results in a sensitivity parameter of $\alpha = -3.3$. Similar results were obtained for the other detectors discussed in the previous section [151,152,217,219].

[4] Haller-Beeman Assoc. Inc., El Sobrante (CA), USA.

[5] Epoxy Technology Inc., Billerica (MA), USA.

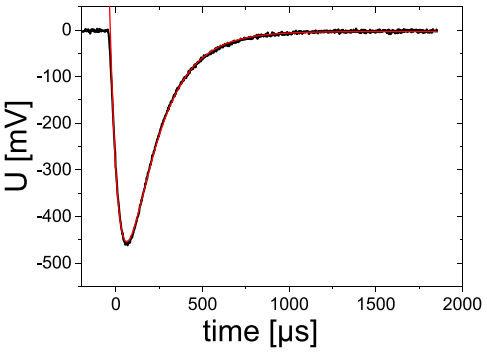

Fig. 3.4. The α-signal of a CLTD with a germanium thermistor was averaged from 100 signals of the α-source with three nuclides. The amplification factor of the preamplifier is 5000, the measurement current is 4 µA. The red curve describes a fit to the data according to Eq. (2.18). The decay time constant deduced from the fit is $\tau_{eff} = 185(7)\,\mu s$ [164].

Characterization with α-particles

As a second characterization step, all detectors were irradiated with α-particles from a combined source which contains ^{239}Pu, ^{241}Am, and ^{244}Cm. For all detectors, the shape of the α signals as well as pulse height spectra were recorded. Fig. 3.4 shows the signal shape of a composite CLTD with a semiconductor thermistor [164]. The signal was averaged from 100 single preamplifier signals of the α-source with three nuclides. The shape of the signal is well described by Eq. (2.18). The negative sign of the voltage signal is a result of the negative dR/dT characteristics. The decay time constant $\tau_{eff} = 185(7)\,\mu s$ determined from the fit allows for a maximum count rate of around 1–3 kHz for this detector if pile-up should be avoided. The voltage amplitude U_{max} should be inversely proportional to the detector heat capacity (Eq. (2.19)), while the effective time constant τ_{eff} should be directly proportional to it. Therefore, the signal shape offers two different means to experimentally determine the heat capacity and compare it to the expected value, namely from τ_{eff} according to Eq. (2.16) and from U_{max} according to Eq. (2.19).

To compare these values with the heat capacity calculated from literature values, the following parameters were used (for details see [164]):

- Specific heat for sapphire: $c_{sapphire} = (3.4 \pm 0.1) \times 10^{-7}\, T^3\, \frac{\mathrm{J}}{\mathrm{cm^3\,K}}$
- Specific heat for germanium: $c_{germanium} = (3.03 \pm 0.05) \times 10^{-6}\, T^3\, \frac{\mathrm{J}}{\mathrm{cm^3\,K}} + (1.8 \pm 0.2) \times 10^{-6}\, T\, \frac{\mathrm{J}}{\mathrm{cm^3\,K}}$

The second term for germanium accounts for the heat capacity of the electrons. In addition, the heat capacities of the glues GE7031 and H20E may lead to additional contributions which are difficult to quantify because the volume of these glues is not easily determined.

The detector with which the signal displayed in Fig. 3.4 was taken consists of a thin sapphire absorber of $3 \times 3 \times 0.05\,\mathrm{mm^3}$, glued to a germanium thermistor of $0.5 \times 0.5 \times 0.5\,\mathrm{mm^3}$. For this constellation, the heat capacity is clearly dominated by the germanium thermistor:

- Heat capacity of the sapphire: $C = (0.74 \pm 0.09)\,\frac{\mathrm{nJ}}{\mathrm{K}}$ at $T = 1.67\,\mathrm{K}$
- Heat capacity of the germanium: $C = (2.1 \pm 0.3)\,\frac{\mathrm{nJ}}{\mathrm{K}}$ at $T = 1.67\,\mathrm{K}$
- Total heat capacity: $C = (2.8 \pm 0.4)\,\frac{\mathrm{nJ}}{\mathrm{K}}$ at $T = 1.67\,\mathrm{K}$

For comparison, the heat capacities determined from U_{max} and τ_{eff} result in $C = (8.4 \pm 0.5)\,\frac{\mathrm{nJ}}{\mathrm{K}}$, and $C = (5.1 \pm 0.1)\,\frac{\mathrm{nJ}}{\mathrm{K}}$, respectively. The reason for this discrepancy is not yet understood. One possibility is that the thermal coupling which was determined from $I(V)$ curves [164] is not correct. A contribution of the GE7031 low temperature varnish or the H20E glue for the electrical contact may also not be excluded.

3.2.3. CLTDs based on superconducting phase-transition thermometers

The other established technique for resistance-based CLTDs are superconducting phase-transition thermometers, also called transition-edge sensors (TES) (see Section 2.2.2). K. D. Irwin and G. C. Hilton give an extensive overview on the operation principle and the basic theory in [180], and an overview on recent developments is presented in [17]. The use of a superconductor in its transition from the normal to the superconducting state allows for very high values of the sensitivity parameter α (see Section 2.2). In addition, the value of dR/dT is more or less constant in a certain range of the transition. Therefore, the energy response function of a TES is usually quite linear.

For sapphire (Al_2O_3), nature offers us a perfect fit: aluminum is a type I (i.e. BCS) superconductor [188] with a transition temperature of $T_C = 1.2\,\mathrm{K}$. For thin films, the transition temperature can be increased up to 1.7 K [220,221]. Thin aluminum films can be deposited very well onto sapphire substrates, because aluminum fits well into the sapphire crystal lattice [27].

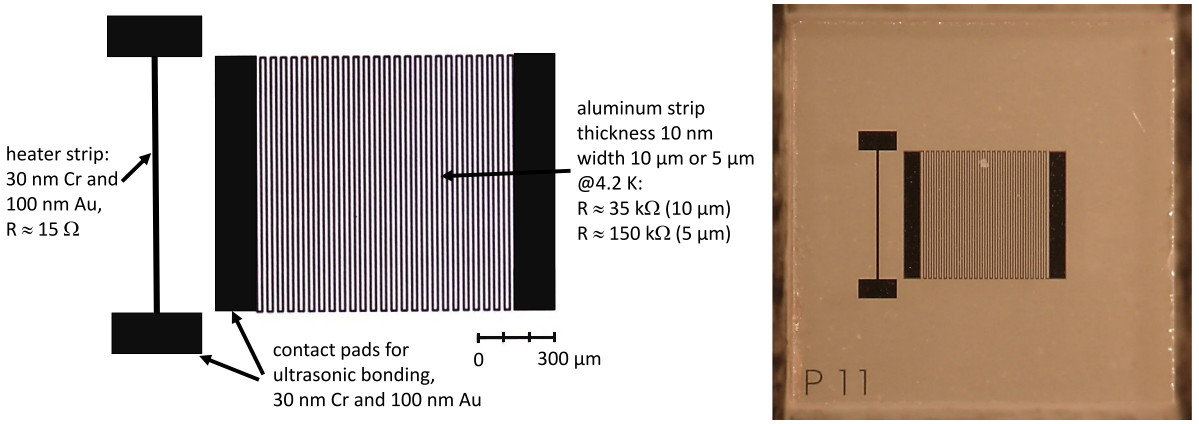

Fig. 3.5. On the left-hand side, a schematics of the aluminum TES structure is displayed. The thin aluminum film is structured by means of photolithography in the form of a meander with a long wire to obtain resistances in the transition in the range of kΩ. On the right-hand side, a picture of a thermistor on a sapphire crystal of $3 \times 3 \times 0.44\,\mathrm{mm}^3$ is displayed [155].

3.2.3.1. Detector design

K. W. Shepard et al. [35] investigated the response of thin films of aluminum, which were deposited onto sapphire substrates, to α-particles. They investigated the thermal response by observing the voltage signal induced by the resistance change and made a profound analysis of the thermal processes in the sapphire absorber, as well as in the aluminum film. But no spectra were recorded.

Based on these investigations, the development of composite CLTDs with sapphire absorbers, which provide low heat capacity and good radiation hardness (see Section 3.2.1), and aluminum TES was started in 1989 at the University of Mainz, Germany [149,220] with the aim to use this technique for the detection of energetic heavy ions. The first step was to determine the ideal film thickness and to establish the production process. For a good energy-sensitive detector, several demands on the aluminum film had to be met:

- a homogeneous transition from the superconducting to the normal-conducting state with a constant value of dR/dT in the whole transition range;
- a narrow transition width for obtaining a large value of dR/dT for high sensitivity;
- a transition temperature of around 1.4–1.5 K which can be reached with a pumped ^{4}He bath cryostat;
- a resistance at the operating temperature which allows for the use of conventional preamplifiers (see discussion in Section 3.3).

Over the years, several attempts have been made to meet these requirements and continuous improvements on the performance were obtained [150,153,162,164,184,218,220–223]. It turned out that reaching the aim of aluminum structures with narrow, homogeneous and reproducible transitions was a challenging task which demanded considerable efforts. At the beginning of the development, aluminum strips with different film thicknesses between 5 nm and 40 nm were evaporated onto sapphire substrates and characterized with respect to transition temperature T_C and transition width δT [220]. It turned out that thicker films yielded smaller transition widths, but also smaller resistances. In addition, if the film thickness was chosen too small, the transitions became inhomogeneous. As a compromise, a film thickness of 10 nm was chosen which has been maintained for all further detector developments of this type. A. Echler [221] made some tests with sputtered films with a thickness of 15 nm, but as these films showed a larger δT and, accordingly, a lower dR/dT, the concept was not pursued. Interestingly, the transition temperature of the sputtered films did not show a considerable dependence on the film thickness, at least not in the investigated range of thicknesses. Rather, a variation of the transition temperature of up to 0.2 K was observed from one detector to the next even within the same production badge [155,221]. The sputtered films reached higher transition temperatures of up to 1.7 K, but at the cost of lower sensitivity. On the other hand, aluminum films which were deposited on very thin sapphire samples with a different crystal orientation did not become superconducting even at temperatures close to the 1.2 K of the bulk material [164]. These findings indicated that the microstructure of the deposited films has a rather large influence on the transition temperature. However, controlling this microstructure turned out to be very difficult.

To match the impedance of the aluminum thermistors to conventional preamplifiers, and to realize a large dR/dT, the aluminum films were structured in the form of a thin meander-like structure by means of photolithography [150, 164,218,220]. Three different stripe geometries were tested [164]. Wider stripes are easier to produce and less prone to failures, but the resistance is smaller which leads to a smaller dR/dT. Thinner stripes place higher demands on the production process, but the higher resistance results in larger dR/dT which ultimately was found to produce a better energy resolution. Accordingly, for detectors only the geometries with a length of 50 mm and a width of 10 µm, and with a length of 102 mm and a width of 5 µm were further used.

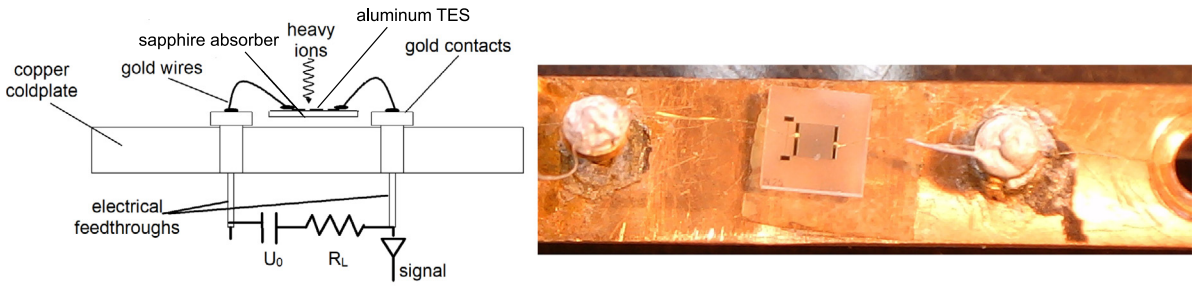

Fig. 3.6. The left-hand side shows a schematics of the setup of the first generation of a composite CLTD with a TES thermistor on a sapphire absorber, with gold wires for thermal and electrical contact (adapted from [15]). The support of the absorber, as well as the thermal link to the heat sink is realized only by the gold wires. The right hand panel shows a photo.

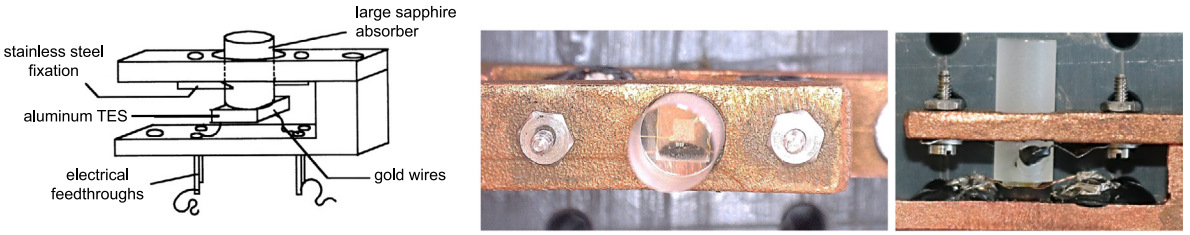

Fig. 3.7. Left-hand side: schematics of a CLTD for the detection of heavy ions with higher energies. Onto the sapphire crystal of a standard CLTD with aluminum TES as discussed above, an additional sapphire crystal with larger volume was glued in order to increase the absorber thickness. On the right-hand side, corresponding photos are displayed.

Photolithography[6] is performed on sapphire wafers with a diameter of 2 inch (About 200 individual sensor structures can be put onto one sapphire wafer.) It is performed in two steps: In the first step, the aluminum film is deposited onto the sapphire wafer and structured in the form of a meander. For the quality of the aluminum TES, an excellent vacuum and clean conditions during the evaporation process are of vital importance [164,184]. In the second step, the contact pads for ultrasonic bonding are realized. They consist of 30 nm Cr which helps to fix the layer of 100 nm Au onto the sapphire surface. In the second detector design, the small gold contact pads were replaced by gold stripes to allow the placement of more than one bond [164]. In the third generation of thermistors, an additional strip of gold was added which was used as a heater for the individual temperature stabilization of each detector in a detector array (see Section 3.2.4) [184,223]. Fig. 3.5 shows an example for the third generation of detectors with a schematics on the left-hand side and a picture on the right-hand side.

After the structuring is completed, the wafers are cut with a diamond saw into pieces of either $2.5 \times 3 \times 0.33\,\mathrm{mm}^3$ [164, 218] or $3 \times 3 \times 0.44\,\mathrm{mm}^3$ [184,221]. Electrical contacts are provided by gold wires with a thickness between 17 and 25 μm, which are attached to golden contact pads at the ends of the aluminum meander structures by means of ultrasonic ball bonding [164,184,218,220,221]. The detector pixels are mounted on copper holders similar to the ones for the CLTDs with germanium thermistors described in Section 3.2.2.1. In the first attempts, the sapphire crystals were glued onto the copper holders by means of the GE7031 varnish to realize an optimal thermal coupling. However, this setup was found to yield bad performance. Accordingly, in the later design the detectors were connected to the heat sink only via the gold bond wires, which are, therefore, also used as mechanical support. Fig. 3.6 shows a scheme of the setup and a photo.

For the detection of ions with higher or even relativistic energies, which cannot be stopped in the standard absorber thickness of 330 μm (see Table 3.1), the absorber thickness had to be adjusted to the individual experimental conditions. Therefore, detectors with additional sapphire absorbers with larger volumes (6 mm^3 and 120 mm^3 [153]) were realized. For this purpose, sapphire crystals of $2.5 \times 3 \times 0.33\,\mathrm{mm}^3$ with aluminum TES were glued onto the additional larger sapphire crystals with GE7031 varnish. The larger absorbers are fixed by specially shaped copper support structures in order to minimize thermal contact to the environment. A schematics and photos of this setup are displayed in Fig. 3.7.

6 Photolithography was performed by different institutions: for the first generation of detectors by K. Haberle et al., Institut für Halbleitertechnik, Technische Universität Darmstadt, Schlossgartenstrasse 8, D-64289 Darmstadt, Germany, [164,218], for the second generation by C. Enss et al., Kirchhoff Institute, Im Neuenheimer Feld 227, D-69120 Heidelberg, Germany, [221], for the third generation by the Fraunhofer-Institut für Mikrotechnik und Mikrosysteme IMM, Carl–Zeiss–Strasse 18–20, D-55129 Mainz, Germany [184].

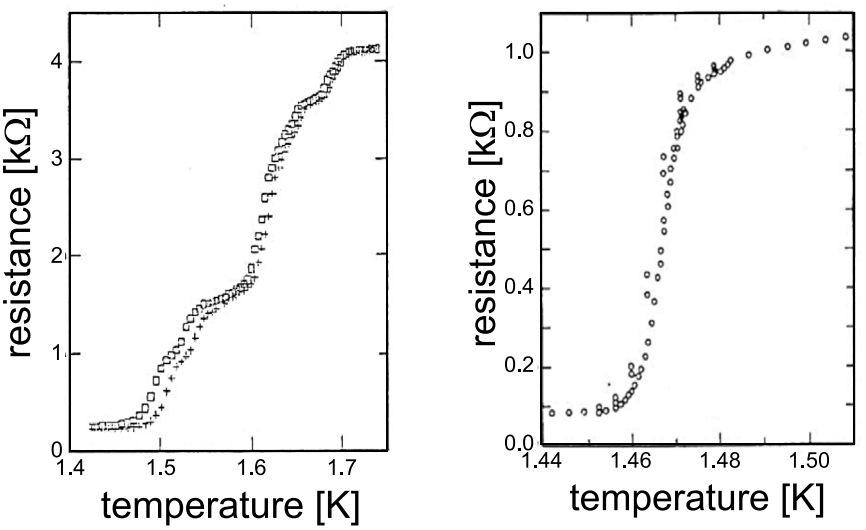

Fig. 3.8. The homogeneity of the transition curve is strongly dependent on the aluminum film thickness. Whereas a film with a thickness of 5 nm (left-hand side) results in a transition with steps, a film thickness of 12 nm (right-hand side) yields a homogeneous transition with a well-defined dR/dT [220].

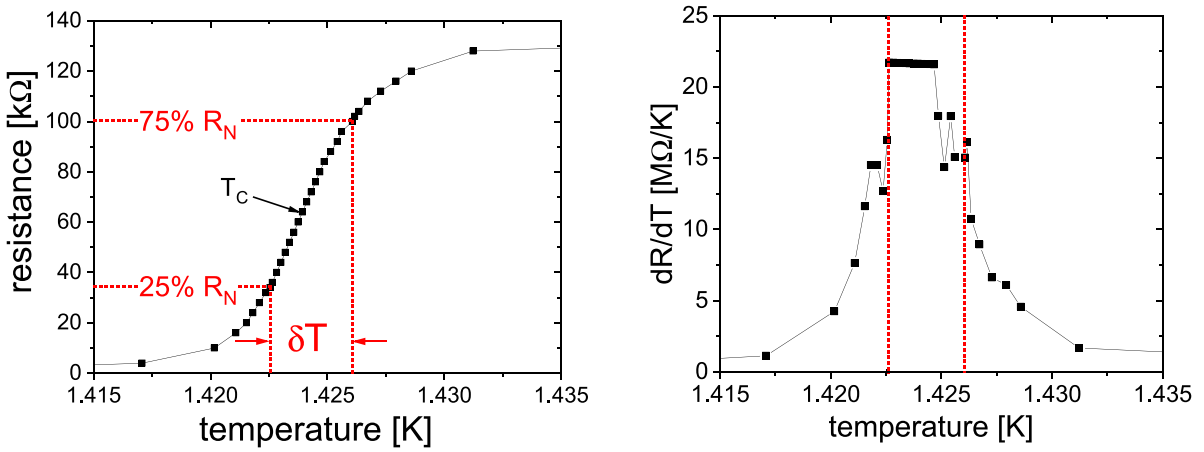

Fig. 3.9. The panel on the left-hand side displays an example for a homogeneous transition curve of an aluminum TES with a film thickness of 10 nm. The transition temperature is 1.424 K, the transition width is 3.5 mK. The panel on the right-hand side shows the corresponding point-by-point derivative dR/dT. In the region from 25%R_n to 75%R_n, the average slope is $dR/dT = 19.9(4)\,\mathrm{M\Omega/K}$ which results in a sensitivity parameter of $\alpha = 406$. The maximum derivative is slightly higher with $dR/dT = 21.7(1)\,\mathrm{M\Omega/K}$.

3.2.3.2. Detector characterization

R(T) curves

As was discussed for the germanium CLTDs, $R(T)$ curves are the first step to characterize CLTDs. For TES sensors, in addition to the transition temperature, the homogeneity and the width of the transition are of primary importance. A small transition width δT results in a high dR/dT, but also in a smaller dynamic range. A homogeneous transition is mandatory for a linear energy response of the detector.

Since the beginning of the developments, around fifty CLTDs based on aluminum TES's were characterized [150,164,184,218,220,221,223]. Figs. 3.8 and 3.9 display three examples of transition curves. Fig. 3.8 illustrates how sensitively the homogeneity of the transition depends on the film thickness. Whereas an aluminum film with a thickness of 5 nm results in an inhomogeneous transition with steps, a film thickness of 12 nm yields a homogeneous transition with a well defined, constant value of dR/dT, as is illustrated by the example in Fig. 3.9. For this example, the film thickness is 10 nm. The aluminum strip has a length of 102 mm and a width of 5 μm. It should be pointed out that ultra-clean conditions during the evaporation of the aluminum film onto the sapphire wafers were mandatory in order to obtain homogeneous and reproducible transition curves [164,221].

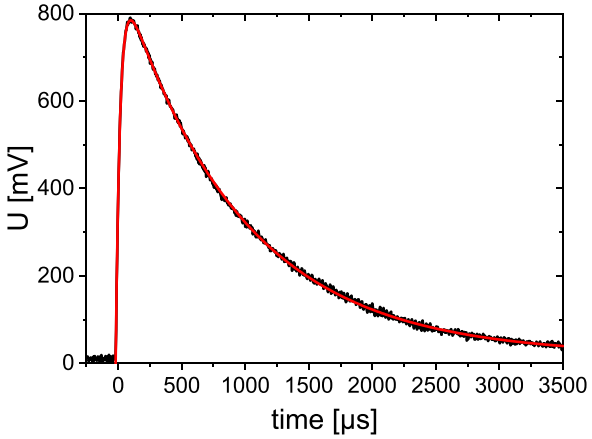

Fig. 3.10. This example of a preamplifier signal averaged of 100 signals from the three-line-α-source was taken with the detector whose $R(T)$ curve is displayed in Fig. 3.9. The red line shows a fit with the function described in Eq. (2.18). The rise time and the decay time of the thermal signal were determined to be $\tau_{rise} = 34(2)$ μs, and $\tau_{eff} = 936(2)$ μs, respectively.

Further examples for transition curves are displayed in Fig. 2.5 in Section 2.2.2 and Fig. 3.12 in Section 3.2.4. Even when considering detectors of the same production run, it is unavoidable that the transition temperatures as well as the widths of the transition curves have slight variations within about 0.02 K. It turned out that tiny variations in the film thickness have a large impact on these characteristic values [164,184]. As a general rule, each detector pixel has to be characterized individually concerning its transition temperature and its dR/dT. Concerning the overall variation of all transition curves obtained over the years with different generations of detectors, a wider range of parameters was found:

- T_C : $1.45 - 1.7$ K
- δT : $4 - 15$ mK
- dR/dT : $1 - 20$ MΩ/K
- α : $150 - 600$

The point-by-point derivative of a typical transition curve is displayed on the right-hand side of Fig. 3.9. The value of dR/dT is constant over most of the transition region which ranges from 25% to 75% of the resistance R_N in the normal conducting state. The point-by-point derivative yields an excellent value of $dR/dT = 21.7(1)$ MΩ/K. A linear fit to the $R(T)$ curve in the transition region yields a value of $dR/dT = 19.9(4)$ MΩ/K which is slightly smaller due to the smaller slope in the upper part of the transition. However, optimal performance is achieved in almost the whole transition region.

When a current is applied to a superconductor, its transition temperature and transition width changes due to Joule heating (see Section 2.3). Therefore, TES's are usually operated in the constant voltage mode and the change in current is detected. Opposite to this practice (discussed in more detail in [180]), the aluminum TES in our case are operated in the constant current mode. This means that a constant current is applied by a battery or the preamplifier, and the temperature change is read out as a voltage signal. The main reason is the use of conventional preamplifiers for the present investigations as discussed in Section 3.3. As a consequence, the determination of the optimal measurement current was another important issue when characterizing the detectors. It was found that the transition temperature decreases by up to 1% when the current is increased from 50 nA to 3000 nA [220]. The transition becomes narrower with increasing current, too. From these results, the conclusion is that a measurement current as small as possible is favorable. On the other hand, smaller measurement currents result in a smaller voltage signal which in turn will decrease the signal-to-noise-ratio and, therefore, may worsen the energy resolution. The optimal measurement current was determined by investigation of the response of the detectors to α-particles as discussed in the following section.

Characterization with α-particles

For characterization with α-particles, again a combined α-source which contains ^{239}Pu, ^{241}Am, ^{244}Cm, as discussed in Section 3.2.2.2, was used. First tests were performed using an oscilloscope to record the signal shape. For the recording of spectra, the data acquisition described in Section 3.3 was used. An example of a typical preamplifier signal is displayed in Fig. 3.10. It can be described very well by the relation described in equation (2.18), as is shown by the red curve which represents a fit to the data. The rise time in this particular case is $\tau_{rise} = 34(2)$ μs, and the thermal time constant is $\tau_{eff} = 936(2)$ μs. In general, the decay constant is tuned by varying the thermal coupling to be between 200 μs and 1000 μs, allowing for count rates of around 0.3–1 kHz without substantial pile-up. The optimal measurement current was determined by varying the current and measuring the signal amplitude [164,220]. It was found to be between 500 nA and 700 nA for all detectors. Most of the measurements presented in Sections 4 and 5 were performed with a measurement current of 500 nA.

In the case of the CLTD based on a germanium thermistor, the comparison of the heat capacities determined from the voltage amplitude U_0, from the decay time constant τ_{eff} and calculated from the detector volume showed considerable differences (see Section 3.2.2). This was not observed for CLTDs with aluminum TES. The heat capacities determined by the three different methods (calculated from the volume of the sapphire absorber V, U_{max} and τ_{eff} of the voltage signal) agree very well in most cases. For the example in Fig. 3.10, the three values of the heat capacities amount to $C(V) = 2.3(7)\,\mathrm{nJ/K}$, $C(U_{max}) = 2.0(1)\,\mathrm{nJ/K}$, and $C(\tau_{eff}) = 2.1(5)\,\mathrm{nJ/K}$, respectively. Within the uncertainties, all three values are in rather good agreement. The reason is probably that the contribution of the aluminum TES to the overall heat capacity is negligible. Thermal coupling between absorber and thermometer is only limited by the electron–phonon-coupling in the aluminum. Thus, the detector consisting of a sapphire absorber and an aluminum TES turns out to be an almost optimal CLTD concept.

3.2.4. Detector arrays

For most of the detector tests discussed in Sections 3.2.3 and 3.6.1, the operation of single detector pixels with an active area of $3 \times 3\,\mathrm{mm}^2$ was sufficient. On the other hand, it is obvious that for the application of CLTDs in experiments (see Sections 4 and 5) detectors with larger active areas are needed, dependent on the experimental demands.

As is discussed in Section 1 and Section 2.2, the heat capacity of the absorber constrains, besides the operation temperature, the detector volume of a single pixel. Therefore, for a given operation temperature, the detector volume should be chosen sufficiently small so that a high temperature signal is achieved in order to obtain a high sensitivity and a high signal-to-noise ratio. But it should also be chosen large enough so that the temperature rise does not exceed the width of the transition (although it is possible to operate the CLTD below the transition, but at the cost of energy resolution [218]). In addition, the absorber should be thick enough to fully stop the incident ions (see Section 3.1). Considering all these constraints, the lateral size, i.e. the active detector area, is a rather constrained parameter. Therefore, in many cases the application of detector arrays, consisting of many individual detector pixels, is the only way to achieve a sufficiently large active area and thus large solid angles of CLTD detectors.

3.2.4.1. Design of detector arrays

In a detector array, the relatively loose support structure of the detectors by their gold wires is not a feasible option, because each detector pixel has to be held firmly in its place. The distance between neighboring pixels has to be kept as small as possible to cover a large active detector area with a minimum of insensitive area, but sufficiently large to avoid thermal contact and thermal cross talk. At the same time, the thermal coupling to the heat sink cannot be made too strong, because that deteriorates the energy resolution as the maximum of the voltage signal is not reached [220]. As a solution, the sapphire crystals are glued onto a Marcor ceramic holder with two tiny dots of Stycast 2850F epoxy[7]. The design is displayed in Fig. 3.11. The panels in the upper row display the detector array with five modules carrying two detector pixels each [184,221]. Five modules were mounted on a copper holder to form an array of two by five single detectors. In this geometry, the detector response, as well as thermal cross talk was investigated. Based on the results obtained with this first detector array, a second array with five detectors in each module was deployed [223,224]. The panels in the lower row display this second array.

Both detector arrays follow the same design. The individual pixels are glued onto a ceramic holder made of Marcor by means of GE7031 varnish such that the backside of the pixel is facing the ion beam and the aluminum TES is not irradiated. To realize a defined thermal coupling of the detector pixels to the heat sink despite of varying glue spot sizes and to minimize thermal cross talk, two thin spacers of single crystal sapphire were sandwiched between the absorber crystal and the ceramic [224]. The thermal coupling is then defined by the dimensions of these so-called *sapphire spacers*. The ceramic holders are sandwiched between two pieces of copper and glued by GE7031 low-temperature varnish. This on the one hand ensures good thermal coupling between ceramic and copper. On the other hand, the varnish mediates between the two different thermal expansion coefficients. Inside the copper, copper wires for electrical contact are guided. The golden bond wires from the thermistors are fixed to the copper wires by means of silver epoxy and – in a later version – by soldering to avoid contact noise. The copper wires are soldered to wires of phosphor-bronze which in turn provide the leads to the readout electronics at room temperature.

In summary, the present design of CLTD arrays enables the adjustment of the detector arrays to the individual experimental conditions. Its modular structure allows fitting the active detector area to any detector geometry demanded by the experiment. Moreover, each detector module can be individually replaced.

3.2.4.2. Characterization of the detector arrays

The CLTD pixels used for setting up the arrays have relatively small transition widths of around 10 mK, and on the other hand considerably varying transition temperatures, because the transition temperature depends on the microstructure of the thin aluminum film. Therefore, the variation of the transition temperatures often exceeds the transition widths. Even if all detectors of an array are hand-picked and from the same production badge, it is impossible to operate them all at the same temperature. This is illustrated in Fig. 3.12. It shows transition curves of different detector pixels which belong to the two detector arrays displayed in Fig. 3.11. The detector pixels were hand-picked from the same production badge to make their transition temperature as closely matching as possible [184,221,223]. Still, the transition temperatures vary too strongly (up to 20 mK in this example) to operate all detectors at the same temperature. Accordingly, each detector has to be temperature-stabilized individually in its operating point. The detailed procedure is described in Section 3.5.2.

[7] Henkel Electronic Materials (Belgium) N.V., Westerlo, Belgium

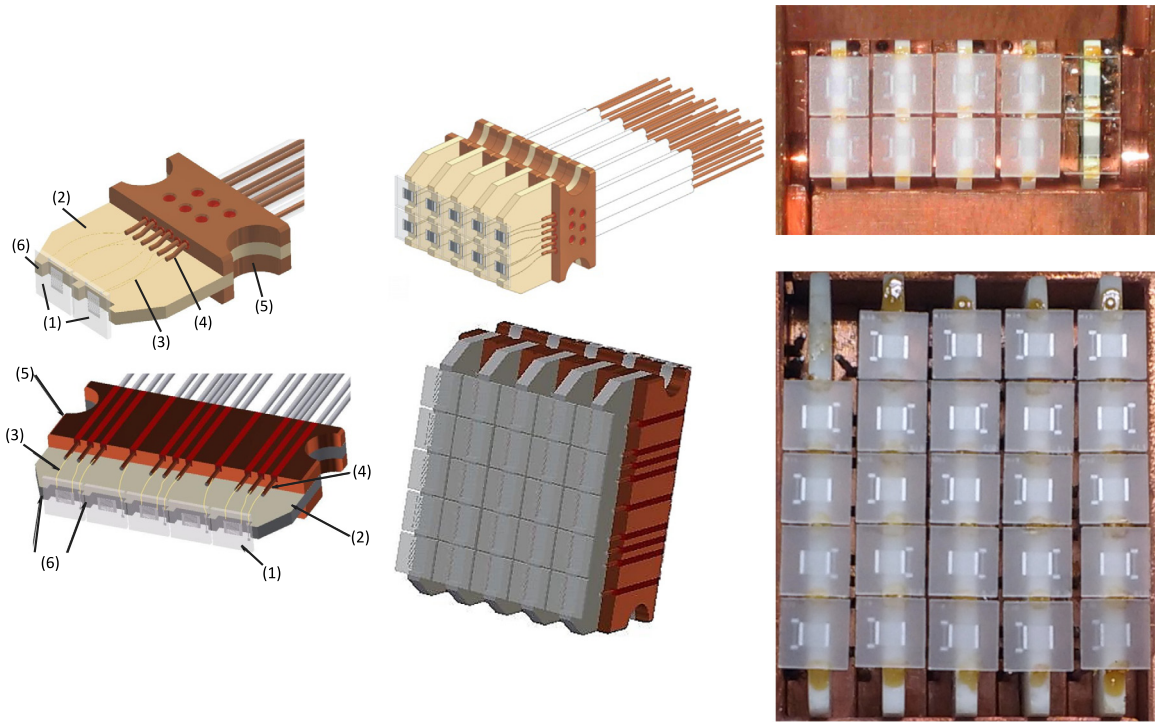

Fig. 3.11. Left-hand side: schematics of one element of a detector array with 2 × 5 pixels (upper panel) [184,221] and with 5 × 5 pixels (lower panel) [223,224]. All detector pixels are aluminum TES structures with sapphire absorbers. (1) detector pixel(s), (2) ceramic holder, (3) gold wire, (4) copper wire, (5) copper holder, (6) glue point(s).
Middle: schematics of the two composite arrays.
Right-hand side: photographs of the two arrays. (for discussion see text). In the nominal 5 × 5 pixel array, the upper left pixel is missing.

3.3. Detector readout

The principle detector readout scheme for a single CLTD with aluminum TES has been discussed in Section 2.3 (see also Fig. 2.7). The detectors are operated in the *constant current mode*, i.e. a constant current through the detector is provided by a battery via a parallel load resistor. The change of the resistance of the thermistor leads to a change in the voltage across the resistance which is detected by a voltage-sensitive preamplifier. Naturally, the preamplifier should display low noise and should be matched to the resistance of the CLTD in the operating point. To facilitate operation, the aim was to use conventional low-noise preamplifiers which are readily available for conventional, ionization-based semiconductor detectors. In the case of the germanium thermistors, the resistance in the operating point is around 200 kΩ. In the case of the aluminum TES, a resistance of the order of 40 – 100 kΩ in the operating point is obtained. A preamplifier with an input impedance of several MΩ as is used for ionization-based detectors, is therefore well suited.

In most of the development work and also in the early experiments, voltage-sensitive preamplifiers of the type *HMS ITHACO 1201* were used. This very versatile preamplifier has a large amplification range of 1–10 000 and a tunable set of high-pass and low-pass filters. The total bandwidth can be chosen in a range from 0.03 Hz (minimum low-pass frequency) up to 400 kHz (maximum-high pass frequency). In addition, the ITHACO offers the possibility of DC amplification for the temperature stabilization (see Section 3.5.1). As amplifiers of the type HMS ITHACO are no longer commercially available, and because the detector arrays demanded for a more compact solution (see Section 3.2.4), two dedicated preamplifiers were developed. The first type was designed by the company *FEMTO*.[8] It is based on their model *DLPVA-S*, but it was modified to provide a second path for DC amplification, as well as an internal current source with a load resistor of 5.6 MΩ [221]. The DC amplification is fixed to 200, while the AC amplification and the bandwidth can be chosen according to experimental needs. This amplifier is designed as a stand-alone module with an individual power supply for each amplifier. For the reading out of detector arrays with 25 or more detectors this design was not feasible. Therefore, a NIM module containing two amplifier channels was developed by the company Surface Concept[9] based on the DPLVA-S design. Its AC amplification can be varied from 250 to 2000, while the DC amplification can be varied from 50 to 200. The

[8] FEMTO Messtechnik GmbH, Klosterstr. 64, 10179 Berlin, Germany.
[9] Surface Concept GmbH, Am Sägewerk 23a, D-55124 Mainz, Germany.

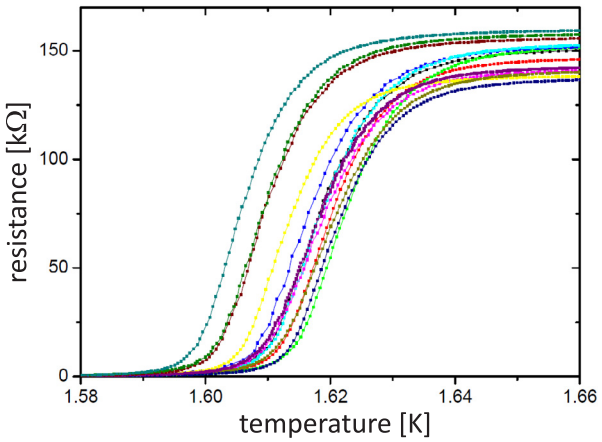

Fig. 3.12. Transition curves for different detector pixels which were selected for the two detector arrays displayed in Fig. 3.11 [184,223]. Although the pixels were hand-picked from the same production badge, the transition temperatures vary too strongly to operate all detectors at the same temperature.

bandwidth for the AC path is adjustable from 10 Hz to 300 kHz. Both preamplifier types were used in several experiments and have shown excellent performance. Further details will be presented in the according sections.

The preamplifier signal was further amplified by a second, shaping amplifier stage. Standard shaping amplifiers are adapted to the time constants of ionization detectors which are in the range of $10 - 30\,\mu s$. Therefore, they are not suited for the long decay times of CLTDs. Accordingly, it was necessary to develop amplifiers with shaping times of up to $200\,\mu s$ to account for the long decay times of the thermal signals. The first shaping amplifier used had been modified by the GSI electronics workshop [218] for a shaping time of $100\,\mu s$. The second shaping amplifier was developed by the company *Silena*.[10] Its shaping time can be selected in steps of $25, 50, 75, 100, 125, 150\,\mu s$. For germanium thermistors, as well as for aluminum TES, shaping times of $100\,\mu s$ were found to be sufficient to realize a good energy resolution [164,217].

After the shaping amplifier, the signals were digitized by *Silena 7420/s* **A**nalog-to-**D**igital **C**onverter**s** (ADCs) with a frequency of 400 MHz. For the comparably slow signals of CLTDs, these ADCs were operated in the peak detection mode and gated by an external gate in order to detect the correct maximum of the signals. Details of this readout scheme can be found in [164,217,218]. Fast flash ADCs, which digitize voltage signals point by point over the whole signal length with frequencies of MHz, are of course nowadays state of the art in detector readout. Such a readout scheme was also implemented for the experiments presented in Sections 4 and 5. Tests were performed with several different modules [164]. The current setup uses so-called **F**ield **P**rogrammable **G**ate **A**rray**s** (FPGAs) of the company *National Instruments*.[11] The modules PXI-7833R and PXI-7852R digitize the signals from the preamplifiers with a digitizing frequency of 200 kHz, and 750 kHz, respectively. These frequencies are more than sufficient for the rather slow CLTD signals with time constants of many microseconds. The FPGAs are operated and read out by a data acquisition program based on the National Instruments software Labview [184]. Fig. 3.13 displays a schematics of the readout and temperature regulation for a detector array using an FPGA as well as a digital PID regulator which is discussed in Section 3.5.

In the offline analysis, the procedure of *optimal filtering* is often applied for CLTDs [164,178,225]. It minimizes electronic noise by applying an optimized filter algorithm in the frequency domain, thus optimizing the energy resolution for each measurement. The digital filter is calculated based on the Fourier transformed frequency spectrum of an averaged signal and the noise spectrum according to

$$H = \sum \frac{D(f) \times S(f)}{N^2(f)} \tag{3.1}$$

where H denotes the filtered signal amplitude and $D(f)$, $S(f)$ and $N(f)$ denote the real signal, the averaged signal and the noise in the frequency domain, respectively [225]. The data acquisition records not only the full signal point by point, it also regularly records noise signals which are averaged and used to create the optimal filter (see [164] for a detailed discussion).

In some experiments, the application of this procedure improved the already excellent energy resolution of CLTDs for heavy ions as well, although in most cases the signal-to-noise ratio was not the limiting factor (see Section 3.6.2).

10 Silena International S.p.A, Cernusco s/Naviglio (MI), Italy.

11 National Instruments, Newbury, Berkshire, RG142PS, UK.

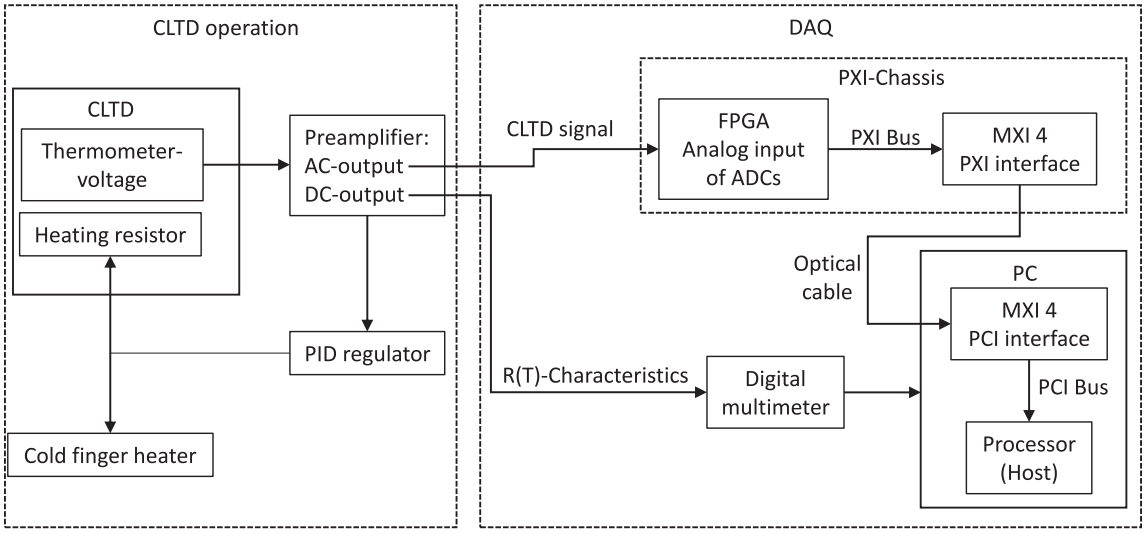

Fig. 3.13. Schematics of the readout of a detector array including the temperature regulation discussed in Section 3.5 [224].

3.4. The cryostats

To cool the CLTDs to their operating temperature of around 1 K, cryostats are mandatory. Most of the measurements which are presented in the following sections have been carried out in a window-less pumped continuous-flow ^{4}He bath cryostat produced by the company CryoVac[12] with a base temperature of ≈1.2 K. In this cryostat, the detectors were mounted in a vacuum chamber which can be connected directly to the beamline of a heavy ion accelerator. Fig. 3.14 shows a schematic overview.

The CLTDs are coupled via a *cold plate* to a small volume named *1 K pot* which in turn is connected to the ^{4}He bath by a very thin capillary. As liquid helium is a superfluid, it flows through the capillary without resistance and continuously refills the 1 K pot which is emptied by pumping, thus maintaining the operating temperature T_{bath} of about 1.2 K. The bottom of the 1 K pot is coupled to a thick copper plate called *cold plate*. The cold finger with the detectors is in turn connected to the cold plate. This design allows for a continuous operation at 1.2 K and refilling the cryostat without warming up the detectors to 4 K and thereby potentially changing the experimental conditions. To further reduce the heat load from the surroundings, the N_2 and He reservoirs are mounted in an insulating vacuum vessel and wrapped in several layers of so-called *superinsulation foil*, an aluminum-coated thin foil of mylar [184].

To reach the operation temperature, a good coupling of the detectors to the helium bath is mandatory, in particular for the transition-edge sensors discussed in Section 3.2.3. On the other hand, temperature fluctuations of the helium bath may cause fluctuations in the operating temperature which in turn might deteriorate the detector performance. As a compromise, the detector holders (see Sections 3.2.2.1 and 3.2.3.1) are mounted on a solid block of copper (mass around 1.3 kg). The copper block itself is fixed to the cold plate by means of four thin rods of stainless steel. This means that the copper block is not thermally connected very strongly to the helium bath. While that may seem counter-productive at first sight, it is needed to realize a thermal low-pass filter. A well defined thermal connection is obtained by using copper wires of well-known diameter and length. These wires are soldered to a copper ring on each end. The copper rings in turn are screwed to the bottom of the cold plate, as well as on the copper block. Depending on the experimental demands, the thermal connection can be varied and adapted, i.e. to different heat loads. For example, a thermal conductivity of 760 μW/K results in a thermal time constant of the copper block of around 40 s. This is sufficiently slow to level out most temperature fluctuations of the helium bath, but still strong enough to realize a stable operation. For experiments with detector arrays (see Section 3.2.4), the thermal coupling was adapted to a larger detector solid angle. The cryostat was designed for a cooling power which allows to cool down a detector array of $30 \times 80\,\mathrm{cm}^2$.

However, íf the vacuum chamber with the detectors is connected to a beamline, its opening is basically a black body at room temperature. The heat radiation from this black body reaches the detectors and heats them up. This will shift the operating temperature of the detectors to higher values. Accordingly, the detectors are surrounded by heat shields at 77 K, 4 K, as well as at 1.2 K. A system of several apertures with variable size is mounted in front of the detectors to minimize the heat radiation (see Fig. 3.14). For high ion energies, even the application of thin cooled foils in front of the detectors may be feasible. Moreover, the cryostat is equipped with additional cooled shield extensions towards the

[12] CryoVac Gesellschaft für Tieftemperaturtechnik mbH & Co. KG, Langbaurghstr. 13 D-53842 Troisdorf, Germany.

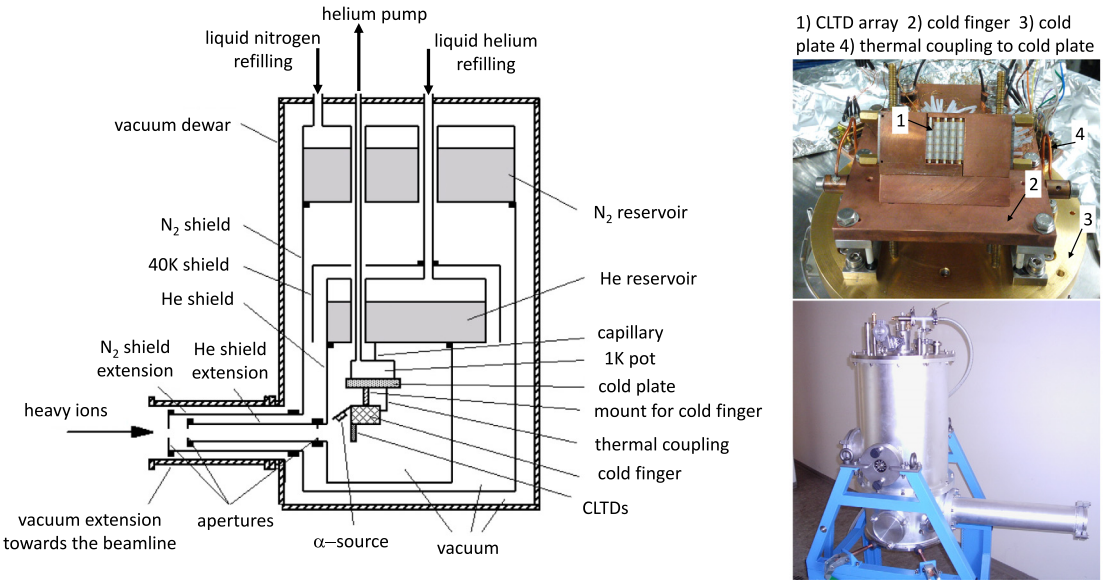

Fig. 3.14. On the left hand side, a schematics shows the basic design of the window-less continuous flow cryostat. Liquid helium is stored in a reservoir which feeds a small volume denoted *1 K pot* via a small capillary. The 1 K pot is continuously pumped and kept at 1.2 K. The detectors are mounted on the *cold finger* which is thermally coupled to a *cold plate*. The vacuum extension towards the beamline for heavy ions contains shields at N_2, and He temperature, respectively, which reduce the black body radiation from the environment [184]. On the right hand side, a photo of the CLTD array mounted in the cryostat, as well as a photo of the cryostat in its mount are displayed [224] (for details see text).

beamline in front of the detectors. Different apertures can be mounted on these shields according to experimental needs. The number, position and dimension of the apertures is variable and can be adjusted to the experimental conditions [164,184,224].

The cryostat is mounted in a very versatile frame (see Fig. 3.14, right-hand side) and can be flipped by 180° to work on the cold finger without the need for a lifting device. The frame has a bottom counterpart which can be moved in all three dimensions as well as rotated to precisely adjust the cryostat alignment to the beamline.

The consumption of liquid helium is a considerable drawback for the operation of low-temperature detectors in experiments. In the last decade, a new cooling concept has been established which reaches base temperatures of around 3 K without the need for cryogenic liquids. This cooling concept is based on so-called *pulse tube coolers* [226]. It uses compression and decompression of a closed volume of helium gas in a Stirling cooler with a pulse tube instead of a second piston. Such a cryostat was recently commissioned and successfully tested in experiments with heavy ions. On the 3 K stage, an internal helium liquefier produces 0.5 l of liquid helium per hour when supplied with gaseous helium from a gas bottle. From the liquefier, the helium is fed to a 1 K pot very similar to the continuous flow system described above. A cold plate is coupled to the 1 K pot, and detectors are mounted on a cold finger weakly coupled to the cold plate.

3.5. Stabilization of the operating temperature

For a good and stable CLTD performance, the operating temperature should be as stable as possible. For semiconductor thermistors, dR/dT is directly proportional to $1/\sqrt{T^3}$ [179], so small fluctuations in the operating temperature will directly translate to fluctuations in the signal amplitude. For superconducting transition-edge sensors, dR/dT is approximately constant in the temperature range in which the detector is operated (see Section 2.2 and Section 3.2.3.2), and is thus expected to be less sensitive to small temperature fluctuations, but the small width of the transition demands for a good temperature stabilization. The same is the case for semiconductor detectors. Accordingly, great care was taken to realize an optimal temperature stabilization circuit.

3.5.1. Temperature regulation for single detector pixels

The temperature of the copper block, which is thermally connected to the detector pixel, is monitored by means of a calibrated temperature sensor which is read out by a four-wire-resistance bridge. Active temperature stabilization is realized by applying a small current through a heater resistance of 100 Ω which is glued into a hole in the copper block with *Stycast 2850 FT*, another epoxy varnish suitable for low temperatures. Temperature regulation is provided by a **P**roportional–**I**ntegral–**D**erivative (PID) controller of the company *Linear Research*.[13] This very versatile controller

[13] Linear Research Ass. Inc., 5244 Perry Lity Road, Trumansburg (NY), USA.

is usually operated with the input from a four-wire-resistance bridge and stabilizes to its reference value. This scheme was also applied in the first experiments with CLTDs [217,218,220,227]. A temperature stability of the detector of around 5 μK at time scales of seconds was achieved. As will be shown later, this temperature stability allowed for excellent results in heavy ion test experiments. However, on the time scale of hours, slow drifts of the operating temperature were observed [218] due to heat radiation on the detector from the environment, which are prone to changes over long time scales, and which are not seen by the temperature sensors on the copper block and are therefore not corrected for. As the detector resistance in the operating point is very sensitive to temperature changes, it was a natural move to use this resistance itself as a temperature reference in a second generation of measurements. The temperature controller of Linear Research offers the unique possibility to provide a *voltage* reference rather than a temperature reference. The amplifiers used provide an AC as well as a DC amplification path [164,184,221]. The DC path produces an offset which in turn is fed to the voltage reference of the PID controller. The need to split the input signal from the CLTD into a DC and an AC path did not deteriorate the detector performance [164]. On the opposite, temperature fluctuations were reduced to around 1 μK. Even more important, longterm drifts of the operating temperature were completely removed. From one experiment to the next, the operating point of the CLTDs was reproduced with a precision of 0.1 mV.

3.5.2. Temperature regulation for detector arrays

Due to the fluctuation of the transition temperatures of individual pixels of an array (see Section 3.2.4.2), each CLTD pixel needs its individual temperature regulation. For this purpose, a thin gold strip with a width of 10 μm and a thickness of 120 nm is deposited onto the sapphire crystal close to the aluminum structure (see Fig. 3.5). The geometry results in a heater resistance of around 15 Ω. As the heater strip is directly deposited onto the sapphire crystal, the coupling between heater and absorber is optimal. If a well-regulated heating current is applied to the gold wire, each CLTD pixel can be individually stabilized in its individual operating point. This is electronically realized by a PID feedback system based on the FPGA module of the readout system (see Section 3.3), and a digitally regulated heating current [221]. The optimal working point is chosen as a reference voltage. The real detector voltage is supplied by the DC output of the preamplifier. The digital PID feedback regulates the current through the gold heater and thus provides the temperature stabilization. Special care has to be taken to choose the time constants for the PID such that fast temperature fluctuations as from an ion signal are not counter-regulated but a longterm temperature stability of better than 1 μK is maintained. For the temperature regulation, it was found that a two-staged approach was the most feasible [221]: To suppress signal deterioration due to fast temperature fluctuations of the helium bath, the whole cold finger with its heavy copper mass is temperature-regulated to the operating temperature of the CLTD pixel with the lowest transition temperature. All other detector pixels are then stabilized in their individual operating points by applying a current to the gold heaters on the pixels [184].

3.6. Detector performance under heavy ion irradiation

The detector performance of the CLTDs was studied in the frame of various test measurements and also during the experiments discussed in Sections 4 and 5. The measurements were performed at various accelerator facilities, namely at the GSI facilities UNILAC (universal linear accelerator), SIS (synchrotron), ESR (storage ring), at Jyväskylä, Finland (cyclotron), as well as at tandem accelerator facilities at Heidelberg and Munich, Germany, and Vienna, Austria. In addition, experiments at the research reactor at Grenoble, France, were conducted. Either Rutherford-scattered beams (see for example Fig. 3.15 where the experimental setup at the UNILAC at GSI is displayed) or intensity-degraded direct beams were used for the measurements. Details of the experimental setups have been reported in [164,184,217,218,224,227].

3.6.1. CLTDs based on semiconductor thermistors

Three different composite detectors with semiconductor thermistors were exposed to several different beams of heavy ions at the GSI Darmstadt [124]. Most of the experiments were performed at the UNILAC, a linear heavy ion accelerator which provides ion energies between 1.4 and 11.4 MeV/u for any ion species. As the ion intensity cannot be decreased arbitrarily far and CLTDs are by nature rather slow devices, the ion beams were Rutherford-scattered elastically on heavy, thin metal foils of gold or nickel. A schematics of the setup is displayed in Fig. 3.15. To detect the scattered particles, the cryostat was mounted on a rotating arm, and the scattering chamber was also mounted on a rotating table. This setup provides the additional advantage that – besides the ion intensity – the ion energy can be varied by changing the scattering angle without changing the energy of the incident ion beam. For further energy variation, energy degrader foils were mounted on a movable vacuum feedthrough and could be inserted in front of the CLTDs. Dependent on the nuclear charge and energy of the ion beam, different degrader foils were used.

For the experiments with heavy ions, three different composite CLTDs with germanium thermistors were investigated:

- One CLTD, further referred to as *Germanium 1*, consisted of a germanium crystal of $3 \times 1 \times 0.5\,\mathrm{mm}^3$ glued onto a sapphire absorber of $2 \times 1 \times 0.33\,\mathrm{mm}^3$ [152,217].
- In a second campaign [152,227], an additional large cylindrical sapphire absorber of $7\,\mathrm{mm}^2 \times 6\,\mathrm{mm}$ was glued onto the detector Germanium 1 to adapt it for higher ion energies. This campaign was performed at the heavy ion synchrotron SIS-18 at GSI which can accelerate even the heaviest ions up to several hundred MeV/u. This detector shall further be referred to as *Germanium 2*.

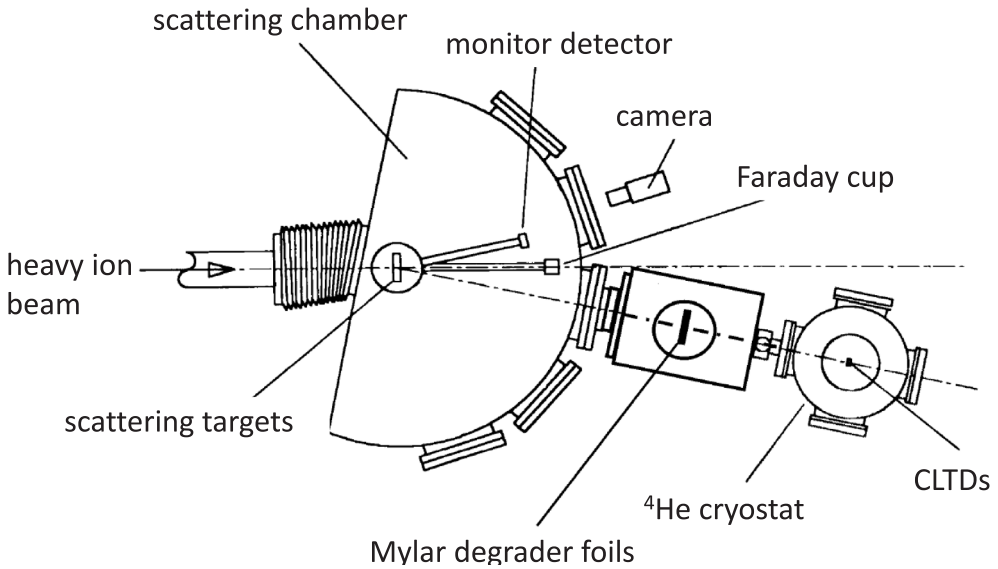

Fig. 3.15. Schematics of the setup used at the beamline of the UNILAC accelerator at the GSI Darmstadt, Germany, for various measurements. The cryostat is mounted on a movable arm which allows to adjust the scattering angle and with that the count rate to the individual experimental conditions.

Table 3.2
This table summarizes results of test measurements with composite CLTDs with germanium thermistors. The last two columns report the obtained absolute FWHM and the relative energy resolution for each ion and incident energy.

Detector	Ion	Energy [MeV/u]	ΔE (FWHM) [MeV]	$\Delta E/E$ [$\times 10^{-3}$]	Ref.
Germanium 1	^{20}Ne	11.4	1.4	6.2	[217]
	^{209}Bi	11.4	4.3	1.8	[151,152,217]
Germanium 2	^{20}Ne	100	7.4	3.7	[227]
	^{209}Bi	100	113	5.4	[227]
Germanium 3	^{95}Mo	4.4	2.8	6.7	[164]

- The aim of combining a germanium thermistor with a very thin sapphire absorber was to reduce the heat capacity and increase the signal-to-noise ratio in order to optimize the performance at very low ion energies down to 0.1 MeV/u. This CLTD, as described in Section 3.2.2.1, was designed for low ion energies with a thin sapphire absorber of $3 \times 3 \times 0.05\,\text{mm}^3$, glued to a germanium thermistor of $0.5 \times 0.5 \times 0.5\,\text{mm}^3$ [164]. This detector shall further be referred to as *Germanium 3*.

3.6.1.1. Energy resolution

A typical preamplifier signal for the impact of a 11.4 MeV/u ^{136}Xe ion onto the CLTD *Germanium 1* is displayed in Fig. 3.16. From the observed pulse height, a temperature rise of the CLTD of 9.5 mK at an operating temperature of 1.7 K was obtained. The decay time of $\tau_{eff} = 250\,\mu\text{s}$ is determined by the thermal coupling to the heat sink. Table 3.2 summarizes the results of test measurements for the different detectors, ions and ion energies, as well as the obtained absolute and relative energy resolutions. It should be mentioned that the energy resolution, which was determined from the measured energy spectrum, contains, besides the intrinsic detector resolution for heavy ions, the contribution of the energy width of the incident ion beam, the contributions due to the scattering geometry, the energy loss straggling in the scattering target used, and the contribution due to the signal-to-noise-ratio and the stabilization of the operating temperature (see also Section 3.6.2.1), dependent on the individual experimental conditions.

All relative energy resolutions are below 1%. The value of $\Delta E/E = 1.8 \times 10^{-3}$ for ^{209}Bi ions represents one of the best energy resolutions obtained with CLTDs for heavy ions. The corresponding energy spectrum is displayed in Fig. 3.17. For the incident ions, a clean spectrum showing a narrow Gaussian peak is obtained. This result represents a considerable improvement as compared to conventional ionization detectors, in particular for such very heavy ions. No conventional ionization detector has ever been reported to obtain such an excellent performance.

When considering which factors eventually limit the energy resolution, we have to compare our experimental results with the theoretical values calculated in Table 2.3. Although the measurements presented here were performed at considerably higher ion energies, these calculations may serve as a lowest limit for the expected energy resolution. For uranium ions with a total energy of 18 MeV, i.e. 0.08 MeV/u, the sum of all predicted conversion noise contributions is

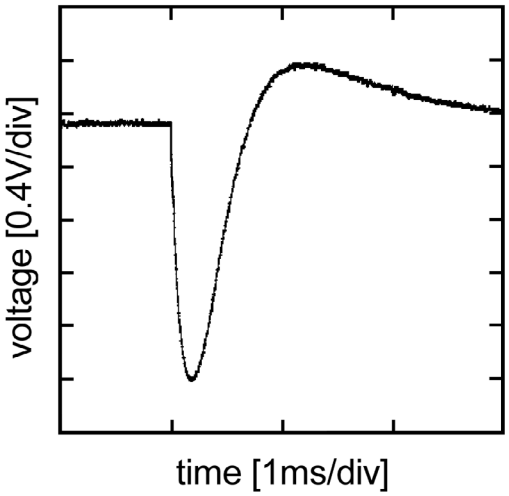

Fig. 3.16. Preamplifier signal due to the impact of a 11.4 MeV/u ^{136}Xe ion onto the detector *Germanium 1* [151].
Source: Reprinted from [15] with kind permission of Springer.

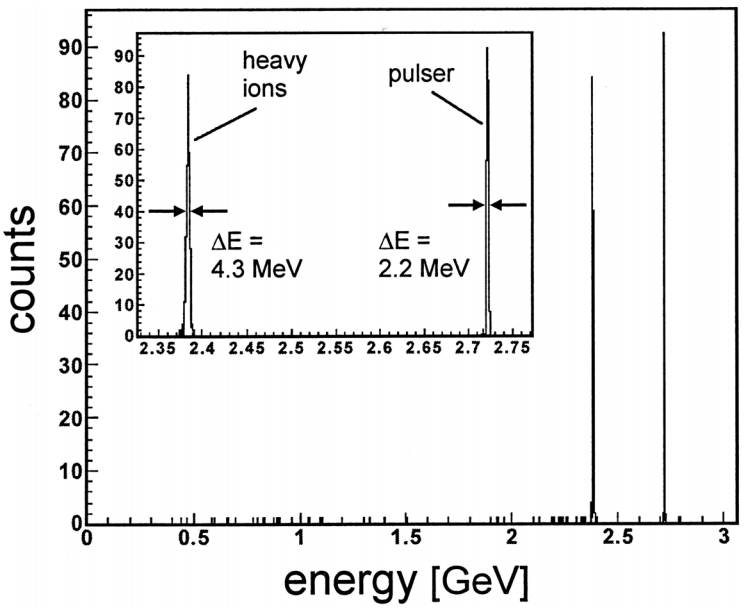

Fig. 3.17. Energy spectrum for ^{209}Bi ions with an energy of 11.4 MeV/u obtained with the composite CLTD with a germanium thermistor *Germanium 2*. The relative energy resolution is $\Delta E/E = 1.8 \times 10^{-3}$. The baseline noise was determined with a pulser which was applied to the preamplifier (see insert) [151,152,217].
Source: Reprinted from [15] with kind permission of Springer.

given as 429 keV. This would result in a relative energy resolution of $\Delta E/E = 2.4\%$. Clearly, conversion noise is rather overestimated by the calculations according to the model of H. H. Andersen [54]. The present investigations rather point to the fact that the relative energy resolution obtained is in all cases limited by the energy distribution of the incident ion beam [218].

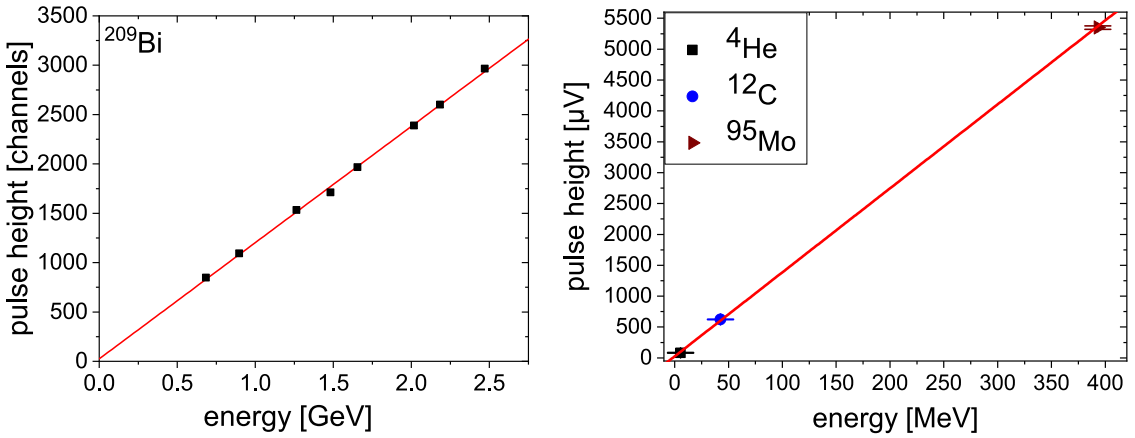

Fig. 3.18. This figure demonstrates the linearity of the energy response function for a composite CLTD with a germanium thermistor (*Germanium 2*) for ^{209}Bi ions with a total incident energy of 0.7 to 2.4 GeV (left-hand side, reproduced from [152] with kind permission), and with different ions in the energy range from 5 to 400 MeV, obtained with the detector *Germanium 3* (right-hand side) [164].

3.6.1.2. Linearity of the energy response

Another important consideration concerning the performance of any detector is the linearity of the energy response function. Fig. 3.18 (left-hand side) displays the measured pulse height as a function of ion energy for ^{209}Bi ions in an energy range of 0.7 to 2.4 GeV, obtained with the detector *Germanium 2*. The variation in energy was obtained by varying the scattering angle as well as by using several energy degraders of aluminum [152,217]. The energy response function is linear within error bars over the full energy range. For an ion energy of 2.4 GeV, a temperature change of about 10 mK can be estimated. Within this small temperature interval, dR/dT can be considered approximately constant and the approximation for small temperature signals obviously holds. This is, among others, a very important prerequisite for many applications as discussed in Section 4.2.

While the linearity of the energy response function is one concern, the response to different ion species with different masses or nuclear charges Z is another important issue. In ionization detectors, a considerable difference is observed between the energy signal caused by a low-Z ion and by a high-Z ion, even if both ions have the same kinetic energy. This phenomenon, commonly referred to as *pulse height defect* [154,207–210] (see also Section 2.5), is in many cases a severe limitation of experiments using ionization detectors. Fig. 3.18 (right-hand side) shows the signal amplitude for three different ion species at three different ion energies, obtained with detector *Germanium 3*. Within error bars, also in this case the energy response is perfectly linear. Moreover, no difference between the energy response of molybdenum and the energy response of carbon or helium is observed, meaning that no pulse height defect is visible. This result is expected from the detection principle of CLTDs, because the detection of phonons also includes the energy of recombined ion/electron pairs. It was confirmed further in investigations with aluminum transition-edge sensors and will be presented in the next section (see also Fig. 3.21).

3.6.2. CLTDs based on superconducting phase-transition thermometers

3.6.2.1. Energy resolution

Sections 4 and 5 will present the rich experimental program that has been performed with CLTDs for heavy ions based on aluminum superconducting phase-transition thermometers. Each of the experiments was prepared by feasibility studies and the investigation of the detector performance for the ion species and energy range under consideration. Over three decades, the CLTDs were applied for the detection of heavy ions covering the full mass range from ^{4}He to ^{238}U in a wide range of kinetic energies from 0.05 MeV/u up to 360 MeV/u.

Figs. 3.19 and 3.20 show examples for some of the best energy resolutions which were obtained for uranium and for samarium, i.e. a very heavy and a medium heavy ion. In three very different ranges of kinetic energies (0.07–360 MeV/u), an excellent relative energy resolution is obtained. The preamplifier signal displayed in Fig. 3.19 on the left-hand side has an effective decay time constant of $\tau_{eff} = 206\,\mu s$ which is a typical value for this type of CLTDs. It allows for count rates of up to 1 kHz without substantial pile-up. The solid line in the right panel of Fig. 3.19 is the result of a fit with a Gaussian to the data resulting in a width of $\Delta E = 80$ keV, corresponding to a relative energy resolution of $\Delta E/E = 4.6 \times 10^{-3}$ for 0.07 MeV/u ^{238}U ions, which represents the best result obtained at energies below 1 MeV/u at present. The shoulder on the low energy side is due to scattering of ions from the entrance slits of the beam line. The excellent result of 0.9×10^{-3} for 3.6 MeV/u ^{152}Sm ions, and 1.1×10^{-3} for 360 MeV/u ^{238}U ions, the latter obtained for cooled ions extracted from the storage ring ESR, has never been obtained with an ionization detector for heavy ions. A direct comparison of the energy resolution obtained with a CLTD and with a conventional silicon surface barrier detector under the same experimental

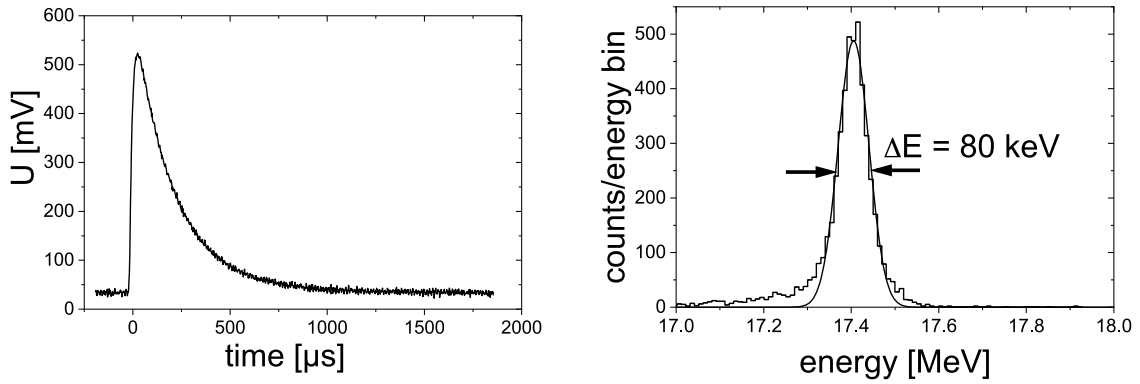

Fig. 3.19. Preamplifier signal (left-hand side) and energy spectrum (right-hand side) for ^{238}U ions at $E = 17.39$ MeV obtained with a CLTD with an aluminum thermistor. The relative energy resolution is $\Delta E/E = 4.6 \times 10^{-3}$. The decay constant of the thermal signal of $\tau_{eff} = 206\,\mu s$ allows for count rates of up to 1 kHz without significant pile-up [154,164].
Source: Reprinted from [15] with kind permission of Springer.

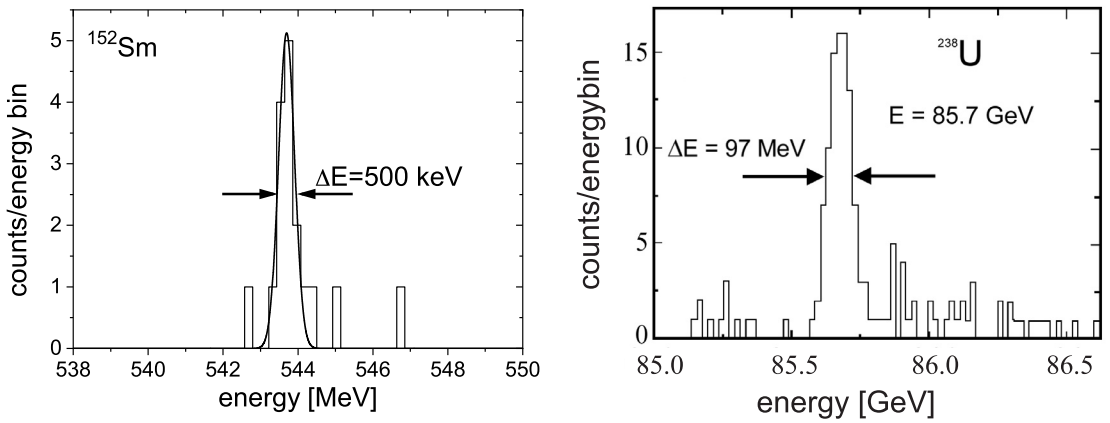

Fig. 3.20. These two energy spectra display two examples for the best energy resolutions which have been obtained for heavy ions with aluminum CLTDs. The relative energy resolution of 0.9×10^{-3} on the left hand side for 3.6 MeV/u ^{152}Sm ions [221] (reprinted from [154] with kind permission of AIP), and of 1.1×10^{-3} on the right hand side, obtained for cooled ^{238}U ions which were extracted from the storage ring ESR at 360 MeV/u, [153,228] (reprinted from [15] with kind permission of Springer) are unparalleled with conventional ionization detectors to our best knowledge.

conditions is displayed in the upper part of Fig. 3.21 for 20.85 MeV ^{238}U ions. For this case of very heavy ions at a very low energy, the FWHM of the CLTD is about a factor of 30 smaller than the FWHM of the silicon detector.

Table 3.3 gives an overview of the energy resolutions obtained for the various ion species and ion energies. In all cases, the relative energy resolutions are well below 1% for all ions and energies, and of the order of $(1 - 4) \times 10^{-3}$ in most cases. This represents a considerable improvement as compared to conventional ionization chambers or silicon detectors, which usually do not exceed an energy resolution of $\geq$ 1–5% for ions heavier than neon [54,156]. However, the energy resolution varies considerably for different measurements (see Table 3.3). There is no obvious dependence on the ion nuclear charge or ion mass nor on the ion energy. Also for measurements under similar conditions with detectors with very different absorber volumes, no difference was observed, indicating that the results are independent of the heat capacity of the detectors [153]. This rises the justified question which of the following factors actually limit the energy resolution of CLTDs:

- theoretical intrinsic limit of the energy resolution of a CLTD
  In Section 2.4, it was discussed that the energy resolution is ultimately limited by the fluctuations of the phonons between absorber and heat bath. This limit is independent of the ions or ion energies. It only depends on the mass of the absorber and the operating temperature, as described in Eq. (2.26). For the largest CLTDs used, this contribution is only of the order of 14 keV at 1.5 K. Even for the lowest ion energies, namely for uranium and gold ions at 0.08 MeV/u, this is a contribution of around 10% to the total FWHM.

Table 3.3
Results on the relative energy resolution $\Delta E/E$ obtained with various types of CLTDs with aluminum TES (see Sections 3.2.3 and 3.2.4) for various ion species and incident energies.

Ion	Energy [MeV/u]	$\Delta E/E$ [$\times 10^{-3}$]	Facility	Ref.
^{16}O	8.5	3.9	UNILAC, GSI, Darmstadt, Germany	[218]
^{20}Ne	5	2.5	Synchrotoron, Jyväskylä, Finland	[229]
^{20}Ne	8.5	2.8	UNILAC, GSI, Darmstadt, Germany	[218]
^{20}Ne	100	2.0[a]	SIS, GSI, Darmstadt, Germany	[153,227,228]
^{32}S	1	4.1[b]	Tandem, Heidelberg, Germany	[184]
^{32}S	1.9	3.2[b]	Tandem, Heidelberg, Germany	[184]
^{32}S	3.2	1.8[b]	Tandem, Heidelberg, Germany	[184]
^{40}Ar	2.5	3.7	Synchrotoron, Jyväskylä, Finland	[229]
^{40}Ar	5	1.8	Synchrotoron, Jyväskylä, Finland	[229]
^{63}Cu	0.8[b]	6.0	Tandem, Heidelberg, Germany	[184]
^{58}Ni	4.8	1.6	UNILAC, GSI, Darmstadt, Germany	[218,222]
^{64}Ni	4.8	4.4[b]	UNILAC, GSI, Darmstadt, Germany	[221]
^{109}Ag	0.6	3.3[b]	Tandem, Munich, Germany	[223]
^{109}Ag	0.7	2.3[b]	Tandem, Munich, Germany	[223]
^{127}I	0.6	3.0[b]	Tandem, Munich, Germany	[223]
^{130}Te	0.3–0.4–0.5	4.3[b]	Tandem, Munich, Germany	[230]
^{132}Xe	4.8	7.2[b]	UNILAC, GSI, Darmstadt, Germany	[221]
^{152}Sm	3.6	0.9[b]	UNILAC, GSI, Darmstadt, Germany	[221]
^{197}Au	14	4.0	UNILAC, GSI, Darmstadt, Germany	[218]
^{197}Au	0.09–0.3	6.6	VERA Tandem, Vienna, Austria	[154,164]
^{206,208}Pb	0.08	9.8	VERA Tandem, Vienna, Austria	[154,164]
^{208}Pb	5.9, 11.8	3.6, 3.8	UNILAC, GSI, Darmstadt, Germany	[218,222]
^{209}Bi	4.8	7.5	UNILAC, GSI, Darmstadt, Germany	[164]
^{209}Bi	100	4.0	SIS, GSI, Darmstadt, Germany	[227,228]
^{238}U	0.08–0.11	4.6	VERA Tandem, Vienna, Austria	[154,164]
^{238}U	70	1.4[c]	ESR, GSI, Darmstadt, Germany	[153,228]
^{238}U	360	1.1[c]	ESR, GSI, Darmstadt, Germany	[15,153,228]

[a]Measured with a composite detector consisting of a sapphire crystal of $2.5 \times 3 \times 0.33\,\mathrm{mm}^3$ with an aluminum TES onto which an additional sapphire crystal with a thickness of 5 mm and a diameter of 1 mm was glued.

[b]Measured with detectors of a detector array as described in Section 3.2.4.

[c]Measured with a cooled ion beam extracted from the Experimental Storage Ring ESR using a composite detector consisting of a sapphire crystal of $2.5 \times 2.5 \times 0.33\,\mathrm{mm}^3$ with an aluminum TES onto which an additional sapphire crystal with a thickness of 9.5 mm and a diameter of 4 mm was glued.

- energy distribution of the incident ion beam
  The distribution of the kinetic energies in the ion beam of an accelerator is usually considered as a Gaussian. Its standard deviation or FWHM is dependent on the emittance of the accelerator which in turn depends on the type of the accelerator and its technical details. It is often difficult to estimate the exact value of this energy spread. For the UNILAC and the SIS accelerators at GSI, it is of the order of about $\Delta E/E = (1-2) \times 10^{-3}$, but it depends strongly on the beam preparation and the optimization of the energy width. Therefore, in the experiments at these accelerators, the measured energy resolution may in some cases not be limited by the performance of the detector, but rather by the accelerator adjustment.
  One of the main advantages of tandem accelerators is the relatively small spread of the kinetic energy of the beam which is usually well below $\Delta E/E = 10^{-3}$ [134]. Even better beam qualities can be obtained for beams extracted from heavy ion storage rings, for example the Experimental Storage Ring (ESR) at the GSI Darmstadt, Germany, due to beam cooling, where the interaction with a mono-energetic electron beam provides a relative energy spread below $\Delta E/E \leq 10^{-4}$ [231]. Accordingly, the best results on energy resolution were obtained for beams from tandem accelerators and for beams extracted from the ESR storage ring (see Table 3.3). The energy resolution of $\Delta E/E = 1.1 \times 10^{-3}$, which is a world record for uranium as far as we know, was obtained with a cooled beam extracted from the ESR and is limited by intrinsic detector properties, because the contribution of noise in the spectrum was much lower [228].
- scattering geometry
  For all investigations of the energy resolution using heavy ion beams which are Rutherford scattered from a target (see Section 3.6.1), the contribution of energy loss straggling in the target may contribute to the measured energy resolution. Another contribution may be caused by the scattering geometry, because the ion energy depends on the scattering angle and, therefore, the angular acceptance of the experimental setup may lead to an additional broadening of the distribution of ion energies.
- signal-to-noise-ratio
  Even though CLTDs are operated at low temperatures, the readout electronics is operated at room temperature and creates electronic noise (amplifier noise). This noise is usually referred to as *baseline noise*. It is approximately

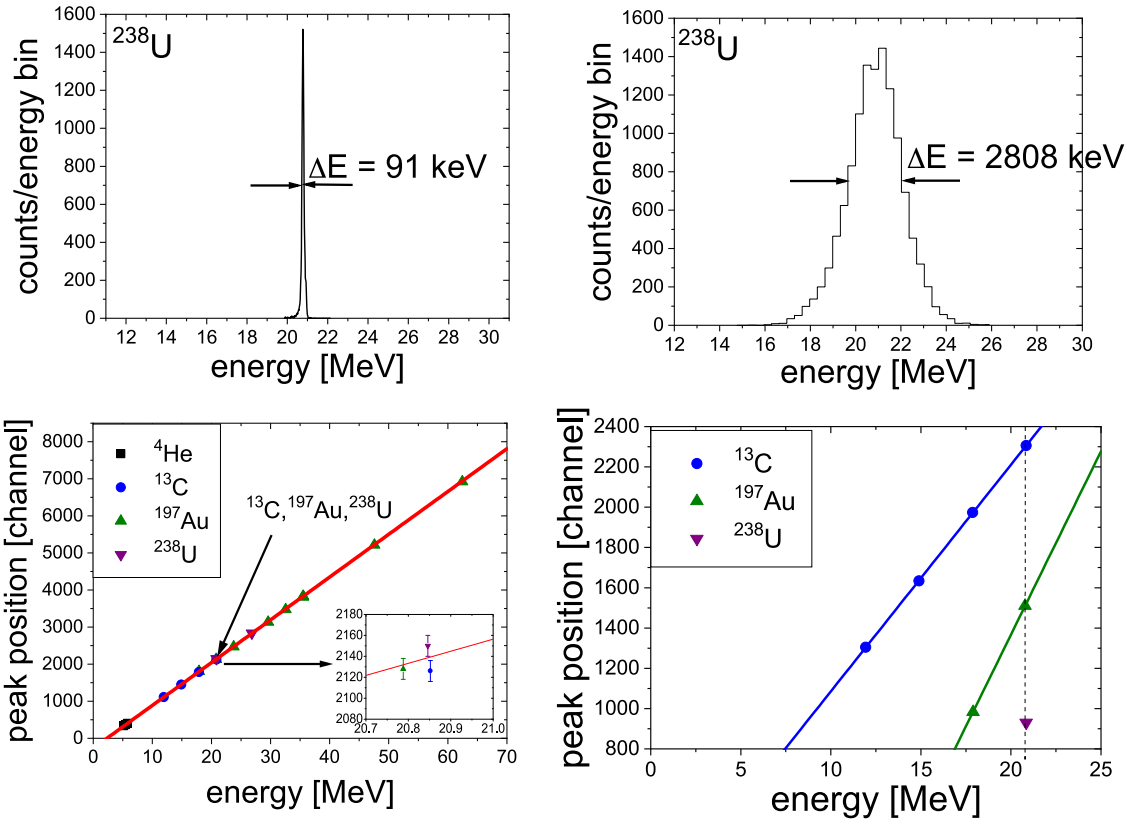

Fig. 3.21. This figure shows a direct comparison of the performance of a CLTD (figures left-hand side) and a conventional silicon surface barrier detector (figures right-hand side), obtained under identical experimental conditions. The panels on the left-hand side show a spectrum for ^{238}U at 20.85 MeV on the top and the measured pulse height in ADC channels for different ion species and energies on the bottom for the CLTD. In the panels on the right-hand side, the corresponding plots for the silicon detector are shown [154,164]. The relative energy resolution is $\Delta E/E = 4.4 \times 10^{-3}$ for the CLTD, and 135×10^{-3} for the silicon detector, respectively. Whereas a pronounced pulse height defect of up to 60% is observed for the silicon detector (lower plot on the right), no indication of a pulse height defect is observed for the CLTD (lower plot on the left). The inlay shows part of the data on an expanded scale. The peak positions for three ions with three different masses and nuclear charges (^{13}C, ^{197}Au, ^{238}U) agree within the uncertainties.
Source: Lower figures adapted from [154].

constant and independent of the properties of the ion beam. Even more severe are contributions to the baseline noise which are due to low or high frequency signals from sources of the environment which may couple to the readout circuit even after optimized shielding and the use of an isolating transformer. This problem is particularly prominent at the beamlines of HF accelerators. Baseline noise can be minimized with various filtering techniques including digital filters (see Section 3.3), but it can be the limiting factor of the obtained energy resolution under certain experimental conditions. If the signal-to-noise-ratio limits the energy resolution, ΔE is constant and the relative energy resolution should be proportional to $1/E$.

- stability of the operating temperature
  As was discussed in Section 3.5, the stability of the operating temperature may influence the energy resolution if the $R(T)$-curve is not completely homogeneous. Variations in the value of dR/dT will directly translate to a larger FWHM if the operating temperature changes during a measurement. This fact limited the energy resolution in early measurements to 2.2% before active regulation of the operating temperature was implemented (see Section 3.5) [232]. However, with an active temperature regulation the fluctuations of the operating temperature were limited to 1 μK [164]. With an average width of the transition of 10 mK, this corresponds to a relative variation of around 10^{-4}. A strong variation of dR/dT on this scale does not seem very likely [218]. However, a contribution to the energy resolution cannot be excluded for some of the measurements [228].
- condensation of residual gas on the absorber
  While no inherent loss processes affect the longterm stability of the energy response, it might deter if residual gas condensates on the detector during an extended measurement campaign. A surface at 1.5 K in vacuum acts like a perfect cryo-pump. When molecules from the residual gas in the vacuum chamber hit the detector surface, they are adsorbed and stay there until the detector is warmed up well above liquid nitrogen temperature. The best

protection against this effect is an excellent vacuum with low residual gas concentration. But even for a low pressure of 10^{-7} mbar in the accelerator beamline in front of the cryostat, its effect is visible.
The layer of frozen residual gas is amorphous and has a considerably larger specific heat capacity than sapphire, which means that even very thin layers lead to an increase in heat capacity which decreases the signal and distorts the energy resolution. Fortunately, for sufficiently low pressure the process is rather slow and can be corrected for by a linear function according to [184]

$$U(t) = \frac{U_0}{1 + b\,t} \tag{3.2}$$

where $U(t)$ describes the decreasing amplitude as compared to the initial amplitude U_0. In this regard, the absence of a pulse height defect in CLTDs is again of big advantage: signals from the $\alpha-$source which is mounted inside the cryostat can be used as a reference to monitor the decrease in signal amplitude. The according correction can be applied to all ions and ion energies [164,221].

- conversion noise
  Another limiting factor in energy resolution may be the transfer of the ion energy to the absorber, i.e. conversion noise, also discussed in Section 2.4. In Table 2.3, for ^{238}U with a total energy of 18 MeV, an estimate for this contribution is calculated to be 429 keV. The FWHM which was obtained at the VERA tandem accelerator for the same ion and energy was 80(1) keV (see Fig. 3.19), which is a factor of five smaller. Obviously, the creation of Frenkel pairs and other contributions to the conversion noise are considerably overestimated by the approach of H. H. Andersen [54] that was used for the calculations in Table 2.3. Furthermore, if the creation of Frenkel pairs would influence the FWHM, this effect is expected to be considerably larger for uranium than for the much lighter carbon ions. However, systematic investigations showed that for the same ion energy no difference in the FWHM was observed between uranium and carbon ions (see Fig. 3.22) [154,164].
- position dependence of the CLTD response function
  In very recent investigations [224], an indication was obtained that the energy response of the CLTDs used was slightly (on the level of a few times 10^{-3}) dependent on the position of the impact of the heavy ion on the absorber. It is still unclear whether this effect, which was observed for one individual detector sample only, is a general feature of all CLTDs used for the present experiments, or if it is a property of one detector. The effect may be explained due to radiation damage of this particular sample during beam adjustment. Further investigations are necessary to clarify this open question. For the case of a position dependence of the detector response function, probably by inhomogeneous thermalization of the absorber (see also [178]), further improvements of the detector design are currently under investigation.

Energy response to the impact of very slow heavy ions

For some potential applications (see Sections 4 and 5), high resolution detectors for relatively low ion energies of ≤ 1 MeV/u are needed. Therefore, the response of CLTDs to the impact of very low energetic heavy ions was systematically studied [154,164] using ^{13}C, ^{197}Au and ^{238}U beams at various incident energies ranging from total energies of $E = 10$ MeV to $E = 60$ MeV, corresponding to about $0.1 \leq E \leq 1$ MeV/u. In addition, data for 5.5 MeV α-particles provided by a ^{239}Pu/^{241}Am/^{244}Cm source, mounted inside the cryostat, were taken. The present measurements were performed at the 3 MV Tandem accelerator of the VERA facility at the university of Vienna, Austria [134,135]. This facility is discussed in detail in Section 4.3.2, where also the experimental arrangement is displayed in Fig. 4.44. The present measurements took advantage of the excellent beam qualities provided by this facility, the energy spread being of the order of $\Delta E/E \leq 10^{-4}$, and of the fact that changing from one ion species to another is a fast and relatively easy operation which facilitates systematic investigations with various ion species at various energies.

For a direct comparison, a conventional silicon surface barrier detector was mounted at the same beamline (see Fig. 4.44) and could be moved in front of the CLTD, thus allowing measurements under practically identical experimental conditions. The result of such a measurement for ^{238}U ions at $E = 20.85$ MeV is displayed in Fig. 3.21. As discussed above, the relative energy resolution of the CLTD of $\Delta E/E = 4.4 \times 10^{-3}$ is more than one order of magnitude better than the resolution of $\Delta E/E = 135 \times 10^{-3}$ achieved with the silicon detector. Furthermore, a relatively fast decrease of the energy resolution of the silicon detector throughout several hours of measuring time was observed, most probably due to radiation damage, whereas the CLTD showed no evidence of such behavior even after irradiation with integrated ion doses as high as 10^9 ions/cm^2.

Results of a systematic study on the energy resolution obtained for all ions and energies investigated are summarized in Fig. 3.22. At low energies ($E < 20$ MeV), an increase of $\Delta E/E$ for α-particles and ^{13}C is observed. This behavior may be explained by a lack of sensitivity of the present detectors due to their relatively large heat capacity, and could be improved in future by using substantially thinner absorbers as compared to $d = 330\,\mu$m in the present setup. For energies $E \geq 20$ MeV, the relative energy resolution is approximately constant, independent of ion species and incident energy. The solid line in Fig. 3.22 is the result of a fit to the data using the ansatz:

$$\frac{\Delta E}{E} = \frac{1}{E}\sqrt{\Delta E_{BLN}^2 + (\beta E)^2} \tag{3.3}$$

Hereby, ΔE_{BLN} represents the contribution of the baseline noise, amounting to 60(2) keV in this measurement, which is supposed to limit the signal-to-noise-ratio for low energies and describes the increase in relative energy resolution for

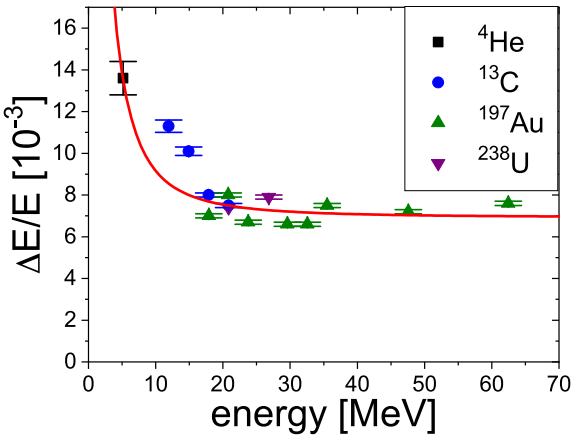

Fig. 3.22. The relative energy resolution $\Delta E/E$ of a CLTD with aluminum TES was systematically investigated at the VERA tandem accelerator for different ions, charge states and energies. The red line shows a fit to the data (for details see text).
Source: Figure adapted from [154].

$E < 15$ MeV. For the higher energies, the term $\Delta E \sim E$ dominates, β being a proportional constant. This term is most probably due to intrinsic detector properties like conversion noise, etc. (see previous section). But it could also be caused by a position dependence of the detector response function due to incomplete thermalization of the whole absorber [178]. Further detailed investigation of the energy deposition processes will be necessary for a full understanding of the obtained detector performance.

3.6.2.2. Linearity of the energy response

To investigate the energy response function, experiments with different ions and different ion energies were performed at the VERA tandem [154,164] and the Heidelberg tandem [184,221]. In both cases, the energy response function is perfectly linear. The results for ion energies between 5 and 60 MeV, obtained at the VERA tandem, are displayed in Fig. 3.21 (lower panel on the left-hand side). The solid line represents a linear fit to the data. No deviation from linearity was observed over the whole energy range. Even more remarkable, the peak positions for the three different ions ^{13}C, ^{197}Au, ^{238}U at the same energy agree within 0.1%, showing no evidence of a pulse height defect (see insert in Fig. 3.21) [154,164]. In contrast, for the conventional silicon detector a considerable pulse height defect of up to 60% was observed when comparing the peak position of ^{13}C to that of ^{238}U (see Fig. 3.21, lower panel on the right-hand side). As already discussed in Section 2.5, both, the limited energy resolution, as well as the pulse height defect of ionization detectors, are due to incomplete energy detection because of charge recombination in regions of high charge densities which happens before the ionization signal is created. Besides the good energy resolution of the CLTDs, we consider the non-existence of a pulse height defect to be a considerable advantage over ionization detectors, important for many applications (see Sections 4 and 5). Furthermore, this result allows to set an upper limit on the existence of Z-dependent energy loss processes in CLTDs, like creation of Frenkel pairs etc. (see Section 2.4.2), and on their contribution to the energy resolution.

3.6.3. Detector arrays

The best energy resolutions for the detection of heavy ions with CLTDs are listed in Table 3.3 in Section 3.6.2. The best relative energy resolution is 0.9×10^{-3}, obtained with one pixel of the two-by-five pixel array. The average relative energy resolution of this measurement for eight of the ten pixels (two were not functional during the measurement) is $(2.6 \pm 0.2) \times 10^{-3}$, where the error denotes the standard deviation. For both arrays used in various measurements, the relative energy resolution is between 1.8×10^{-3} and a few times 10^{-3}. The linearity of the detector response function was also not deteriorated by the new temperature regulation for arrays (see Section 3.5.2). All detector pixels show a linearity of better than 1.5% over an energy range of 5 to 100 MeV. The small non-linearity can be corrected for by a third order polynomial [184,223].

With this performance, the application of the two arrays in different experiments led to improved results for several physics questions and opened the door to new applications. These all will be discussed in Sections 4 and 5.

4. Application of CLTDs in heavy ion physics

4.1. Investigation of Z-yield distributions of fission fragments from thermal neutron induced fission

4.1.1. Motivation

Nuclear fission is a complex multi-faceted many-body phenomenon resulting from collective and intrinsic excitation within the nucleus in which fine structure effects and energy dissipation plays a crucial role. The understanding of the

re-ordering of the nucleons from an excited nucleus into two or more fragments, where nuclear shell and pairing effects play an important role, is one of the most challenging problems of nuclear physics.

Since its discovery [233–235], about 80 years ago, a huge amount of experimental data has been collected and various theoretical investigations have been undertaken in order to understand all details of the fission process. For an overview the reader may be referred to a collection of reviews concerning this topic [236–250]. In particular, the nuclear liquid-drop model [251] and the nuclear shell model [252,253] have been cornerstones for the present understanding of nuclear fission. During the last decades, many of the data collected world wide were incorporated in nuclear data libraries, prominent examples being JEFF-3.3 [254], ENDF/B-VIII.0 [255], JENDL-4.0 [256] and the GEF code GEFY [246].

Over the years, a number of important research topics connected with the phenomenon of nuclear fission, reaching from nuclear and particle physics to practical applications like reactor physics, were identified (see for example [257]), which address, among others:

- the basic theoretical understanding of the fission process with all its facets and tests of theoretical predictions
- information about the nuclear structure (shell effects, pair breaking, etc.) by the spectroscopy of exotic nuclei
- the understanding of the element synthesis in the universe, in particular of the astrophysical r-process taking place in the region of fission fragments
- particle physics, in particular neutrino physics
- reactor physics and technology
- nuclear energy and disposal management of radioactive waste

Despite of the big experimental and theoretical efforts mentioned above, due to its complexity the many-body phenomenon *nuclear fission* is not yet satisfactorily understood, including many discrepancies in the data, and a number of still open questions, thus demanding for new, improved data sets and more sophisticated theoretical attempts, (such as statistical models [240], microscopic–macroscopic models [242], pure microscopic models including a dynamical treatment [243], etc.). Here, besides high-energy experiments [258–268], low-energy experiments (as will be discussed in the following) are of particular importance.

The typical characteristics of low-energy fission, such as for example spontaneous or thermal neutron induced fission, is the asymmetric mass distribution of fission fragments. A nucleus is excited by capturing a low energy neutron and in turn splits (for the most probable case of binary fission) in two fragments which carry away most of the energy released as kinetic energy, and about one to three neutrons, as well as $\gamma-$rays, are emitted. As illustrated in Fig. 4.1 for the case of thermal neutron induced fission of ^{235}U, the symmetric splitting in two fragments of roughly equal mass is strongly suppressed, whereas the asymmetric splitting in a light and a heavy fragment is much more probable. As can be also seen in Fig. 4.1, thermal neutron induced fission typically leads to a multitude of about $>$ 400 different nuclei, which can be grouped in 3 mass regions, the light fragment group, the symmetry region and the heavy fragment group. The kinetic energies of the fission fragments span an interval from typically about 40 to 110 MeV for the present example.

One of the most important tools for a better understanding of the fission process, in particular for providing information on its dynamics and for a sensitive test of theoretical models describing the fission process, are precise data on the characteristics of fission fragment distributions in terms of mass distribution, nuclear charge distribution, kinetic energy distribution, excitation distribution, and correlations between these quantities. In particular, the study of isotopic fission yields as a function of fragment mass and kinetic energy allows a very detailed insight into the sharing of nucleons between the light and heavy fragments in binary fission, and the dynamics of the fission process from the saddle point to scission (see [250] and references therein). Among others the influence of shell effects, as well as pairing correlations and odd–even effects on the isotopic distributions are of particular interest.

A huge amount of data on fission yields has been collected by a worldwide scientific community since first investigations in 1941 [269]. In particular, thermal neutron induced fission of actinides has been in the focus. However, not all actinides have been scrutinized in the same detail. In particular, experiments with shorter-lived target nuclides are challenging due to their high activity. For example ^{241}Pu ($T_{1/2}$ = 14.35 a) has a specific activity of 3.8 GBq/mg and only few direct yield measurements of ^{241}Pu(n_{th}, f) have been published so far, e.g. by J. K. Dickens [270], H. Thierens et al. [271] and P. Schillebeeckx et al. [272].

^{239}Pu(n_{th}, f) and, at higher burnup, also ^{241}Pu(n_{th}, f) play an important role in nuclear reactor fuel, and together with ^{235}U(n_{th}, f) are also important for our understanding of reactor antineutrino spectra. Thus, these nuclei are in the scope of the JEFF evaluation program of fission yields [254]. This work is based on experimental data and fission models, including the nuclear charge repartition models. Today, the Z_p model of A. C. Wahl [237] is commonly used in the evaluation, but the weakness is the important dependency on fractional independent yield data. Uncertainties of the resulting fission product inventory are most pronounced outside the fission peaks, i.e. in the symmetric and far asymmetric fission regions [273]. Complementary experimental data including isotopic yields could reduce these ambiguities.

Fragment yields for thermal neutron induced fission were and presently are investigated at various research reactors all over the world using various experimental methods (see for example [250] and references 5–53 therein). One of the most prominent examples is the combination of the LOHENGRIN recoil mass separator [274,275] with the high-flux research reactor at the Institute Laue-Langevin (ILL) at Grenoble, France [145] with which outstanding contributions to our knowledge of mass, nuclear charge and energy distributions of fission fragments from actinides could be made in the

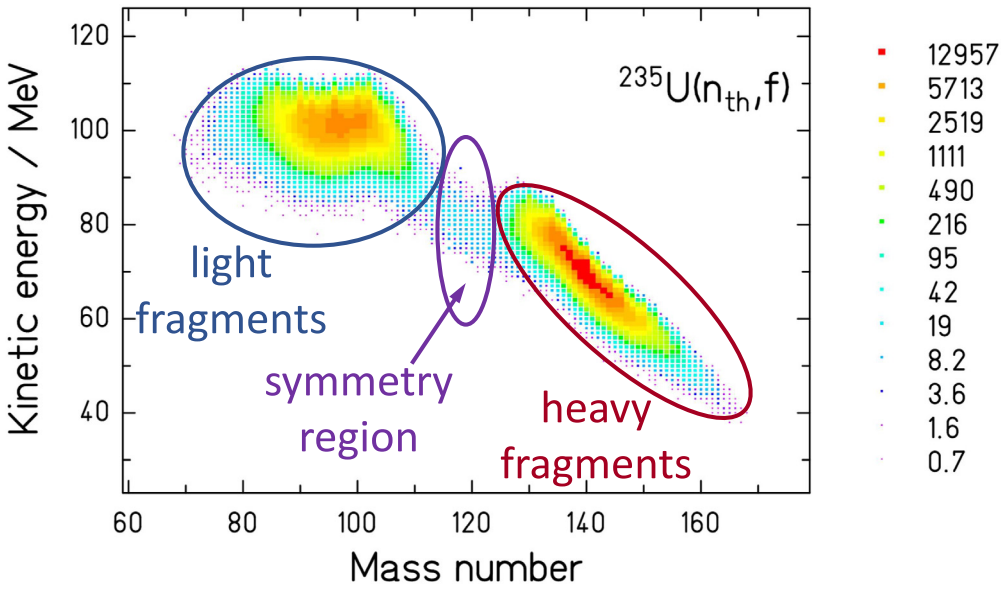

Fig. 4.1. The distribution of the kinetic energy of the fission fragments as a function of the mass number A is displayed for the case of thermal neutron induced fission of ^{235}U. The color code represents the calculated number of nuclides of a given mass number A, produced at a particular kinetic energy. The calculation was performed using the GEF model [246].
Source: Figure adapted from [246].

last 4 decades [239,244,276–282]. The basic advantage of this combination is one of the highest thermal neutron fluxes in the world together with the excellent mass and energy resolution provided by LOHENGRIN.

Fission fragments emerging from a thin fissile target, located very close (about 50 cm) to the reactor core with a thermal neutron flux of about $5 \times 10^{14}\,\mathrm{n\,cm^{-2}\,s^{-1}}$ are separated according to mass and kinetic energy with high resolution (typically $M/\Delta M > 400$, and $E/\Delta E > 100$ [274,275]). There is, however, a serious limitation: while mass and energy measurements are straight forward, the determination of the nuclear charge Z is less evident at LOHENGRIN, and requests additional experimental efforts. In the past, several experimental methods have been used for this purpose (see [244,250] and references therein, [248,249,283–285] for a detailed overview). Radiochemical methods [250] and references therein, [269,284–287] or $\gamma-$spectroscopy [244,281], [248] and references therein, [270,288–290], for instance, enable measurements in a larger range of fragment masses, but are limited to specific radioactive isotopes, depending on their lifetimes, their decay or chemical properties, as well as the limited knowledge on their decay schemes [161]. A more universal method, applicable principally to all elements, is the passive absorber method [291–293] that exploits the $Z-$dependent energy loss of fission fragments in an energy absorber for a given velocity. Here, as will be discussed in more detail in the next section, the fission fragments, separated with respect to mass and energy, pass an absorber foil, and the residual-energy which principally contains, due to the $Z-$dependent energy loss, the information on the isotopic yield distribution, is detected in an energy sensitive detector, usually in an ionization chamber or a Si detector. However, it has turned out in the past that the quality of this method, i.e. the $Z-$resolution, decreases towards higher masses, which is partly due to the limited performance of residual-energy detectors used up to date [294]. Therefore this method has been limited up to now to the region of light fission fragments up to $Z \sim 42$ [239,293–295] (see also Fig. 4.15). On the other hand, it is of high interest to get experimental access to the investigation of isotopic yield distributions in the symmetry region and the heavy mass region of the fragment mass distribution (see Fig. 4.1). The lack of data in these mass regions is very regrettable since, as symmetric and asymmetric fission are discussed as two distinct modes of decay, the comparison of charge odd–even effects in the two modes could become a crucial contribution to our understanding of the fission process. Moreover, the measurement of charge distributions in the heavy mass group by physics methods and their comparison with results from radiochemistry and $\gamma-$ray spectroscopy are, besides being relevant for our understanding of the fission process, also of technological importance in the development of future reactor generations.

Having in mind that the limitation of the passive absorber method to the light fragment group is due to the limited performance in energy resolution and energy linearity (due to the pulse height defect) of conventional detectors, such as ionization chambers or Si detectors (see Section 2 and [294]), the new detector technology of CLTDs was identified as a potential improvement for the investigation of isotopic distributions for heavier fragments. Consequently a specially designed experimental setup with a CLTD array was used in the present work for the first time for the investigation of isotopic distributions of fission fragments by the passive absorber method.

The advantages of the application of CLTDs for this research topic are in detail:

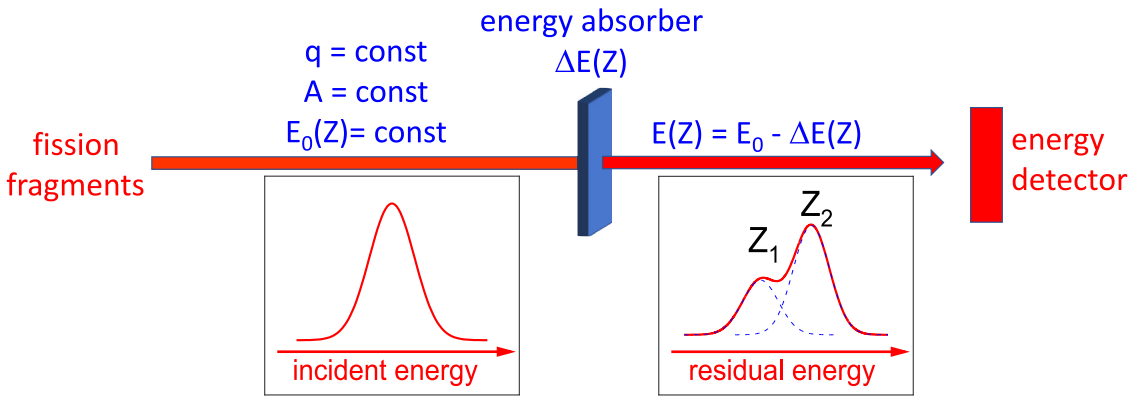

Fig. 4.2. Principle of the passive absorber method: it uses the Z dependence of the energy loss of ions in matter. The fission fragment beam from a mass separator like LOHENGRIN consists of ions with well defined mass number A, kinetic energy E_0 and ionic charge state q, but different nuclear charge Z. When passing through a homogeneous absorber medium, the Z-dependent energy loss $\Delta E(Z)$ separates the different nuclear charges Z corresponding to the different peaks in the residual-energy spectrum.

- the better energy resolution, in particular for heavy low energetic fission fragments, providing an improved $Z-$resolution in the residual-energy spectra (see Section 4.1.5),
- the better linearity of the energy response which enables systematic studies over a wider energy- and $Z-$range. This is of particular importance for a proper $Z-$identification of fission fragments (see Section 4.1.6),
- the high granularity of the CLTD array presently used, which allows systematic studies and a good control of systematic effects such as subtle shifts of the beam position in the focal plane (for details see [224]).

In the following, after a detailed description of the experimental setup and the experimental procedure, first very promising results are displayed for different regions of the mass distribution for thermal neutron induced fission of ^{235}U and ^{239,241}Pu.

4.1.2. Z-identification with the passive absorber method

As already discussed in the previous section, a rich program of the experimental determination of $Z-$yields of fission fragments has been performed at the LOHENGRIN facility at the Institut Laue Langevin at Grenoble. LOHENGRIN is a combination of electrostatic and magnetic fields which separates fission fragments from a nuclear reactor according to mass and kinetic energy, but it does not provide $Z-$separation. Besides radiochemical and $\gamma-$spectroscopy methods for the $Z-$identification of mass-separated fission fragments, which suffer from individual limitations (see previous section), a more versatile method uses the dependence of the energy deposition of heavy ions in matter, also known as the *specific energy loss*, on the nuclear charge of the incident ion.

Here, the Z-identification by means of the specific energy loss is referred to as *passive absorber method* [291–295]. It is based on the fact that the stopping power of heavy ions in matter [296] depends, among other parameters, on the nuclear charge Z of the incident ions. The principle is displayed in Fig. 4.2: Incoming ions, in the present case fission fragments, have a well defined mass, energy and ionic charge state after passing a mass separator. In the energy absorber, they deposit energy $\Delta E(Z)$ which is dependent on their nuclear charge Z. This leads to a separation of the different nuclear charges in the residual-energy spectra. The amount of deposited energy per path length in the absorber is described by the stopping power or the specific energy loss [297]. The stopping power depends on the mass A, the nuclear charge Z and the energy of the incident ions, and on the properties of the absorber material [298]. As already discussed in Section 2.3.1, the energy loss is essentially determined by two types of interaction, namely electronic and nuclear interaction. *Electronic stopping* refers to the energy loss due to inelastic collisions between the incident ions and the bound electrons in the absorber medium. *Nuclear stopping* refers to elastic collisions between the incident ions and the nuclei of the target medium. Other processes like emission of Cherenkov radiation, bremsstrahlung and nuclear reactions [2] also contribute to the energy loss, but are not relevant for the energy range of heavy ions of interest in the present fission yield studies.

For fission fragments from LOHENGRIN, the energy loss is, at least for thin absorbers and a relatively small energy loss, dominated by electronic stopping processes. Electronic stopping is described by the Bethe–Bloch formula [2,299]:

$$-\frac{dE}{dx} \equiv S_{el}(q_{eff}) = \frac{4\pi e^4}{m_e}\left(\frac{q_{eff}}{v}\right)^2 n Z_A \left[\ln\left(\frac{2m_e v^2}{\mathcal{I}}\right) - \ln(1-\beta) - \beta^2 - \frac{P_K}{Z}\right] \tag{4.1}$$

with q_{eff} = effective ionic charge of the ion, Z_A = nuclear charge of the absorber material, n = absorber density, $\mathcal{I}$ = mean excitation potential of the absorber material, v = velocity of the incident ion, $\beta = \frac{v}{c}$ and P_K = ionization probability for the K shell. The effective ionic charge q_{eff} of the ion is usually parameterized as [300,301]

$$q_{eff} = Z\left[1 - C(Z)\exp\left(-\frac{D\,v}{Z^{\delta}\,v_0}\right)\right]. \tag{4.2}$$

In this parameterization, Z denotes the nuclear charge of the incident ion, $C(Z)$, D and δ denote parameters which are determined from experimental values, while v_0 denotes the Bohr velocity. From Eqs. (4.1) and (4.2) it is evident that the electronic energy loss is approximately proportional to the square of the nuclear charge Z of the incident ion. The other parameters influencing the electronic energy loss depend on the target material, with the exception of the velocity v of the incident ion. Therefore, the energy loss of ions which have the same kinetic energy depends on their nuclear charge Z and on their mass A. Accordingly, the incident ions can be separated with respect to Z if all other parameters are fixed.

Like any statistical process, the mean energy loss is subject to statistical fluctuations in the number of collisions and in the energy transferred in each collision. So, when a mono-energetic ion beam passes through an absorber material with fixed thickness, the kinetic energy of the ions after the interaction becomes a distribution in energy rather than a delta function with a peak energy corresponding to the initial energy minus the mean energy loss. This effect is generally referred to as *energy loss straggling*. As long as the absorber is not too thin, but the energy loss is still small compared to the initial ion energy, the final energy distribution of an initially mono-energetic ion beam is – in first approximation – Gaussian with a standard deviation $\sigma \sim Z_A$ [302], where Z_A is the nuclear charge of the absorber material. For very thick absorbers, where a substantial amount of energy is lost, this assumption breaks down and the description becomes more complex. The energy loss straggling poses an inherent limitation to the quality of Z separation. From $\sigma \sim Z_A$ it can be deduced that light target atoms are favorable. In addition, inhomogeneities in the absorber material and/or channeling effects may cause an additional line broadening or even an asymmetric line shape (for details see Section 4.1.4.2, [223,224]).

In principle, it is possible to measure Z yields for all kinds of fission fragments with the passive absorber method. But it should be kept in mind that the width and the separation of the individual $Z-$peaks in the residual-energy spectra, which finally determine the quality of the $Z-$resolution (see Section 4.1.5), depend on the following parameters, which need to be optimized for the individual experimental conditions:

- energy width of the energy E_0 of the fragment beam
- energy loss straggling in the absorber medium, determined by the incident energy E_0 and the thickness and the type of the absorber medium
- the homogeneity of the absorber medium over the area where the incident ions pass through
- the intrinsic energy resolution of the residual-energy detector

In the past, it turned out that with the use of conventional ionization detectors and Parylene-C foils as energy absorbers, the passive absorber method has been limited to nuclear charges of the fission fragments below $Z = 42$ [293–295] (see also Fig. 4.15). It was evident that for the residual-energy detection a detector system with better energy resolution and linearity of the energy response in combination with more homogeneous passive absorber foils was needed to study the symmetry region and the heavy mass region of the fission fragments. Accordingly, in the present work the passive absorber method was combined with the new detector technology of CLTDs and a new type of absorber material, namely silicon nitride (SiN), to further improve the scope of this technique.

4.1.3. The experimental setup

4.1.3.1. The LOHENGRIN mass separator

As discussed in Section 4.1.1, LOHENGRIN [274,275] is a mass and energy separator which is installed at the research reactor of the Institut Laue Langevin (ILL) at Grenoble. The high-flux research reactor provides a neutron flux of about $5 \times 10^{14}\,\mathrm{cm}^{-2}\,\mathrm{s}^{-1}$ at the position of the fission target. This high neutron flux allows for measurements of fission fragment yields as low as 10^{-9}. A schematic view of the layout of LOHENGRIN is displayed in Fig. 4.3. A fissile target [303] is placed in a vacuum tube which protrudes into the heavy water moderator of the reactor. Recoiling fission fragments leave the target as highly charged ions after a small energy loss which is due to the target's protective backing. At 8 m from the target, the ionized fragments enter the horizontally deflecting homogeneous magnetic field which separates them according to their ratio of momentum to ionic charge, p/q. Afterwards, the fragments pass through the vertically deflecting condenser which separates them according to the ratio of kinetic energy to ionic charge, E/q. Accordingly, LOHENGRIN is a spectrometer which separates the fission fragments according to the ratios A/q, i.e. atomic mass to ionic charge state, and E/q. Hence, fission fragments having the same A/q ratio and the same velocity are focused along a parabola. For an energy acceptance of 10%, this parabola can be approximated by a straight line [294], but this line is tilted against the horizon by 45°. A variation in mass of 1% corresponds to 32 mm in the focal plane, and a variation in energy of 1% corresponds to 72 mm. With these features, LOHENGRIN provides excellent resolution of mass (0.3%) and energy (1%) for a standard target size of 70 × 10 mm. The flight time through the whole spectrometer is of the order of 2 µs, allowing for the determination of independent $Z-$yields as the fission fragments reach the detector before undergoing $\beta-$decay.

4.1.3.2. The fissile targets

For measurements with the LOHENGRIN mass separator, relatively thin actinide targets with a thickness of the order tens of $\mu g/cm^2$ are used for the precise fission yield measurements, whereas up to 1 mg/cm^2 thick targets are employed for nuclear spectroscopy applications. With relatively thin targets the correction for the energy loss in the target is minimized which enables the precise determination of the kinetic energy distributions of the fission fragments (see Section 4.1.6).

To obtain individual fission fragment yields, high isotopic purity of the targets is mandatory. Therefore, radiochemical separation is not sufficient in many cases, and the target atoms have to pass a mass separator before use, making the

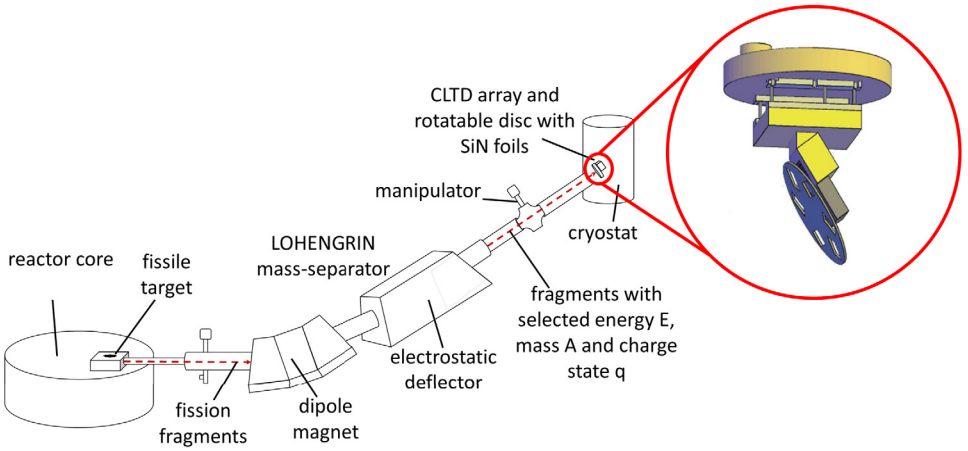

Fig. 4.3. Schematic view of the experimental setup for isotopic yield measurements at the LOHENGRIN mass separator [274,275], using the passive absorber method in combination with a CLTD: After exiting LOHENGRIN, the fission fragments pass the SiN absorber foils which are mounted directly in front of the detectors. A rotating disk (displayed on the right hand side [304]) allows for choosing different absorber thicknesses (1 μm, 4 μm, 5 μm, 6 μm, 7 μm). The manipulator serves to mount the PIN diodes as well as additional absorber foils.
Source: Adapted from [159,304].

target preparation an elaborate and expensive procedure. The LOHENGRIN targets [303] are produced by deposition of the actinide material as oxide on a 0.2 mm thick platinum-coated high purity titanium backing of dimension $9 \times 2\,cm^2$ which is fixed on a titanium support frame by spot welding. Usually, the targets are covered by a 250 nm thick nickel foil (except for the relatively thick ^{235}U targets, which are covered with ≈100 nm tungsten foils) to reduce the loss of the target material due to sputtering and to guarantee a smoother burnup. On top of the target, a diaphragm is placed to customize the size of the target corresponding to the need of the experiment. In Sections 4.1.7 to 4.1.9, the different targets used for the different measurements will be discussed in greater detail.

4.1.3.3. The passive absorber setup for the Z-yield determination

The experimental setup which was installed at the exit of the LOHENGRIN beamline is schematically displayed in Fig. 4.3 (for details see [224]). The ^4He bath cryostat (see Section 3.4) with the CLTD array for the measurement of the residual-energy was coupled – without any entrance foil – to the straight exit flange of LOHENGRIN, inclined by 35°. To ensure a sufficiently large solid angle for the detection of the fission fragments, a detector array consisting of 25 pixels in a 5 × 5 matrix with a total active area of ≈ $15 \times 15\,mm^2$ was deployed. This detector array is described in detail in Section 3.2.4 and is displayed in Figs. 3.11 and 3.14.

In order to keep the heat radiation from the environment on the CLTDs on a minimum, the shield tubes shown in Fig. 3.14 (on liquid helium, liquid nitrogen and room temperature) had to be adapted to the LOHENGRIN beamline (see Fig. 4.3). Fig. 4.4 shows the two variations with the array mounted vertically (for measurements with stable beams at the MLL, see Section 4.1.4), and under 35° (for measurements at LOHENGRIN). In front of the detectors, a rotating disk with different absorber foils is mounted at a distance of only a few millimeters from the CLTD array.

The manipulator between the LOHENGRIN exit and the detector array served two different purposes. On the one hand, it held a PIN diode which was used for complementary measurements of the ionic charge and kinetic energy distributions of the respective fragment masses [160,224] (see also Section 4.1.6). In addition to the SiN absorber foils mounted on the rotating disk, SiN absorber foils mounted on the manipulator could also be moved into the path of the fragments.

In the first experiment with CLTDs at LOHENGRIN as reported in [223,305], only the absorber foils which were mounted on a movable feedthrough (the *manipulator* in Fig. 4.3) at a distance of about 95 cm from the CLTD array were used. This large distance between absorber and residual-energy detector drastically affected the overall detection efficiency. Due to scattering processes in the absorber foil, a considerable part of the fission fragments did not reach the detector array. Therefore, the detection efficiency for these measurements was limited to less than 5% which would not have been sufficient to investigate fission fragments towards the symmetry region. In addition, an increased background from neighboring mass lines leaking through the LOHENGRIN separator was observed [223]. To counter these problems, a rotating disk was incorporated into the cryostat in the later experiments. In order to place the absorber foils as close as possible to the detectors, the foil stacks were mounted on this disk as shown in Figs. 4.3 and 4.4. It gave the flexibility to choose between five different absorber thicknesses (1 μm, 4 μm, 5 μm, 6 μm, 7 μm) and thus to optimize the absorber thickness with respect to the individual experimental conditions such as fragment mass and energy. In addition, a three-line α-source was mounted for energy calibration, as well as for monitoring the detector performance. This arrangement allowed the placement of the absorber foils very close (3 — 5 mm) to the CLTD array, and hence significantly improved the detection efficiency to almost 100% [223].

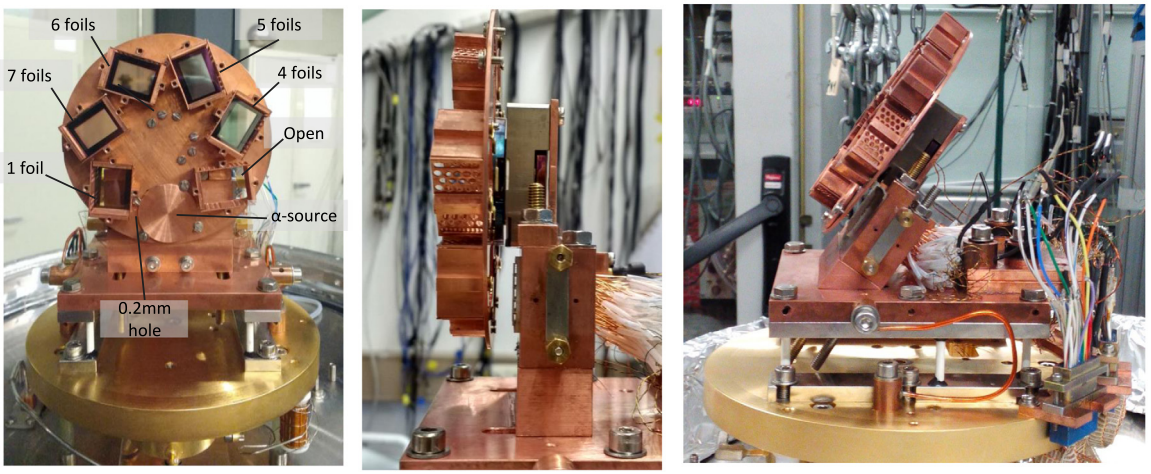

Fig. 4.4. These pictures display (a) a front view of the rotating disk with the different SiN absorber foils in front of the detector array, (b) a side view of the detector array mounted in the strictly vertical position used for the measurements with stable ion beams at the MLL (see Section 4.1.4), (c) tilted by 35° with respect to the horizontal position to match the LOHENGRIN beamline. The rotating disk was equipped with different SiN stacks with nominal thicknesses of 1 μm, 4 μm, 5 μm, 6 μm, 7 μm. In addition, one position was left open to allow for measurements without an absorber foil. The α-source is used for calibration, as well as to monitor the signal amplitude.

The rotating disk was driven by a remotely controlled piezo-driven rotary stepper positioner. In this work, we used the system ANR240/RES from Attocube,[14] which consists of a positioner with resistive encoder and the controller ANC350. The device operates under vacuum and at temperatures as low as 10 mK, and allows a reproducible positioning with an accuracy of 0.05° (30 μm for the current design) based on a slip stick driving mechanism. As only moderate voltages are needed for this positioner and as zero voltage is applied after movement, noise introduction into the readout circuit of the CLTDs is minimal which is very important to maintain the high energy resolution of the detectors. After operation of the positioner, it took only five minutes for the detector system to recover thermal equilibrium and operate without degradation of the energy resolution [224]. An α-source, also positioned on the disk, was used to calibrate the position of the rotating disk in front of the detector array. The alpha intensity was recorded for rotation steps of 5° to determine the angular position of the α-source on the disk. The α-intensity was recorded over the entire range of the encoder readout angle for which non-zero alpha intensity was observed on the detectors. The position of optimal central alignment of the α-source was determined by determining the encoder readout for which the α-intensity peaked for the central pixel C2. This allowed the calibration for all the other SiN foil positions on the manipulator which are symmetrically distributed on the disk. With this procedure, the exact orientation of the SiN foils for different measurements was reproduced with a precision of 0.03 mm.

4.1.3.4. The silicon nitride absorber foils

As is detailed in Section 4.1.2, the energy loss of the fission fragments is used to determine the nuclear charge Z. In the experiments reported in [291,293–295], foils of Parylene C were used for this purpose, because Parylene C was found to provide the best homogeneity in thickness. Inhomogeneities in the foil thickness cause an additional broadening of the energy loss distribution because the energy loss may vary depending on the position of incidence of the fragment onto the degrader foil. The homogeneity of the absorber thickness is, therefore, an important parameter that determines the Z-resolution. An additional factor is the energy loss straggling in the absorber foil which should be kept as low as possible. The energy loss straggling depends on the target material, but as a general rule, it is smaller for thin targets. But for thin targets, also the energy loss and, therefore, the Z-separation is smaller. Therefore, a compromise between energy loss and energy loss straggling has to be found for optimal Z-resolution (see also Section 4.1.4).

In recent years, the production of thin foils of silicon nitride (SiN) with excellent homogeneity has made considerable progress. The material has become an interesting alternative for entrance windows of ionization chambers [141] or time-of-flight detectors. Therefore, it was decided for the present experiments to combine the high-resolution CLTDs with absorber foils of this new material to further improve the Z-resolution. The silicon nitride (SiN) foils used in this work were manufactured by the company Silson[15] which produces and supplies ultra-thin foils with thicknesses varying from 30 nm to 1000 nm using lithographic techniques. They also produce these foils in different sizes. Regarding the nomenclature,

14 Attocube systems AG, Eglfinger Weg 2, D-85540 Haar, Germany.

15 http://www.silson.com/, Silson Ltd, Insight Park, Welsh Road East, Southam, Warwickshire, CV47 1NE, UK.

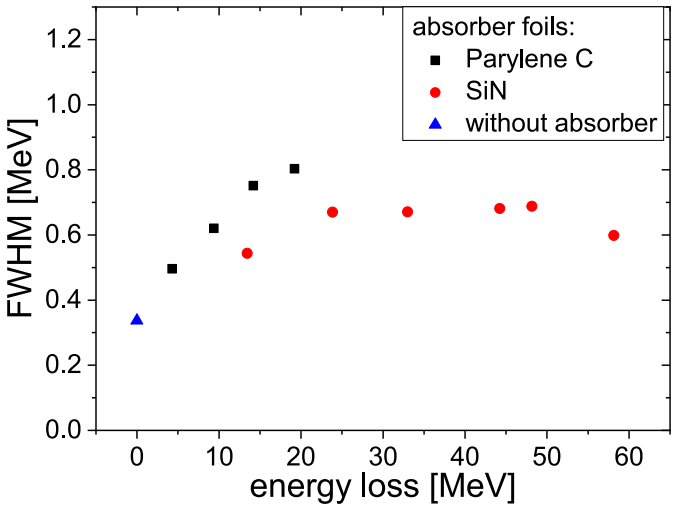

Fig. 4.5. Performance test for different types of absorber foils: The FWHM of the residual-energy spectrum for ^{109}Ag ions with an incident energy of 68.6 MeV as a function of the energy loss is shown [223].

silicon nitride is abbreviated to SiN in this work. Traditionally, silicon nitride has the stoichiometry of Si_3N_4. However, due to the high stress on Si_3N_4, it is not possible to produce membranes with a thickness greater than 200 nm–250 nm, especially for larger membranes. The thicker membranes will break. So, **Si**licon-**R**ich **N**itride (SiRN) is used instead, which has a higher Si content, more like Si:N = 1:1. It has much lower stress, typically 200 MPa – 300 MPa rather than 1 GPa in case of Si_3N_4. It is also less dense so it has a higher transmission. On the other hand, there are larger batch-to-batch variances in terms of density for SiRN than for Si_3N_4.[16] The color of the SiN foils is very sensitive to the thickness, ranging from violet to red. Varying the thickness by less than 50 nm completely changes the color. This provides a very good method for checking the relative variation of the SiN foil thickness. In addition, the density of several foils was determined using the energy loss of α-particles [306]. It was found that the homogeneity of foils from one production batch is excellent.

It was already proven in the previous investigations [223] that the SiN foils survive the cooling down and warming up procedures in the cryostat. The same measurements also demonstrated that the performance of the SiN foils was better than the performance of the Parylene C foils [294] used previously for the passive absorber method. The FWHM of the measured ion energies after passing through the foil was found to be around 15% smaller with SiN foils than with Parylene C absorbers (see Fig. 4.5) [223]. On the other hand, these foils are very sensitive and demand special care while handling.

4.1.4. Feasibility studies and performance tests with stable beams

Two crucial parameters that determine the quality of the nuclear charge determination using the absorber method are the line width in the measured residual-energy spectra and the separation, that means the energy loss difference for adjacent Z, for a given initial velocity and a fixed absorber thickness. At the LOHENGRIN mass separator, only the total widths in the residual-energy spectra, which are a sum of the detector resolution, the beam energy width which is mainly due to the target length (see Section 4.1.4.2, [223]), the absorber-foil inhomogeneity and the energy loss straggling within the absorbers, can be measured. However, to optimize the measurements for different fission-fragment mass and energy regions, the various contributions to the energy width have to be determined separately. Moreover, the precise knowledge of the line shape of the $Z-$peaks in the residual-energy spectrum is important for the fitting procedure for cases of overlapping $Z-$peaks. For this purpose, feasibility tests with isotopically pure ion beams were performed at the tandem accelerator facility at the **M**aier-**L**eibnitz **L**aboratory Munich (MLL) [307].

4.1.4.1. Experimental setup and experimental procedure

A tandem accelerator is an ideal tool for such feasibility studies, as heavy ion beams in the energy range of a few MeV to about 100 MeV can be provided with a very narrow energy distribution. Accordingly, tests at the tandem accelerator were performed with the aim to optimize the energy resolution of the new CLTD pixels, to check the quality of the new SiN foils stacks, and to precisely determine the energy loss, as well as energy loss straggling as a function of the initial ion velocity and the absorber thickness. Furthermore, it was investigated which thickness of the SiN absorber foils provides the best Z-separation.

16 Private communication with the manufacturers.

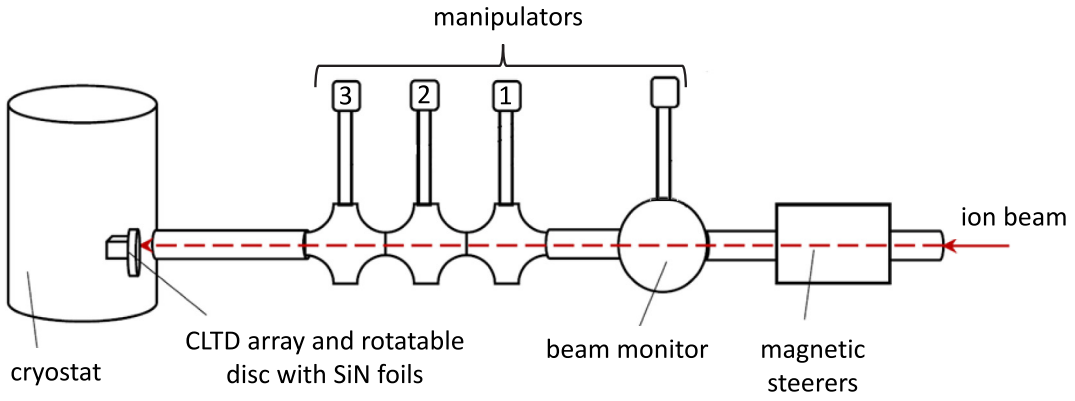

Fig. 4.6. Experimental setup at the tandem accelerator of the MLL [224]. For the test measurements, the detector array was mounted vertically with the rotating disk in front of it. Additional SiN foils were mounted on manipulators in front of the cryostat.

Ideally, to determine the quality of the Z-separation one would choose ion beams with neighboring Z values and identical mass. However, such a combination was not available in the Z region of interest ($Z \sim 50 - 55$), because a tandem accelerator demands the injection of stable negative ions which are not available for all elements for the same mass. A feasible compromise was the choice of ^{130}Te (tellurium, $Z = 52$) and ^{127}I (iodine, $Z = 53$). Based on the typical energies of fission fragments, the energy range was defined to be $50 - 85$ MeV.[17] In this energy range, the resolution of the ion beam from the accelerator is expected to be of the order of $\Delta E/E = 10^{-3}$ or better.

Fig. 4.6 shows a picture of the respective setup. The ions are delivered by the tandem accelerator from the right-hand side. The beam was adjusted to the beamline by magnetic steerers and was monitored by a beam monitor in front of a scintillating view screen. The beam intensity was adjusted by using degraders in the form of grids to a rate of <100 ions/s. The manipulators 1, 2 and 3 were used to mount additional SiN absorber foils to realize a higher thickness and to compare measurements between foils mounted on the disk and foils mounted on the manipulator for a thickness of 4 μm. The detector array in the cryostat is mounted vertically (see also Fig. 4.4) with the rotating disk in front of it. Fig. 4.4(a) shows the picture of the rotating disk mounted in front of the CLTD array, installed in the cryostat. The figure also shows the position of different SiN foil stacks with nominal thicknesses of 1 μm, 4 μm, 5 μm, 6 μm, 7 μm (for details see [224]). One position was left without absorber to investigate the energy resolution of the detectors alone.

4.1.4.2. Energy width and shape of the residual-energy spectra

As was discussed in Section 4.1.2, energy loss straggling widens an initially mono-energetic ion beam to a Gaussian line shape if the absorber is not too thick and the energy loss is not too large. However, in the case of thick absorbers, nuclear energy loss becomes more and more important. The elastic scattering of the ion on target nuclei causes not only energy transfer, but it may also alter the direction of the ion propagation which then will have to travel through a larger absorber thickness before reaching the detector. This scattering process may cause a low-energy shoulder in the otherwise Gaussian distribution. In the present setup, the distance of the absorber foils to the detectors is only about 5 mm. Accordingly, the number of scattered ions which reach the detector after traveling through a larger absorber thickness is not negligible.

Fig. 4.7 displays an example of data which are necessary for a straight-forward analysis of fission fragment data. It shows spectra of ^{127}I ions with an incident energy of 66.9 MeV after passing through a stack of SiN foils with different thicknesses. The low-energy shoulder increases with increasing foil thickness and is clearly visible for the thicker foil stacks. To account for this non-symmetric line shape, the Gaussian was modified by an exponential term containing a tailing parameter:

$$f(x) = \frac{A}{t_0} \exp\left(\frac{x - x_c}{t_0} + \frac{\sigma^2}{2t_0^2}\right) \operatorname{erfc}\left(\frac{1}{\sqrt{2}}\left(\frac{x - x_c}{\sigma} + \frac{\sigma}{t_0}\right)\right) \tag{4.3}$$

Hereby, A is the area under the Gaussian, x_c and σ are the Gaussian peak position and the standard deviation. t_0 is the tailing parameter of the exponential shoulder. *erfc* denotes the error function. To account for the tailing parameter t_0, the FWHM of the Gaussian is modified to

$$\mathrm{FWHM} = 2.35\sigma + C_r t_0 \tag{4.4}$$

The parameter C_r was determined from the ratio σ/t_0 according to [308]. In the following discussion, the term *energy resolution* ΔE refers to the FWHM determined by this equation. The *peak position* of the modified Gaussian corresponds to the most likely value of the distribution, i.e. its maximum.

[17] Since LOHENGRIN separates both mass and velocity simultaneously, it results in an energy separation, but intrinsically it is a velocity filter. Hence, the energies of the two ion beams were chosen such that the ions had the same velocity.

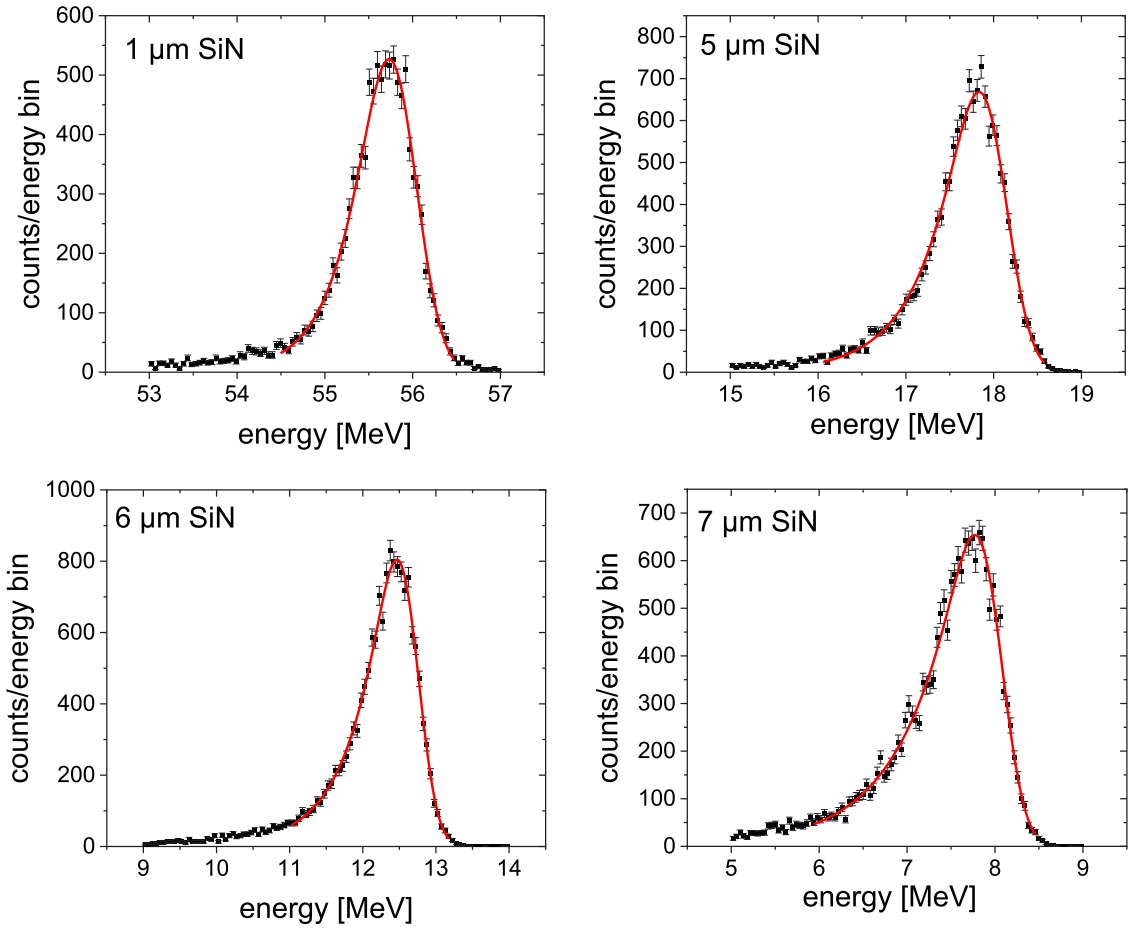

Fig. 4.7. Residual-energy spectra of ^{127}I ions with an incident energy of 66.9 MeV after passing through a stack of SiN foils with a total thickness of 1 µm, 5 µm, 6 µm, and 7 µm, respectively. The shoulder on the low-energy side is most probably due to scattering processes from nuclear energy loss. The red lines show fits with the function described by Eq. (4.3) [224].

The results of a measurement of the energy width (FWHM) for ^{130}Te ions with four different incident energies and different absorber foil thicknesses as a function of the residual-energy are summarized in Fig. 4.8. The measured data are taken from [230]. To enhance the influence of the SiN foils, the FWHM for measurements without absorber foils was subtracted quadratically for each incident energy. The corresponding values for the energy loss and stopping powers will be published in a dedicated article [306]. As expected, the FWHM increases with increasing absorber thickness (i.e. decreasing residual-energy) due to energy loss straggling. However, the FWHM increases steeply for small absorber thicknesses, then it becomes more or less constant before it increases steeply again. This effect is more pronounced at higher incident energies. In contrast, the tailing factors, determined from the same series of measurements (Fig. 4.9), do not vary strongly with the incident energy. The contribution of the shoulder increases with increasing foil thickness rather smoothly.

An interesting observation was made from the measurements where the energy width for two different stacks of SiN absorber foils with the same number of foils from the same production batch was compared. One stack was mounted on the disk at a distance of ≈5 mm from the CLTD array, the other stack was mounted on a manipulator at a distance of ≈1 m from the CLTD array. Fig. 4.10 compares the FWHM for different energy settings. The FWHM for the SiN stack mounted on the disk, i.e. closer to the CLTD array, is always higher than the one for the stack mounted on the manipulator relatively far from the detector array. The foil stack positioned closer to the array results in bigger solid angle acceptance of the beam passing through the absorber foils, whereas the foil stack positioned on the manipulator at a distance of 1 m results in a significantly smaller solid angle acceptance compared to the foil stack on the disk. The nuclear energy loss is connected to considerably larger scattering angles and hence its contribution to the energy resolution can potentially be reduced by the small solid angle acceptance of the detectors. This effect is more pronounced at lower incident ion energies.

It was hence realized with this test measurement that the gain in detector efficiency and flexibility in the choice of the SiN thickness for the experiment with fission fragments comes at the cost of a slight decrease in energy

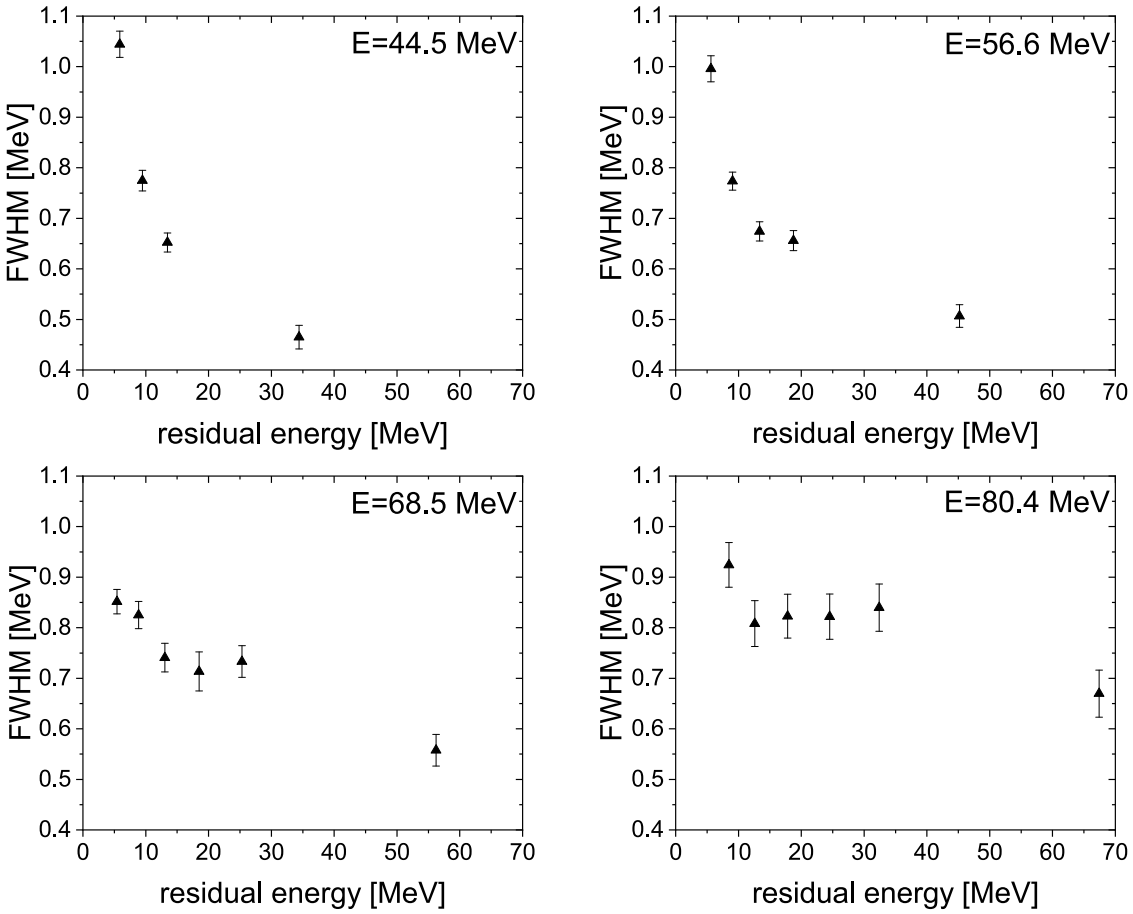

Fig. 4.8. Energy width (FWHM) obtained for ^{130}Te ions with four different incident energies as a function of the residual-energy, which is defined by the different absorber foil thicknesses (1 μm to 8 μm). The measured data were taken from [230], but the FWHM of the ion beam without SiN foils was subtracted quadratically to demonstrate the dependence on the absorber foil thickness.

resolution. However, the advantage of better efficiency outweighed this small loss in resolution. Although the theoretical understanding of its origin is still missing, the regime of constant FWHM provides a choice of absorber foil thicknesses for energies between 80 MeV and 100 MeV which are typical for LOHENGRIN. This allows adjusting the foil thickness to the optimum separation of Z which shall be discussed in the next section.

Concerning the energy width obtainable in measurements with fission fragments, it should be mentioned that the contribution from the energy resolution of the fragment beam to the overall energy width cannot be neglected. LOHENGRIN provides a nominal mass resolution of 0.3% and a relative energy resolution of 1% (see Section 4.1.3.1). However, the mass resolution and the energy resolution also depend on the length of the fissile targets. Since the magnification at LOHENGRIN from the object (fissile target) to the image (focal plane) is 1:1, for a 8 mm wide target a 8 mm wide mass-defining slit provides a mass resolution of $A/\Delta A \approx 400$ while by reducing the target width to 3 mm with a 3 mm wide exit slit improves the resolution to $A/\Delta A \approx 1000$ [224]. In [223], the influence of the target length on the overall energy resolution when using CLTDs at LOHENGRIN was investigated for two target lengths of 2 cm, and 4 cm of ^{235}U, respectively, with ions of mass $A = 92$ and $A = 102$ at an energy of $E = 97$ MeV. It was found that the FWHM for the target length of 4 cm of ^{235}U was up to 11% larger than for the target length of 2 cm. From these investigations it has to be concluded that shorter targets improve the energy resolution, but the reaction rate is also reduced. A compromise between reaction rate and energy resolution has to be made, in particular for investigations in the symmetry region where the reaction rates are low (see Section 4.1.8). Hence, the fissile targets used had surface areas ranging from few mm^2 to a maximum of $\sim 72 \times 10$ mm^2 [223,224].

4.1.4.3. Z-separation in the residual-energy spectra

To determine the Z-separation, the energy loss difference of ions with neighboring Z but same mass is required. Because ions with neighboring Z and the same mass were not available from the Munich tandem, measurements were performed with ^{127}I and ^{130}Te as detailed in Section 4.1.4.1. However, for a realistic estimate on the $Z-$separation using

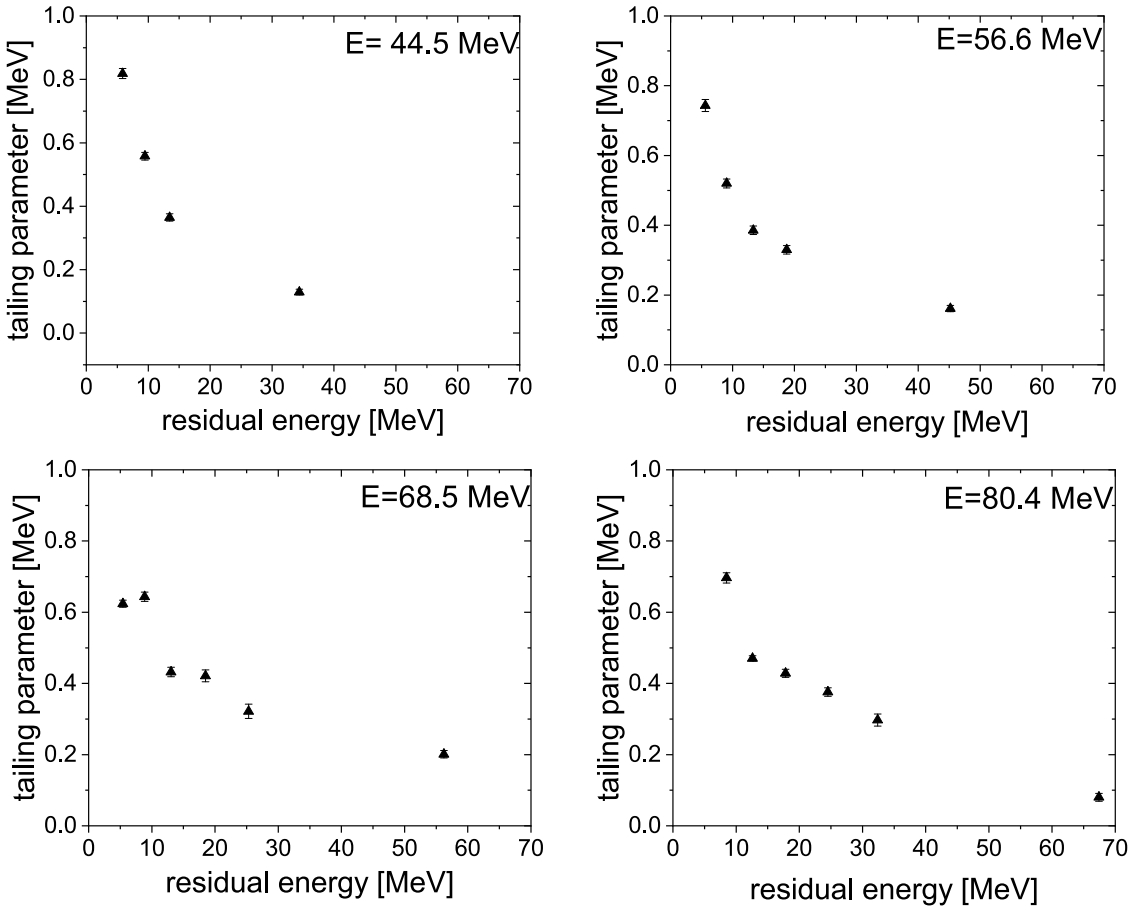

Fig. 4.9. Tailing factors deduced from the same measurements as displayed in Fig. 4.8 [230].

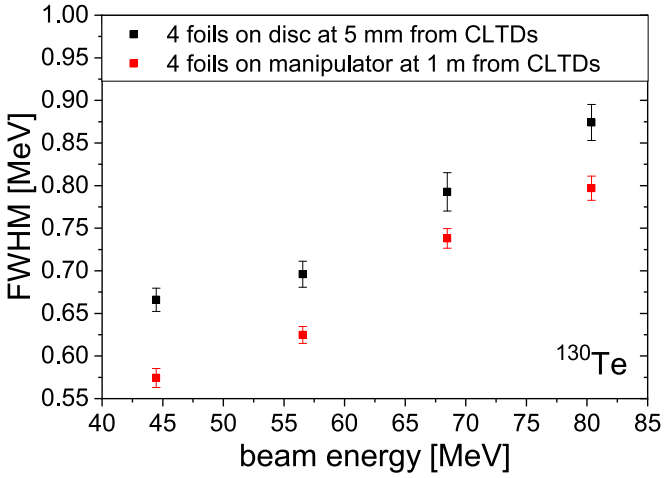

Fig. 4.10. This figure summarizes the energy width (FWHM) for ^{130}Te ions for all incident beam energies and for two absorber foil positions. In one setting, the absorber foils were positioned directly in front of the detector on the disk. In the second setting, the absorber foils were mounted on a manipulator at a distance of about 1 m from the detectors.

these beams, the dependence of the energy loss on the atomic mass *A* has to be taken into account. The correction for this mass dependence was approached in two independent ways by using SRIM calculations, and by using semi-empirical calculations [309] based on the theory of N. Bohr. A detailed discussion is given in [224,306].

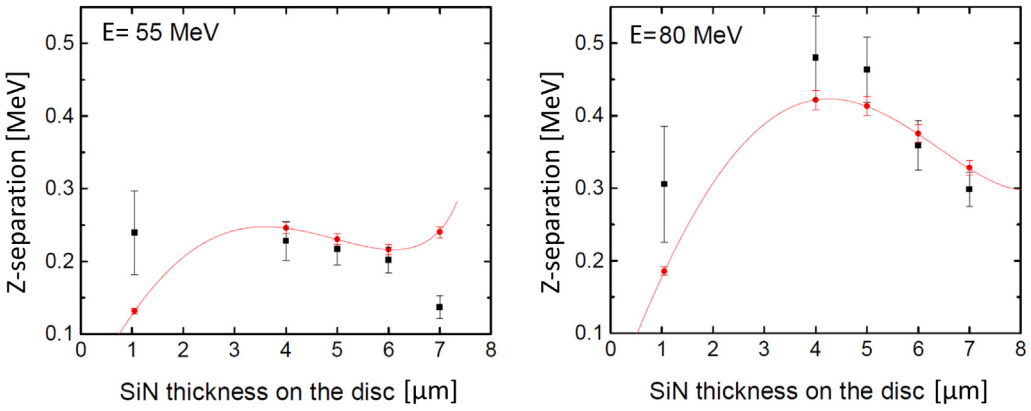

Fig. 4.11. This figure summarizes the $Z-$separation which is expected from the measurements with stable ^{127}I and ^{130}Te beams as a function of the absorber foil thickness. The correction for the A-dependence is estimated using SRIM, as shown in black, and by semi-empirical calculations developed by G. N. Knyadzeva [309] based on the classical Bohr theory, as shown in red [224].

Fig. 4.11 shows the results of the expected $Z-$separation from measurements with stable ^{127}I and ^{130}Te beams as a function of the absorber thickness. For both models, taking into account the predictions on the A-dependent correction, the data agree reasonably well within error bars. According to the calculations, the optimal $Z-$separation is obtained for an absorber foil thickness of about 4 μm. As expected, the separation increases for small absorber thickness with increasing incident energy.

4.1.5. Z-resolution

The quality of the nuclear charge resolution with the passive absorber method depends on several criteria:

- proper choice of the energy loss $\Delta E(Z)$ of the fragment beam in the absorber by choosing the appropriate absorber material and absorber thickness
- energy loss straggling within the absorber as discussed in the last section
- homogeneity of the absorber
- quality of the fragment beam (energy and mass resolution)
- energy resolution of the energy detector

The commonly used figure of merit to quantify the quality of the Z-resolution is defined as Z times the difference between the energy losses of neighboring Z (Z-separation) divided by the full width half maximum of the energy distribution according to

$$\frac{Z}{\Delta Z} = Z \cdot \frac{\Delta E(Z) - \Delta E(Z-1)}{FWHM} \tag{4.5}$$

There exists a general trend that the FWHM is increasing with increasing absorber thickness (most pronounced for smaller energies in Fig. 4.8), and also the Z-separation increases with increasing absorber thickness up to a maximum (see Figs. 4.11 and 4.14), but both findings depend on the incident energy and on Z. Therefore, an optimum needs to be found for the individual experimental conditions with respect to these parameters.

Fig. 4.12 shows the results of the expected $Z-$resolution $Z/\Delta Z$ from measurements with stable ^{127}I and ^{130}Te beams as a function of the absorber foil thickness. Again, the results for two models of the A-dependence correction are shown. The maximum is observed at an absorber foil thickness of about $4-5$ μm. At 80 MeV, the $Z-$separation of 0.45 MeV corresponds to a Z-resolution of $Z/\Delta Z \approx 25$. As the estimate was performed for rather large masses around $A = 127$ and $A = 130$, these results indicate the possibility of determining fission fragment yields also in the region of very heavy masses.

It should be mentioned that the predicted Z-resolution from the data with stable tandem beams do not include the contributions of the quality of the fragment beam to the energy width (FWHM). Therefore, even more realistic estimates on the Z-resolution are obtained from measurements at LOHENGRIN. Accordingly, the first part of the measurement campaign at the LOHENGRIN mass separator with CLTDs was dedicated to the optimization of the detector setup for the isotopic yield determination. Measurements were performed with different SiN foil thicknesses for masses $A = 89$ and $A = 96$ for ^{235}U(n_{th}, f) in order to study the effect of the SiN foil thickness on the nuclear charge resolution. Fig. 4.13, for example, shows spectra for mass $A = 89$ for ^{235}U(n_{th}, f) measured with different SiN foil thicknesses at a LOHENGRIN energy of $E_L = 94$ MeV and an ionic charge state of $q = 19$ [224]. These spectra are fitted with a sum of Gaussian distributions according to Eq. (4.7).

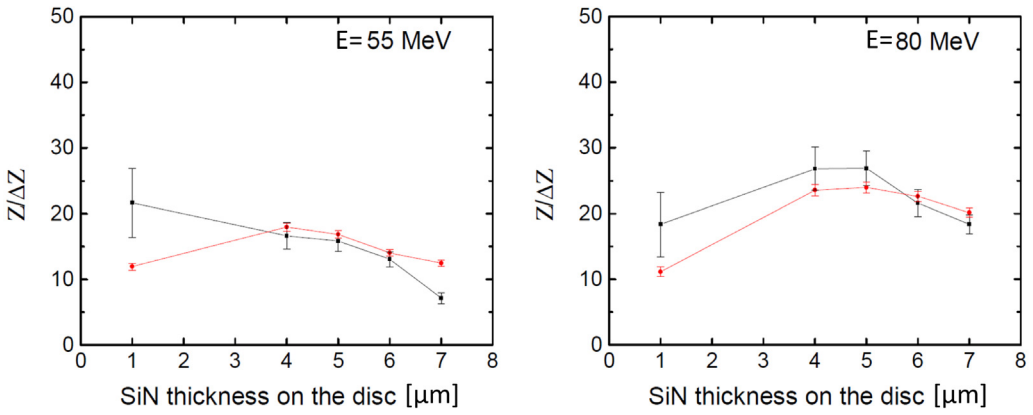

Fig. 4.12. This figure summarizes the expected quality of the $Z-$resolution $Z/\Delta Z$ which is expected from the measurements with stable ^{127}I and ^{130}Te beams as a function of the absorber foil thickness. The correction for the A-dependence is estimated using SRIM, as shown in black, and by semi-empirical calculations developed by G. N. Knyadzeva [309] based on the classical Bohr theory, as shown in red [224].

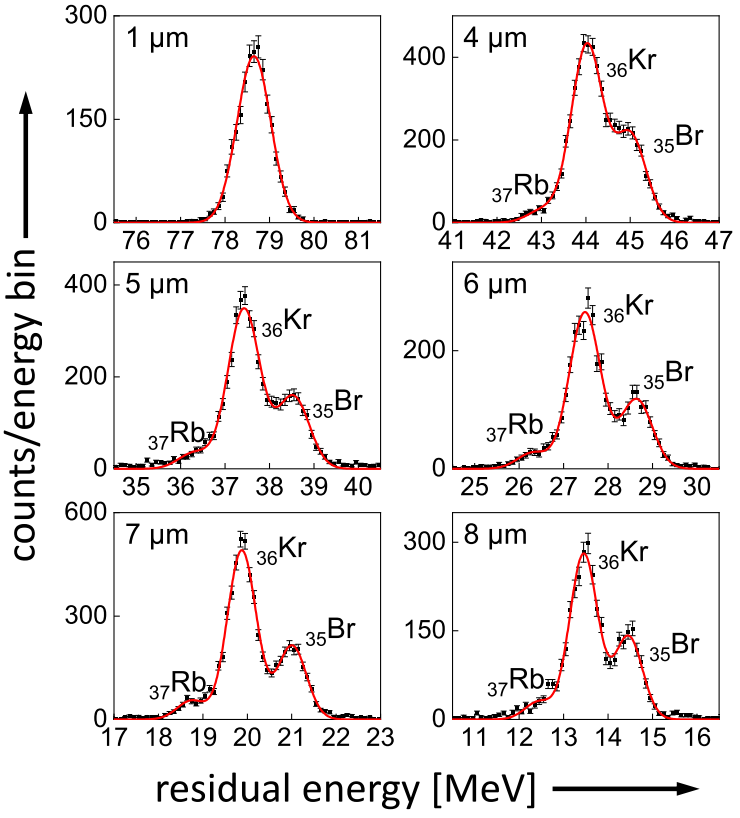

Fig. 4.13. Residual-energy spectra from a measurement for the mass $A = 89$ at a LOHENGRIN energy of $E_L = 94$ MeV for ^{235}U(n_{th}, f) for different SiN absorber foil thicknesses (1 μm, 4 to 8 μm). The increasing Z-resolution with increasing absorber foil thickness is clearly visible [224].

In Fig. 4.14 (left-hand side), the Z-resolution as a function of the SiN foil thickness is displayed [224]. The data points in red correspond to the measurement with mass $A = 89$, the black points to the one with mass $A = 96$, respectively. In both cases, the values correspond to the $Z/\Delta Z$ value for the central nuclear charge, $Z = 36$ for mass $A = 89$, and $Z = 38$ for mass $A = 96$. Also plotted (right-hand side) is the corresponding FWHM of the individual Z peaks, and the Z-separation. All data points are connected with lines to guide the eyes. The Z-resolution initially increases with increasing thickness of the SiN foil stack. It reaches a maximum of $Z/\Delta Z \sim 53$ at 7 μm foil thickness for mass $A = 89$ before it starts to decrease again.

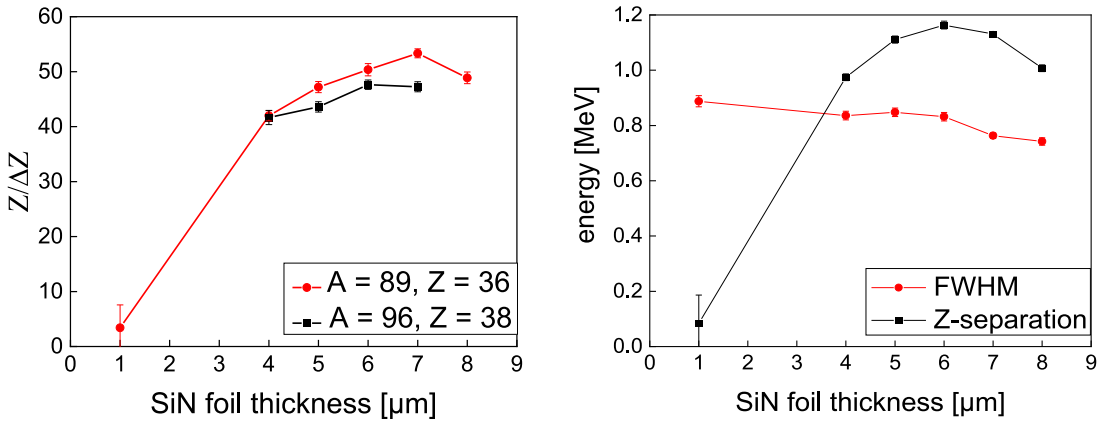

Fig. 4.14. The Z-resolution $Z/\Delta Z$ versus the SiN absorber foil thickness for masses $A = 89$ and $A = 96$ for $^{235}U(n_{th}, f)$ at a LOHENGRIN energy of $E_L = 94$ MeV is displayed on the left-hand side. The panel on the right-hand side shows the FWHM and the Z-separation for neighboring Z peaks. The data points are connected with lines to guide the eyes [224].

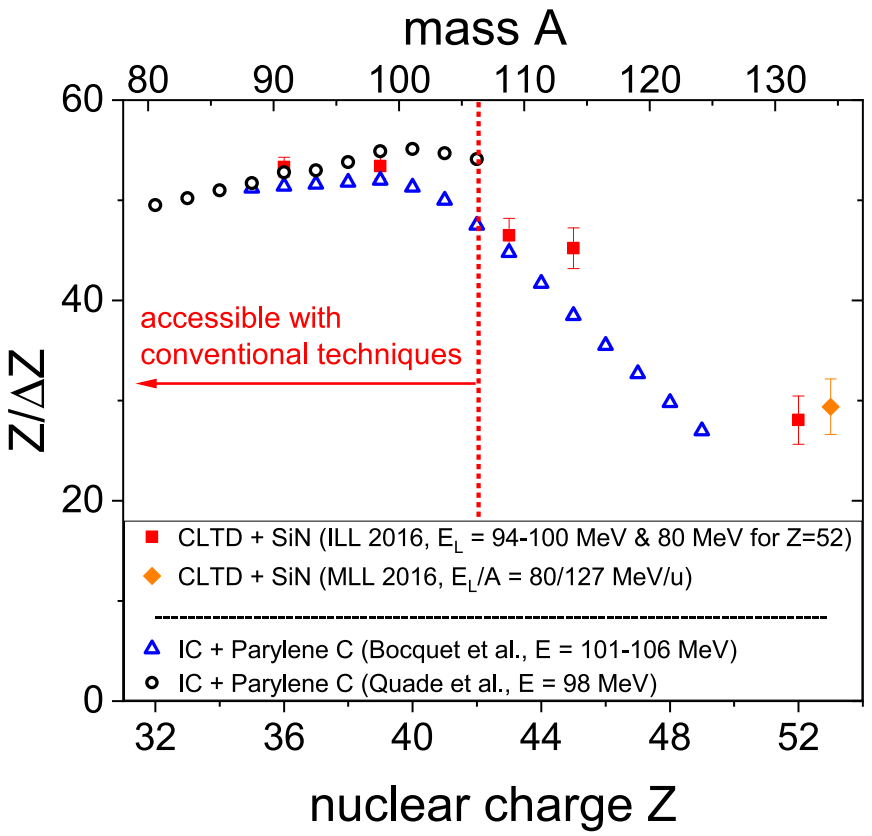

Fig. 4.15. Z-resolution ($Z/\Delta Z$) versus nuclear charge Z for Z-yield measurements using the passive absorber method, obtained with CLTDs and SiN absorbers for fission fragments at the ILL Grenoble and with stable beams at the MLL Munich [223,224]. The data are compared to data measured by U. Quade et al. [291] and J. P. Bocquet et al. (partly predictions) [294]. The latter are obtained for the condition with conventional detection techniques for the residual energy measurement, namely ionization chambers, and Parylene C as absorber foils. The limit for the application of conventional detection techniques for fission yield measurements was identified to be around $Z = 42$ [239,293–295].
Source: Adapted from [304].

Summarizing all available data, the Z-resolution $Z/\Delta Z$ (see Eq. (4.5)) is plotted as a function of mass A and nuclear charge Z in Fig. 4.15. The measurements obtained at the Munich tandem and at the LOHENGRIN are shown by the red data points. The results are compared to literature values from U. Quade et al. [291] (shown by black symbols) and J. P. Bocquet

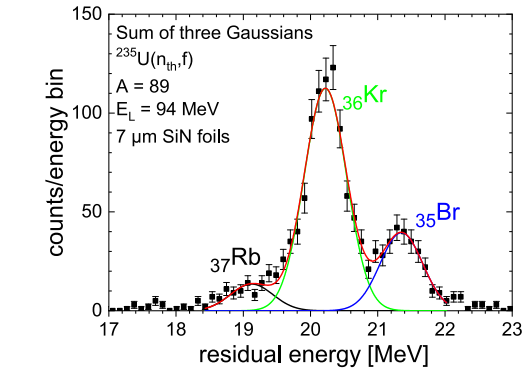

a)

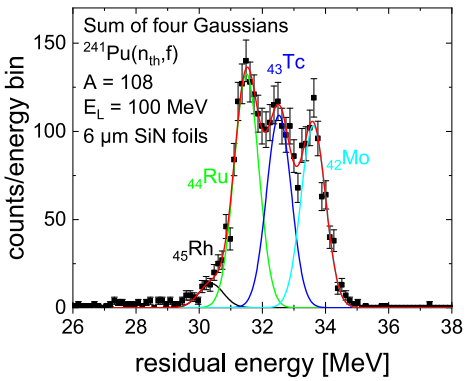

b)

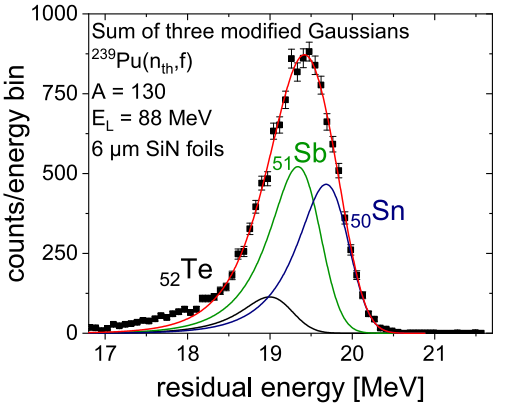

c)

Fig. 4.16. Examples for residual-energy spectra obtained for different mass regions of fission fragments. Whereas the spectra for the light (a) and symmetry (b) mass regions were fitted with a sum of Gaussians, a fit with modified Gaussians including a tail-contribution was applied to the spectrum in the heavy mass region (c) (for details see text) [224].

et al. [294] (shown by blue symbols). For the light fragment group, the historically best Z-resolution, e.g. $Z/\Delta Z = 53$ for $Z = 36$, achieved with a conventional setup of Parylene C absorbers and an ionization chamber [239,293–295], was already reached. The FWHM of the CLTDs for the fission fragments with 7 µm SiN foil thickness is typically about 800 keV for an initial kinetic energy of around 95 MeV (see Fig. 4.14). Most of the Z-yield measurements with light masses performed with 4 µm thick SiN foils have a FWHM of 850−900 keV and a Z-separation of around 1 MeV for a mean kinetic energy of around 95 MeV. Near the symmetry region of nuclear fission, we already see improvements in the Z-resolution, e.g. $Z/\Delta Z = 45$ at $Z = 45$ with the CLTD and SiN foils, compared to the values given in J. P. Bocquet et al. [294] (partly predictions) for measurements with a conventional ionization chamber. The FWHM and the energy loss difference obtained with the present setup in this region is typically 810 keV, and 880 keV, respectively. For the heavy mass region, constrained fits on the overlapping peaks in the residual-energy spectra yield a Z-resolution of $Z/\Delta Z = 28$ for $Z = 52$. This value is also in very good agreement with the estimate on $Z/\Delta Z$ from the test measurements at the Munich tandem accelerator with stable ^{130}Te and ^{127}I ion beams, shown in orange in Fig. 4.15. It demonstrates a significant improvement as compared to predictions for a conventional residual-energy detector as presented in Bocquet et al. [294] (blue symbols in Fig. 4.15). The FWHM and the Z-separation obtained for the heavy masses with 6 µm thick SiN foils are 225 keV, and 375 keV, respectively [224].

The presently reached performance allowed to apply the combination of SiN absorber foils and CLTDs at the LOHENGRIN to investigate Z yields towards the symmetry region of fission fragments and, for the first time with the passive absorber method, in the heavy mass region from $A = 92$ to $A = 133$. The results of these measurements will be presented in the following sections.

4.1.6. Procedure for the determination of Z-yields of fission fragments

The precise determination of isotopic yield distributions requires several steps concerning the data taking and data analysis:

- fitting of the individual residual-energy spectra:
In a first step, a proper fitting of the residual-energy spectra measured with the CLTDs is necessary. As the quality of the data depends on several parameters (see Section 4.1.5), a proper adjustment of these parameters for the measurement of the spectra to the individual experimental conditions is necessary (for details see [159,160,223,224,306]).
Examples for residual-energy spectra of mass- and energy-separated fission fragments from the LOHENGRIN separator after passing through SiN absorber foils are displayed in Fig. 4.16. Due to the energy-loss dependence fragments with different nuclear charge Z are separated. In order to deduce the content of counts for the individual $Z-$peaks, the spectra are fitted with a *sum-of-Gaussian* fitting function $f(x)$, in some cases with pure, symmetric Gaussians:

$$f(x) = \frac{A_1}{\sigma\sqrt{\pi/\ln(2)}}\exp\left[-\ln(2)\left(\frac{x-(x_c-d)}{\sigma}\right)^2\right] + \frac{A_2}{\sigma\sqrt{\pi/\ln(2)}}\exp\left[-\ln(2)\left(\frac{x-x_c}{\sigma}\right)^2\right] + \frac{A_3}{\sigma\sqrt{\pi/\ln(2)}}\exp\left[-\ln(2)\left(\frac{x-(x_c+d)}{\sigma}\right)^2\right] + \cdots \tag{4.6}$$

where x denotes the channel number, A_1, A_2, A_3, ... stand for the area under the peak 1,2,3, ..., σ is the standard deviation (with the FWHM $= 2.35\sigma$), x_c is the peak position of the second peak from the low energy side of the residual-energy spectrum (central peak for the case of 3 Gaussians), and d denotes the energy separation between two neighboring Z-peaks.
In some other cases – where necessary –, modified asymmetric Gaussians including an exponential term containing a tailing parameter need to be used to allow for a proper description of low energy tails of the individual peaks (see Section 4.1.4.2 and Eq. (4.3)):

$$f(x) = \frac{A_1}{t_0}\exp\left(\frac{x-(x_c-d)}{t_0}+\frac{\sigma^2}{2t_0^2}\right)\mathrm{erfc}\left[\frac{1}{\sqrt{2}}\left(\frac{x-(x_c-d)}{\sigma}+\frac{\sigma}{t_0}\right)\right] + \frac{A_2}{t_0}\exp\left(\frac{x-x_c}{t_0}+\frac{\sigma^2}{2t_0^2}\right)\mathrm{erfc}\left[\frac{1}{\sqrt{2}}\left(\frac{x-x_c}{\sigma}+\frac{\sigma}{t_0}\right)\right] + \frac{A_3}{t_0}\exp\left(\frac{x-(x_c+d)}{t_0}+\frac{\sigma^2}{2t_0^2}\right)\mathrm{erfc}\left[\frac{1}{\sqrt{2}}\left(\frac{x-(x_c+d)}{\sigma}+\frac{\sigma}{t_0}\right)\right] + \cdots \tag{4.7}$$

where t_0 denotes the tailing parameter of the exponential component, σ stands for the standard deviation of the Gaussian distribution, and *erfc* for the Gaussian error function. The FWHM is given by Eq. (4.4).
All the residual-energy spectra measured for the present investigations showed a number of $i = 2$ to maximum $i = 4$ individual Z-peaks. All additional contributions of Z-peaks turned out to have negligible intensities. In order to minimize the number of free parameters, each spectrum was analyzed under the assumption that the width 2σ of the individual Z-peaks, the separation d of neighboring Z-peaks, and the tailing parameter t_0 are constant for the individual spectrum. Following this procedure all measured spectra could be well described by the results of the fits (see also Fig. 4.16).
As already discussed in Section 4.1.5, the Z-resolution, the FWHM of the Z-peaks, the separation of neighboring Z-peaks, the shape of the Z-peaks, and the appearance of unwanted contributions of contamination from neighboring masses (leaking through the LOHENGRIN mass separator [223,224,306]), depend on the energy and the nuclear charge Z of the fragments, as well as on the absorber thickness (number of absorber foils) used. Therefore, compromises have to be made for each individual measurement series for obtaining overall optimum conditions. Generally, the Z-resolution $Z/\Delta Z$ is improving with the increasing number of absorber foils up to a maximum (see Figs. 4.12 and 4.14 in Section 4.1.5). On the other hand, contributions due to neighboring masses which may leak through the LOHENGRIN mass separator for some individual experimental conditions of fragment mass, energy, and ionic charge state, and which then are due to scattering processes in the absorber foils scattered to the region of interest for the main mass, thus disturbing the Z-peak analysis (for details see [223,224,306]). Moreover, for increasing foil thickness and for increasing nuclear charge Z of the fragments, asymmetric Z-peaks appear showing low energy tails (see Section 4.1.4.2 and Fig. 4.7). This effect is attributed to an increasing amount of nuclear energy loss in the absorber foils where the relatively large scattering angles lead partly to larger paths through the absorber foils and consequently larger energy loss (for details see [224,306]).
For all present measurements performed for the low mass region and the symmetry region of fission fragments (see Sections 4.1.7 and 4.1.8), well separated symmetric Gaussian-shaped Z-peaks are obtained already for an absorber foil thickness less then required for an optimum Z-resolution. In fact, an absorber thickness of 4 μm for measurements in the low mass region and in the symmetry-region was used. Therefore, the appearance of contaminations from neighboring masses and the appearance of asymmetric shapes of the Z-peaks could be avoided.
In contrast, for the heavy mass region with $A \geq 128$ (see Section 4.1.9), due to a decreasing Z-resolution with increasing Z (see Fig. 4.15), even for an optimum foil thickness the separation of neighboring Z-peaks was not sufficient to resolve individual peaks, but overlapping Z-peaks with asymmetric shapes with low energy tails were obtained (see Fig. 4.16). Therefore, a special fitting procedure was required for this part of the present data (for

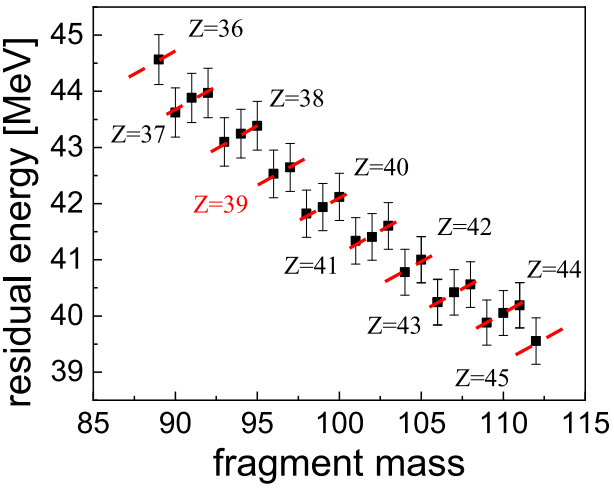

Fig. 4.17. Illustration of the Z-identification: The peak position of the second Z-peak from the low-energy (left) side of the residual-energy spectra is plotted versus the fragment mass. The data shown are extracted from measurements in the mass range $89 \leq A \leq 112$ for ^{241}Pu(n_{th}, f) at $E_L = 94$ MeV. Each red line corresponds to a unique nuclear charge Z. $Z = 39$ (marked in red) was identified from known Z-yield distributions for mass $A = 96$ [254].
Source: Reprinted from [160] with kind permission of the American Physical Society.

details see [224,306]) which followed a method described in [310]. This method is well established in high-precision mass spectrometry. Constrained fits for the deconvolution of the measured residual-energy spectra could be reliably performed, provided that the spectra were measured with sufficiently high statistics, and that the response function (that means the spectral shape of the Z-peak) was precisely known. For the latter constraint, a measurement with a beam containing one single Z-component only, but with the same energy and absorber thickness, performed at the tandem accelerator of the MLL Munich (see Section 4.1.4), was mandatory. It should be also pointed out that the excellent energy stability of the CLTDs throughout longer measurement periods was important for the success of the experiments in the heavy mass region.

- Identification of the nuclear charge Z:
  One of the crucial steps in the data analysis is the reliable identification of the nuclear charge Z corresponding to the individual peaks in the residual-energy spectra. Therefore, a systematic approach was followed which is illustrated in Fig. 4.17 for the example of measurements with the ^{241}Pu target for the mass range of $A = 89$ to 112 (for details see [160,224]). All measurements were performed with the same energy settings of LOHENGRIN E_L, and with the same thickness of SiN degrader foils (4 μm thick). This provided a very consistent Z-identification technique based on the energy loss dependence on mass and nuclear charge as shown in Fig. 4.17. The peak position of the second peak from the left side in the residual-energy spectra is plotted against the fragment mass, resulting in a step-like structure (see Fig. 4.17). The second Z-peak was chosen as it is usually the central peak with relatively high intensity making it a good choice for the systematic studies. The data points on the red dashed lines correspond to the fragments with the same nuclear charge but different mass number. The nuclear charge $Z = 39$ marked in red was identified from the known Z-yield distributions for the mass $A = 96$ [254]. Fig. 4.17 is in addition a clear representation of the different scale of energy loss dependence on the ion mass and the nuclear charge. A weaker dependence of the energy loss on the ion mass as compared to the dependence on the nuclear charge is observed as expected [295]. On average, the energy separation between adjacent masses with the same nuclear charge is about 150 keV, whereas the energy separation between fragments of adjacent nuclear charges but the same mass is about 750 keV (see Fig. 4.17). These values were also confirmed by semi-empirical calculations for the energy loss [224,306]. It should be noted here that it is due to the good energy linearity of the CLTDs, which makes it possible that such a Z-identification procedure works. Unlike the conventional detectors, where these systematics in energy loss cannot be observed due to the pulse height defect in the detectors, CLTDs offer an energy detection not affected by pulse height defects, and therefore allow to exploit the nature of energy loss for the Z-identification. Examples for the Z-identification in the heavy-mass region are displayed in Fig. 4.31 (for details see [161,224]).
- determination of isotopic yields:
  In the following, we need to distinguish between the observables *independent yields, fractional independent yields* and *cumulative yields*: Independent yields describe the probability of formation, expressed in percent, of a fission product with mass number A and nuclear charge Z after prompt neutron emission and before radioactive decay [237]. Fractional independent yields describe the fractions of the different elements with nuclear charge Z for a given mass A. The fractions add up to unity (100%) for every mass [224,244]. Thus independent yields can be determined from

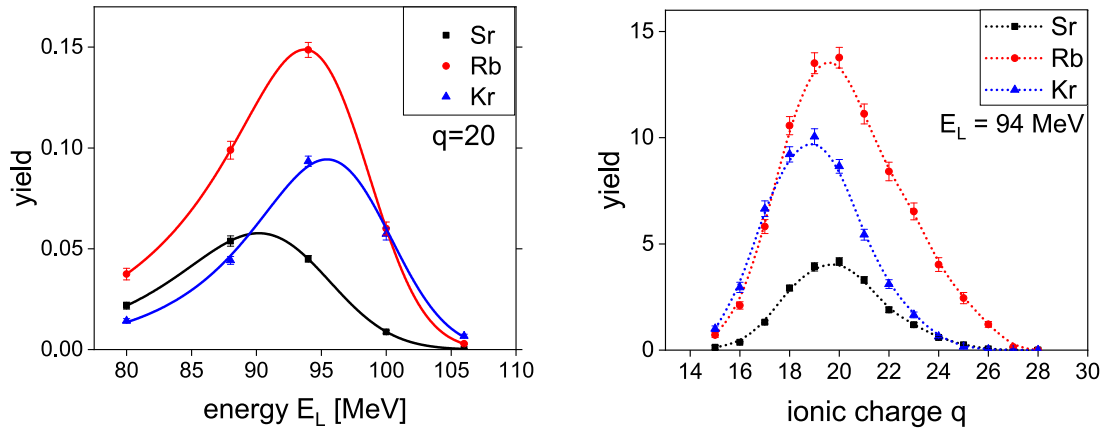

Fig. 4.18. Examples for kinetic energy (left-hand side) and ionic charge state (right-hand side) distributions of isotopic yields of mass $A = 92$ for $^{235}U(n_{th}, f)$. The solid lines on the left are exponentially modified Gaussian fits and the dotted lines on the right are used to connect the data points to guide the eyes.
Source: Reprinted from [159] with kind permission of the American Physical Society.

fractional independent yields by a multiplication with the mass yields. Whereas the independent yield describes the probability of formation directly in fission, the cumulative yield is defined as the probability of its accumulation from fission plus through the radioactive decay of its precursor(s) plus and/or minus through delayed neutron emission. It should be pointed out that the determination of independent or cumulative yields is a separable problem where mass yields and fractional yields can be determined in different experiments and later combined. The particular strengths of using CLTDs are their high and reproducible Z-resolution and, due to the granularity of the detector array, moreover the perfect control of systematic effects such as subtle shifts of the beam position in the focal plane (see also [224]). Therefore, the present work is mainly focused on a new independent determination of fractional yields, while the absolute mass yields were taken from literature, and were complemented with consistency checks against other masses in the region with well-known yields.

The determination of the final isotopic yields is performed in the following way: In a first step, from the fits of the residual-energy spectra, measured with the CLTDs (see above), the individual peak areas divided by the sum of the peak areas in the spectrum provide directly the relative nuclear charge distributions for given masses, ionic charge states and kinetic energies selected by the LOHENGRIN mass separator. As fission yields generally depend on the ionic charge state and the kinetic energy, these relative Z-yields for individual measurements at different LOHENGRIN energies and ionic charge states were convoluted with ionic charge state and kinetic energy distributions of the respective masses measured with the PIN-diode (see Fig. 4.3 in Section 4.1.3) to determine the ionic charge state and kinetic energy distributions of the corresponding nuclear charges. Examples for such distributions for the measurements in the light mass region of fission fragments are displayed in Fig. 4.18. The complete data sets are presented in [224]. The ionic charge state and kinetic energy distributions thus obtained are denoted by $Y(A, Z, q_i, E_j)$. The fractional independent yields which correspond to the integral over the ionic charge state and the kinetic energy distributions are generally given by evaluating the following sum of integrals:

$$Y(A, Z) = \sum_i \int_E Y(A, Z, q_i, E)\, dE \tag{4.8}$$

As it is a time-consuming procedure to perform measurements for all possible ionic charge state and kinetic energy settings at LOHENGRIN, a simpler approach [244,311] to estimate the yields was applied in the present work which is given by:

$$Y(A, Z) = \frac{\int_E Y(A, Z, \bar{q}, E)\, dE \times \sum_i Y(A, Z, q_i, \bar{E})}{Y(A, Z, \bar{q}, \bar{E})} \tag{4.9}$$

With this procedure, yields can be determined by measuring a single ionic charge state distribution at a mean kinetic energy $\bar{E}$ and a single kinetic energy distribution at a mean ionic charge state $\bar{q}$. Measured kinetic energy distributions are fitted with exponentially modified Gaussian functions as shown in Fig. 4.18, and both the quantities $\int_E Y(A, Z, \bar{q}, E)\, dE$ and $\sum_i Y(A, Z, \bar{E}, q_i)$ are determined from the values of the Gaussian integral, and sum, respectively. Finally, to determine the independent yields which correspond to the yields directly from fission, fractional independent yields were multiplied by the mass yields determined with the PIN-diode, and normalized to data from the literature.

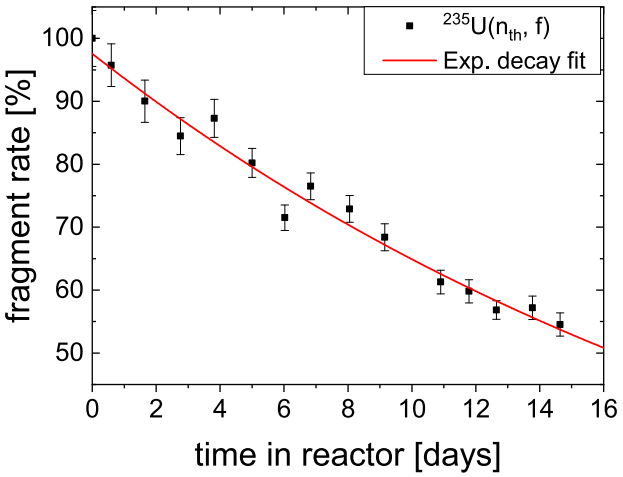

Fig. 4.19. Typical example of the fragment rate as a function of time for $^{235}\mathrm{U}(n_{th}, f)$ due to the target burn-up. The data are well described by an exponential decay function [224].

- normalization of count rates:

  (a) Energy acceptance of the LOHENGRIN mass separator: The relation between the kinetic energy E_L of the fragments measured by LOHENGRIN and the LOHENGRIN energy acceptance ΔE which is, due to the small acceptance ($\Delta E_L \ll E_L$) given by the linear equation:

  $$\Delta E_L/E_L = \Delta x/D_E \tag{4.10}$$

  where $D_E = 7.2\,\mathrm{m}$ is the energy dispersion of the spectrometer. The acceptance Δx is given by the detector size, so the ratio $\Delta x/D_E$ is constant. The accepted energy range is therefore proportional to the chosen energy. To correct for this effect, all count rates are divided by the energy set at the LOHENGRIN mass separator for normalization.

  (b) Target burn-up: When placed in a high neutron flux, the fission rate of the target decreases with time due to the loss of target material [303]. To account for the target burn-up, the decrease in fission rate was monitored regularly (once to twice a day) by measuring a reference mass. The target burn-up curve thus obtained (a typical example for the case of the ^{235}U target is displayed in Fig. 4.19) is described with an exponential decay curve, and corresponding corrections were applied in the yield calculations.

- Corrections due to the energy loss in the fission target and due to the target purity:
  The fission fragments undergo energy loss in the target and the cover of the target before they pass through the LOHENGRIN mass separator. The original kinetic energies E of the fission fragments are therefore derived by calculating this energy loss in the target and its cover and adding it to the LOHENGRIN energy setting E_L. The calculated energy losses in the target and the cover foil of the target amount to values of 5–7 MeV for the fissile targets used [159–161]. These targets were highly enriched: ^{235}U ($>$ 99%), ^{239}Pu (99.98%), and ^{241}Pu (71.1%). The ^{235}U and ^{239}Pu targets can be considered as "pure" since $\gg$ 99.9% of the fission rate stems from the isotope of interest. For the ^{241}Pu target the remaining fraction is composed of non-fissile ^{240,242}Pu and 7.7% ^{241}Am produced by $\beta-$decay of ^{241}Pu appearing since the Pu/Am separation before the target preparation. Due to its small fission cross section, $^{241}\mathrm{Am}(n_{th}, f)$ contributes only with 0.03% to the total fission rate, but $\approx$ 1.1% of the fission rate is due to double neutron capture reactions $^{241}\mathrm{Am}(n,\gamma)^{242g}\mathrm{Am}(n,f)$, and $^{241}\mathrm{Am}(n,\gamma)^{242m}\mathrm{Am}(n,f)$, respectively. The reaction of interest $^{241}\mathrm{Pu}(n_{th}, f)$ represents therefore 98.9% of the total fission rate.
- Error analysis:
  Various sources of errors are identified and taken into account in the total error budget (for details see [159–161, 224]). The statistical error including the fit error was determined using the OriginLab software for each residual-energy spectrum measured with the CLTDs. Additionally, an error of less than 0.6% was estimated due to the thermal neutron flux instability [244]. The systematic uncertainty due to the approximation used for fractional independent yield calculations (see Eq. (4.9)) leads to an error of less than 1.3% (see also [223,224,244]). Additional errors propagate from the errors in mass yields used to determine the independent yields from the fractional independent yields. We note that some of the systematic uncertainties, namely a possible bias due to the chosen ionic charge state or the kinetic energy settings on the fractional independent yields, could be reduced by additional measurements at more q and E settings. In particular, the appearance of non-Gaussian distributions of ionic charge states due to nanosecond isomers [159,244,312,313] could be then completely taken into account. The values of the independent yields include moreover the normalization uncertainty of the available mass yields.

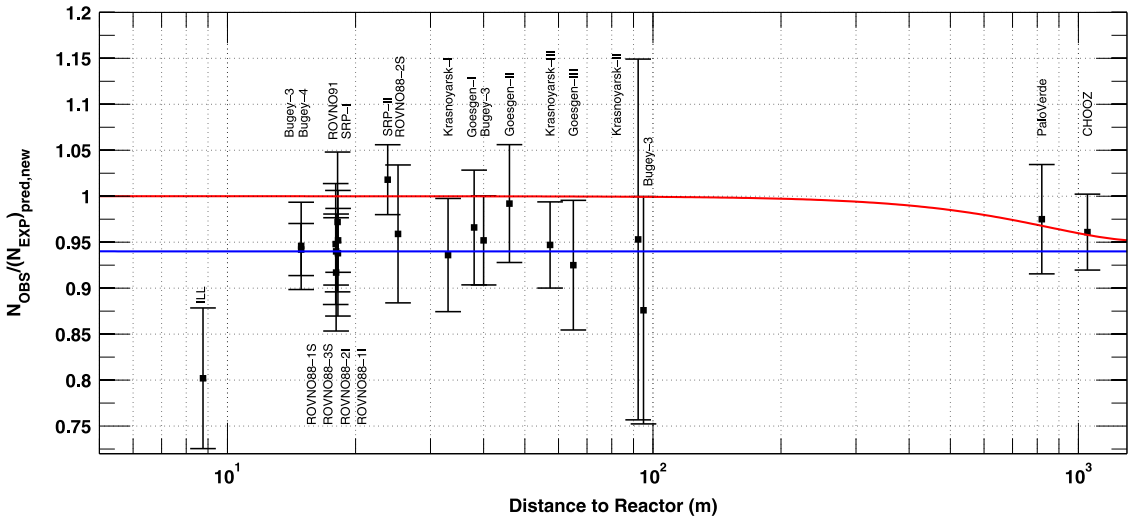

Fig. 4.20. Illustration of the short baseline reactor antineutrino anomaly. The ratio of the predicted values of the antineutrino rates to the experimental values is plotted versus the distance of the detectors to the reactor, taking into account the latest evaluation of antineutrino spectra. The mean averaged ratio is 0.943 ± 0.023. The red line shows a possible 3 active neutrino mixing solution. The blue line displays a solution including a new neutrino mass state (for illustrative purpose only).
Source: The figure is reproduced from [314] (with kind permission of the American Physical Society), where further details are presented.

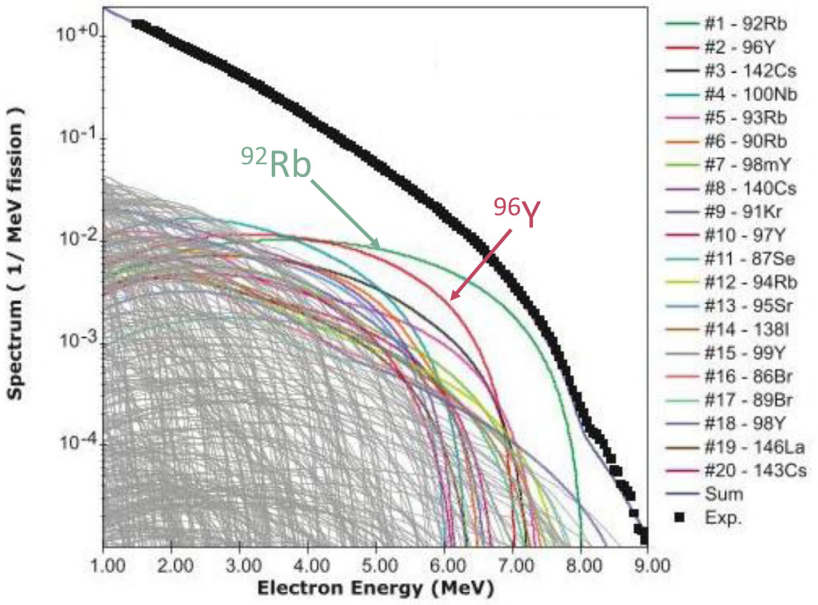

Fig. 4.21. Calculated electron spectra (solid blue line) following thermal neutron induced fission of ^{235}U compared to data from ILL (black squares). The thin gray lines indicate the individual β spectrum from each fission fragment. The colored lines highlight the 20 most important individual contributors at 5.5 MeV. The contribution of ^{92}Rb and ^{96}Y are marked by arrows.
Source: The plot is reproduced from [315] with kind permission of the American Physical Society.

4.1.7. Investigations in the light mass region: precise ^{92}Rb and ^{96}Y yields for thermal neutron induced fission of ^{235}U and ^{239,241}Pu

4.1.7.1. Motivation: the reactor antineutrino anomaly

The so-called reactor antineutrino anomaly [314], an apparent $\approx 2.5\sigma$ deficit in antineutrino rate from the Standard Model, has been derived by comparing measured antineutrino rates from nuclear reactors with those computed from integral fission product beta spectra measured previously by K. Schreckenbach et al. with the BILL spectrometer at the

Table 4.1
List of the measurements for different fissile targets to determine the isotopic yields for masses $A = 92$ and $A = 96$ at different settings for the LOHENGRIN energy E_L and the ionic charge state q.

Target	$A = 92$	$A = 96$
^{235}U	E scans at $q = 20$ and 25 for $E_L = 80$, 88, 94, 100 and 106 MeV. q scans at $E_L = 94$ MeV for all q settings between 16 and 26	E scans at $q = 18$ and 21 for $E_L = 74$, 80, 88, 94, 100, 102 and 106 MeV. q scans at $E_L = 84$, 94 and 102 MeV for all q settings between 16 and 26
^{241}Pu	E scans at $q = 21$ and 25 for $E_L = 86$, 94, 100 and 106 MeV	E scans at $q = 21$ for $E_L = 86$, 94 and 100 MeV, as well as for $E_L = 94$ MeV at $q = 18$
^{239}Pu	E scans at $q = 21$ and 25 for $E_L = 94$, 100 and 106 MeV. q scans at $E_L = 100$ MeV for $q = 17$, 20, 21, 24 and 25	

ILL [316–319]. The discrepancy is particularly pronounced for antineutrinos in the energy range from 4 to 6 MeV [320–322]. The observed reactor antineutrino anomaly could either have a particle physics explanation, namely the existence of a fourth *sterile neutrino* [314], as illustrated in Fig. 4.20, or a nuclear physics explanation, namely a problem in the conversion of beta to antineutrino spectra. Independently, from a conversion of integral beta spectra, the expected antineutrino spectra can also be computed by the summation method where the contributions of all known decay branches of fission fragments are summed, weighted with their fission yields [315,323,324]. Only few fission products with very high Q-value for beta decay contribute to the high energy part of the antineutrino spectra as illustrated in Fig. 4.21. The two main contributors are ^{92}Rb and ^{96g}Y [315,325]. It turned out [315] that, for example, ^{92}Rb has a 21.6% contribution to the antineutrino spectrum from ^{235}U at 5.5 MeV. Vigorous efforts of the neutrino community are ongoing to accurately measure reactor antineutrino spectra at short distances [326–330]. Complementary effort is required for nuclear physics experiments, evaluation and theory, to improve the knowledge of the beta spectra of the key contributors and to reduce uncertainties on their fission yields. The former data are obtained by measurements with total absorption gamma ray spectrometers [331–334], while consistency checks of nuclear data libraries already allowed to identify and eliminate certain artefacts [335]. We report in the following on new measurements of the fission yields of the two key contributors ^{92}Rb and ^{96g}Y, the former measurement explicitly requested by D. A. Dwyer and T. J. Langford [325] and by A. A. Sonzogni et al. [315]. Particular effort was devoted to the measurement of thermal neutron induced fission of ^{235}U since these results are relevant for the STEREO [326] and PROSPECT [327] experiments which measure at research reactors with pure ^{235}U core. Moreover, the yields were determined for ^{239}Pu and ^{241}Pu which have additional contributions in power reactors, thus affecting the antineutrino spectra studied by the Double Chooz [336], RENO [320,328], Daya Bay [321,329] and NEOS [330] collaborations. Precise yield measurements for ^{92}Rb and ^{96}Y were hence performed by applying CLTDs at the LOHENGRIN mass separator for a more precise knowledge of the contribution of these nuclei to the antineutrino flux, and to resolve the discrepancy in the ^{92}Rb contribution between the standard data base JEFF [254] and another independent measurement by S. V. Tipnis et al. [334].

4.1.7.2. Measurements and data analysis

Measurements were performed at different LOHENGRIN kinetic energy E_L and ionic charge state q settings to determine independent and cumulative fission yields of ^{92}Rb and ^{96}Y for ^{235}U(n_{th}, f), and ^{239,241}Pu(n_{th}, f), respectively. Three fissile targets of highly enriched ^{235}U ($>$ 99% enrichment), ^{239}Pu (99.98%) and ^{241}Pu (71.1%) were used, all in the form of oxide deposits on thick titanium backings. A detailed description is presented in Section 4.1.3.2 and Section 4.1.6.

For each target the effective area visible by the spectrometer was either defined by the area of the deposit, or constrained by a thick titanium diaphragm mounted on top of the target. The ^{235}U target had an effective area of $4 \times 0.4\,\mathrm{cm}^2$, was $128\,\mu\mathrm{g\,cm}^{-2}$ thick and was covered by a sputtered tungsten layer of $\approx$ 100 nm to reduce losses by self-sputtering [303]. The ^{239}Pu target had an effective area of $4 \times 0.3\,\mathrm{cm}^2$, was $38\,\mu\mathrm{g\,cm}^{-2}$ thick and was covered by a 0.25 μm Ni foil. The ^{241}Pu target had an effective area of $4 \times 0.5\,\mathrm{cm}^2$, was $24\,\mu\mathrm{g\,cm}^{-2}$ thick and was covered by a 0.25 μm Ni foil.

A list of all measurements performed for determining the isotopic yields of mass $A = 92$ and mass $A = 96$ is presented in Table 4.1. The complete set of data is presented in [224], and original data files are available via [337,338]. In addition, for both masses under investigation ($A = 92$ and 96) and other masses used for normalization, measurements were performed with the complementary PIN-diode detector mounted on the manipulator at the exit of LOHENGRIN (see Fig. 4.3), to determine the energy and ionic charge state distributions of these masses in order to normalize the isotopic yields determined from the measurements with the CLTDs [223,224].

After the analysis of the spectra taken with the CLTDs (see Section 4.1.6), the results for the relative Z-yields for measurements at different LOHENGRIN energies E_L and ionic charge states q were convoluted with ionic charge state and kinetic energy distributions of the respective masses measured with the PIN-diode to determine the ionic charge state and kinetic energy distributions of the corresponding nuclear charges. Examples for such distributions are displayed in Fig. 4.18. The complete data sets are presented in [224]. Fractional independent yields were then determined using Eq. (4.9) (see Section 4.1.6 for details). Finally, to determine the independent yields which correspond to the yields directly from fission, fractional isotopic yields were multiplied by the mass yields determined with the PIN-diode, normalized to data of F. L. Lisman et al. [339]. The mass yields determined for $A = 90$, 95 and 99 from PIN-diode measurements,

Table 4.2
Fractional independent yields for mass $A = 92$, Y_{frac} (%), and independent yield per fission Y_{ind} for mass $A = 92$ for thermal neutron induced fission of the three targets ^{235}U and ^{239,241}Pu. The last row represents the cumulative yields for ^{92}Rb.
Source: Data taken from [159,224].

Isotope	^{235}U(n_{th}, f)		^{239}Pu(n_{th}, f)		^{241}Pu(n_{th}, f)	
	Y_{frac} (%)	Y_{ind}	Y_{frac} (%)	Y_{ind}	Y_{frac} (%)	Y_{ind}
^{92}Br	<0.5	<0.0003	<0.5	<0.0001	<0.5	<0.0001
^{92}Kr	32.0(18)	0.0190(11)	11.6(16)	0.0035(5)	17.2(12)	0.0038(3)
^{92}Rb	51.7(31)	0.0308(18)	49.7(47)	0.0150(14)	62.5(30)	0.0139(8)
^{92}Sr	15.6(11)	0.0093(7)	37.9(53)	0.0115(16)	19.6(26)	0.0044(6)
^{92}Y	<1	<0.0006	<1	<0.0003	<1	<0.0002
Cum. ^{92}Rb		0.0499(8)		0.0186(15)		0.0178(8)

Table 4.3
Fractional independent yields, Y_{frac} (%), and independent yields per fission, Y_{ind}, for mass $A = 96$ for thermal neutron induced fission of the two targets ^{235}U and ^{241}Pu. The last two rows represent the cumulative yields for ^{96}Sr and the ratio of the independent yield of $^{96g+m}$Y to the cumulative yield of ^{96}Sr.
Source: Data taken from [159,224].

Isotope	^{235}U(n_{th}, f)		^{241}Pu(n_{th}, f)	
	Y_{frac} (%)	Y_{ind}	Y_{frac} (%)	Y_{ind}
^{96}Kr	<0.6	<0.0004	<0.6	<0.0003
^{96}Rb	4.2(3)	0.0026(2)	3.8(4)	0.0016(2)
^{96}Sr	54.4(21)	0.0339(13)	57.9(29)	0.0251(14)
^{96}Y	34.1(14)	0.0212(9)	32.9(30)	0.0143(13)
^{96}Zr	6.3(5)	0.0039(3)	4.4(9)	0.0019(4)
^{96}Nb	<1.6	<0.001	<1.6	<0.0007
Cum. ^{96}Sr		0.0366(11)		0.0268(16)
$^{96g+m}$Y/^{96}Sr		0.579(29)		0.532(55)

normalized to the mass yields for $A = 92$ and $A = 96$, are fully consistent with the respective values from F. L. Lisman et al. [339] and the JEFF-3.3 data library [254]. Masses 90, 95 and 99 were chosen because the cumulative fission yields of ^{90}Sr, ^{95}Zr and ^{99}Mo cover > 99.9% of the respective mass yields and these cumulative yields are accurately known also from radiochemical measurements.

We note that ^{96}Y has two beta-decaying states, the 0^- ground state ^{96g}Y ($T_{1/2} = 5.34$ s) and the 8^+ isomeric state ^{96m}Y ($T_{1/2} = 9.6$ s). Both are populated in nuclear fission, but only the beta decay of ^{96g}Y contributes significantly to antineutrino spectra above 4 MeV while the beta decay of ^{96m}Y feeds higher-lying high-spin levels in ^{96}Zr, which increases the fraction of the Q-value released as γ-rays at the expense of energy released by betas and antineutrinos. The method used in the present experiment is only sensitive to isotopes but not to isomers. Thus we report the isotopic yield ^{96}Y which represents the sum of the yields of both beta-decaying isomers ^{96g}Y and ^{96m}Y. An additional measurement with an independent method, e.g. γ-ray spectrometry at LOHENGRIN, is required to obtain the isomeric ratio ^{96g}Y/^{96m}Y and thus transform the ^{96}Y sum yield reported here into the individual yield of ^{96g}Y relevant for the antineutrino spectra (for details see [159]). Since ^{96g}Y decays dominantly to the ground state of ^{96}Zr or to the first excited 0^+ state, only few γ-rays accompany this decay and their intensities carry large uncertainties. Thus, a more precise value for the individual ^{96g}Y yield can be obtained by comparing the ^{96m}Y and ^{96}Sr yields which emit both intense gamma rays with well-known intensities, then subtract the so determined ^{96m}Y yield from the total $^{96g+m}$Y yield. For this purpose we provide also the newly measured independent and cumulative ^{96}Sr yield and the $^{96g+m}$Y/^{96}Sr yield ratio, respectively, where some experimental uncertainties cancel.

4.1.7.3. Results and discussion

The fractional and independent isotopic yields for mass $A = 92$ for the three targets under investigation are listed in Table 4.2. The last row of the table presents the cumulative yields of ^{92}Rb. Table 4.3 lists the fractional and independent isotopic yields for mass 96 for thermal neutron induced fission of the two targets ^{235}U and ^{241}Pu. Also presented in this table are the cumulative yields of ^{96}Sr and the $^{96g+m}$Y/^{96}Sr yield ratios. These data are relevant for a precise yield determination of ^{96g}Y in the future by γ-spectroscopy (for details see [159]).

A detailed discussion of the results can be found in [159,224]. In all the measured spectra of mass 92, three isobars were identified as ^{92}Kr, ^{92}Rb and ^{92}Sr, while only upper limits were determined for isobars with other nuclear charges Z, namely < 0.5% for ^{92}Br and < 1% for ^{92}Y. Correspondingly, for mass $A = 96$ four isobars were identified and upper limits were derived for the non-observed isobars < 0.6% for ^{96}Kr and < 1.6% for ^{96}Nb. These limits are accounted for in the calculation of cumulative yields by symmetrizing the upper limits. The cumulative yield of ^{92}Rb for ^{235}U(n_{th}, f) was also determined in the first attempt [223,305] of isotopic yield determination with the CLTDs, with the reported value of 0.0471 ± 0.0037 which is in good agreement with the present result.

The first generation of fractional fission yield measurements at LOHENGRIN had been performed with one or few q and E settings close to the peak of the distributions [276,340,341]. As evident from Fig. 4.18, and as discussed

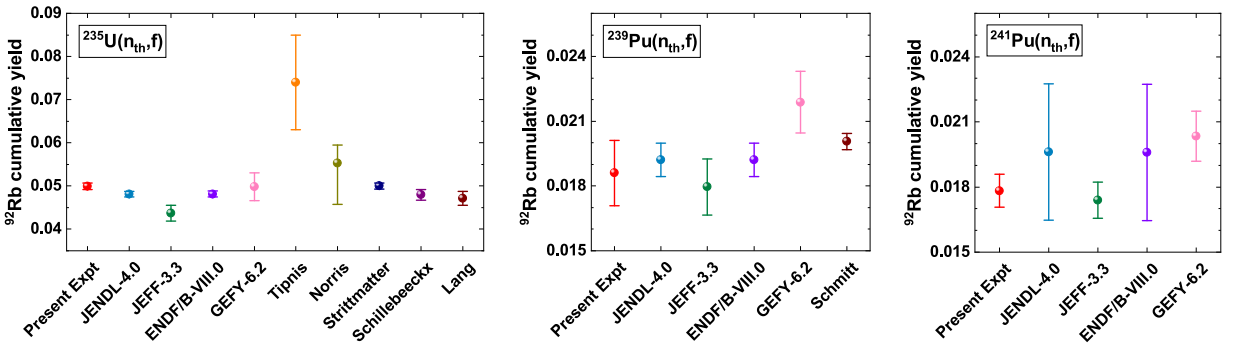

Fig. 4.22. The cumulative yields of ^{92}Rb, as determined for the three fission targets under investigation are presented in red. The present results are compared to literature values from nuclear data libraries and from experimental data [159,224].
Source: Reproduced from [159] with kind permission of the American Physical Society.

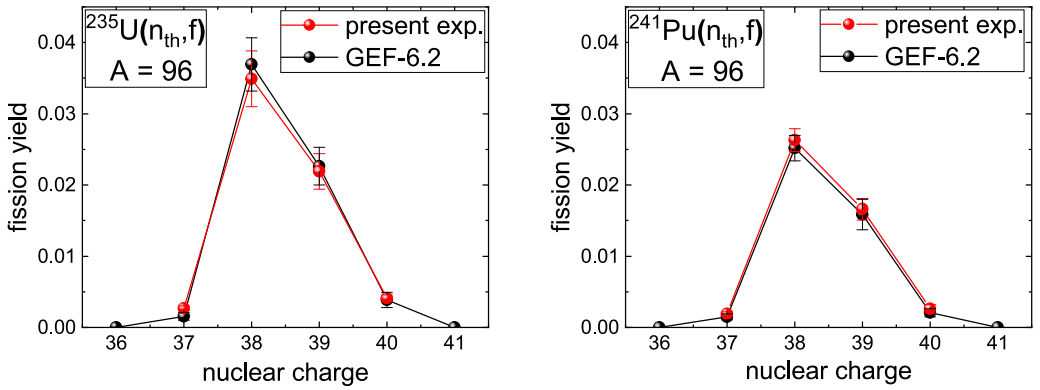

Fig. 4.23. Independent isotopic yield results from the present experiment for mass A = 96 in comparison with the GEF calculation [342].
Source: Reproduced from [159] with kind permission of the American Physical Society.

in detail by H. Wohlfarth et al. [312], for some nuclides with particular ionic charge state distributions (e.g. ^{92}Rb) measurements at the peak of the distribution are not fully representative for the average fractional yield in fission. Later measurements took this observation into account and covered a wider q range [277,292] as also done in the present investigations [159,223,224]. Another difference to previous LOHENGRIN measurements is the target coverage. Experiments that measured the "unperturbed" kinetic energy distributions in the same run prefer minimum energy corrections and would use uncovered targets. However, such targets are also prone to very rapid and less regular burn-up and their ionic charge state distributions may evolve significantly during burn-up [292]. In contrast to prior single-detector measurements, the use of a detector array with 24 independent pixels in the present experiment allowed to cross-check and validate the individual spectra, and to eliminate artifacts from neighboring A/q ratios that may spill in at the edge of the mass-defining slit (for details see [224]).

In Fig. 4.22, the cumulative yields for ^{92}Rb, determined in the present work, are compared with values reported in nuclear data libraries JENDL-4.0 [256], JEFF-3.3 [254], ENDF/B-VIII.0 [255], and the GEF Code GEFY-6.2 [246,342] and the experimental values from [272,277,292,334,343,344]. E. Norris et al. [343] and P. Schillebeeckx et al. [272] determined fractional independent yields. For the purpose of plotting we summed these values and multiplied them with the mass yield from F. L. Lisman et al. [339]. For the most important fissioning system ^{235}U(n_{th}, f) the newly measured value is in good agreement with nuclear data libraries and the GEF Code, and most previous measurements performed with different techniques and instruments. However, a clear disagreement is observed for the ^{92}Rb cumulative yield published by S. V. Tipnis et al. [334] who reported a 50% higher cumulative yield as compared to the yield determined in the present work. We conclude that the value of S. V. Tipnis et al. has to be considered as clear outlier. Computing the reactor antineutrino anomaly based on the yields reported by S. V. Tipnis et al. for ^{92}Rb, the high energy part of the antineutrino spectra would further increase the anomaly by 8%. With the new independent measurement resulting in high accuracy yields in the present work, we could confirm that the yields reported in the nuclear data libraries are indeed more reliable, and therefore could reduce the nuclear physics uncertainties in the investigation of the antineutrino anomaly and numerous other applications. We may conclude that, independently of the measurement of S. V. Tipnis et al. [334], which may have suffered from additional problems (for a detailed discussion of this topic see [159]), γ-ray spectrometric

Table 4.4
List of measurements for ^{241}Pu(n_{th}, f) at different LOHENGRIN energies E_L and ionic charge states q.

A	E_L (MeV)	q	A	E_L (MeV)	q
89	94, 100	20	101	94, 100	22
90	94, 100, 106	20, 24	102	94, 100	23
91	94, 100	20	103	86, 94, 100	19, 22, 23
92	86, 94, 100, 106	21, 25	104	86, 94, 100	19, 23
93	94, 100	21	105	86, 94, 100	20, 23, 24
94	94, 100	21	106	86, 94, 100	20, 23, 24
95	94, 100	21	107	86, 94, 100	20, 23, 24
96	86, 94, 100	18, 21	108	86, 94, 100	20, 24, 25
97	94, 100	22	109	86, 94, 100	20, 24, 25
98	94, 100	22	110	86, 94, 100	20, 24, 25
99	94, 100	22	111	86, 94, 100	20, 24
100	94, 100	20, 22	112	86, 94, 100	21, 24, 25

Table 4.5
List of measurements for ^{239}Pu(n_{th}, f) at different LOHENGRIN energies E_L and ionic charge states q.

A	E_L (MeV)	q
109	80, 84, 90, 94, 98	20, 24
110	80, 84, 90, 94, 98	20, 24
111	84, 90, 94	20, 24
112	80, 90	20
113	86	21

yield determinations may have intrinsic shortcomings in particular for those fission products which are most relevant for the high energy part of reactor antineutrino spectra. Yields determined by direct ion counting are clearly preferred for these cases.

It is also noteworthy that for the fissioning systems ^{239}Pu(n_{th}, f) and ^{241}Pu(n_{th}, f), the present cumulative fission yields for ^{92}Sr, and ^{92}Y, respectively, match well those determined by J. K. Dickens et al. [270,345] by γ-spectrometry, i.e. with a method not relying on normalization with mass yields. Moreover, the independent fission yields given by the GEF code GEFY-6.2 [342] match also remarkably well with those measured for $A = 96$, see Fig. 4.23.

4.1.8. Investigations in the mass region near symmetric fission: fission yields for thermal neutron induced fission of ^{239,241}Pu *for the masses* $89 \leq A \leq 113$

4.1.8.1. Motivation

^{239}Pu(n_{th}, f) and, at higher burn-up, also ^{241}Pu(n_{th}, f), play an important role in nuclear reactor fuel. Thus these nuclei are in the scope of the JEFF evaluation program of fission yields [254]. This work is based on experimental data and fission models, including the nuclear charge repartition models. Today, the Z_p model of A. C. Wahl [237] is commonly used in the evaluation, but the weakness is the important dependency on fractional independent yield data. Uncertainties of the resulting fission product inventory are most pronounced outside the fission peaks, i.e. in the symmetric and far asymmetric fission regions [273]. Complementary experimental data including isotopic yields could reduce these ambiguities.

We note that low-energy fission of the compound nucleus ^{240}Pu is considered a benchmark reaction in many theoretical fission studies, see the review by N. Schunck and L. M. Robledo [247] and references therein. In theory the interplay between symmetric and asymmetric fission has been studied by inspecting the shape of the **P**otential **E**nergy **S**urface (PES) near the saddle point. Microscopic calculations have been performed, e.g. by J. F. Berger et al. [346], H. Goutte et al. [243], P. Möller et al. [242] or J.-F. Lemaitre et al. [347]. The transition region from asymmetric to symmetric fission is of particular interest since there three main fission modes are contributing, according to U. Brosa et al. [241]: a *symmetric mode* (SL) and two *asymmetric modes* (StI and StII). The SL mode is understood in the classic **L**iquid **D**rop **M**odel (LDM) while for the modes StI and StII shell stabilizing effects in the fragments have to be invoked. Precise experimental data on isotopic yields can provide insight into the interplay between modes coming into view in the nuclear charge polarization ΔZ (see Section 4.1.8.3), i.e. a shift of the actual fragment charges away from the Z/A ratio equal to that of the fissioning system, and in the odd–even effect of nuclear charge yields.

It is therefore of great physics interest to push measurements towards the symmetric mass region, e.g. in order to study significant nuclear charge polarizations not predicted by the LDM, or odd–even effects in the nuclear charge yields. It is evident from cross section data and, perhaps even more directly, from mass distributions as a function of the excitation energy of the fissioning compound that asymmetric and symmetric fission are two distinct fission modes. In the review "The Nuclear Fission Process", edited by C. Wagemans [238], there are numerous examples of mass distributions for neutron induced fission of actinides as a function of the neutron energy, demonstrating the distinct energy dependencies of asymmetric and symmetric fission. It is so far conjectured from structures in the mass yield curves that, in contrast to asymmetric fission, only a small odd–even effect in the charge yields should be present in symmetric

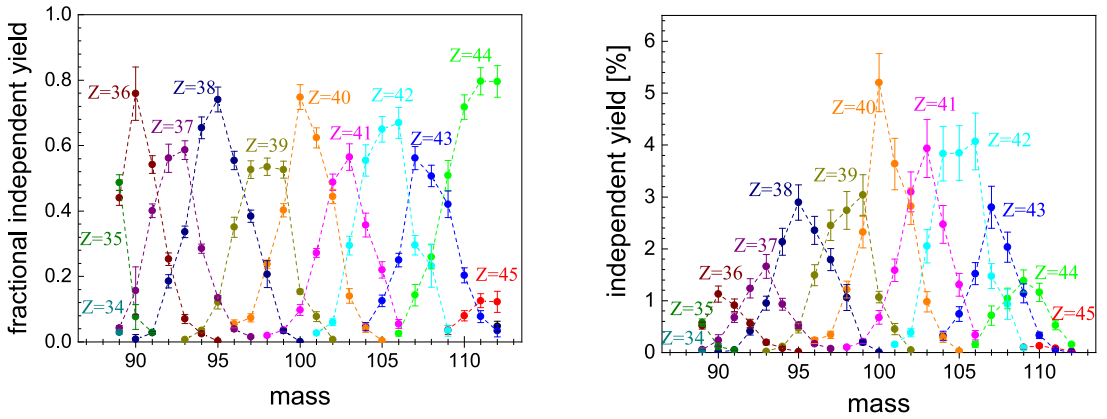

Fig. 4.24. Fractional independent yields (left) and independent yields (right), averaged over kinetic energies and ionic charge states, are plotted for atomic masses $A = 89$ to 112 for ^{241}Pu(n_{th}, f). The data points are connected with lines to guide the eyes.
Source: Reproduced from [160] with kind permission of the American Physical Society.

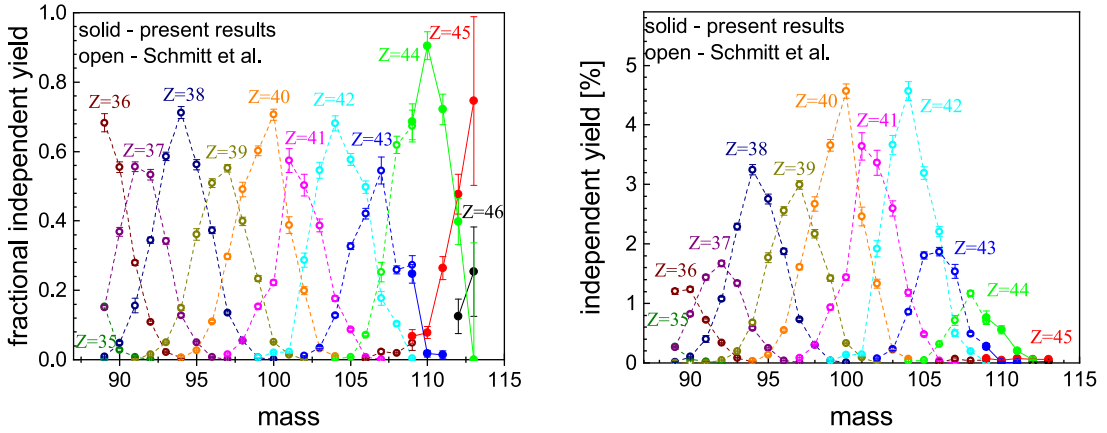

Fig. 4.25. Fractional independent yields (left) and independent yields (right), averaged over kinetic energies and ionic charge states, are plotted for atomic masses $A = 89$ to 113 for ^{239}Pu(n_{th}, f). The solid dots for $A = 109$ to 113 correspond to the present results and the open dots to data from C. Schmitt et al. [277] for comparison. The data points are connected with lines to guide the eyes.
Source: Reproduced from [160] with kind permission of the American Physical Society.

fission. However, on the way from asymmetry to symmetry, LOHENGRIN experiments point to the onset of a sizeable odd–even effect [276,277,292] right at the turnover from asymmetry to symmetry. Extending the nuclear charge yield measurements in the light fragment group by a few more masses towards symmetry would hence allow a noteworthy progress in confirming (or rejecting) the onset of a pronounced odd–even effect.

4.1.8.2. Measurements and data analysis

For the isotopic yield determination, a series of measurements were performed for 24 masses in the range $A = 89$ to $A = 112$ for ^{241}Pu(n_{th}, f) for the first time with the LOHENGRIN mass separator. Moving from asymmetric to symmetric fission, known data were supplemented for masses from $A = 110$ to $A = 112$ for ^{241}Pu(n_{th}, f), and from $A = 109$ to $A = 113$ for ^{239}Pu(n_{th}, f). All measurements were performed with a 4 μm thick SiN degrader foil stack as passive energy absorber on the disk installed inside the cryostat (see Figs. 4.3 and 4.4). The lists of measurements performed at different LOHENGRIN energies E_L and ionic charge states q for ^{241}Pu(n_{th}, f) and ^{239}Pu(n_{th}, f) are displayed in the Tables 4.4 and 4.5. The complete set of data is published in [160,224,337,338].

The fissile targets used are described in Section 4.1.3.2. The procedure of the $Z-$identification is demonstrated in Section 4.1.6 (see Fig. 4.17). The procedure of the data analysis and the application of the necessary corrections are described in Section 4.1.6 (for further details see [160,224]). Finally fractional independent yields were determined using Eq. (4.9). Independent yields are determined by multiplying the fractional independent yields with the mass yields determined with the PIN-diode, and normalized to the mass yields from P. Schillebeeckx et al. [272] for ^{241}Pu(n_{th}, f), and to the mass yields from C. Schmitt et al. [277] for ^{239}Pu(n_{th}, f), respectively. We note that high accuracy mass yield measurements have been performed recently for ^{241}Pu(n_{th}, f) at the LOHENGRIN mass separator [348,349]. Combined with

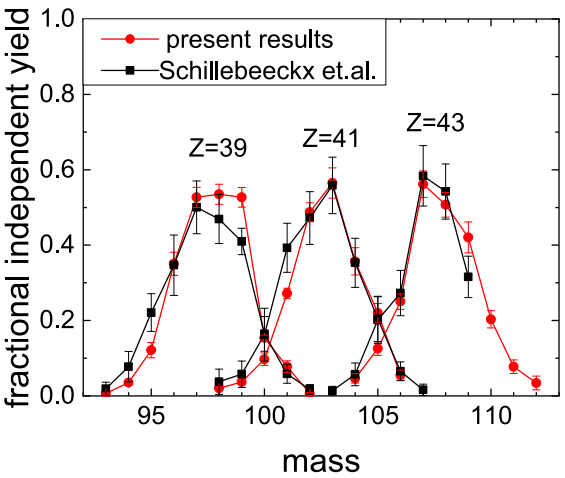

Fig. 4.26. Fractional independent yields for $Z = 39, 41$ and 43 for ^{241}Pu(n_{th}, f) from the present work (red data points) in comparison with data from P. Schillebeeckx et al. [272] (black data points). The data points are connected with lines to guide the eyes.
Source: Reproduced from [160] with kind permission of the American Physical Society.

the present nuclear charge distributions, this will lead to a new and independent set of isotopic yields for ^{241}Pu(n_{th}, f) measured with the same instrument.

4.1.8.3. Results and discussion

The results for the isotopic yields $Y(A, Z)$ determined for the two reactions ^{241}Pu(n_{th}, f) and ^{239}Pu(n_{th}, f) investigated in the present work are displayed in Figs. 4.24 and 4.25. Data in numerical form are published in [160]. The errors reported for the isotopic yields are the total uncertainties with contributions from statistical and systematic uncertainties as discussed in [159,160,224]. The systematic uncertainties are dominating for all but the heaviest measured masses ($A = 112$ for ^{241}Pu, and $A = 113$ for ^{239}Pu). We note that some of these systematic uncertainties, namely a possible bias due to the chosen ionic charge or kinetic energy settings on the fractional independent yields [159], could be reduced by additional measurements at more q and E settings. The values of the independent yields moreover include the normalization uncertainty of the available mass yields [272,277]. For ^{241}Pu(n_{th}, f), new mass yields with higher accuracy will become available in future [348,349].

The statistical error including the fit error was determined using the OriginLab software for each residual-energy spectrum measured with the CLTDs. Additionally, an error of less than 0.6% was estimated due to the thermal neutron flux instability [244]. The systematic uncertainty due to the approximation used for fractional independent yield calculations (see Eq. (4.9)) leads to an error of less than 1.3% (see also [224,244]). Additional errors propagate from the errors in mass yields used to determine the independent yields from the fractional independent yields.

Results for the fractional independent and independent yields obtained from the present experiment for thermal neutron induced fission of ^{241}Pu are plotted in Fig. 4.24 versus the atomic mass. The data points in the same color correspond to a particular nuclear charge as marked on the plot with the same color. The lines passing through the data points in Fig. 4.24 guide the eye for individual nuclear charges. Similarly, the yields obtained in the present experiment are plotted for thermal neutron induced fission of ^{239}Pu with solid data points in Fig. 4.25. The isotopic yields measured in the present experiment are compared to previously published data and are found to be consistent with the available data in the literature from P. Schillebeeckx et al. [272] for ^{241}Pu, measured with the Cosi-Fan Tutte spectrometer for the three nuclear charges $Z = 39, 41$ and 43 (see Fig. 4.26), and from C. Schmitt et al. [277] measured at LOHENGRIN for ^{239}Pu for mass $A = 109$ (plotted with open data points in Fig. 4.25). The agreement of the present results with measurements with completely different experimental setups [272,277] gives confidence in the methodology applied for the present investigations.

In the left part of Figs. 4.24 and 4.25, we observe the odd–even staggering in the fractional independent yields. The even $Z-$peaks are consistently higher compared to the odd $Z-$peaks. The evident reason for this staggering, which enhances even charge splits, is proton pairing in fragments from fission of even-Z compounds (plutonium with an even $Z = 94$ in this case). For thermal neutron induced fission, a dominant odd–even effect is observed, reflecting that the nuclear pairing effect plays a major role.

However, since fission fragment yields vary as function of both, proton and neutron number of the respective fragments, subtle underlying structures may be less evident when regarding only these fractional independent or independent yields or summed mass or elemental yields. Certain derived differential quantities are better suited for this purpose. A key indicator of shell effects not foreseen in the **L**iquid **D**rop **M**odel (LDM) is the so-called charge polarization of fragments usually represented by ΔZ (not to be confused with the quantity ΔZ which is discussed in Section 4.1.5 for

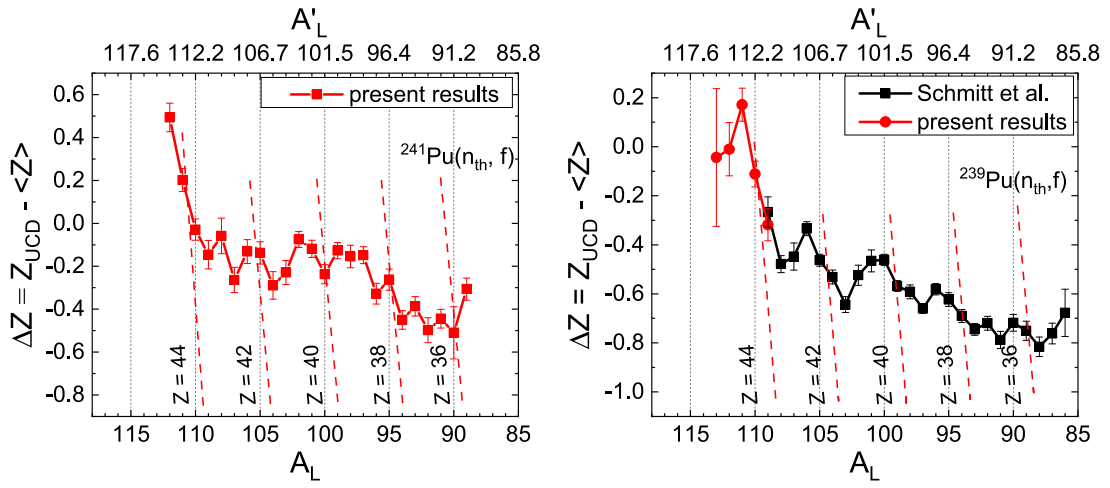

Fig. 4.27. Charge polarization ΔZ as a function of the secondary mass A_L in the light (towards symmetry) fragment group for ^{241}Pu(n_{th}, f) (left-hand side) and for ^{239}Pu(n_{th}, f) (right-hand side). The corresponding approximate primary masses A'_L are given on top of the graph (corresponding masses connected by vertical gray lines), but these carry an inherent uncertainty due to the statistical nature of the neutron evaporation. For ^{239}Pu(n_{th}, f), the present results are combined with results of C. Schmitt et al. [277]. The dashed red lines mark the respective mean Z for corresponding masses. The data points are connected with lines to guide the eyes.
Source: Reproduced from [160] with kind permission of the American Physical Society.

the definition of the Z-resolution). The charge polarization ΔZ measures the deviation of the mean nuclear charge $\langle Z\rangle$ for a fixed primary mass A'_L from an **U**nchanged **C**harge **D**ensity (UCD). It is given by

$$\Delta Z = Z_{\mathrm{UCD}} - \langle Z\rangle \quad \text{with}\, Z_{\mathrm{UCD}} = \left(\frac{A'_L}{A_F}\right) Z_F \tag{4.11}$$

Here, Z_{UCD} is the unchanged charge distribution identical to the A_F/Z_F ratio of the fissioning nucleus, and $\langle Z\rangle$ is the average value of the measured nuclear charge distribution integrated over the kinetic energy distribution. The quantity A'_L is the primary light fragment mass number before neutron evaporation, defined as $A'_L = A_L + \nu(A'_L)$ with A_L being the mass number after neutron evaporation as measured in the present experiment, and $\nu(A'_L)$ being the average number of neutrons emitted from the primary fission fragment. The masses A'_L for ^{239}Pu(n_{th}, f) were determined using the most recent and accurate mass-dependent neutron emission data ("neutron sawtooth") from A. Göök et al. [350]. As approximation, the same data were also adopted for ^{241}Pu(n_{th}, f) since no experimental neutron sawtooth data are available for this system.

The charge polarization ΔZ for the two reactions ^{241}Pu(n_{th}, f) and ^{239}Pu(n_{th}, f) is shown in Fig. 4.27 as a function of the masses after and before neutron evaporation, A_L, and A'_L, respectively. We note that the bottom scale A_L represents the accurate masses, measured with "perfect" mass resolution due to negligible cross-talk of neighboring masses in the LOHENGRIN mass separator. However, the approximate pre-neutron mass scale A'_L on top has a larger uncertainty which is dominated by the uncertainties of the experimental neutron sawtooth data.

The evaluation of ΔZ for ^{241}Pu(n_{th}, f) and ^{239}Pu(n_{th}, f) is based on the measured isotopic yield distributions shown in Fig. 4.24 for ^{241}Pu(n_{th}, f) and in Fig. 4.25 for ^{239}Pu(n_{th}, f). The modulations of ΔZ in Fig. 4.27 follow the same trend of systematically larger yields for even charges Z as compared to odd charges. However, catching the eye in Fig. 4.27, for both plutonium isotopes ^{241}Pu and ^{239}Pu are the steep surges of ΔZ, observed for the light fragment charge $Z_L = 44$. This broad impact at charge $Z_L = 44$ in the light fragment group appears to mirror the importance of the complementary charge number $Z_H = 50$ in the heavy group for Pu with the charge of the fissioning compound $Z_F = 94$. It is recalled that nuclides close to the doubly magic ^{132}Sn play a key role in asymmetric fission. This most striking effect is not foreseen in the LDM, but it is readily understood.

For complementary fragments, light L and heavy H, the following relations hold for the yields of primary masses A' and charges Z in binary fission of a compound nucleus F:

$$A_F = A'_L + A'_H = \text{const}, \quad \text{and} \quad Z_F = Z_L + Z_H = \text{const} \tag{4.12}$$

In a binary fission process, the yields for the two fragments L and H are strictly equal:

$$Y(A'_L) = Y(A'_H), \quad \text{and} \quad Y(Z_L) = Y(Z_H) \tag{4.13}$$

The enhanced yields of the magic heavy fragments with $Z_H = 50$ (tin) thus impose the same enhanced yields in the light fragment for $Z_L = 44$ (ruthenium).

In the present experiment, for the first time the stabilizing feature of the $Z_H = 50$ shell in the heavy fragment directly shows up like a mirror in the light group for the two Pu-isotopes. The outstanding role of the charge $Z_L = 44$ is seen in

the fractional independent yields in Fig. 4.24 for ^{241}Pu(n_{th}, f) and in Fig. 4.25 for ^{239}Pu(n_{th}, f). For a primary mass near $A'_L = 112$ the contribution of $Z_L = 44$ comes close to 80%.

It should be stressed that there is no stabilizing shell effect known for nuclei with charge number $Z_L = 44$, nor for neutron numbers near $N = 66$. Only in binary fission with a complementary heavy fragment with the magic charge $Z_H = 50$, the conservation of nuclear charge in fission imposes a mirror effect in the yield of the complementary non-magic fragment with $Z_L = 44$. But how the large yield of $Z_L = 44$ can produce such a huge effect in the charge polarization ΔZ in Fig. 4.27 remains a question still to be investigated in more detail.

A further noteworthy phenomenon in low energy fission are charge odd–even effects in the isotopic yields as a function of the fragment mass A. In Fig. 4.24 for ^{241}Pu(n_{th}, f) and in Fig. 4.25 for ^{239}Pu(n_{th}, f) it is a general observation that the yields for even charges are larger than the yields for odd charges. The reason for this staggering with even charges being enhanced is proton pairing in fragments from fission of even-Z compounds. In the case of thermal neutron induced fission, this odd–even effect is very pronounced, bringing to evidence that nuclear pairing effects are important. The odd–even staggering in charge yields is therefore a critical test of theoretical calculations of pair-breaking in fission.

Following the definition of a local neutron odd–even effect by B. L. Tracy et al. [351], W. Lang et al. [292] calculated the local proton odd–even effect δp based on a method of differences, given by

$$\delta p = \frac{1}{8} \cdot (-1)^{Z+1} \left[\left[\ln\Big(Y(Z+3)\Big) - \ln\Big(Y(Z)\Big) \right] - 3 \cdot \left[\ln\Big(Y(Z+2)\Big) - \ln\Big(Y(Z+1)\Big) \right] \right] \tag{4.14}$$

The natural logarithms of independent yields for four charges Z, $Z+1$, $Z+2$ and $Z+3$ are employed. A non-zero $\delta p \neq 0$ is taken as a measure of a local odd–even effect in the charge yields averaged over the four charges considered. The odd–even effect is attributed to the midpoint charge $\bar{Z} = (Z + 1.5)$.

W. Lang et al. [292] applied this prescription to isotopic fission yields of ^{235}U(n_{th}, f), which were measured at LOHENGRIN, and observed a significant rise of the proton odd–even-effect δp at $Z = 42$ (or more precisely at $\bar{Z} = 41.5$). Previously, H. G. Clerc et al. [276] had already speculated that the rise of elemental yields at $Z = 42$ and the drop at $Z = 43$ could be related to the $Z = 50$ shell of the complementary fragment. More measurements, e.g. for fission of plutonium isotopes, were recommended to clarify this point. Provided that the above discussion of the charge polarization is generally valid, one should expect for Pu isotopes large odd–even-effects at $Z = 50$ in the heavy fragment group and at $Z = 44$ in the light group. The present experiment confirms this expectation.

In the studies by C. Schmitt et al. [277] of the ^{239}Pu(n_{th}, f) reaction, besides the charge polarization ΔZ also the odd–even-effect was evaluated. Results for the fission reaction of ^{239}Pu(n_{th}, f), complemented by the present results, are plotted together with the data for ^{241}Pu(n_{th}, f) from the present experiment and, in addition, for ^{235}U(n_{th}, f) from W. Lang et al. [292] in one common figure. The data are shown in Fig. 4.28 as a function of the nuclear charge Z. It is obvious that the behavior of the δp distributions is similar for both uranium and plutonium targets, but shifted by two charges. At mid-charges there is first a minimum of the odd–even effect, and then a maximum at the largest charges that could be analyzed. Remarkably, the maxima of δp are seen at $Z = 42$ for ^{236}U* and at $Z = 44$ for both, ^{240}Pu* and ^{242}Pu*. With the definition according to Eq. (4.14) for the local-effect δp, these charge numbers become $Z = 41.5$, and $Z = 43.5$, respectively. Making use of the standard technique for $Z-$identification C. Schmitt et al. could not, however, check the predictions for the Pu-isotopes due to difficulties in the identification of charges near $Z = 45$. The present experiments have now overcome this technical limitation and allowed to measure isotopic yields up to $Z = 46$. They clearly demonstrate the presence of shell effects in binary fission as previously indicated by yield evaluations of light and heavy fragments performed by A. C. Wahl [237,352]. We note that the proton odd–even effect is not fully understood theoretically [239]. Various models have been proposed [262,353–355], but these explanations predict a local proton odd–even effect that is monotonously dropping towards symmetry. This is in conflict with the present observations.

Comparing Fig. 4.27 for the charge polarization ΔZ and Fig. 4.28 for the local odd–even-effect δp, it is evident that the surges for ΔZ and the spikes in the odd–even effect δp are found at the same charge numbers $Z = 42$ (molybdenum) for ^{235}U(n_{th}, f), and at the charge number $Z = 44$ (ruthenium) for ^{239}Pu(n_{th}, f) and ^{241}Pu(n_{th}, f). These singled-out charge numbers in the light fragment group are both complementary to the magic $Z = 50$ (tin) in the heavy group. It is hence evident that both effects have as a common origin the shell effect in the heavy fragment for $Z = 50$. However, in the light group the complementary charges carry no genuine shell effect, so we see simply a virtual effect mirroring that of the heavy complement.

4.1.9. Investigations in the heavy mass region: fission yields for thermal neutron induced fission of ^{239}Pu *for the masses* $128 \leq A \leq 137$

4.1.9.1. Motivation

As already discussed in Section 4.1.1, the investigation of fission fragments in the heavy mass region (see Fig. 4.1) is of high interest because it allows access to regions of fragment masses where other (direct) methods, like γ-spectroscopy, are not easily or not at all applicable. Moreover, such investigations allow a comparison of charge odd–even staggering and charge polarization in both asymmetric (light and heavy) mass regions, and thus to study mirror effects of these observables. The application of CLTDs has for the first time allowed to perform such measurements in the heavy mass region up to mass 137 for thermal neutron induced fission of ^{239}Pu by the universal passive absorber method.

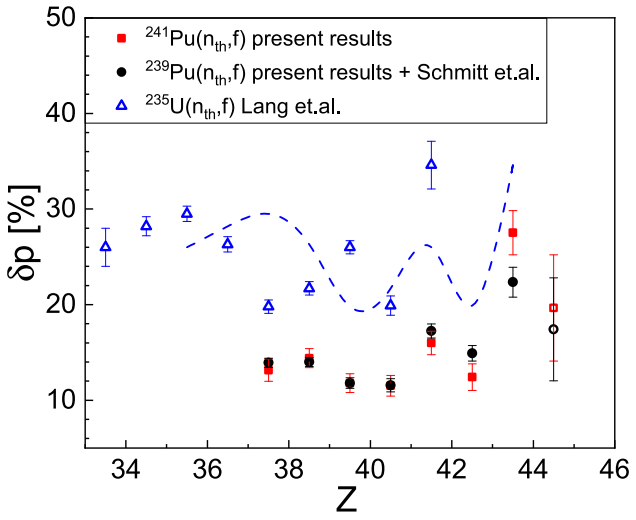

Fig. 4.28. Local proton odd–even effect δp versus the nuclear charge Z for the (n_{th}, f) reactions on ^{235}U (blue triangles), ^{239}Pu (black points) and ^{241}Pu (red squares). Results from the present experiment are displayed together with results from C. Schmitt et al. [277] and from W. Lang et al. [292]. We remind that δp is calculated as a third difference from the elemental yields of four consecutive nuclear charges (Z to $Z+3$). δp is then plotted for the midpoint $Z+1.5$. The last point at $Z=44.5$ is plotted as open symbol to show that it carries an additional, not quantifiable, systematic uncertainty due to the contribution of non-measured masses ($A>112$ for ^{241}Pu and $A>113$ for ^{239}Pu) to the elemental yields of $Z>44$. The dashed blue line corresponds to the ^{235}U data shifted by two nuclear charges towards the right.
Source: Reproduced from [160] with kind permission of the American Physical Society.

4.1.9.2. Measurements and data analysis

For the isotopic yield determination a series of measurements was performed for 10 masses ($128 \leq A \leq 137$) at energies of $E_L = 80$ MeV and $E_L = 88$ MeV. The fast target burn-up for ^{239}Pu(n_{th}, f) allowed measurements at only these energies due to time constraints at this first experimental run in the heavy mass region (for details see [224]). The experimental setup and the fissile target used are described in Section 4.1.3. All measurements were performed with 6 μm thick SiN absorber foils. The procedure of the data analysis is described in Sections 4.1.6 and 4.1.7 (for details see [161,224]).

As already discussed in Section 4.1.6, the data analysis for the present measurements was rather challenging because the residual-energy spectra comprised of overlapping nuclear charge peaks. The technique implemented here to retrieve the Z-yields was to perform constrained fits with iterations (see [161,224]). The problem of identification and separate quantification of overlapping peaks is present in many fields of research and various computational approaches for this deconvolution problem have been reported in the literature [310]. Basically, the quality of the results depends on the knowledge on spectroscopic parameters, such as peak width, separation, the shape of the response function, and, last not least, on the available counting statistics. For all present measurements, over 10 000 counts were obtained in the peaks, and the fits were performed with a sum of three modified Gaussians defined in Eq. (4.7). An example spectrum with fits for mass $A = 130$ is displayed in Fig. 4.16. From the measurements at the MLL tandem accelerator, information on the width 2σ and the tailing parameter t_0 of the modified Gaussians were known for mass $A = 130$ (see Section 4.1.4.2), and were used as a starting point. With this knowledge, the first iteration of the fits was performed with all free parameters of Eq. (4.7). The results are presented in Fig. 4.29 for an energy of $E_L = 80$ MeV. From these first iteration fits the mean width 2σ and the mean tailing parameter t_0 were determined. For the second iteration of the fits, the width and tailing parameters were fixed to the mean value obtained from the first iteration. From the second iteration of fits, the mean Z-separation between the neighboring nuclear charges was determined (see Fig. 4.30), and the final iteration of fits was performed with fixed width, tailing parameter and Z-separation determined from the first two iterations. A similar analysis was performed for the measurements at $E_L = 88$ MeV where a first iteration of fits was performed to determine the mean width and the tailing parameter which were then fixed for the next iteration to determine the relative Z-yields. Due to the higher energy setting at $E_L = 88$ MeV, a better Z-resolution is achieved, and already with two iterations consistent fits with reasonable uncertainties were possible. The numerical results can be obtained from [161,224]. Please note that these results are still preliminary. For the nuclear charge identification, a similar procedure as described in Section 4.1.6 was followed. Measurement series for all masses with the same LOHENGRIN energies at 80 MeV and 88 MeV allowed for a consistent nuclear charge identification. The results on the nuclear charge identification and the relative Z-yields are presented in Fig. 4.31 for two LOHENGRIN energies.

4.1.9.3. Results and discussion

The results for the relative Z-yields, obtained at $E_L = 80$ MeV, determined from the present data in the heavy mass region for the reaction ^{239}Pu(n_{th}, f) are presented in Fig. 4.32, left-hand side, (solid data points) [161,224]. Please note

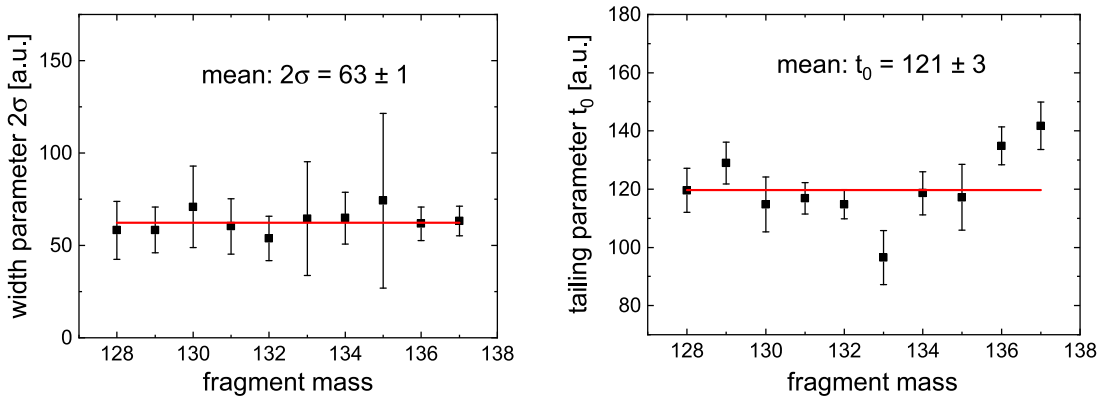

Fig. 4.29. Fit results from the first iteration of fits to determine the width parameter 2σ and the tailing parameter t_0 for heavy masses in the range $A = 128$ to $A = 137$ at $E_L = 80$ MeV for ^{239}Pu(n_{th}, f).

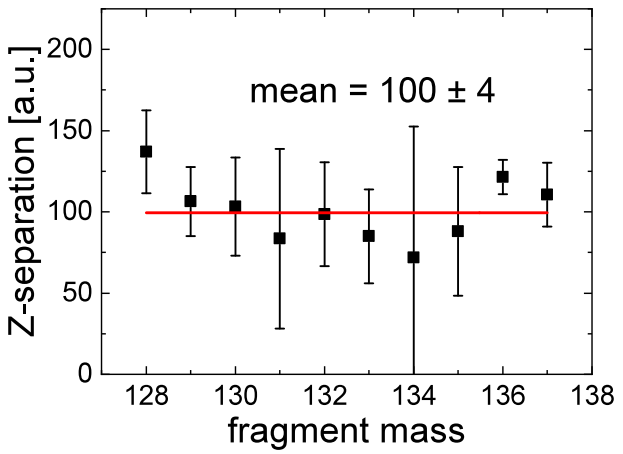

Fig. 4.30. Fit results from the second iteration of fits with fixed width and tailing parameter obtained from the first iteration to determine the Z-separation for heavy masses in the range $A = 128$ to $A = 137$ at $E_L = 80$ MeV for ^{239}Pu(n_{th}, f).

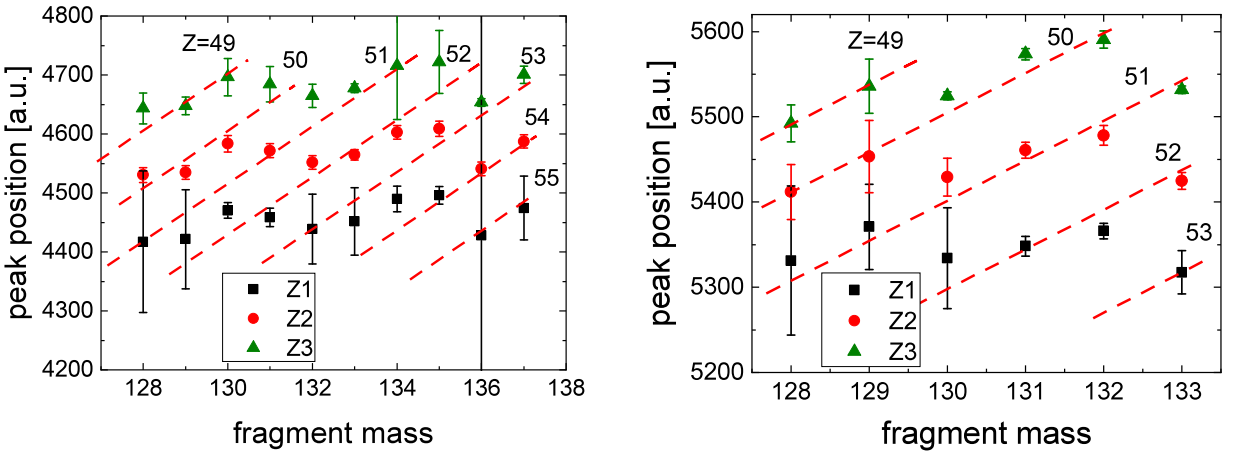

Fig. 4.31. Results on the Z-identification for heavy masses in the range $A = 128$ to $A = 137$ at $E_L = 80$ MeV (left-hand side), and in the range $A = 128$ to $A = 133$ at $E_L = 88$ MeV (right-hand side) for ^{239}Pu(n_{th}, f). The results were obtained from constrained fits with fixed width 2σ and tailing parameter t_0 determined from the iterations shown in Figs. 4.29 and 4.30. Please note that these data are still preliminary [161].

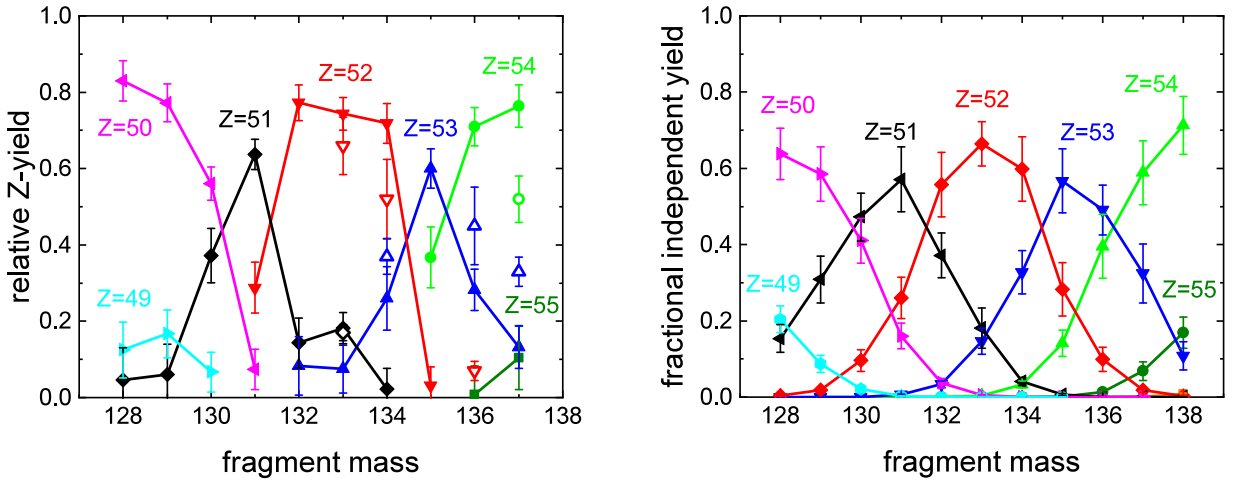

Fig. 4.32. Left: Relative $Z-$yields in the heavy mass region for ^{239}Pu(n_{th}, f), determined from the present measurements with CLTDs and SiN foils (solid data points). Please note that these data are still preliminary. The present results are compared to recent measurements by γ-ray spectrometry [244] (open data points) for masses for which such data are available. Right: Calculated fractional independent Z-yields from the nuclear data library JEFF 3.1.1 for comparison. The data points are connected with lines to guide the eyes [161,224].

that these data are still preliminary. It should be mentioned that the data displayed in Fig. 4.32, left-hand side, are – due to the limited beam time in this first experiment in the heavy mass region – based on measurements at two energies only, and therefore may bear additional uncertainties. Further measurements in the whole energy range may therefore reduce these uncertainties. Nevertheless, the present data can already be compared to data from γ-spectroscopy and from predictions of data tables.

The available data from γ-spectroscopy for some masses [244] are plotted with open circles in Fig. 4.32 (left-hand side). A reasonable agreement within uncertainties is obtained in most cases except for $Z = 54$. It is also obvious from Fig. 4.32 (left-hand side) that, besides the possibility to cross-check already available experimental Z-yields, the present investigations allowed to complete the experimental data set with data for masses $A = 130 - 132$ and $A = 135$, which are either not easily or not at all accessible by γ-spectroscopy.

The present data can also be compared to data predicted from the nuclear data library JEFF 3.1.1 [254] (Fig. 4.32, right-hand side). It turns out that an overall good agreement is obtained which demonstrates the present experimental method to be reliable. A more pronounced odd–even staggering obtained in the present data, as compared to the predictions, may be attributed to the fact, that the present data were evaluated from measurements at two energies only, which lie at the upper end of the kinetic energy distribution where a stronger odd–even staggering is expected [356]. In contrast, the predictions of the data library are integrated values over the whole energy distribution. Also here, further measurements in a complete energy range may solve this open question.

4.1.10. Future perspectives

In several feasibility studies and in the application in first experiments, CLTDs have already been demonstrated to be valuable tools for the determination of Z-yields of thermal neutron induced fission fragments. Besides the investigations in the light mass region, the application of CLTDs was particularly successful towards the symmetry mass region, and also for the first time with the passive absorber method in the heavy mass region, and interesting physics questions concerning the antineutrino anomaly, the behavior of proton odd–even staggering and the charge polarization at the borderline between asymmetric and symmetric fission, and for some cases in the heavy mass region, hardly or not accessible before, could already be addressed.

As only a small portion of a wealth of interesting data could, due to the lack of more beamtime, be already taken, mainly with the aim to demonstrate the feasibility and the potential of the new method, a lot of additional data, in particular in the symmetry region and the heavy mass region, wait to be taken using the new method (passive absorber method in combination with CLTDs and SiN absorber foils). This undertaking may in the future solve a couple of interesting, still open questions concerning the understanding of the fission process and its dynamics and will allow further sensitive tests of fission models. Using prinicpally the present experimental setups, an optimization regarding the acceptance (active length) of the fissioning target may already improve the performance with respect to the Z-resolution.

In order to further improve the performance of the experimental setup for future experiments, the development and construction of a thin CLTD detector, designed as a ΔE transmission detector, would be an important step forward. Having in mind that this task would be technologically rather challenging, its realization would allow to replace the passive SiN absorber foil by the ΔE transmission CLTD as active absorber. Such an *active absorber method* could be favorably used

to – at least partly – compensate the energy loss straggling in the absorber, and therefore considerably improve the Z-resolution, thus allowing a much better performance, especially important for investigations in the heavy mass region. It is needless to say that the development of a CLTD-based $\Delta E - E$ telescope could be also of interest for a number of other applications in nuclear and particle physics.

4.2. Precise determination of electronic stopping powers of heavy ions in matter

4.2.1. Motivation

Precise data on electronic stopping powers, i.e. specific energy loss dE/dx, for heavy ions are of high interest in various fields of basic and applied science [183,357,358], such as atomic, nuclear, solid-state and applied physics. Besides the wish to improve our basic understanding of the interaction mechanisms of heavy ions with matter, prominent examples for applications where precise stopping power data are required are, among others, in-flight separation of radioactive heavy ion beams [298,359], heavy ion tumor therapy [360], heavy-ion driven inertial fusion [361], heavy ion channeling [362,363], and material science, such as the investigation of crystal structures after radiation damage [187]. However, as the number of potential projectile–target combinations is very large, and the energy range for required stopping power data spans over several orders of magnitude, it is impossible to obtain all desired data experimentally, a fact that makes precise theoretical predictions indispensable. Despite the progress in the accuracy of theoretical ab-initio models [364–367] describing the interaction of energetic particles with matter, the most precise predictions are nowadays still obtained using semi-empirical computer codes [213,357,358,368], which rely on best fits on experimental data. To improve the reliability of these calculations as much as possible, stopping power data for different projectile/target combinations at various projectile energies are required. For a detailed overview on the knowledge about the field of slowing down of ions in matter the reader may be referred to several review articles [183,296–298,357,369,370].

As compared to standard experimental techniques, originally used for the determination of electronic stopping powers [183], new techniques, which use combinations of **T**ime-**o**f-**F**light (ToF) and energy detectors – therefore called *ToF-E method* – to collect continuous dE/dx data over a wide range of energies in a single measurement [209,371–373], have been successfully applied since more than one decade in various experiments. A leading part in these developments was taken by a group at the University of Jyväskylä, Finland, which has significantly improved the ToF-E method [209,372], and invented the B-ToF method [373]. While these methods proved to be very successful, they both rely primarily on the time-of-flight for the determination of the energy. Although ToF-based energy measurements are a well established method, a verification of the energy by an independent, high-precision method is desirable, in particular for low ion velocities. However, for high ion masses and low ion energies, this is a challenging task, as the commonly used ionization based energy detectors suffer from systematic uncertainties in a proper energy calibration due to incomplete energy detection, resulting in pulse height defects [207–210] and a relatively poor energy resolution. In particular, pulse height defects which are $Z-$ and energy-dependent make an absolute energy calibration based on $\alpha-$sources unreliable [209], and the limited energy resolution makes the determination of the very small energy differences, required for very thin material samples, hard or even impossible.

At this point, considerable improvements can be achieved by using CLTDs which provide an energy measurement without any pulse height defect and a substantially better energy resolution for low energy heavy ions (see Section 3.6), as compared to conventional ionization detectors. Therefore, the application of CLTDs in a ToF-E measurement offers an opportunity to minimize systematic uncertainties, and to improve the accuracy of the energy loss determination, in particular in the low energy and heavy mass regime, where stopping power data are nowadays still scarce, and discrepancies between predicted and measured values are often observed [208,209,371,374].

It should be finally mentioned that calorimetric low temperature detectors were already used in the last century for stopping power measurements, but with a, as compared to the present investigations, different detection scheme, namely the calorimetric-compensation method [375,376]. Albeit both detection concepts are based on an energy measurement by the determination of heat, H. H. Andersen et al. have been measuring the heating power dissipation of a particle flux within an absorber and a detector, while the CLTDs presented here are used for a precise energy determination of single particles.

4.2.2. The ToF-CLTD spectrometer — a new experimental technique for stopping power measurements

The experimental setups used for the present investigations of electronic stopping powers for heavy ions are based on the ToF-E method [209,371–373]. This method was modified by the application of a CLTD instead of a conventional ionization-based semiconductor detector, and is therefore called *ToF-CLTD* method in the following. The use of a CLTD provides a better energy determination due to its energy linearity, and a better sensitivity for small energy losses due to the better energy resolution.

Within the present research project, two experimental campaigns were undertaken, one at the GSI Darmstadt, Germany [155,184], and the other at the University of Jyväskylä, Finland [162,184,377]. The experimental setups used, which are quite similar in principle, are displayed schematically in Fig. 4.33. In the first section of these setups (left-hand side), a mono-energetic heavy ion beam provided by an accelerator is used to produce a broad projectile energy distribution. The second section (right-hand side) allows for a transmission-type energy loss measurement, where a ToF spectrometer in front of an absorber and an energy detector behind the absorber are used for a simultaneous

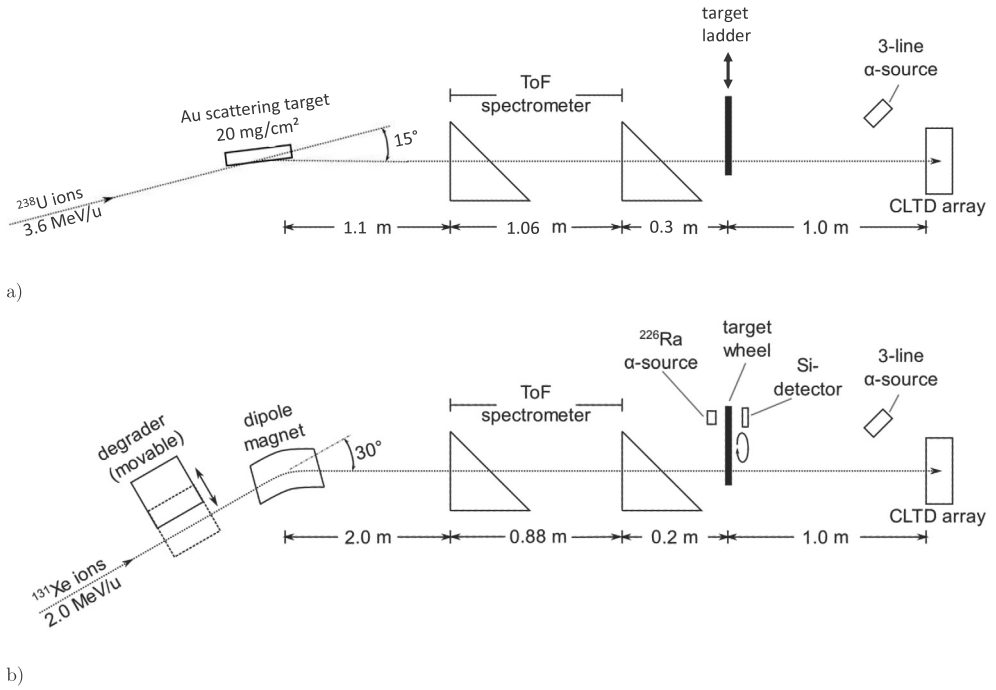

Fig. 4.33. Experimental setups for stopping power measurements for the two experimental campaigns presented in the present article: The incident ions (^{238}U or ^{131}Xe) hit a thick scatterer (a) or a degrader (b), which produce ions with a broad energy spectrum. A time-of-flight spectrometer is used to determine the energy for each single incident ion. After passing the energy loss target(s), the residual-energy of each single ion is determined with the CLTD. A direct correlation between time-of-flight and CLTD measurement provides the incident energy and the energy loss for each single event, thus allowing for the investigation of stopping powers in a broad range of incident energies in one experimental run (for details see text). *Source:* Figure adapted from [162,184].

determination of the initial and the final energy of the projectiles with respect to the absorber. The absorber foils (targets) to be investigated are mounted on a movable target ladder or a rotary wheel, which is installed between the ToF spectrometer and the CLTDs, and allows to mount several different absorber targets. One position is kept empty for measurements without an absorber. This empty slot enables a cross-check of the energy determination of the heavy ions by the ToF spectrometer and the CLTDs.

The absorber targets used for the energy loss measurements are thin self-supporting foils, each mounted on an aluminum frame with an oval aperture of $12 \times 9\,\mathrm{mm}^2$. They have been produced at the target laboratory of the GSI. To obtain a relative energy loss within the absorbers of about 10%–50% with respect to the initial energy, thinner foils ($\approx 50-360\,\mu\mathrm{g/cm}^2$) have been selected for lower projectile energies of $0.05-0.5$ MeV/u. For carbon and nickel absorbers also thicker foils ($\approx 600\,\mu\mathrm{g/cm}^2$) for measurements in a higher energy range of $0.3-1$ MeV/u have been used (for details see [162,184]). For the Jyväskylä measurements, a ^{226}Ra $\alpha-$source and a PIN diode with a size of $2 \times 2\,\mathrm{cm}^2$ have been placed parallel to the beam axis at the opposite side of the target wheel for an online inspection of the absorber foils and for the thickness determination of the absorbers by determination of the energy loss of α–particles.

The ToF spectrometer used for the determination of the ion energies prior to the absorber foils consists in both experimental setups of two identical **M**icro**C**hannel **P**late (MCP) based time pickoff detectors placed in a distance of about $0.9-1$ m. Each time pickoff detector is equipped with a carbon converter foil ($4\,\mu\mathrm{g/cm}^2$ thick at the GSI-setup, and $10\,\mu\mathrm{g/cm}^2$ thick at the Jyväskylä-setup) with a size of $9 \times 12\,\mathrm{mm}^2$ for the generation of secondary electrons during ion passage, and a 45° electrostatic mirror for deflection of these electrons to an electron detector (two MCPs in chevron configuration). A description of the basic principles of that type of time pickoff detectors may be found for example in [209,378].

The energies of the ions after transmission through an absorber foil are determined by a CLTD array. To operate the low temperature detectors the windowless pumped ^{4}He bath cryostat, which was described in detail in Section 3.4, is used, providing a direct transmission of the ions to the detectors without influencing their energies by entrance windows or foils. For calibration of the CLTDs in the low energy range, as well as for stability monitoring of the detectors and the readout electronics, a 3-line $\alpha-$source (^{239}Pu, ^{241}Am, ^{244}Cm) is mounted within the cryostat. The $\alpha-$source is placed diagonally in front of the detectors, ensuring a free ion passage from the accelerator beam line. For the present investigations, the CLTD detector array consisted of 8 detector pixels with a total active area of $12 \times 6\,\mathrm{mm}^2$ (see Fig. 3.11 in Section 3.2.4). With transition widths of the TES of about 10 mK and a detector heat capacity of about $5-6\,\mathrm{nJ/K}$ at 1.6 K, the present

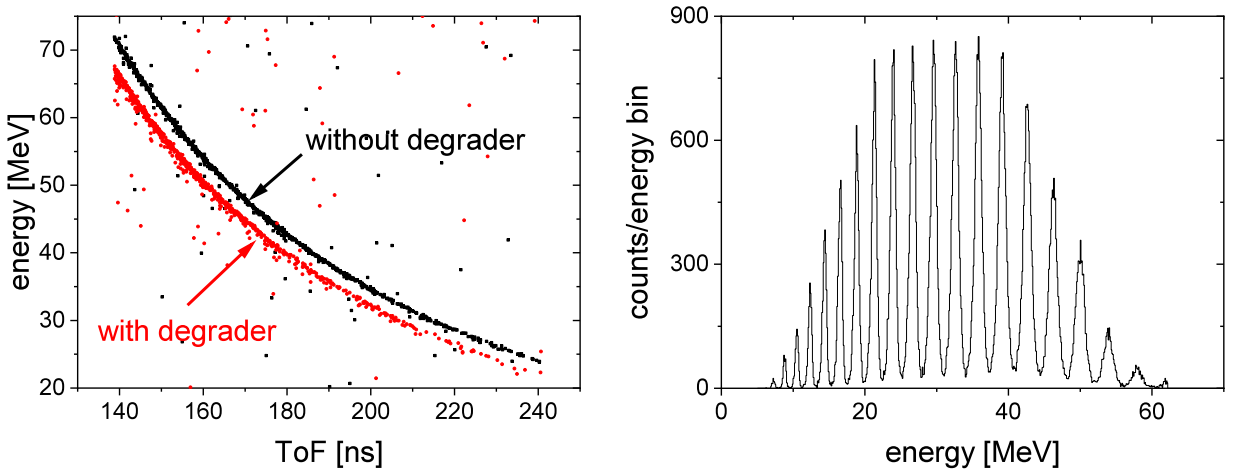

Fig. 4.34. Examples for energy distributions obtained after degrading the incident heavy ion beam: On the left-hand side, the continuous energy distribution which is produced by a thick scattering target is displayed versus the time-of-flight obtained with and without the degrader target. The quadratic dependence of the energy on the time-of-flight leads to a parabola [184]. On the right-hand side, the energy distribution of 2 MeV/u ^{131}Xe ions after passing through a specially designed energy degrader and a dipole magnet is shown. Each peak corresponds to a single ionic charge state, with all peaks having an identical momentum to charge ratio p/q.
Source: Reproduced from [162].

CLTDs were designed and optimized for the detection of projectile energies ranging from a few MeV up to 350 MeV. The decay constants of the thermal signals of about 0.5 ms allowed for count rates for the individual pixels of these detectors up to a few hundred particles per second (for details see Section 3.2.3).

The basic difference between the two experimental setups used (see Fig. 4.33) is the method how the broad energy distribution of the incident beam is produced. For the measurements at GSI, the primary beam is scattered from a 20 mg/cm^2 thick Au foil, mounted under an angle of 7.5° towards the ToF-CLTD setup, thus providing a broad continuous energy distribution of Rutherford-scattered beam particles from lowest energies up to almost the maximum energy defined by the energy of the primary beam. An example is displayed in Fig. 4.34, left-hand side (for details see [162,184]). For the measurements at Jyväskylä, the primary beam passes through a special degrader, designed to produce a broad energy and ionic charge state distribution. Thus a broad bell-shaped energy distribution is created. After passing through a 30 degree dipole magnet, working as a $q-$filter, the originally broad spectrum obtains a characteristic picket fence structure (Fig. 4.34, right side), that can be shifted to the desired measurement range by variation of the magnetic field. For further details concerning the experimental setups, see [184].

For the data acquisition, as well as for online monitoring and online analysis, an FPGA-based data acquisition system has been used. Assignment of coincident ToF and CLTD data have thereby been obtained by means of event timestamps, allowing for a full and independent recording of the ToF and CLTD signals. More details concerning the readout electronics and the data acquisition may be found in [184,379].

The advantage of the present experimental ToF-CLTD method for the determination of stopping powers of heavy ions in matter can be summarized as follows:

- the simultaneous energy measurement before and after the absorber foil allows for the determination of the energy loss on an event by event basis, As compared to investigations with only one energy measurement after the absorber foil, where the energy loss is determined from the measured energy distribution with and without absorber, this method allows to reduce systematic errors and makes the measurement independent of the energy width of the primary heavy ion beam,
- moreover the determination of the energy loss on a event by event basis allows for the investigation of the energy loss for a broad energy distribution in one single measurement which enables the consistent and fast determination of the energy dependence of stopping powers, and thus to reduce individual systematic uncertainties.

Whereas the previous arguments hold already for the previously used ToF-E method, the application of CLTDs for the energy determination in the new ToF-CLTD method provides additional advantages:

- the more complete energy measurement due to the absence of entrance windows and dead layers, and, due to the absence of pulse height defects, allows for a much better energy calibration, independent of the Z and the energy of the ions used, and in particular allows for the energy calibration with $\alpha-$particles without any corrections due to pulse height defects,
- the better energy resolution allows for a higher sensitivity and accuracy of energy loss measurements, which is in particular important for investigations with very thin absorber foils and for low incident energies.

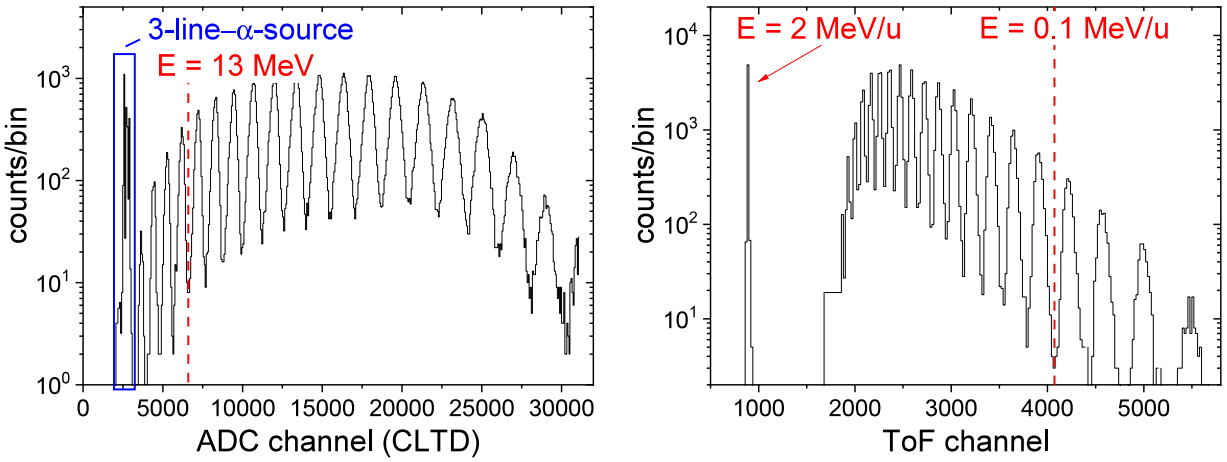

Fig. 4.35. The two panels show pulse height spectra of the CLTD (left-hand side) and of the time-of-flight spectrometer (right-hand side) of ^{131}Xe ions after a degrader was inserted. In the spectrum of the CLTD, the peaks of the 3-line α-source can be seen as well. The peak of the incident ^{131}Xe ions at 2 MeV/u, which is displayed in the time-of-flight spectrum, was recorded in a separate measurement and is not seen in the CLTD spectrum because the total energy exceeds its dynamic range. The vertical dashed lines in both spectra correspond to an absolute projectile energy of 13 MeV, i.e. 0.1 MeV/u for ^{131}Xe ions, marking the energy range in which the $\alpha-$calibration of the CLTDs is considered to be valid.
Source: Reproduced from [162].

4.2.3. Measurement procedure and data analysis

Prior to the measurement of stopping powers, preparatory studies were performed concerning the energy calibration and the determination of the absolute thickness and the homogeneity of the absorber foils. One of the possible sources of systematic uncertainties in previous stopping power measurements was the energy calibration of the detector system. Due to the pulse height defect of the formerly used Si-detectors, the energy calibration was obtained solely from the ToF spectrometer using monoenergetic heavy ion beams provided by the accelerator, and radioactive sources with energies higher than 1 MeV/u [208,209,372]. Hence, for measurements at very low energies in the range of a few 100 keV/u and below, which is the focus of the present experiments, a verification of the linear ToF calibration down to the energy range of interest is desirable to exclude possible systematic errors.

The replacement of the Si-detector by the CLTD array for the current setup enables additional calibration opportunities at very low energies by using $\alpha-$sources. As the pulse height of a CLTD is independent of the projectile mass and Z (see Section 3.6.2.2), an $\alpha-$calibration at absolute energies of a few MeV can be used without additional corrections for an energy measurement of the much heavier ^{131}Xe or ^{238}U ions in the same range of absolute energies, meaning in that particular case several 10 keV/u. Therefore, calibration lines from two independent sources are available below ($\alpha-$source) and above (monoenergetic 3.6 MeV/u ^{238}U beam or 2 MeV/u ^{131}Xe beam from the accelerator) the desired measurement range for ion energies of about $0.05 - 1$ MeV/u, allowing for a reduction of calibration uncertainties, as well as a verification of the linearity of the ToF spectrometer.

In the following, the procedure of the energy calibration is described for the example of the measurements with a 2.0 MeV/u ^{131}Xe beam from the K130 cyclotron of the University of Jyväskylä. The energy calibration for the measurements with the 3.6 MeV/u ^{238}U beam from the UNILAC accelerator at the GSI Darmstadt was performed in a similar way (for details see [184]). Fig. 4.35 shows the pulse height spectra of the CLTD (left-hand side) and of the ToF spectrometer (right-hand side) obtained from a measurement with ^{131}Xe ions. In addition to the picket-fence structured energy distribution of the ^{131}Xe ions, the CLTD spectrum contains also the peaks from the 3-line α-source. Moreover, in addition to the picket-fence structure, the non-degraded peak of the 2 MeV/u ^{131}Xe ions, which has been recorded in a separate measurement without the degrader, has been included in the ToF spectrum.[18] The energy calibration of the detector system was obtained in three steps. In a first step, the CLTDs have been calibrated in the low energy part using the 3-line α-source (^{239}Pu, ^{241}Am, ^{244}Cm, $E = 5 - 6$ MeV). For the validity range of that calibration, twice the energy of the $\alpha-$calibration lines, i.e. $E \approx 13$ MeV, was assumed, as the calibration uncertainties due to small non-linearities of the CLTDs are below 1% within this energy range [184], see also Section 3.6.2.2. This $\alpha-$calibration was used to determine the energies for the Xe ions with $E < 13$ MeV (see Fig. 4.35) and, due to the coincident detection of these ions with the ToF spectrometer, to obtain calibration points in the low energy part of the ToF spectrum (see Fig. 4.35, right-hand side). Here, the energy loss of the ions within the carbon converter foil of the second time pickoff detector was taken into account using SRIM [213,368] calculations. In the second step, these calibration points at energies $E < 13$ MeV and the point

[18] The 2 MeV/u-line does not appear in the CLTD spectrum (Fig. 4.35 left-hand side) because the detector parameters have been optimized for the best performance at lower energies at the cost of a reduced dynamic range, which shifted in that case below the total energy of 262 MeV.

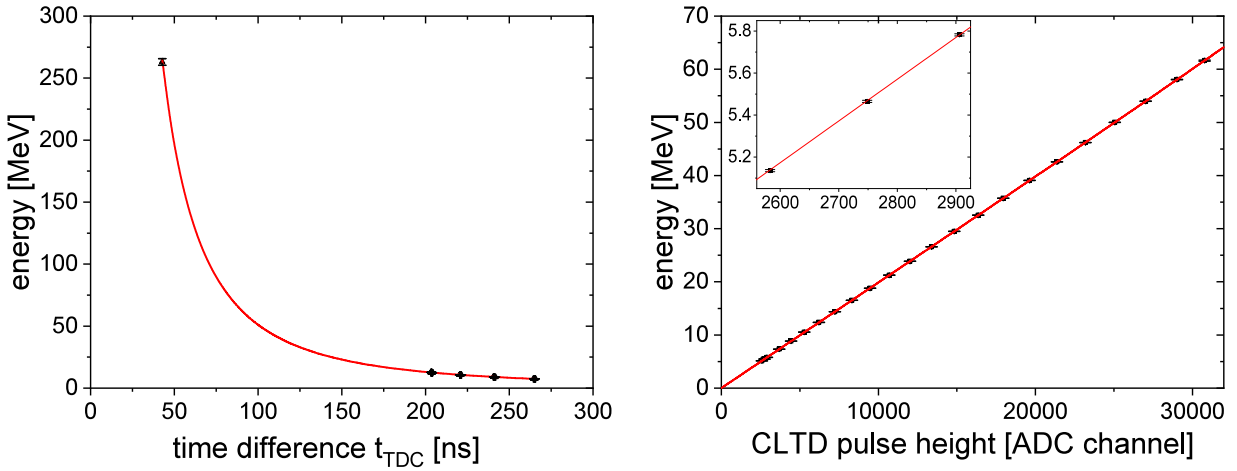

Fig. 4.36. The energy of ^{131}Xe ions as a function of the time difference t_{TDC}, measured with the TDC of the ToF spectrometer, (left-hand side) is described by the function $E \sim 1/(t_0 + t_{TDC})^2$. The error bars are smaller than the displayed data points. The red curve shows a fit to the data which is used as calibration function of the ToF spectrometer. The energies determined by the ToF spectrometer were in turn used to calibrate the CLTD over the full energy range. The resulting calibration plot (values determined with the ToF spectrometer and with the α-particles as a function of the CLTD pulse height), displayed on the right-hand side, is described by a 3rd order polynomial. The fit is again shown as a red curve. The insert shows the region of the α–particles in an expanded scale.
Source: Reproduced from [162].

at $E = 262$ MeV (measurement without degrader) (see Fig. 4.36, right-hand side) have been taken to calibrate the ToF spectrometer (for details see [162,184]). The calibration of the time axis of the TDC, i.e. the relation between measured TDC channel and the time interval between the start and the stop signals t_{TDC}, has been obtained using an Ortec Time Calibrator 462. The relation between t_{TDC} and the energy is displayed in Fig. 4.36 (left-hand side). As the final step, the energy calibration of the CLTDs in the complete measurement range was obtained from the ^{131}Xe−peaks in Fig. 4.35 with the energies determined from the ToF spectrometer (measurement with degrader but without target). As before, the energy loss within the carbon foil of the second time pickoff detector was taken into account using SRIM calculations. In addition, also the 3 peaks from the α−source have been taken as supplementary calibration lines in the low energy regime. To account for small non-linearities of the CLTD pulse height as a function of the projectile energy, a 3rd order polynomial has been used to fit the calibration points presented in Fig. 4.36 (right side). However, the deviations of this fitting function from a linear calibration, using only the 3 α−lines at energies of $5 - 6$ MeV, are less than 1.5% up to projectile energies of 130 MeV, showing the extraordinary linearity of the CLTDs as compared to ionization based energy detectors [208]. The overall systematic error in the absolute energy determination is quoted to be about 1% (for details see [162,184]).

Concerning the performance of the ToF and CLTD detectors with respect to time- and energy-resolution we report the following results which were obtained under experimental conditions at accelerator facilities. For the relative energy resolution, values around $\Delta E/E = 3 - 4 \times 10^{-3}$ were obtained for the measurements with a ^{238}U beam at the GSI Darmstadt, and values around $\Delta E/E = 6 - 7 \times 10^{-3}$ were reported for the measurements with the ^{131}Xe beam at Jyväskylä [184]. For the time-resolution, values around 150–250 ps were obtained [184]. It should be pointed out that, as there was no need to optimize the detector resolution for the present energy loss experiments, these results are partly limited by noise contributions, and therefore can be considered only as upper limits of the intrinsic detector resolutions.

As an ingredient for precise stopping power measurements, an accurate determination of the mean areal density, i.e. the thickness, and homogeneity of the absorber foils, is mandatory. For the present measurements, two different independent methods have been applied (for details see [162,184]). A standard method which is supposed to be, at least for thicker target foils, the least critical and most precise method is a direct determination of the areal density by weighing the foil and determining the size of its surface area. For that purpose, upon completion of the experiment, the irradiated parts of the targets have been cut off their frames and weighted using a precision balance (with an accuracy of $\pm 10\,\mu$g), while the corresponding surface areas have been determined from a digital image. For the case of measurements performed under the same experimental conditions with thicker and thinner target foils, the thickness ratio of the thinner foils with respect to the thick foils of the same material can be determined by matching the measured heavy ion stopping power curves within an overlap region of identical projectile energies, thus improving the accuracy on the thickness of the thinner foils.

To obtain a cross-check of the results, the target thicknesses have additionally been determined by measuring the energy loss of α–particles and comparing it to SRIM calculations. Whereas for the measurements performed at GSI a 3-line α-source was used, the measurements at Jyväskylä have been performed with a ^{226}Ra source, which provides 5

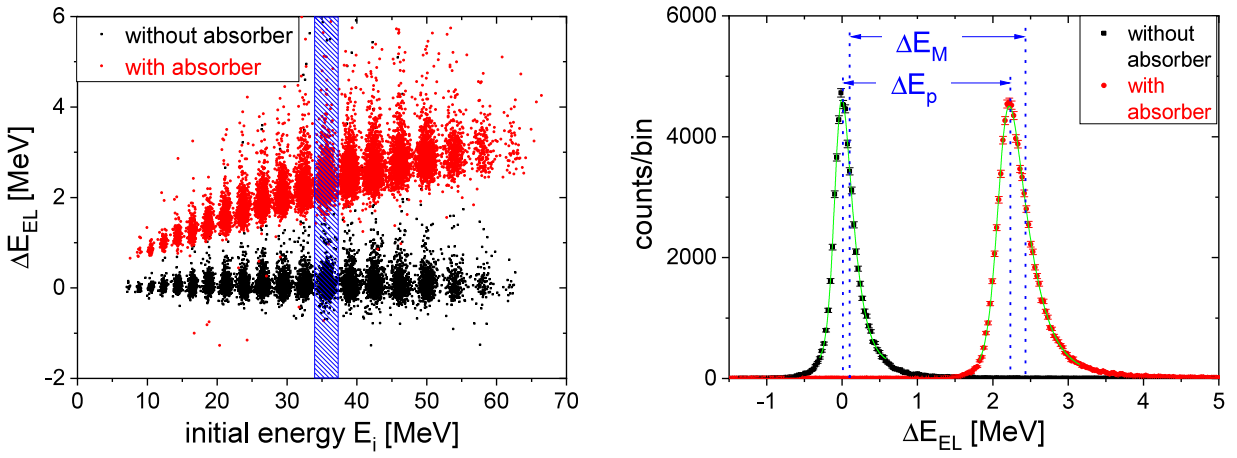

Fig. 4.37. Left-hand side: The measured energy difference $\Delta E_{EL} = E_i - E_f$ is displayed as a function of E_i for ^{131}Xe ions from measurements without and with a 53 µg/cm^2 thick carbon target. Right-hand side: the corresponding histogram for the energy range shaded in the panel on the left-hand side is displayed. The curves show fits to the data (for details see [162,184]). The mean energy loss ΔE_M and the most probable energy loss ΔE_p (peak energy loss) are determined from the difference between the corresponding mean or peak values in the distributions of the measurements with and without target.
Source: Reproduced from [162].

$\alpha-$lines at energies between 4.7 and 7.6 MeV, as well as with 440 keV and 1400 keV ^{4}He ions delivered by the pelletron accelerator at the University of Jyväskylä. The energies of the $\alpha-$particles have thereby been determined with a PIN diode.

Besides the determination of the mean thickness also the homogeneity of the targets is of importance. Inhomogeneities in the thickness distribution of the foils may lead to deviations between the measured mean thickness, and the actual mean thickness in these parts of the targets, which have been irradiated with the heavy ion beam during the transmission measurements. Fortunately, the granularity of the presently used CLTD energy detector with several independent single pixels provides the opportunity to investigate the targets concerning potential inhomogeneities. The idea behind this is, that ions, which have been detected with different CLTD pixels, in the average have passed through different parts of the target, which in first approximation correspond to a projection of the pixel geometry on the target foil. Comparing the ratio of the energy loss determined with different CLTD pixels gives therefore an information on the ratio of the mean thicknesses in the corresponding irradiated parts of the target, and hence an information about the target homogeneity on larger scales. The results of this analysis [184] have shown that the variations in the thickness distribution of the targets are less than 2% for all target foils used. For the thick targets the variations are even below 1%, which may be a result of a better relative homogeneity, but may also be attributed to a decreasing sensitivity of this method due to the increased scattering processes within the target. The obtained values give a direct information on the maximum systematic error in the mean target thickness, that results from foil inhomogeneities. The results of all thickness and homogeneity measurements including an error evaluation are summarized in [162,184].

The absolute energy loss $\Delta E_{EL} = E_i - E_f$ within the absorber targets has been measured on an event-by-event basis, meaning that the initial energy E_i and the final energy E_f have been determined for every single ion by the ToF spectrometer, and the CLTDs, respectively. Considering the energy loss ΔE_{MCP} within the thin carbon converter foil of the rear time pickoff detector, the initial energy is given by $E_i = E_{ToF} - \Delta E_{MCP}$ with the energy E_{ToF} measured by the ToF spectrometer. Thereby, the values for ΔE_{MCP} have been calculated using SRIM. Fig. 4.37 shows, for the example of the measurement at Jyväskylä, the measured energy loss of ^{131}Xe ions in a thin carbon target as a function of the initial energy, as well as the corresponding data from the measurements without target. In principle it is possible to obtain the desired energy loss curves as a function of the energy from a parameterization of the data points in Fig. 4.37, e.g. with a higher order polynomial, as it has been done for example in [371]. However, in the analysis presented here, the final values used for the stopping power determination have been obtained from ΔE-histograms, created in discrete intervals of the initial energy E_i as it is illustrated in Fig. 4.37. This procedure provides also the possibility to investigate structures within the energy loss distributions, and in particular to determine the mean energy loss ΔE_M and the most probable (peak) energy loss ΔE_p separately.

The quantities ΔE_M and ΔE_p are defined as illustrated in Fig. 4.37, right-hand side. Whereas ΔE_p denotes the energy difference of the peak positions of the peaks measured with and without absorber, ΔE_M denotes the energy difference between the mean-value of the two peaks. Both quantities are obtained from fits to the data (solid lines in Fig. 4.37, right-hand side), for details see [162,184]. As long as the shapes of the energy distributions determined with and without absorber target are equal, there will be no difference between ΔE_p and ΔE_M. However, as it becomes obvious from Fig. 4.37, right-hand side, an asymmetric shape exhibiting a tail on the high energy side is obtained for the energy distribution measured with absorber, leading to different values for ΔE_p and ΔE_M. This effect, which turned out to be a

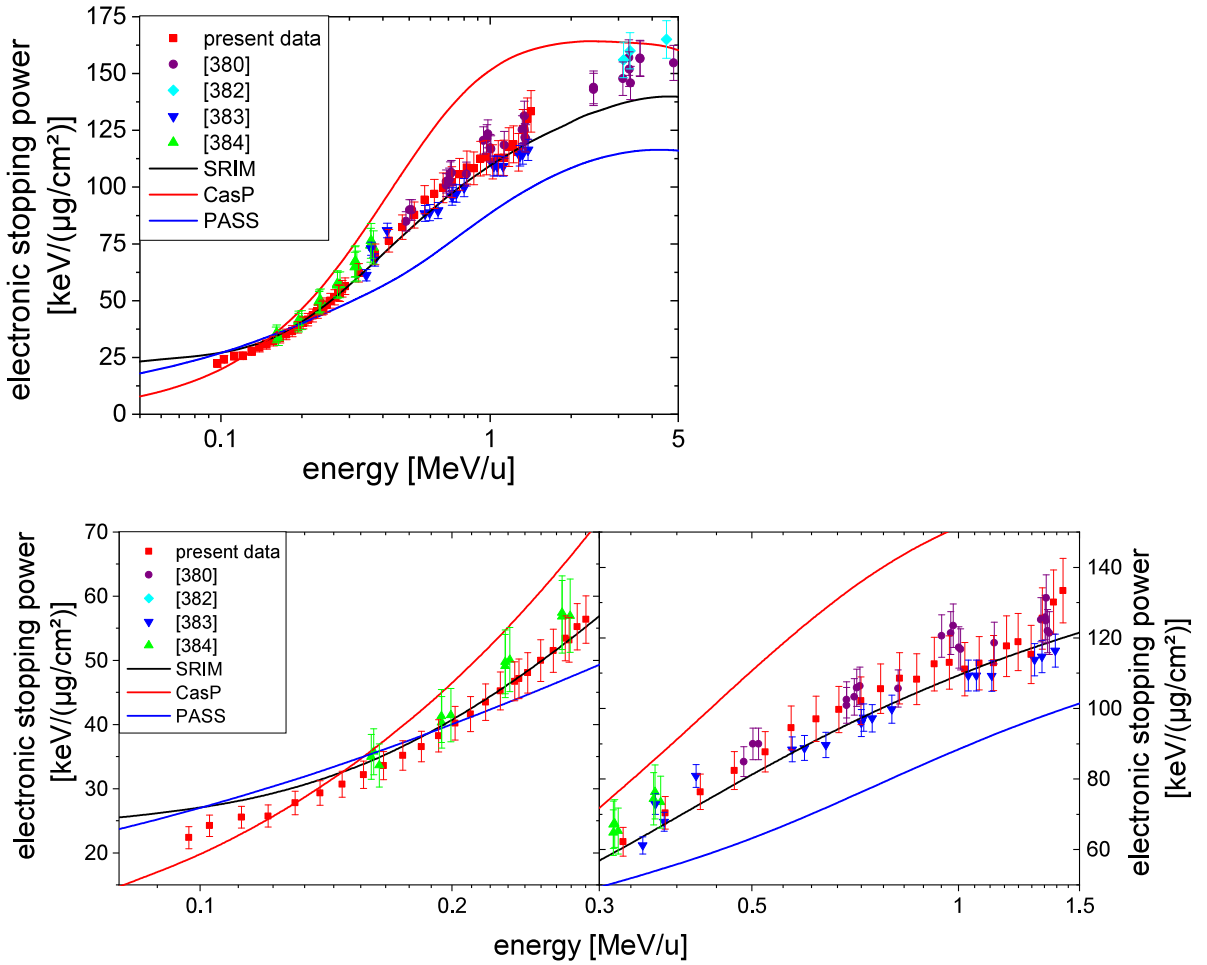

Fig. 4.38. The electronic stopping power data of ^{238}U ions in carbon absorbers as a function of the energy, obtained in the present experiment (red squares) are compared to data from the literature [374,380,382–384], as well as semi-empirical (SRIM [213,368]) and theoretical (PASS [364,365], CasP [366,367]) stopping power calculations. The present data and the literature data are displayed with the total experimental errors. For a more detailed view, the data from the upper panel are presented on an enlarged scale for different energy regions in the two lower panels.
Source: Adapted from [377].

common characteristics in the present experiments, is attributed to the appearance of the portion of nuclear energy loss, leading to high momentum transfer, and eventually thickness inhomogeneities of the absorber foils. Having in mind that the present investigations are aiming to determine purely the electronic stopping powers, the mean energy loss ΔE_M was chosen for the further data analysis. Nevertheless, the portion of nuclear energy loss leading to lower momentum transfer may still give rise to a non negligible contribution in ΔE_M. This is in particular true for the relatively small projectile energies used in the present experiment, which reach to a range, where electronic and nuclear stopping power are of the same order of magnitude [183,297]. Although the major part of the nuclear stopping power S_n does not contribute due to the quite low solid angle covered by the individual pixels of the CLTD array, a remaining contribution has to be considered, as a determination of the pure electronic stopping power S_{el} is intended. Therefore, SRIM calculations have been used to apply a nuclear stopping power correction on the measured total stopping powers (for details see [162]). The results show, that despite the relatively small solid angle covered by the CLTD detector, the contribution of nuclear stopping is up to 5%–10% in the lowest part of the examined energy range, and therefore, cannot be neglected for the present experiment, and thus needs to be corrected for. However, at ion energies above 0.3 MeV/u these corrections are with values below 1% already much smaller than the experimental uncertainties.

The stopping power, more precisely the mass stopping power,

$$S(E_{eff}) = -\frac{1}{\rho}\frac{dE}{dx}(E_{eff}) = \frac{\langle \Delta E \rangle}{\langle \Delta x \rangle} \tag{4.15}$$

at an effective ion energy E_{eff} within the target, was determined as the ratio of $\langle \Delta E \rangle$ and the mean areal density of the target $\langle \Delta x \rangle$. Due to the low relative energy losses $\Delta E/E_i < 15\%$ in the measurements with the thinner targets, E_{eff} can be

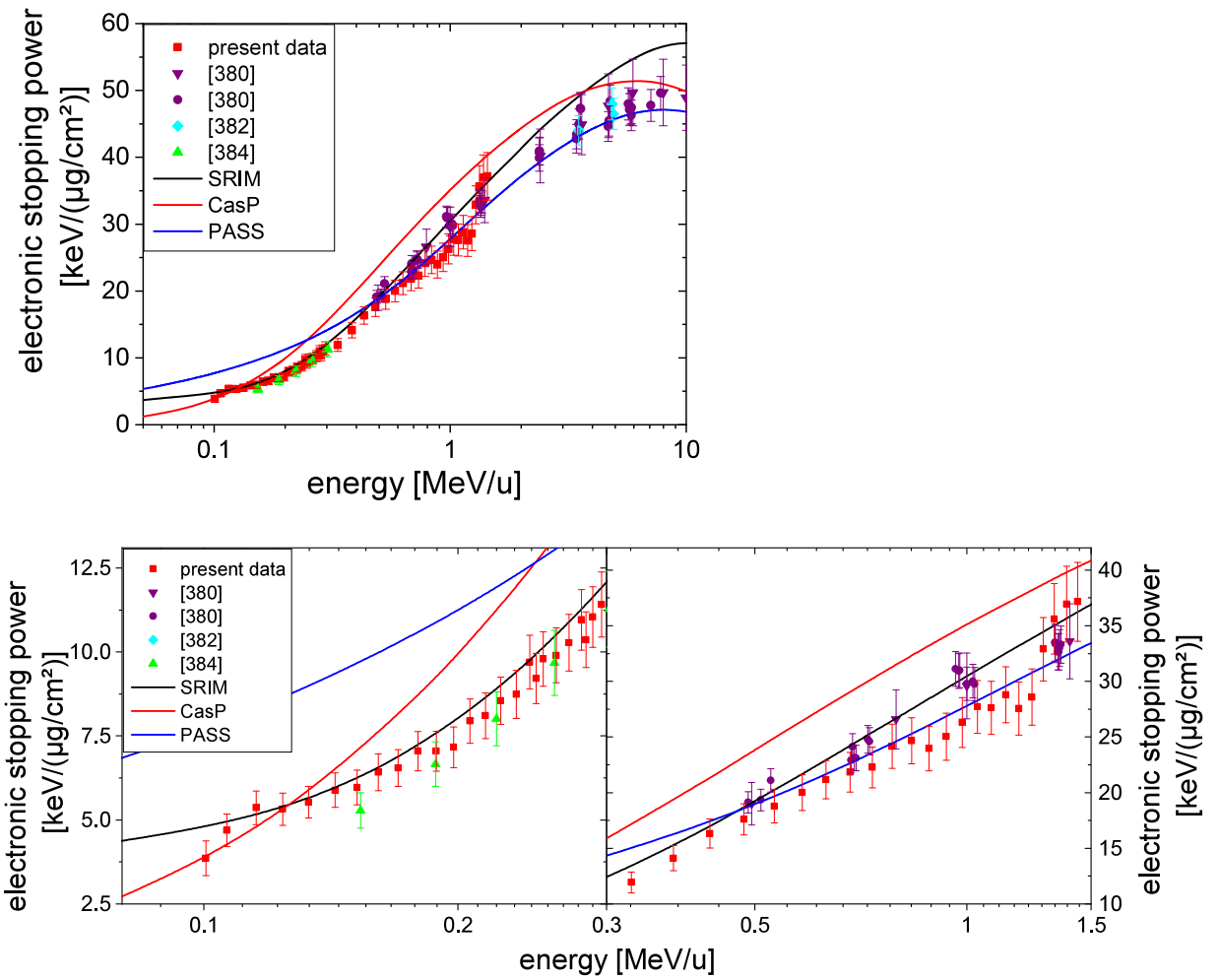

Fig. 4.39. The electronic stopping power data of ^{238}U ions in gold absorbers as a function of the energy, obtained in the present experiment (red squares) are compared to data from the literature [374,380,382,384], as well as semi-empirical (SRIM [213,368]) and theoretical (PASS [364,365], CasP [366,367]) stopping power calculations. The present data and the literature data are displayed with the total experimental errors. For a more detailed view, the data from the upper panel are presented on an enlarged scale for different energy regions in the two lower panels.
Source: Adapted from [377].

approximated by the arithmetic mean of initial and final energy

$$E_{eff} \approx E_{av} = E_i - \Delta E/2 \tag{4.16}$$

However, as for the thick C- and Ni-targets the relative energy losses $\Delta E/E_i$ were up to 55%, the non-linear dependence of the stopping power as function of the ion energy within the target has to be taken into account. The corrections on E_{av} have been determined in an iterative procedure (for details see [162]).

A careful evaluation of all kinds of systematic uncertainties has been performed for the results of both measurement campaigns at GSI and Jyväskylä (for details see [162,184]). For both cases the systematic error is dominated by the uncertainties on the properties of the absorber targets, namely the mean target thickness, as well as the inhomogeneity (6%–8% for the measurements at GSI, and 2%–5% for the measurements at Jyväskylä), whereas uncertainties due to the absolute energy calibration, the correction for the nuclear energy loss, etc. contribute only less then 1%–2% in both cases. The resulting total systematic uncertainty (quadratic sum of all contributions) amounts to 6%–9% for the GSI measurements, and to 3%–6% for the Jyväskylä measurements, and exceeds in all cases the statistical uncertainties.

4.2.4. Results and discussion

4.2.4.1. Electronic stopping powers for 0.1–1.4 MeV/u ^{238}U ions in C and Au absorbers

The results on the measured electronic stopping powers for ^{238}U ions in carbon and gold, obtained in the experimental campaign at the UNILAC accelerator of the GSI Darmstadt, are displayed in Figs. 4.38 and 4.39 (red data points)

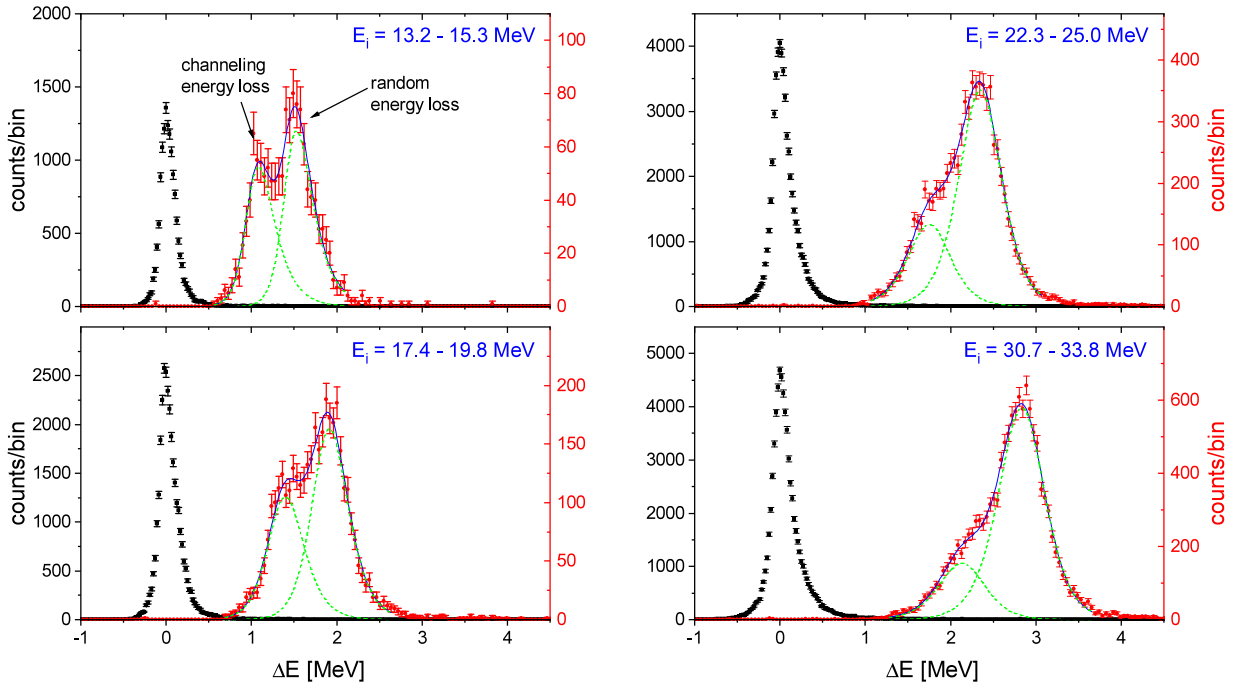

Fig. 4.40. ΔE-distributions of ^{131}Xe ions for different energy intervals for measurements without (black squares) and with a gold absorber target (red circles). The double peaks in the ΔE distributions of ^{131}Xe ions with target are attributed to channeling in polycrystalline regions of the gold target. An effect of the ion beam or the detector can be excluded because the distribution without target shows no double peak structure.
Source: Reproduced from [162].

together with literature values from previous measurements, and with the results of different theoretical predictions and calculations (for details see [184,377]). For both absorber targets, new data for low incident energies could be measured, thus extending, as compared to previously published data, the data sets down to energies around 0.1 MeV/u. This can be considered as a significant input for the improvement of theoretical predictions of semi-empirical computer codes, in particular concerning the energy dependence of electronic stopping power data at small incident energies. For higher incident energies the present data are, within the experimental uncertainties, including statistical and systematic errors, in good agreement with data of H. Geissel et al. [374,380,381], R. Bimbot et al. [382], H. Pape et al. [383], and M. D. Brown et al. [384]. Slight systematic deviations of the data sets of M. D. Brown et al. (higher values for the carbon absorber, and lower values for the gold absorber), and of H. Pape et al. (for the carbon absorber) may be attributed to uncertainties in the determination of the thickness of the absorber targets.

Predictions from the semi-empirical computer code SRIM [213,368] show a remarkably good agreement in the low-energy region of the data for the Au absorber target, but slight disagreements are obtained in the higher energy range. For the C absorber target the SRIM predictions overestimate the data at very low energies, and underestimate the data at high energies. As expected, the predictions of the ab initio computer codes PASS [364,365] and CasP [366,367] show bigger discrepancies for both absorber targets. The best agreement with the experimental data is obtained for the PASS predictions for the C absorber target at low energies, and for the Au absorber target at high energies.

4.2.4.2. Observation of channeling effects for the interaction of ^{131}Xe ions with Ni and Au absorber foils

Before the results on stopping powers obtained in the second experimental campaign at Jyväskylä will be presented (see next section), the surprising appearance of channeling effects during these measurements, their confirmation and the resulting data on channeling stopping powers, which can be considered as an unexpected by-product of the present investigations, will be discussed in this section (for details see [162,184]). While the measurements with the carbon targets, as illustrated in the example for an energy loss spectrum in Fig. 4.37, do not show any irregularities, a high and a low energy-loss component have been observed in the ΔE-distributions for the measurements with the two thin nickel absorber targets, and especially pronounced for the gold absorber target, as can be seen in Fig. 4.40. Thereby, the intensity ratio of the two peaks R_I shows a strong energy dependence, and also the ratio of the peak positions of the two components $R_{\Delta E}$, i.e. of the energy losses ΔE, is varying with energy (see Fig. 4.41).

A detailed analysis [184] has revealed that the double peak structures arise from channeling effects within polycrystalline regions of the thin metallic target foils (an overview on the phenomenon of the channeling of ions in matter can be found in [362]). Whereas the low ΔE component corresponds to channeled ions, the high ΔE component results from

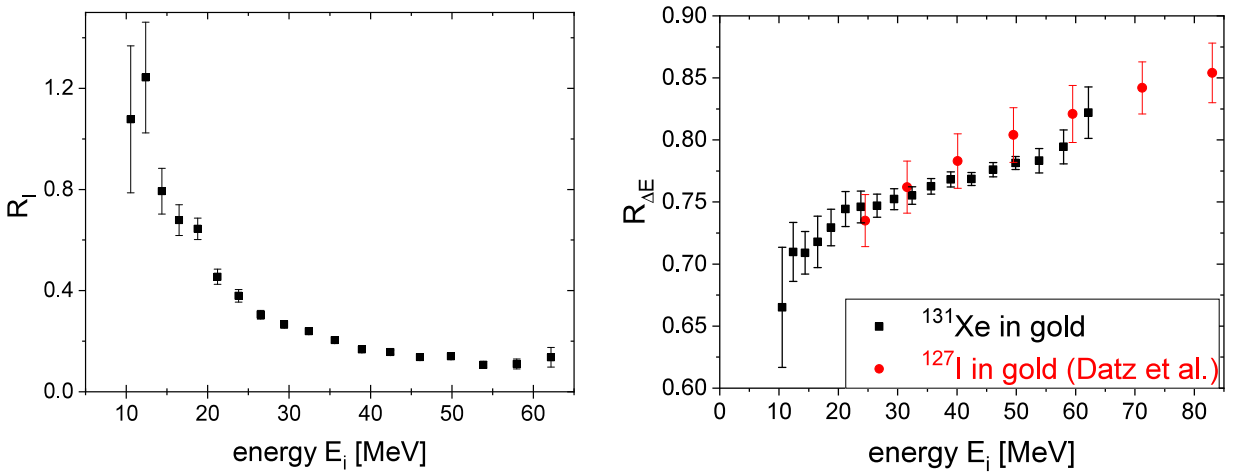

Fig. 4.41. The values R_I and $R_{\Delta E}$ describe the relations between the low (channeling) energy loss and the high (random) energy loss components which were observed in the ΔE distributions for the gold target as a function of the incident energy (black dots). R_I (left-hand side) is the ratio of the peak areas (intensity ratio), and $R_{\Delta E}$ (right-hand side) is the ratio of the peak positions (energy loss ratio) (reproduced from [162]). For comparison, data for $R_{\Delta E}$ from S. Datz et al. [385] for ^{127}I ions are plotted (red dots) on the right-hand side.

the expected random energy loss in amorphous regions of the target. Other possible explanations, like irregularities in the energy measurement, could be excluded, as no double peak structures have been observed in the measurements without a target. Also target defects or effects of target thickness distributions cannot explain the double peak structure, due to the strong energy dependence of the observed effect that can be seen in the graphs of Fig. 4.41. As channeling requires crystalline targets, the structure of the used absorber foils has been inspected by **X**-**R**ay **D**iffraction (XRD) [162,184]. Indeed, a significant signature of polycrystalline structures was found in the Ni and Au targets, whereas no polycrystalline structure was observed for the carbon targets, proving their fully amorphous structure, thus explaining the absence of a double peak in the corresponding energy loss spectra (see Fig. 4.37). Moreover, the results have shown a correlation between the magnitude of the observed effect, i.e. the intensity of the lower $\Delta E-$component, and the amount of polycrystalline regions within the Ni and Au absorber targets. Nevertheless, the observation of channeling and random energy loss of the same order of magnitude for the Ni and Au absorber targets may still be surprising. As only parts of the metallic foils are crystalline, and furthermore, the crystallites have a random orientation, the probability for channeling should be extremely low. In fact, the channeling probability for a ^{131}Xe ion passing through the Au target could be roughly estimated to be in the range of 10^{-3}.

This apparent contradiction to the measurements is dissolved by considering the exit angle distributions for the different energy loss processes, and the relatively low coverage of the detection solid angle by the CLTDs. While the exit angles for channeled ions are very small, and therefore no significant losses in intensity are expected, the primary intensity in the case of the random energy loss is decreased by a factor of about 10^2 due to small angle scattering and a maximum detection angle of only 0.3°. Therefore, and considering the fact that the estimated channeling probability of about 10^{-3} is just a rough estimate, it is absolutely possible to observe ions, having passed a target under the two different energy loss processes, with an intensity of the same order of magnitude. In other words, for the present experimental parameters, i.e. low incident energy and small solid angle coverage by the detectors, the low channeling probability in thin polycrystalline foils is compensated by the high loss in intensity for the random energy loss, resulting from scattering processes within the target. This explanation is also consistent with the strong energy dependence of the peak-intensity ratio R_I in Fig. 4.41 (left-hand side), as for lower energies on the one hand the critical angle for channeling increases with $\Psi_c \approx 1/E^{1/2}$ [362], and on the other hand the count rate for random energy loss decreases, due to the increasing nuclear scattering cross section. As for the ratio of the peak positions $R_{\Delta E}$, a very similar energy dependence is observed for channeling of ^{127}I ions along the (110) planes of a single crystalline Au foil [385] (see Fig. 4.41, right-hand side).

As a consequence of the discussed observations, channeling and random energy loss have to be treated separately to be able to compare the present results to previously determined values from other experiments, as well as to theoretical calculations. For that reason, the mean and peak values ΔE_m and ΔE_p of the corresponding $\Delta E-$distributions have been determined by using a sum of two fit functions, as illustrated in the examples of Fig. 4.40. As a positive side effect, additional data on the ratio of planar channeling energy loss and random energy loss of $10-60$ MeV ^{131}Xe ions in nickel and gold absorbers (see Fig. 4.41 and [162,184]) have been obtained in the present experiment. However, at this point it has to be stated, that no investigations have been carried out to what extent different orientations of the crystal planes have been contributing to the measured channeling energy loss data.

Finally it should be mentioned that for the measurements at GSI with Au absorber foils (see Section 4.2.4.1), there was no indication of a second component in the energy loss spectra. This finding can only be explained by the fact that for the

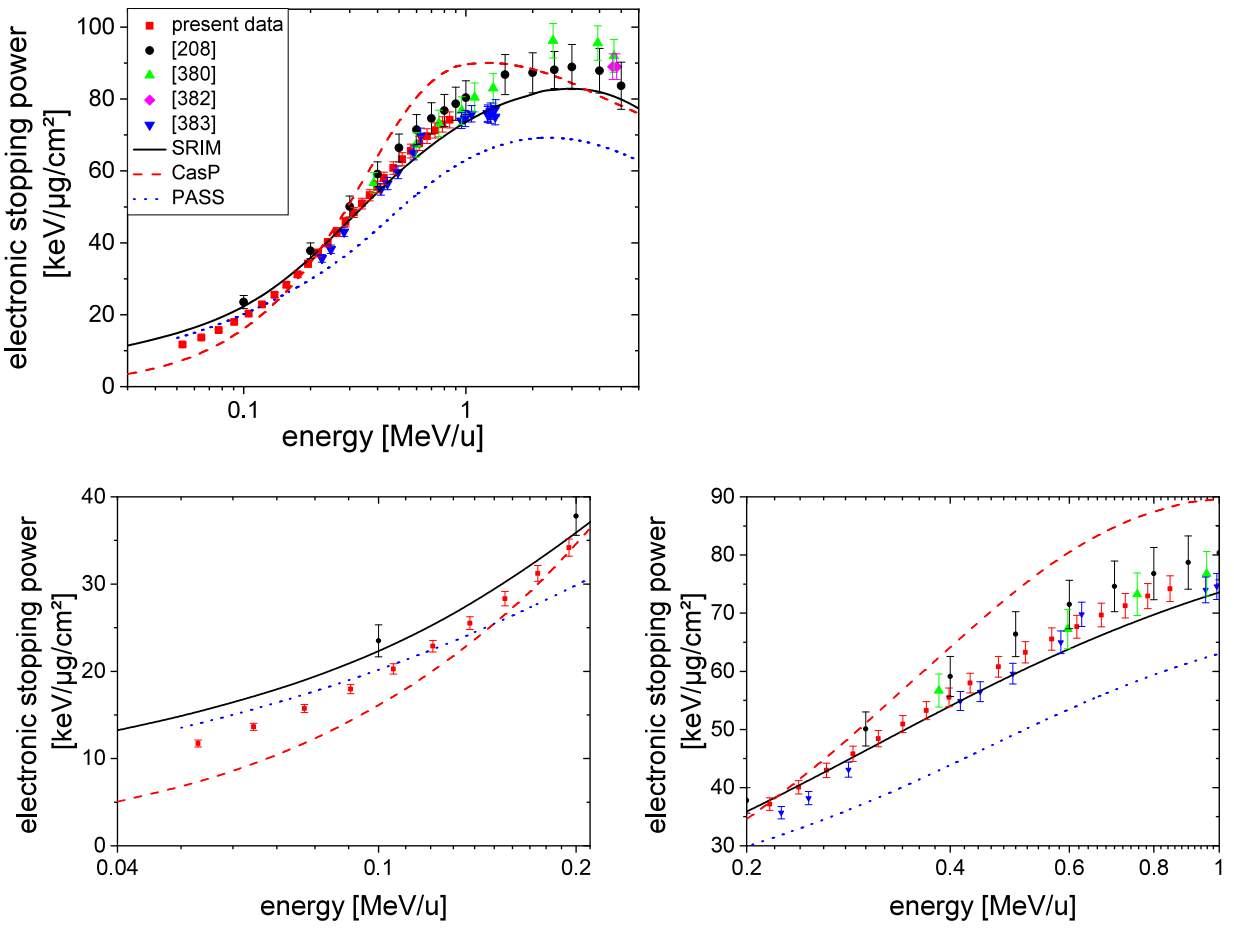

Fig. 4.42. The electronic stopping power data of ^{131}Xe ions in carbon absorbers as a function of the energy, obtained in the present experiment (red squares) are compared to data from the literature [208,374,380,382,383], as well as to semi-empirical (SRIM [213,368]) and theoretical (PASS [364,365], and CasP [366,367,386]) stopping power calculations. The present data and the literature data are displayed with the total experimental errors. For a more detailed view, the data from the upper panel are presented on an enlarged scale for different energy regions in the two lower panels. *Source:* Reprinted from [162].

GSI measurements different samples of the Au absorber foils were used, which do, due to a different production process, not (or only to a very small extend) contain polycrystalline structures.

4.2.4.3. Electronic stopping powers for 0.05–1 MeV/u ^{131}Xe ions in C, Ni and Au absorbers

The results on the measured electronic stopping powers for ^{131}Xe ions in carbon, nickel and gold, obtained in the experimental campaign at the K130 cyclotron of the University of Jyväskylä, are summarized in Figs. 4.42 and 4.43 together with literature values from previous measurements, taken from the database of H. Paul [374], and with results of different theoretical predictions and calculations (for details see [162,184]). As for some of the targets, channeling effects have been observed (see previous section), it should be noted that the results presented here correspond to random stopping power only. The statistical errors are for the major part of the data with less than 1% negligible as compared to the systematic uncertainties. Only for the data points at lowest and highest energies they contribute significantly to the total experimental uncertainty, due to the decreasing count rate.

Comparing the results with previously published data (see Figs. 4.42 and 4.43) shows that within the experimental uncertainties the present results are in agreement with the literature values for most of the data points in the higher energy regime. Slight systematic shifts between different data sets may be attributed to the errors in the determination of the mean target thicknesses. At lowest energies, however, the stopping powers measured in the present experiment show lower values as compared to previously published data [208] for all three absorber targets. As a possible explanation for at least part of these deviations the additional corrections for nuclear stopping power which are taken into account in the present data (see Section 4.2.3 and [162,184]) are identified. For all three target materials the experimental data have been (similarly to the results for ^{238}U, see Section 4.2.4.1) extended, as compared with previously published data, down to very low energies around 0.05 MeV/u, which may again be considered as an important input for future theoretical

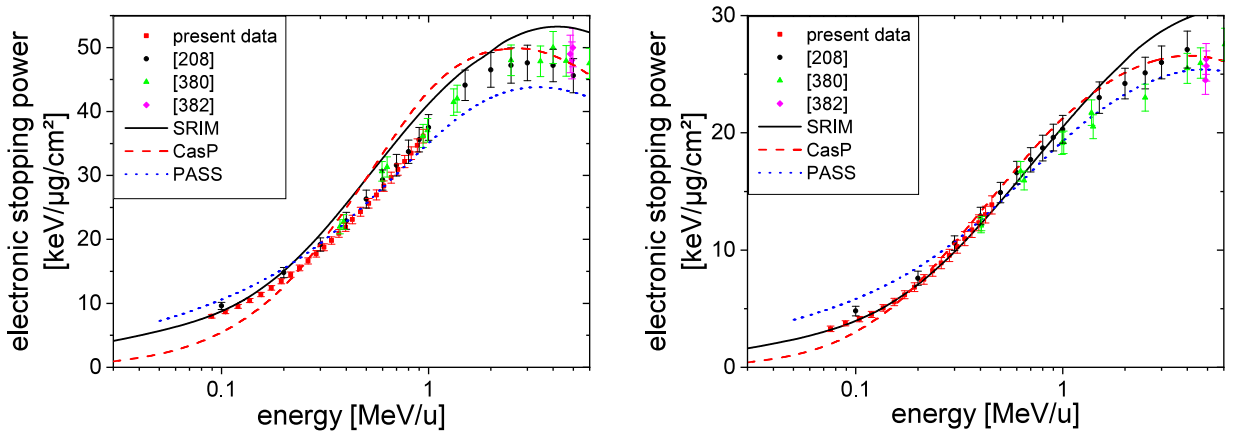

Fig. 4.43. The electronic stopping power data of ^{131}Xe ions in nickel (left-hand side) and gold (right-hand side) absorbers as a function of the energy, obtained in the present experiment (red squares) are compared to data from the literature [208,374,380,382], as well as to semi-empirical (SRIM [213,368]) and theoretical (PASS [364,365], and CasP [366,367,386]) stopping power calculations. The present data and the literature data are displayed with the total experimental errors.
Source: Adapted from [162].

predictions. Moreover, the total errors, in particular the calibration errors, could be reduced as compared to previous measurements [208], where ionization detectors have been used for the energy measurement (for details see [184]).

Predictions from the semi-empirical computer code SRIM [213,368] for carbon absorbers show the behavior which was already discussed in [387], that SRIM typically predicts stopping powers of very heavy ions in light materials too high at very low energies and too low in the region of the Bragg-peak. For the medium-heavy nickel absorbers, the SRIM calculations are above the measured data in the entire examined energy range, while an excellent agreement between prediction and measurement is observed for the heavy absorber material gold in the entire measurement range of 0.08–0.45 MeV/u of the present data. Not surprisingly, the theoretical ab-initio calculations PASS [364,365] and CasP [366,367,386] show larger deviations from the measured values than the SRIM-predictions. However, for carbon absorbers and very low projectile energies, as well as for nickel absorbers at higher energies, the PASS calculations show also very good agreement with the obtained experimental data, while the best predictions using CasP are obtained for the heavy target material gold.

4.2.5. Conclusion and perspectives

A new experimental setup using a CLTD array for the energy determination in a combined ToF-E measurement has been applied to collect continuous stopping power data for 0.1–1.4 MeV/u ^{238}U ions and 0.05–1 MeV/u ^{131}Xe ions in different absorber materials. The results demonstrate that CLTDs are well suited devices for stopping power measurements. A comparison with previously published stopping power values shows a good agreement for most of the data, providing a consistency check of the new experimental setup. In the region of very heavy ions at very low energies, which is hardly accessible with ionization detectors, and where therefore reference data are scarce [374], new stopping power data have been obtained for light, medium-heavy and heavy absorber materials. These data may help to adjust theoretical calculations and therefore to improve the precision of their predictive power.

Comparing the present data to the values of the previous publication [208] is of special interest, not only as these are the only reference data in the lowest part of the examined energy range, but also as an almost similar experimental setup, however with a conventional Si-detector for energy determination, has been used. By replacing the Si-detector with the CLTD array, calibration errors resulting from the pulse height defect of the ionization detector, could be considerably reduced due to the additional calibration options and the excellent energy linearity of the CLTDs. Moreover, an independent verification of the linearity of the ToF spectrometer could be obtained by the additional calibration of the detector system at low ion energies using an $\alpha-$source, a possibility given solely due to the alternative detection principle of the CLTDs. Also the statistical errors could be reduced significantly as compared to the previous measurements presented in [208]. Albeit this argument depends basically on the measurement time, also the better sensitivity due to the improved energy resolution of the CLTDs contributes to a reduction of statistical errors.

Besides the increased accuracy for the determination of small energy losses, the high energy resolution of the CLTDs also enabled for the first time in such experiments a precise investigation of structures in the measured $\Delta E-$distributions. This allowed, for example, a separate determination of the mean and the peak energy loss and also the observation of unexpectedly strong channeling effects. The latter point demonstrates, that under the current experimental conditions, i.e low projectile energy and small detection angle, despite the low channeling probability for polycrystalline samples, a possible contribution of channeled ions to the measured mean energy loss cannot be neglected. In the present data for

instance, the measured mean energy loss, taking all detected ions into account, was for some of the absorber targets up to 15% lower than the pure random energy loss. Therefore, when only the determination of the latter quantity is intended or expected, ignoring the channeling effect represents a significant systematic error source, which is in particular the case for all measurements with conventional energy detection if absorber targets with not identified polycrystalline structures were used. In addition, the identification of channeling effects in parts of the present measurements allowed also to obtain experimental data concerning the ratio between planar channeling and random energy loss of 10–60 MeV ^{131}Xe ions in nickel and gold absorbers.

Another important point concerns the composition of the energy detector of several CLTD pixels which provides additional options for the analysis of the measured stopping power data as compared to a detector without position information. In the present case, for example, the homogeneity of the target foils could be investigated by comparing the energy loss data measured with different CLTD pixels (for details see [184]). In principle, an array of individual detectors is also well suited for the determination of energy loss as a function of the projectile exit angle, what would be of special interest with regard to a separation of nuclear and electronic energy loss. In the data presented here, corresponding investigations could not be carried out, as the small differences in the energy loss determined with different CLTD pixels were dominated by thickness variations of the target foils, and therefore corrections due to the nuclear energy loss had to be estimated by calculations. For the option to obtain angle dependent energy loss data in future experiments, more homogeneous absorbers, as well as a larger covering of the detection angle, the latter being possible by using the new generation of 25-pixel CLTD arrays recently constructed (see Section 3.2.4), are mandatory.

For the future, the present experimental setup for ToF-CLTD measurements provides a large potential for several investigations, which may profit from the excellent energy resolution of CLTDs. Examples are, among others, further investigations of electronic and nuclear stopping powers for various beam–target combinations with the focus on very low incident energies and thin targets, dedicated heavy ion channeling experiments with single-crystal absorbers, with a focus on the energy-loss dependence on the crystal orientation with respect to the incident angle of the heavy ions, and the investigation of charge exchange energy loss straggling in solid absorbers [298,388] in the region of the Bragg peak and at even higher energies.

The investigations in the present article focused on the electronic stopping power of heavy ions. However, in particular for the purpose of cancer treatment, the stopping power at the end of the ion track has to be known with high precision. Cancer treatment with carbon ions is nowadays an established method next to therapy with protons and photons [360]. Several dedicated treatment facilities exist allover the world, e.g. the **H**eidelberg **I**on **T**herapy Center (HIT) at Heidelberg [389], or the **M**arburg **I**on **T**herapy Center (MIT) at Marburg [390] in Germany. With carbon ions, brain and spine tumors can be treated that would not be curable otherwise. An excellent overview of the current status of carbon therapy worldwide is given in [391]. In this reference, the main advantage of using ions as compared to photons is explained: The region of maximum energy loss, which causes the highest damage in the tissue, is confined to a very small volume at the end of the ion track. This means that the tissue in front of the tumor suffers much less damage than it would when using x-ray or $\gamma-$ray photons. In addition, charged particles can be focused very sharply by electromagnetic fields, thus sparing the surrounding tissue. This feature is especially important when treating brain or spine tumors. The region of maximal damage is also referred to as the *Bragg peak*. It becomes sharper as the mass of the ion increases, which means that heavier ions allow for an even more precise tumor treatment [392]. The advent of the new method of *spatially fractionated radiotherapy* has reinitiated the investigation of using ions as heavy as iron for cancer treatment, because they may be more effective when treating very hypoxic tumors [393,394]. It is obvious that precise cancer treatment demands very precise and reliable data on electronic as well as nuclear stopping powers for the ions under consideration. As discussed in Section 4.2.1, such data become more and more scarce for heavier ions. On the other hand, ranges of iron ions in human tissue, which were calculated using codes for medical application, differ by almost 40% from the few measurements that were performed at the GSI [395]. These measurements in turn suffered from the fact that an ionization chamber was used to determine the energy. For the very low ion energies close to the Bragg peak, the energy loss in the entrance foil cannot be neglected. CLTDs for low ion energies provide the optimal tool for such investigations, because they do not need entrance windows at all. A first pilot experiment to investigate the energy loss of ions close to iron in the Bragg peak region is scheduled. It may pave the way for a new understanding of stopping of ions in matter at very low energies.

4.3. Application of CLTDs in accelerator mass spectrometry

4.3.1. Motivation

Accelerator **M**ass **S**pectrometry (AMS) is a well established method for the determination of very small isotope ratios with high sensitivity [135,163,396]. In comparison with conventional mass spectrometry, the use of accelerated ion beams provides substantial advantages in the quality of isotope separation and background suppression, thus allowing the determination of isotope ratios down to a level of $10^{-10} - 10^{-16}$, depending on the ion species. The most prominent example is certainly the ratio of ^{14}C to ^{12}C which is used for radiocarbon dating. However, heavier nuclides have become more and more of interest for AMS investigations also. A special focus lies on trace analysis of actinides which can be used to guard nuclear waste proliferation, as nuclear safeguard, or as oceanographic tracers. An excellent overview is given in [163,396].

^{236}U represents one of the heaviest nuclides of interest for AMS. Being produced in nature by capture of thermal neutrons in the reaction ^{235}U(n, γ)^{236}U and having a half-life of 23.4 million years [397], the relative abundance of ^{236}U provides an excellent neutron flux monitor integrated over geological time scales. Thus, besides other applications, ^{236}U could be used to prove the existence of an enhanced neutron flux due to natural "reactor-like" conditions in the past [134,398]. As a standard, the content of ^{236}U is determined from the ratio to the most abundant isotope ^{238}U. In natural uranium minerals, the isotope ratio ^{236}U/^{238}U is expected to be of the order of $10^{-10} - 10^{-14}$, dependent on the sample's history and surroundings. However, the energy resolution and detection efficiency of conventional heavy ion detection systems limit the sensitivity and demand relatively large amounts of sample material [399,400].

The use of CLTDs can overcome these limitations. AMS is commonly performed at dedicated tandem accelerators with a relatively small terminal voltage of $0.5 - 5$ MeV, so the total energies for heavier ions usually do not exceed 0.3 MeV/u [401]. CLTDs can provide better detection efficiency and a lower detection threshold in this energy range (see Section 3.6.2). Furthermore, their excellent energy resolution can be used to improve the background suppression from neighboring isotopes.

4.3.2. First application of CLTDs for trace analysis of ^{236}U

The systematic investigations which are presented in Section 3.6.2 demonstrate the potential of the CLTDs for the investigation of the ^{236}U/^{238}U ratio by means of AMS. Two types of uranium samples were investigated in this first proof-of-principle campaign performed at the **V**ienna **E**nvironmental **R**esearch **A**ccelerator (VERA) at Vienna, Austria [134, 135]:

- To minimize systematic errors caused by changes in machine performance and experimental setup, AMS measurements are usually performed normalized to a material standard for which the isotope ratio is very precisely known. In the case of the ^{236}U/^{238}U ratio, such a material standard had not been established due to the lack of a suitable material (see also [399]). However, the VERA laboratory possesses a considerable amount of uranyl nitrate from the mine *Joachimsthal*, prepared and stored before 1918 and thus not contaminated by ^{236}U created by human nuclear activities. The ^{236}U content is, therefore, sufficiently low that the ore can serve as a reference material for AMS of geological samples. P. Steier et al. [399,400] performed first measurements on this material with a conventional time-of-flight/energy detection system.
- The ratio of ^{236}U to ^{238}U in water has become a valuable tool, not only for direct measures of nuclear safeguard, but also as a tracer material to investigate water streams across the globe on long time scales [402,403]. The uranium content in these samples is expected to be much lower than in an uranium ore. An enhancement in sensitivity is needed for systematic investigations. As a first test, one sample had been extracted from 5 l of water steming from an uranium containing spring in the region of *Bad Gastein*, Austria. Because the uranium in the water had been washed out from the deep regions of the Alpes, the isotope ratio was not known, but expected to be significantly lower than that of the uranyl nitrate.

4.3.2.1. Experimental setup

The experimental setup is shown schematically in Fig. 4.44. As energy detector, a single pixel CLTD with a $2 \times 3 \times 0.33\,\mathrm{mm}^3$ sapphire absorber and an Al TES was used. A pumped ^{4}He bath cryostat (a predecessor of the one described in Section 3.4), which is described in detail in [164,218], housed the CLTDs. It was connected to the beamline of the VERA facility [134,135], which is a dedicated AMS facility. A cesium sputter ion source produces negative ions which are injected into a tandem accelerator with 3 MV terminal voltage. A high resolving magnetic and electrostatic analyzing system provides heavy ion beams of various ions in an energy range of 6 MeV $\leq E \leq$ 65 MeV with an energy spread as small as $\Delta E/E \leq 10^{-4}$. To suppress background from neighboring uranium isotopes, an additional switching magnet was used for the AMS measurements. Therefore, these measurements were performed at the 20°-beamline. The count rate of the radioisotope ^{236}U was detected in the CLTD, while for the long-lived ^{238}U the beam current was measured in a Faraday cup which was moved in and out of the beam. The results of systematic investigations of the detector performance for these low ion energies were reported in Section 3.6.2. To minimize systematic errors, several targets for the ion source had been prepared from each sample (for details of target preparation see [134]). The measurements with these targets were performed several times in cyclic order. The ^{238}U current was measured alternatingly every 200 s. For a detailed description of the AMS measurement procedure see also [134,399]. In contrast to the setup described in these references, no time-of-flight detector was included in the present measurements.

Under the experimental conditions at the VERA AMS facility, background in AMS measurements for very heavy ions like ^{236}U is mainly due to neighboring isotopes (^{234}U, ^{235}U, ^{238}U), which undergo ionic charge exchange reactions with the residual gas in the accelerator beamline, and afterwards have the same magnetic rigidity mE/q^2 as ^{236}U (m being the mass and q the ionic charge state of the uranium ion). Therefore, the neighboring isotopes can pass through the high-energy magnetic analyzer and – after additional charge exchange – also through the electrostatic analyzer (see [134] for a detailed discussion). The background situation expected for the case of $^{236}U^{5+}$ at $E = 17.54$ MeV is displayed in Fig. 4.45. As the resolution of the magnetic analyzer is very high [134], the condition $mE/q^2 = constant$ leads to well defined energies for the background peaks. Since standard heavy ion detectors (e.g. ionization chambers) do not provide sufficient energy resolution to resolve these background peaks, in the standard measurement procedure [134,399] a time-of-flight (ToF) spectrometer combined with an ionization chamber is used. Due to ion losses in the start and stop foils of the ToF detector

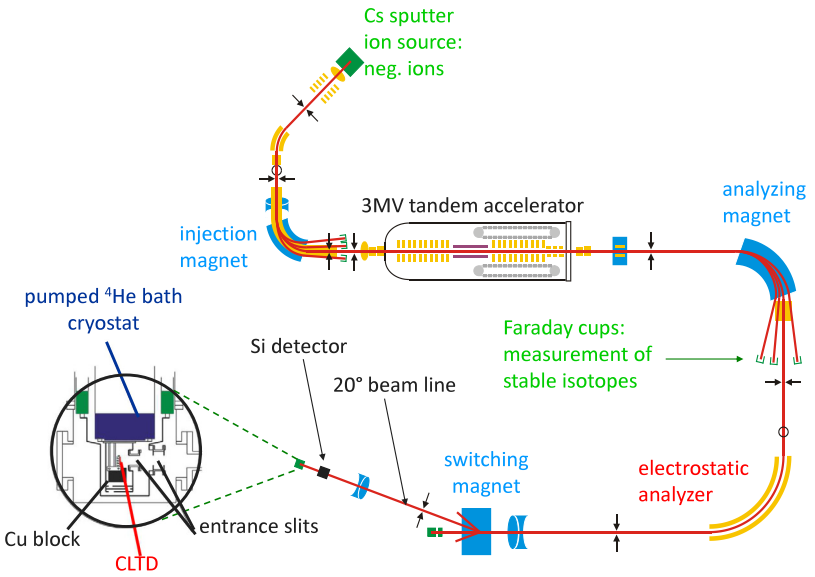

Fig. 4.44. Schematic view of the experimental setup: The pumped ^{4}He bath cryostat was connected directly to the beamline of the Vienna Environmental Research Accelerator VERA. The AMS measurements were performed at the 20°-beamline (for details see text).
Source: Adapted from [154,164].

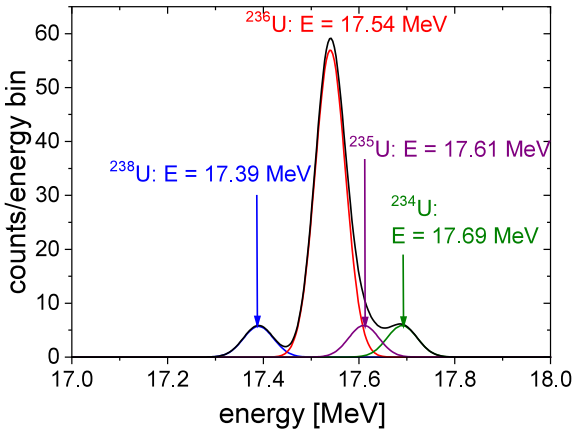

Fig. 4.45. Simulation of the background situation for the AMS experiment under the assumption of Gaussian line shapes. The ratio of ^{236}U to ^{238,235,234}U is assumed to be 10:1, the energy resolution is assumed to be $\Delta E/E = 4.6 \times 10^{-3}$.
Source: Adapted from [154,164].

and in the entrance window of the ionization chamber, the transmission through this detection system is limited to about 31% [404], thus limiting the sensitivity [399]. The use of CLTDs can overcome this obstacle and, therefore, improve the sensitivity.

4.3.2.2. Results and discussion

The results of the present experiment were published in [154] where a more detailed discussion is presented. Table 4.6 summarizes the results of the first application of CLTDs for AMS to determine the ratio of ^{236}U/^{238}U. Fig. 4.46 shows two spectra for two of the investigated samples. For the very first "proof-of-principle" AMS measurement performed with a CLTD, the detector performance under running conditions was unfortunately worse as compared to the results presented in Section 3.6.2. In fact, the energy resolution was about a factor of two worse than could have been expected (see Fig. 4.45). The decrease in energy resolution was caused by additional noise contributions under running conditions, as well as being due to an increase in the heat capacity of the detector by condensation of residual gas onto the detector surface because of the relatively bad vacuum (see also discussion in Section 3.6.2.1). In addition, non-permanent radiation damage during the adjustment process, during which the CLTD was irradiated with a high-intensity beam of ^{238}U ions, cannot be completely excluded. But already with a resolution of $\Delta E/E = 9.1 \times 10^{-3}$, essential parts of background could

Table 4.6
Results of the measurements of the $^{236}U/^{238}U$ isotope ratio to establish a material standard (*Vienna-KkU* and *Joachimsthal 2*), and to improve the sensitivity (*Bad Gastein 1*) (for details see text and [154,164]). For comparison, measurements with the conventional time-of-flight setup are presented [400]. The samples *Bad Gastein 2A* and *Bad Gastein 2B* were prepared from the same water well, but at a later time.

Sample	$^{236}U/^{238}U$ $[10^{-11}]$	Reference
Vienna-KkU	$3.89 \pm 0.08_{stat} \pm 0.35_{syst}$	[154]
Vienna-KkU	$6.98 \pm 0.32_{stat}$	[400]
Joachimsthal 2	$2.29 \pm 0.07_{stat} \pm 0.29_{syst}$	[154]
Bad Gastein 1	$0.61 \pm 0.17_{stat} \pm 0.12_{syst}$	[154]
Bad Gastein 2A	$0.62 \pm 0.23_{stat}$	[400]
Bad Gastein 2B	$0.70 \pm 0.31_{stat}$	[400]

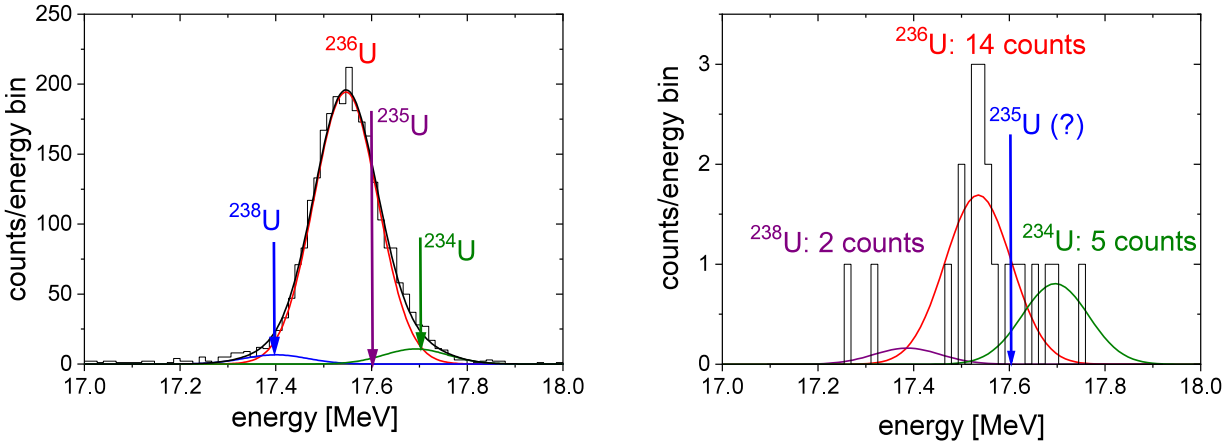

Fig. 4.46. On the left-hand side, an example spectrum obtained for the sample *Vienna-KkU* is displayed, which is used as a material standard for AMS experiments on ^{236}U [154,399]. Background from the isotopes ^{234}U and ^{238}U can be separated, while a possible contribution of ^{235}U is still included in the ^{236}U peak. On the right-hand-side, the spectrum of the only sample extracted from spring water (*Bad Gastein 1*) is displayed. Due to the limited amount of sample material, only one measurement with a duration of 20 min could be performed.
Source: Both figures adapted from [154,164].

be separated, whereas a possible contribution of ^{235}U is still included in the ^{236}U count rate. The systematic error is mainly limited by the determination of the transmission from the Faraday cup to the detector. As compared to a conventional detection system, using a calorimetric detector improved the transmission from about 31% to (65 ± 10)%, in the latter case limited by the active detector area.

- Samples from *Joachimsthal*
  The spectrum for the sample *Vienna-KkU* is displayed on the left-hand side of Fig. 4.46. As compared to the total count rate, the background contribution from ^{234}U is 10(1)%, and from ^{238}U 4(1)%. Therefore, at a level of 10^{-11}, the background is not limiting the sensitivity. The uncertainty is dominated by the systematic uncertainty of the transmission which also limits the precision of the measurement of P. Steier et al. [400]. The result is close to the result of this measurement, but it is clearly smaller. The reason for this discrepancy is yet unclear. Unfortunately, no estimate on the systematic error is given in [400]. The result of the sample *Joachimsthal 2* is considerably smaller than the result of *Vienna-KkU*. However, this is understandable because the sample originates from a different batch of the Joachimsthal ore, and local variations of rock composition, e.g. presence or absence of neutron absorbing or emitting nuclides, can cause variations in the local $^{236}U/^{238}U$ isotope ratio. The present result demonstrates that, once a material standard is established, different samples with different isotope ratios can be characterized and compared with high accuracy.
- Sample from *Bad Gastein*
  Due to the low uranium concentration in the water, the amount of sample material for this sample was limited, and only one measurement of 20 min duration could be performed. The corresponding spectrum is displayed in Fig. 4.46 on the right-hand side. In the case of this sample, the background is dominated by ^{234}U and yields approximately 30% of the total count rate. Therefore, at this level of sensitivity, background starts to play an important role, and a good energy resolution becomes more and more important for background separation.
  The present result for the isotope ratio, $^{236}U/^{238}U = (0.61 \pm 0.21) \times 10^{-11}$ (see Table 4.6), represents the smallest isotope ratio measured for $^{236}U/^{238}U$ up to date. The result was confirmed by P. Steier et al. with the conventional setup and a larger amount of sample material [400] in two other samples which are labeled *Bad Gastein 2A* and *Bad*

Gastein 2B in Table 4.6. As compared to earlier measurements with a conventional setup (see [399]), the sensitivity was enhanced by one order of magnitude by increasing the transmission from 31% to 65%. The uncertainty of the result is dominated by the statistical error. With a detection efficiency of 100% and an improved resolution, as is usually obtained with CLTDs (see Section 3.6.2.1), it will be possible to reduce this error even if an increase in sample material is not easily achievable.

4.3.3. Future perspectives

The first application of CLTDs in AMS demonstrated their great potential, in particular for AMS of actinides. With a detector array as discussed in Section 3.2.4, detection efficiencies close to 100% can be realized. In recent years, the interest in ^{236}U and other actinides has increased considerably [396,400]. ^{236}U can be used as an oceanic tracer to study the transport and mixing of different water streams [402]. During the era of atomic bomb tests, a considerable amount of ^{236}U was released into the atmosphere and distributed allover the world by global winds. As a consequence, the ^{236}U content of ocean water decreases with increasing depth. The content of ^{236}U can therefore be used to investigate global jet streams of deep ocean waters. A feasibility study, which was performed at the VERA laboratory by A. Sakaguchi et al. [403], demonstrated the potential of this new tracer method for oceanography and climate studies. In addition, the proliferation of radioactive material in the ocean after the Fukushima incident in Japan was investigated with AMS of ^{236}U [402]. Other heavy nuclides like ^{239}Pu, ^{240}Pu, ^{137}Cs or ^{241}Am are also of interest for such investigations [404,405]. In AMS of ^{239}Pu, ^{238}U was found to be a major source of background due to the same ionic charge exchange processes along the accelerator beamline which were already discussed as sources for background in the ^{236}U measurements in Section 4.3.2.1 [404]. Accordingly, the application of CLTDs has the potential to improve the sensitivity also for ^{239}Pu which is important to observe mitigation of plutonium in the environment, or to monitor its dispersal from nuclear facilities.

Several AMS facilities around the world, for example at Argonne, USA [406,407], Canberra, Australia [139], Caserta, Italy [138], Sevilla, Spain [140], Florence, Italy [137], Cologne, Germany [136,408], as well as Zurich, Switzerland [141], have joined their efforts to improve the detection efficiency for different uranium and plutonium isotopes (see also [409] and references therein). In parallel, AMS facilities develop towards smaller terminal voltages below 1 MV [401]. Several dedicated accelerators with a terminal voltage of 0.5 MV are already in operation [410]. A machine with a terminal voltage of 0.2 MV is under investigation at the ETH Zurich [410]. This means that the typical kinetic energies for heavy nuclides are of the order of $1-2$ MeV. Such low energies demand for new detection systems, because the overall efficiency of the facility is hampered severely by energy loss processes in thin foils of time-of-flight detectors or ionization chambers. In this case, CLTDs for ion energies below 0.05 MeV/u are needed. In addition, CLTDs hold a lot of potential for applications in the AMS community, because particularly for small facilities the installation of additional magnetic filter stages as presented in [411] is a less feasible option.

5. Perspectives for future applications of CLTDs in heavy ion physics

Whereas several applications of CLTDs in heavy ion physics, which provided already interesting physics results in some fields of heavy ion research, were presented in the previous section, there are a couple of potential future applications which will be discussed in the following section.

5.1. High-resolution nuclear spectroscopy

The investigation of direct reactions, such as elastic and inelastic scattering, few-nucleon transfer reactions, charge exchange reactions, etc., is a well known tool in nuclear physics to obtain information on nuclear structure [128,212,412]. In particular, inelastic scattering allows to study the nuclear multipole response to excitation. Here the investigation of low lying states whose characteristics reflects the deformation, transition densities, as well as the investigation of collective excitation modes in nuclei, including new collective modes and the isospin dependence of giant resonances, are of interest. In the recent past, such investigations performed with radioactive beams in inverse kinematics became of particular importance [128,412,413].

Heavy ion detectors, which detect the scattered particles or the reaction products after the nucleus–nucleus interaction, need to have sufficient energy resolution to separate elastic from inelastic reaction channels, or to identify specific reaction channels. The availability of high-quality heavy ion beams, cooled in storage rings to highest phase space densities with a relative energy spread as good as $\Delta E/E \leq 10^{-4} - 10^{-6}$, and of high resolution detectors opens new possibilities in that field. Here the application of CLTDs may in the future improve the performance of such experiments.

As an example, a scattering experiment [153,218,228], performed with a relativistic heavy ion beam from the SIS18 synchrotron at GSI, representing the first application of a cryogenic detector in nuclear structure physics, will be discussed. The excitation of the giant resonance, which is a collective vibrational mode of nucleons in nuclei [414–416], was investigated for the lead nucleus by separating inelastically from elastically scattered ions in the spectrum for the scattering of 100 MeV/u ^{20}Ne ions from a lead target. Since a beam particle which has excited a giant resonance in a target nucleus essentially loses an amount of kinetic energy corresponding to the excitation energy, the excitation of the resonance can be detected in the total energy spectrum of the scattered ^{20}Ne projectiles. At relativistic energies, a

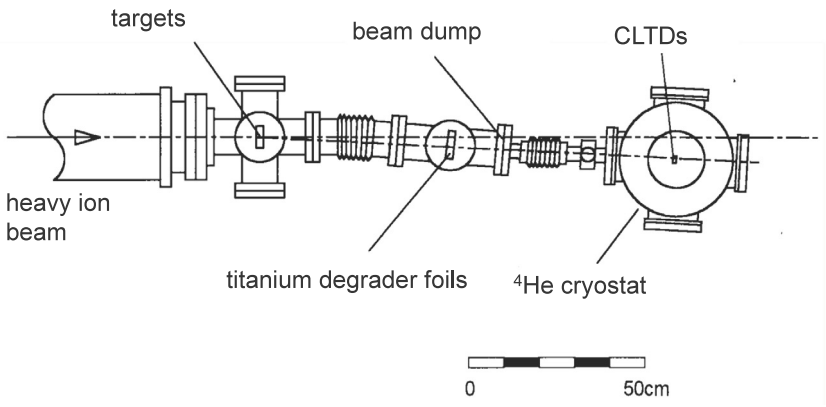

Fig. 5.1. Experimental setup for the investigation of giant resonances with CLTDs [218].

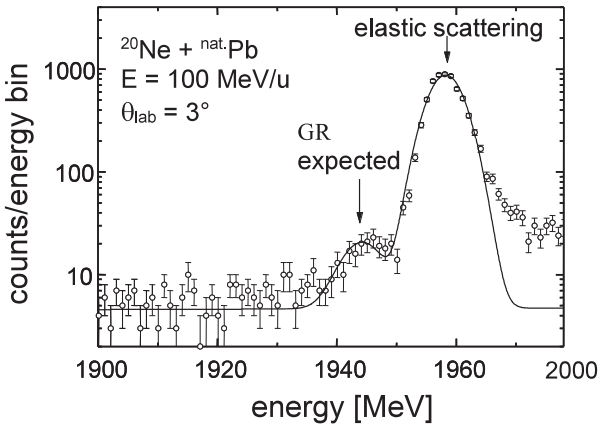

Fig. 5.2. Energy spectrum obtained with an aluminum TES calorimeter for scattering of a 100 MeV/u ^{20}Ne beam from a lead target. The bump due to the excitation of the giant resonance in lead is indicated by the label *GR*. The solid line represents the result of Gaussian fits to the data.
Source: Reprinted from [15] with kind permission of Springer.

relatively high excitation probability for giant resonances is expected for Coulomb excitation at peripheral collisions [414–416]. Theoretical predictions [153,218,228,417] indicate that modes predominantly excited in this system are the isovector giant dipole resonance, the isoscalar giant quadrupole resonance, and the isoscalar giant monopole resonance. It turns out that at a scattering angle of $\theta_{lab} = 3°$ the giant dipole resonance dominates, with small contributions of the other two modes. At this angle, the ratio of the cross section for the excitation of the giant resonance σ_{GR} to the cross section for elastic scattering σ_{el} was calculated to be $\sigma_{GR}/\sigma_{el} = 1.4\%$ with a mean excitation energy of $E^{\star} = 13.1$ MeV (see Table 5.1).

In Fig. 5.1 the relatively simple experimental setup for the present investigations is displayed (for details see [218]). A 100 MeV/u ^{20}Ne beam, extracted from the SIS18 synchrotron, hits a natural (not isotopically enriched) Pb target of 50 mg/cm^2 thickness. The cryostat housing the CLTD was installed on a movable platform and connected to the scattering chamber by two bellows, which allowed to adjust the scattering angle in the angular range of $0° < \theta_{lab} < 5°$. A 90 mg/cm^2 titanium degrader foil, which could be moved in the beam, was used for an energy calibration by a measurement with and without degrader foil. The unscattered beam was stopped in a beam dump mounted between the degrader foil and the cryostat. In order to detect the relativistic ^{20}Ne ions (total energy up to 2000 MeV) a CLTD with an Al-TES thermometer glued on a cylindrical sapphire absorber with 1 mm diameter and 5 mm length was used (see Section 3.2.3.1).

In Fig. 5.2 the energy spectrum measured for ^{20}Ne ions, scattered from a lead target (50 mg/cm^2) at a scattering angle of $\theta_{lab} = 3°$, is displayed. The energy resolution obtained for the elastic peak amounts to $\Delta E = 6.9$ MeV, which is close to the energy resolution of $\Delta E = 6.3$ MeV deduced for a measurement with direct beam [153] (see also Section 3.6.2), which means that contributions to the energy broadening due to the scattering geometry, energy straggling in the target, target inhomogeneity, etc. are of minor importance. Below the elastic peak, a bump appears which is attributed to the excitation of the giant dipole resonance in the lead nuclei. The shoulder at the high energy side of the spectrum is most probably due to pile up, as the relative strength of this shoulder varied with the beam intensity. The positions and the intensities of the two peaks were extracted by Gaussian fits. The excitation probability and the excitation energy as deduced from

Table 5.1
The results of the giant resonance experiment are compared with theoretical predictions [228].

	Experiment	Theoretical prediction
Excitation probability [%]	1.7(0.3)	1.4
Excitation energy [MeV]	14.0(1.2)	13.1
Width [MeV]	7.8(1.2)	5–6

the fits are compared with theoretical predictions in Table 5.1. Both experimental values agree well within errors with the theoretical predictions.

It should be pointed out that similar experiments in future, performed with high quality beams, cooled in storage rings to highest phase space densities with a relative energy spread as good as $\Delta E/E \leq 10^{-4} - 10^{-6}$ [231], and then extracted for experiments, would even improve the quality of such experiments with respect to the energy resolution, as we assume that the energy resolution obtained in the prototype experiment with a ^{20}Ne beam (discussed above) was limited by the energy width of the incident beam [218], and that the full potential of the intrinsic energy resolution of the CLTD (which can be of the order of 1×10^{-3} (see Section 3.6.2) [228]) was not yet exploited.

On the basis of the present results, possible future applications include investigations of giant resonances with stable and radioactive beams of heavy ions. In contrast to standard inclusive detection techniques which require high resolution spectrometers [418] and to exclusive detection techniques [413,416,419], where the giant resonance is excited in the projectile, and thus all decay products of the giant resonance have to be detected for a missing mass reconstruction for measuring all decay channels with sufficient accuracy, requiring a rather extended and complicated experimental setup, the present method allows a relatively simple setup, but requires high energy resolution.

For the future it is planned to continue such investigations. Of particular interest are the excitation of single giant resonances of different multipolarities, the excitation of higher order collective modes, so-called multi-phonon giant resonances [413,416], and new excitation modes, that may allow access to the parameters of the equation of state of nuclear matter. It should be pointed out that for giant resonance studies on radioactive nuclei using the present method, due to the fact that nuclei in which a giant resonance is excited are not particle stable, targets of radioactive nuclei at rest need to be bombarded by stable nuclei. Recent developments on the production of radioactive nuclei stored in traps [420] may allow such investigations in future.

Concerning investigations on heavy ion reactions at energies near the Coulomb barrier the excellent energy resolution of CLTDs will allow to resolve and separate elastic from inelastic reaction channels and/or to identify specific reaction channels with level spacings down to $\geq 100 - 200$ keV, representing the regime of very low excited states. Examples for various experimental studies planned for the future in this field can be found in [128,130].

5.2. In-flight mass identification of heavy ions

The direct in-flight mass identification of ions, atoms, molecules, and other species is an important task for many fields of physics. In particular, the in-flight mass determination of nuclides produced in heavy-ion induced reactions is required in many fields of heavy ion physics, and is in many cases mandatory for a unique identification of rare isotopes and an unambiguous interpretation of experimental data. As the required relative mass resolution for resolving neighboring masses scales with the nuclear mass m according to $1/m$, such a task turns out to be most challenging for the heaviest particle-stable nuclides under investigation.

5.2.1. Detection scheme

Well established methods [421] for the in-flight mass identification are the $B\rho/ToF$ method and the E/ToF method, the latter one being in the focus of the present investigations. Whereas the $B\rho/ToF$ method, where an isotope mass $m = p/v$ is determined by a magnetic rigidity ($B\rho$) measurement of the momentum p and a time-of-flight (ToF) measurement of the velocity v, requires, especially for high energy ions, a big magnet spectrometer, and suffers (in some cases) from limitations due to a relatively small solid angle, a small dynamic range, and, in particular for slow, not fully stripped heavy ions, ionic charge state (q) ambiguities (because $B \cdot \rho = p/q$), the E/ToF method is principally free of such limitations.

The detection principle of the E/ToF method is illustrated in Fig. 5.3. Here, the mass of an isotope $m = 2E/v^2$ is determined by its kinetic energy E and its velocity v, measured again via ToF. Principally there exists also the option to obtain a ToF Stop signal from the energy detector, and therefore to skip the stop detector in the present scheme. In measurements with conventional energy detectors this option is often realized, however, for the present investigations with CLTDs this option was presently not realized because of the relatively long rise times of the CLTDs used here.

For the non-relativistic approach the mass resolution for the E/ToF detection scheme is given by the relation

$$\Delta m/m = \left[(\Delta E/E)^2 + (2\,\Delta t/t)^2\right]^{1/2} \tag{5.1}$$

It is obvious from this relation that the separation of the heaviest nuclides ($M \approx 300\,u$) will require a relative ToF resolution of at least $1 - 2 \times 10^{-3}$, and a relative energy resolution of at least $2 - 3 \times 10^{-3}$ or less, and even better

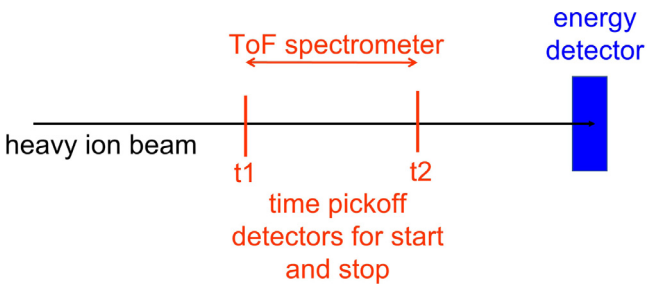

Fig. 5.3. Detection scheme for the in-flight mass determination of heavy ions by the E/ToF method: The velocity v is determined by measuring the flight time (ToF) between a start (t_1) and a stop (t_2) detector. The kinetic energy E is determined by an energy detector.

Table 5.2
Experimental results for the mass resolution (marked in red) obtained in various experimental investigations with the ToF/CLTD method, including all other relevant parameters. Please note that the experimental setups were in some cases not optimized for obtaining the best mass resolution.

Incident ion	Incident energy	Flight path	Energy resolution		Time resolution		Mass resolution		Limiting factor	Reference
			ΔE	$\Delta E/E$	Δt	$\Delta t/t$	Δm	$\Delta m/m$		
	[MeV/u]	[m]	[MeV]	$\times 10^{-3}$	[ps]	10^{-3}	[amu]	$\times 10^{-3}$		
^{63,65}Cu	0.8	1.2	0.33	6.9	680	6.6	0.9	14	ToF res.	[155]
^{63,65}Cu	0.8	1.2	0.30(2)	6.0(4)	560(56)	5.4(5)	0.80(8)	13(1)	ToF res.	[184]
^{131}Xe	0.82–0.88	0.88	0.68	6.6	140	1.4	0.94(5)	7.2(4)	E res.	[184]
^{206,208}Pb	≈0.08	1.52	0.166(5)	9.8(3)	535	1.4	2.43(4)	11.0(2)	E res.	[15,164,430]
^{209}Bi	4.7	2.0	7.33(3)	7.5(1)	205(12)	3.4(2)	1.8(1)	8.6(5)	ToF res.	[164]
^{238}U	0.23–0.63	1.06	0.31	3.5	250	2.0	1.28(4)	5.0(2)	ToF res.	[155,184]

for the case of mass identification of very rare isotopes with a large abundance difference with respect to neighboring isotopes. Whereas the determination of the ion velocity with the required relative resolution is possible with standard ToF techniques [209,399] by using fast channel plate detectors and applying, especially for the case of very slow heavy ions, ultra-thin carbon foils [422] to keep energy-loss straggling on a tolerable level, the required relative energy resolution is the crucial point of this method.

The application of conventional ionization-based heavy ion detectors for this detection scheme has, due to the intrinsic limitations of such detectors (see Section 2.5) which suffer from incomplete energy detection due to charge recombination, resulting in pulse height defects and a non-linear energy response, and a relatively poor energy resolution for very heavy ions, therefore shown only satisfactory results for the mass resolution for light masses ($m \leq 90$) [291,423–428]. This problem can be overcome by replacing conventional detectors by CLTDs for the energy detection, which, due to their excellent energy resolution and energy linearity because of the absence of a pulse height defect (see Section 3.6.2), and their radiation hardness, may in future be favorably used for such purposes.

5.2.2. Mass resolution for the ToF/CLTD method

There have been a number of attempts to determine the performance of ToF/CLTD systems with respect to the mass resolution. Some selected examples will be discussed in the following. It should be pointed out that the results presented here were obtained as by-products of measurements with a different focus (see also Section 4.2.2) and therefore, the experimental setups used were in some cases not optimized for obtaining the best possible mass resolution.

For all measurements presented in this section, CLTD detectors on the basis of sapphire absorbers and Al phase-transition thermometers were used (for details see Section 3.2.3). Several versions of start and stop time pickoff detectors have been used, all working with the same non destructive operation principle [184,208,209,372,378,399,429]: Secondary electrons which are produced during the passage of heavy ions through a thin carbon foil are deflected by a 45° electrostatic mirror, and focused on a fast electron detector, consisting of two micro channel plates in "*Chevron configuration*" (for details see [209,378]). This ToF setup allows a transition-type velocity measurement with low influence on the heavy ion energy. Relatively short flight paths of $1 - 2$ m were chosen for the present investigations, and thin to ultra-thin carbon foils with $0.6 - 10\,\mu g/cm^2$ thickness were used, ensuring that the energy straggling of the heavy ions in the carbon foils was in all cases negligible as compared to the energy resolution of the CLTDs. With these setups time resolutions of the order of $140 - 680$ ps, dependent on the individual experimental conditions, were obtained (see Table 5.2). The flight paths (distance between start and stop detector) were chosen in the present investigations relatively short, and could be in future increased for optimizing the mass resolution.

Results from different measurements concerning the mass resolution obtained with a ToF/CLTD setup for different incident ions and different incident energies are summarized in Table 5.2. For a measurement with the relatively light ^{63}Cu and ^{65}Cu ions a 0.8 MeV/u beam from the MP tandem accelerator at the MPI Heidelberg was used [155,184]. This has the advantage that the energy resolution was not affected by the energy width of the incident beam, which was

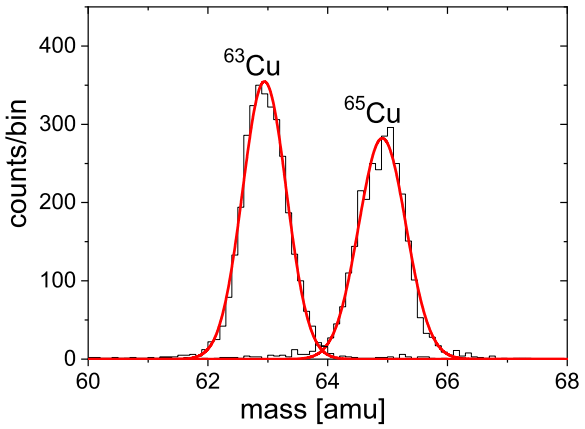

Fig. 5.4. Mass spectrum determined with a ToF/CLTD setup for a 50 MeV ^{63,65}Cu beam. The mass resolution is $\Delta m(FWHM) = 0.80(8)$ amu.
Source: Adapted from [155].

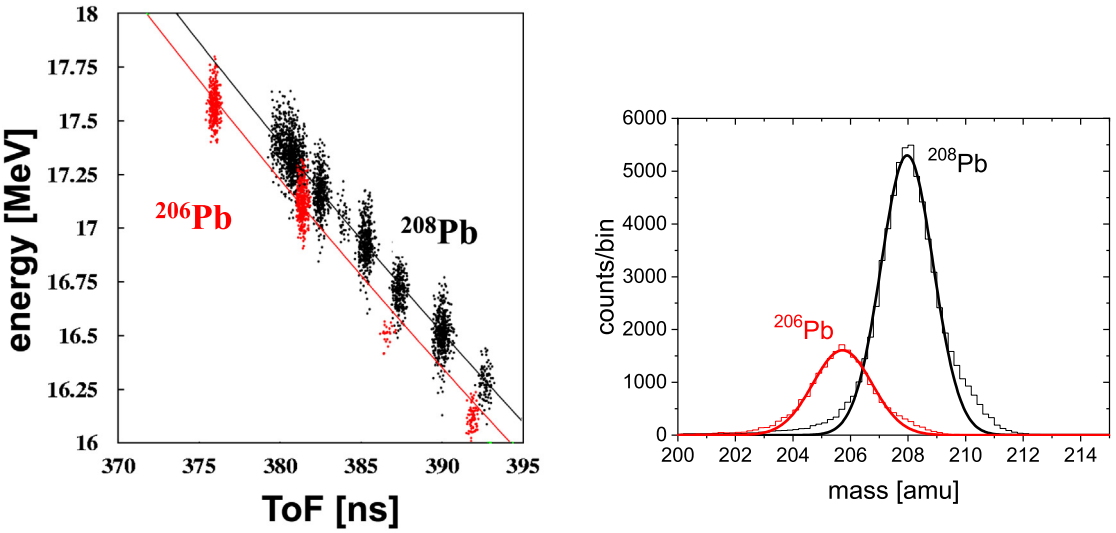

Fig. 5.5. Results of a test experiment for isotope identification by a combined ToF/CLTD measurement for the isotopes ^{206}Pb and ^{208}Pb at several energies around 0.08 MeV/u. The ToF/energy correlation is plotted on the left-hand side. The solid lines represent fits to the data according to the expected kinematic correlation. The corresponding mass spectrum is displayed on the right-hand side. A mass resolution of $\Delta m = 2.43(4)$ amu is achieved.
Source: Adapted from [15].

estimated to be of the order of $\Delta E/E \leq 5 \times 10^{-4}$ [184]. The result is displayed in Fig. 5.4. Well separated peaks are obtained for ^{63,65}Cu, and a mass resolution of $\Delta m(\text{FWHM}) = 0.80(8)$ amu is obtained, in this case still limited by the time resolution. A first attempt with heavier ions was performed [164,430] during a measurement at the VERA facility at Vienna, Austria. Here, a mass resolution of $\Delta m(\text{FWHM}) = 2.43(4)$ amu was obtained with not optimized CLTDs for ^{206,208}Pb ions with a relatively small incident energy of around 0.08 MeV/u (see Fig. 5.5). Even better results were more recently obtained with the experimental setups displayed in Fig. 4.33 as a by-product of experiments on stopping power measurements (see Section 4.2) with mass resolutions of $\Delta m(\text{FWHM}) = 0.94(5)$ amu for $0.82 - 0.88$ MeV/u ^{131}Xe ions, and of $\Delta m(\text{FWHM}) = 1.28(4)$ amu for $0.23 - 0.63$ MeV/u ^{238}U ions [155,184] (see Fig. 5.6).

Having in mind that also in these cases the full potential on the energy resolution of the CLTDs was not realized, these results represent already a substantial improvement for the mass resolution of ToF/E setups, not reachable for such heavy ions with conventional energy detectors, and therefore bear a large potential for future investigations in heavy ion physics.

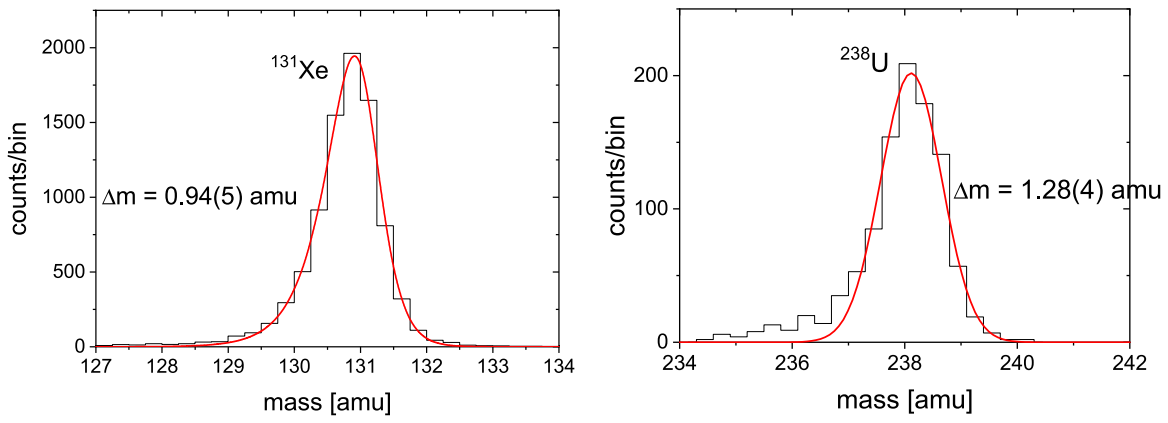

Fig. 5.6. The mass spectrum as derived from a ToF/CLTD measurement for ^{131}Xe ions in an energy interval of 0.82 − 0.88 MeV/u is displayed on the left-hand side. On the right-hand side, the mass spectrum for ^{238}U ions in an energy interval of 0.23 − 0.63 MeV, again derived from a ToF/CLTD measurement, is displayed. The mass resolution corresponds to $\Delta m = 0.94(5)$ amu for ^{131}Xe, and to $\Delta m = 1.28(4)$ amu for ^{238}U, respectively.
Source: Adapted from [184].

5.2.3. Identification of superheavy elements

5.2.3.1. Motivation

The search for new chemical elements has been a driving force for nuclear physics since the days of Marie and Pierre Curie (see [431]). When the *GSI Helmholtzzentrum für Schwerionenforschung*, Darmstadt, Germany, was founded, the search for new elements was a central focus of its research program. A detailed recollection of the very successful story that followed is given by G. Münzenberg in [432]. One successful production process of the socalled *superheavy elements* is the process of *cold fusion* where a projectile of mass around 60 collides with atoms of a heavy target. The collision energy is chosen such that fusion of the two nuclei is just barely possible. As a result, the compound nucleus which is formed has only a very moderate excitation energy and thus a large survival probability. To separate the scarce reaction products from the main ion beam and other background, the mass separator **S**eparator for **H**eavy **I**on reaction **P**roducts (SHIP) [433–436] was commissioned at GSI in 1975. In its now almost fifty years of operation, SHIP has produced a rich spectrum of physics results. The highlight is certainly the first production of the elements with $Z = 107$ to $Z = 112$. The elements *hassium* ($Z = 108$) and *darmstadtium* ($Z = 110$) honor the place of their discovery. The story of superheavy elements is also written at the GARIS separator at RIKEN [437], where $Z = 113$ was discovered, and at the JINR Dubna [438] in Russia with the discovery of $Z = 114-118$ in cooperation with the LLNL, Livermore, USA and the ORNL, Oakridge, USA, produced by the alternative process of *hot fusion* with an actinide target. Recently, also the IMP at Lanzhou, China [439] has started its superheavy research program. The search for superheavy elements is also part of the long-term research program at GSI and FAIR within the NUSTAR program [130,440]. Preparations for the construction of a dedicated accelerator only for superheavy element research are currently underway [441,442]. In 2008, the gas-filled separator **T**rans**A**ctinide **S**eparator and **C**hemistry **A**pparatus (TASCA) was commissioned at GSI [443]. In addition to producing superheavy elements, TASCA uses a gas-filled separation cell to extract the very rare reaction products and to study their chemistry [444,445]. An overview on the status and the perspectives of the research on superheavy elements is given in [446].

Superheavy elements are very rare species with relatively short half lives. For example, the detection rate at SHIP dropped from several per week to a few per month when going from $Z = 108$ to $Z = 112$, despite continuous improvements in accelerator as well as target technologies. Accordingly, the unambiguous identification of a specific nuclide is a demanding but mandatory task. Nuclear structure supports this quest: In the high-Z region, many elements usually decay by $\alpha-$decay which means they emit α-particles with well defined energies and decay constants. The identification of the original nuclide is possible when *climbing up the ladder*, i.e. following the successive $\alpha-$decays from a well-known end up to its beginning [436]. A combination of position-sensitive silicon detectors is used to uniquely assign each $\alpha-$decay chain to the original nuclide. The excellent energy resolution for α-particles in addition to the determination of the decay time allows for the unambiguous identification of each decay chain. However, for higher Z ($Z \geq 112$) and neutron-rich isotopes, the reaction product itself or one of its daughters has a large probability to undergo spontaneous fission [438,443,447] before ending in an α-decay chain with well known $\alpha-$decay signature. In this case, the identification method of the produced isotope used for $Z \leq 112$ is not applicable. Instead, the identification relies on the measurement of excitation functions and $\alpha-$decay chains in combination with nuclear structure calculations, which may be prone to systematic uncertainties. To overcome this problem, it was proposed [15,23] to use a combined ToF/energy measurement, which directly measures the mass of the produced nuclide or of its fission products. In addition, the precise energy of the superheavy nuclide and the half life of potentially occurring $\alpha-$decays should be measured simultaneously. The excellent energy resolution in combination with a good mass resolution and energy linearity makes CLTDs a well-suited tool for the identification of superheavy elements [15]. However, the very rare reaction products demand for detector arrays with large solid angle to achieve a sufficiently large detection efficiency.

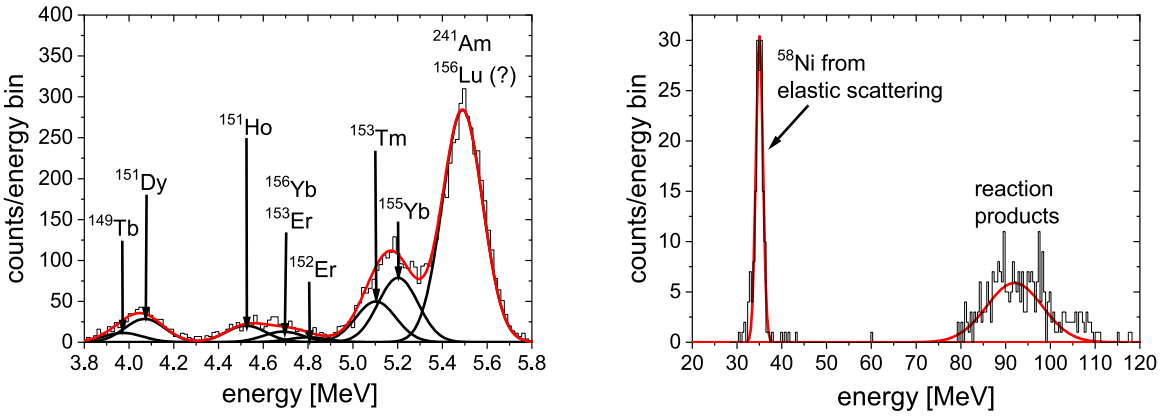

Fig. 5.7. The panel on the left-hand side displays an example of a recorded $\alpha-$spectrum. ^{241}Am is the calibration source. The panel on the right-hand side displays the corresponding energy spectrum of the reaction products. Elastically scattered ^{58}Ni projectiles were also detected. For the heavy ions (right-hand side), the width of the peaks is determined by the velocity acceptance of SHIP, as well as by the kinematics of the nuclear reaction.

5.2.3.2. First feasibility study at SHIP

Experimental setup:

The experimental setup of SHIP for the production and identification of superheavy elements is described in detail in [432,436]: The ion beam from the UNILAC accelerator with an energy of around 100 MeV hits the rotating target wheel where the fusion reactions take place. After being focused by a quadrupole triplet, the produced superheavy elements, as well as the incident ion beam and other (unwanted) reaction products pass through the first filter stage of combined electric and magnetic fields. At the intermediate horizontal focus, the primary beam is separated into a beam dump, while the reaction products pass on to the second filter stage. The second quadrupole triplet focuses the reaction products onto the silicon detectors where they are implanted with their full energy. The last dipole magnet, as well as a short time-of-flight path were added to suppress scattered projectiles. SHIP has a velocity acceptance of $\Delta v/v = 5\%$ and an ionic charge acceptance of $\Delta q/q = 10\%$. The central silicon detector has an active area of $3 \times 8\,\mathrm{cm}^2$ and a position resolution of 150 µm. Four additional silicon detectors detect α-particles which might have escaped from the central detector. The main detector measures the position and time of the heavy ion as well as of the consecutive $\alpha-$decays. If the position of the $\alpha-$decays coincides with the position of the heavy ion, they are assigned to the same $\alpha-$decay chain.

In the present feasibility study,[19] the silicon detector chamber was replaced by a cryostat which housed a single CLTD of $3 \times 3 \times 0.33\,\mathrm{mm}^3$ (for details see [164]). As a test case, a reaction with a rather high reaction cross section was chosen:

$$^{58}\mathrm{Ni} + ^{102}\mathrm{Ru} \rightarrow ^{160}\mathrm{Hf}^{\star},\ Q = 104\,\mathrm{MeV} \tag{5.2}$$

The Ni ions had an incident energy of 4.7 MeV/u. Dependent on the incident energy, the reaction product hafnium evaporates 2−4 protons and up to 8 neutrons with a rather broad mass distribution. The distribution of the kinetic energies is determined by the velocity acceptance of SHIP, as well as by the kinematics of the nuclear reaction. Several of the produced nuclides undergo α-decay. Due to technical reasons in this first feasibility study, the time-of-flight measurement was not integrated into the data acquisition. The goal was to demonstrate that a simultaneous detection of the heavy reaction product and its $\alpha-$decay(s) is possible. The reaction products have a kinetic energy of around 93 MeV, and the α-particles have energies between 3 and 6 MeV (see Fig. 5.7). The dynamic range of the CLTD is sufficiently large to detect both ion species. However, to realize a good energy resolution for the α-particles, as well as for the heavy ions, the detector signal was split and fed into two different main amplifiers (Emetron Shaping Amplifiers, see Section 3.3) with different amplification factors. The time correlation between the events was realized by using a time signal from a frequency generator with a frequency of 160 kHz [164]. The signals of the main amplifiers were fed into the data acquisition system of SHIP [436].

Results:

The left-hand side of Fig. 5.7 displays an example spectrum of the $\alpha-$decays. ^{241}Am is the calibration source. The main contributions of the different reaction and decay products could be identified. The overlapping peaks were deconvoluted by keeping the FWHM fixed and using the literature value of the α-energy. Only the amplitudes of the Gaussians were fitted. Although within rather large error bars, we can state that with the present experimental settings no ^{152}Er and very little ^{153}Er is produced. In contrast, the production cross sections of ^{156}Yb and ^{153}Tm are much larger than predicted.

[19] Performed in cooperation with D. Ackermann, F. Hessberger, S. Hofmann and G. Münzenberg (GSI Darmstadt).

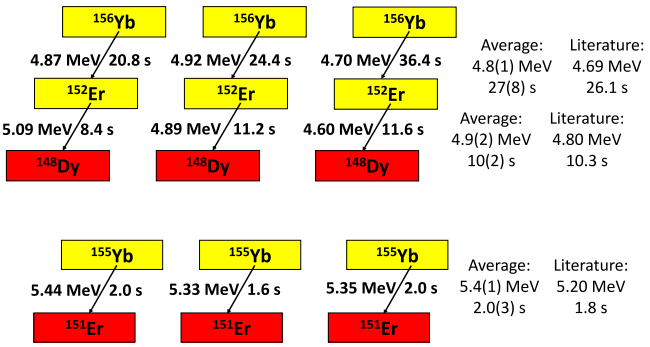

Fig. 5.8. Examples of $\alpha-$decay chains, which were identified in the present feasibility study with CLTDs. The related α-energies and decay times displayed were extracted from the experimental data by using a dedicated software which was used in experiments on superheavy element production [436]. The literature values for the $\alpha-$energies and the half lives are well reproduced. [164].

The small contribution of ^{152}Er can be completely attributed to the decay of ^{156}Yb. On the right-hand side of Fig. 5.7, the corresponding spectrum of the reaction products is displayed. The peak of ^{58}Ni is the result of elastic scattering processes of projectiles. Its width of $\Delta E/E = 5.1(2)\%$ is determined by the velocity acceptance of SHIP. The peak of the reaction products is considerable wider, because the decay processes and emission of nucleons during the flight through the velocity filter broaden the energy distribution.

The main goal of the experiment was to demonstrate that a unique identification of reaction products via the correlated detection of α-decay chains under realistic experimental conditions is possible when using a CLTD as energy detector. For this purpose, the data were analyzed with a dedicated software which is used to identify $\alpha-$decay chains in experiments on superheavy elements [436]. Fig. 5.8 shows examples for different $\alpha-$decay chains that were identified with this method from the present data. The literature values for energy and half life are well reproduced. This example demonstrates that the dynamic range of the CLTDs is in principle large enough to detect $\alpha-$decay chains and the emitting mother nuclide simultaneously and time-resolved. With the best obtained energy resolution for α-particles and the excellent performance for direct mass determination (see Section 5.2), CLTDs bare the potential to provide both, the $\alpha-$decay chains, and the direct mass of the reaction products. In particular, the mass of nuclides which undergo spontaneous fission can also be determined. The main challenge remains to realize detector arrays which provide sufficient detector solid angle to cover the full focal plane of SHIP of $30 \times 80\,\mathrm{mm}^2$, or of other SHE separators. The recent construction and successful application of a detector array with an active area of $15 \times 15\,\mathrm{mm}^2$ (see Section 3.2.4) paved the way for solving this problem, having in mind that the design allows for the construction of even larger arrays with the same concept.

5.2.4. Application for reaction studies with radioactive beams in inverse kinematics

5.2.4.1. Motivation

The investigation of nuclear reactions with isotopic clean radioactive beams is an important tool for addressing many questions of high interest in nuclear physics and nuclear astrophysics, such as for example the isospin dependence of nuclear structure, the mechanisms of nucleosynthesis in the universe, etc. (see for example [128–130,212,412,448]). It allows, among others, to study the structure of very short lived nuclei which are not available as targets. Such investigations are presently performed, or will in future be performed, at various laboratories world wide with radioactive beam facilities existing, under construction, or planned, such as GSI/FAIR [124,128–130], GANIL [125], Argonne National Lab. [126], RIKEN [127], RIB [449], FRIB [131], HIAF [132], RAON [133], etc., with the aim to produce and use radioactive beams of highest quality and intensity, reaching as far as possible outside the valley of stability (see also Sections 1 and 3.1).

Typically, reaction studies with radioactive beams are performed in inverse kinematics, as illustrated in Fig. 5.9. That means that the radioactive beam is interacting with a stable target, and as many as possible reaction products are detected and identified with the highest possible resolution. For an overview on this research field, the reader may be referred to the **Nu**clear **St**ructure, **A**strophysics and **R**eactions (NUSTAR) project [448,450,451], and to selected review articles and white papers [128,130,212,412]. Among others, an important ingredient of such investigations is the direct in-flight mass determination of the reaction products, which is in many cases mandatory for a unique identification of the reaction products, and for an unambiguous interpretation of the experimental data. Here the application of the ToF/CLTD method (see Sections 5.2.1 and 5.2.2) provides advantages as compared to standard conventional detection schemes, and may become in future an alternative tool. In the following some selected examples are discussed.

5.2.4.2. Direct mass identification of reaction products after in-flight $\gamma-$spectroscopy

For present and future investigations concerning the in-flight γ-spectroscopy with radioactive beams, the E/ToF technique is frequently used. Examples are experiments of the RISING-, PRESPEC-, HISPEC- and DESPEC- projects [424,452], the latter ones being part of the future activities of NUSTAR@FAIR [440,450,451] in the **L**ow **E**nergy **B**ranch (LEB) (see

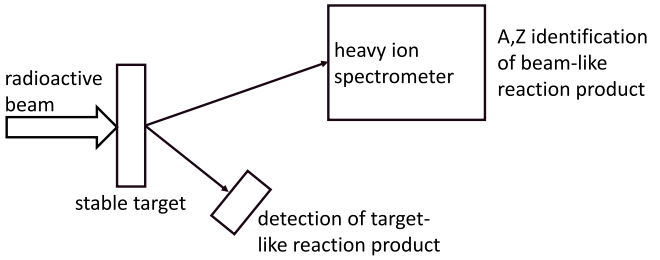

Fig. 5.9. Sketch of a typical experimental setup for the investigation of heavy-ion induced direct reactions with radioactive beams in inverse kinematics. For the identification of the beam-like reaction products, high-resolution CLTDs may favorably be used.
Source: Adapted from [15].

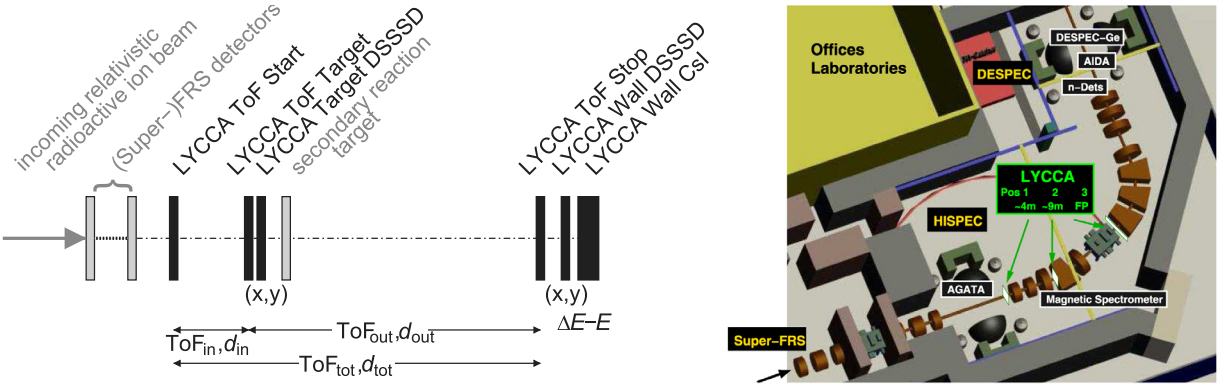

Fig. 5.10. Left-hand side: Sketch of the detection concept of LYCCA. LYCCA-related items are drawn in black (for details, see [426]). Right-hand side: Proposed basic layout of the NuSTAR Low-Energy Branch (LEB) (for details see [453]).

Fig. 5.10, right-hand side). Here, the **L**und-**Y**ork-**C**ologne **CA**lorimeter (LYCCA) detector setup [425,426,453] is foreseen to identify the projectile-like reaction products (see Fig. 5.10, left-hand side). With conventional CsI(Tl) detectors, presently used for the energy determination and for the Stop-ToF signals, a satisfactory mass determination is in many cases limited to the mass range $m \leq 90$ [424–426]. The application of appropriate CLTDs as energy detectors could increase the mass range up to highest masses ($m \sim 250$), and could avoid the application of magnetic spectrometers for the mass determination which are sometimes limited by the small detection efficiency due to small solid angle acceptance, the small dynamic range, and in the case of slow heavy ions by ionic charge state ambiguities. With an improved rise-time behavior, to be developed in future, CLTDs could also serve as STOP detectors for the ToF measurement.

5.2.4.3. Direct mass identification of reaction products from direct reactions

The investigation of direct reactions with radioactive beams is one of the most important tools of nuclear structure- and astrophysics [128,212,412,450], and is therefore a topic in the research program of all radioactive beam facilities existing or planned world wide. A typical scheme for an experimental setup is displayed in Fig. 5.9. A radioactive beam is hitting a stable target, and the target-like and projectile-like reaction products are detected and identified, in the most cases in a kinematically complete way. For the case of NUSTAR@FAIR direct reaction studies are foreseen for basically all parts of the NUSTAR setup [448,450,451]. Whereas in many cases large solid angle magnetic spectrometers are used for the detection and identification of the beam-like reaction products (typical examples are the R3B setup at FAIR [130] and the SAMURAI-setup at RIKEN [127]), alternative techniques like the E/ToF method and others may be better used due to the individual experimental conditions (space limitations, optimization of the detection efficiency, the need for a high dynamic range for a simultaneous measurement, for avoiding ionic charge state ambiguities for slow heavy ions).

Here, again the application of CLTDs for the ToF/CLTD method may provide in future, as compared to conventional detection schemes, an improved performance for the mass determination of heavy ions with masses $m > 90$.

5.2.5. Other applications of mass identification

5.2.5.1. Direct mass identification of fission fragments

The investigation of the characteristics of the fission process, namely the identification of fission fragments and the determination of their yields is an important tool for our understanding of the fission process, and also for more technical topics in reactor physics (see also Section 4.1.1).

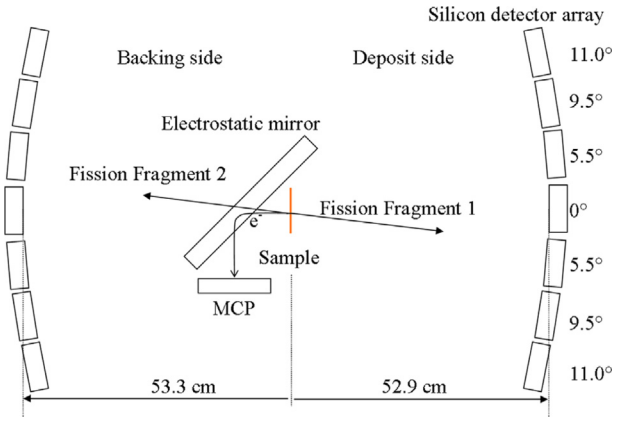

Fig. 5.11. Sketch of the VERDI setup including the central "Fission Electron Time-of-Flight"' start detector and the two energy detector spheres at the end of each ToF section (not to scale). Fragments can be detected by one of the silicon detector pairs, while the electrons, emitted by the target, are deflected by the electrostatic mirror into the direction of the micro channel plate detector.
Source: Reproduced from [455].

Mass identification of the fission fragments is either performed by a magnetic analysis (for example at the LOHENGRIN mass separator [274,275]), or by E/ToF techniques [427,428,454], both methods having advantages and disadvantages. A typical example for a spectrometer operating on the E/ToF principle, and thus superior in detection efficiency as compared to spectrometers using the magnetic analysis, is the "COSI FAN TUTTE" spectrometer [428,454], which was recently replaced by the "VERDI" spectrometer [455]. As an example the detection scheme of the VERDI spectrometer is displayed in Fig. 5.11. Whereas excellent performance is obtained in both cases for the mass resolution of light fragments ($\Delta m = 0.7$ amu for $m < 130$ for COSY FAN TUTTE, and $\Delta m/m = 0.023$ expected for lighter masses for VERDI [455]), the mass resolution is limited in both cases by the energy resolution of the energy detectors (ionization chambers or Si detectors) for the heavier masses [427,428,455]. The application of CLTDs as high resolution energy detectors for such spectrometers could improve the performance considerably for the investigation of heavy mass fragments.

5.2.5.2. Mass spectrometry of biomolecules

In many applications in biology and medicine, the mass identification of biomolecules is mandatory [117]. These molecules have masses of several thousand up to hundred thousand amu. Therefore, the energy-sensitive detection and identification of high-mass biomolecules represents an application which operates in a completely different regime of incident energy and detected mass, as compared to the applications discussed above. As is described, e.g., in [117], mass spectrometry of biomolecules is usually performed in the so-called *MALDI-ToF* setup. *MALDI* stands for **M**olecule **A**ssisted **L**aser **D**esorption **I**onization. This method uses a laser to ionize the large biomolecules without destroying them. An alternative method is electrospray ionization [117], but MALDI is used most frequently. The MALDI method is most efficient for producing molecular ions with one, two or at most a few charges. These ions are then guided through an accelerating voltage of several thousand volts. After acceleration, typical ion energies are in the range of 10 to 100 keV, which is much smaller than the MeV energies which were discussed before. This poses particular demands on the detector technology.

The second term in *MALDI*-**ToF** stands for **T**ime **o**f **F**light as already discussed in Section 5.2.1. However, the low kinetic energy of the ions does not permit the use of time-of-flight detectors as used in nuclear physics experiments, because the ions would not pass even the thinnest foils. Therefore, the energy detector must also serve as the stop detector which demands for a high time resolution. The start time is defined by the application of the laser pulse. As a consequence, MALDI-TOF is performed in a pulsed mode. For the ion detector, this poses two strong demands: Firstly, it has to be fast to provide a good time resolution for the time-of-flight and to provide a high rate capability. Secondly, it should have a large solid angle because there are usually no beam-focusing elements included in the setup. In conventional mass spectrometers for biomolecules, **M**ulti **C**hannel **P**late detector**s** (MCPs, see Section 5.2.2) are used. They are very fast detectors with a high rate capability and active detector areas of up to several square centimeters. However, they suffer from one disadvantage: Their detection efficiency strongly decreases for heavy masses above about 20 kDa (1 Da is equal to 1 proton mass), because the emission of electrons is no longer efficient [117]. In 1996, D. Twerenbold suggested cryogenic particle detectors as an alternative [114], because their detection principle is independent of charge creation and the detection efficiency should, therefore, not depend on the ion mass. To meet the criterion of a short rise time and a high rate capability, he proposed **S**uperconducting **T**unnel **J**unction**s** (STJs) as the most promising detector concept. STJs are no CLTDs in the strict sense. They consist of two superconducting thin films which are separated by an insulating barrier and kept in the superconducting state well below the transition temperature. When a biomolecule hits the upper superconducting layer, its kinetic energy breaks Cooper pairs and creates excess quasiparticles (electrons and hole-like

excitations). These quasiparticles tunnel through the insulating barrier and produce a small tunneling current which is proportional to the number of phonons created by the impact. Details of the operation principle of STJs can be found in [182]. First prototypes were presented at the 7th International Workshop on Low Temperature Detectors (LTD7) by D. Gerber et al. [456], S. E. Labov et al. [115] and G. C. Hilton et al. [116]. All groups demonstrated the feasibility of their detector concepts. In particular, three potential advantages were identified [117]:

- The mass-independent detection efficiency was already mentioned. In particular, the use of cryogenic detectors should extend the mass range of the MALDI-TOF mass spectrometry up to MDa and thus allow for the investigation of DNA, RNA or even viruses.
- MCPs are not energy-sensitive. They can only determine the flight time which depends on the velocity of the ions. The detection of the kinetic energy, which is possible with STJs, would allow resolving m/q ambiguities, i.e. distinguish a doubly charged ion of mass $2m$ from a singly charged ion of mass m.
- The detection mechanism of STJs works also for the impact of neutral molecules which may be created by fragmentation of the initial biomolecule after acceleration. Thus, STJs can be used to overcome the so-called *neutral loss*, and identify these neutral fragments, because due to their lower mass they carry less kinetic energy than the initial biomolecule.

However, one big disadvantage of all these proof-of-principle detectors was their relatively small detector size which ranged from 50 μm × 50 μm [456] to 200 μm × 200 μm [115]. Accordingly, M. Frank states in his review article [117] that STJs will most probably not replace MCPs in standard MALDI-TOF mass spectrometry, also because the cryogenic demands were challenging. However, he also states that STJs have the potential to investigate the systematic effects mentioned above. This was proven by G. Westmacott and coworkers in [457,458]. They used a STJ with an active area of 0.04 mm^2 to measure the efficiency of secondary electron emission of MCPs for masses up to 66 kDa and demonstrated the possibility to resolve different ions with the same mass-to-charge ratio.

Based on these promising results, R. Wenzel et al. presented the first commercially available MALDI-TOF mass spectrometry system with an array of 4 by 4 STJs and an active area of 1 mm^2 [459]. To facilitate its operation, the array is housed in a fully automated multistage sorption cryostat which does not need any liquid helium infrastructure. The authors demonstrated the detection of proteins with masses up to 2 MDa. They even pointed to a first potential clinical application, namely the investigation of a certain class of proteins which causes the so-called *von Willebrandt* disease. The detailed investigation of the mass distribution of the proteins in human blood could be a path to further investigate this rare disease. In the meanwhile, several applications of this commercial detection system can be found in the literature. For example, L. D. Plath et al. reported the investigation of the number of iron ions in the protein ferritin which is important for patients who suffer from anemia or iron deficiency [460]. D. M. Sipe et al., on the other hand, investigated MDa-sized nanoparticles of gold for medical applications, as well as different nanoparticles for quantum dots [461]. In this case, the determination of the mass helped to determine the size of the nanoparticles and its variation much faster than would be possible with an electron microscope. Aside from these applications in medical sciences, the group of M. Ohkubo et al. from AIST, Japan, has developed their own MALDI-TOF mass spectrometry system [462] and combined it with a tandem mass spectrometer to investigate post-source decay and the mass distribution of neutral molecules to overcome the *neutral losses* observed when using MCP detectors [463]. Next to providing important instrumental input for the use of MCPs, these investigations may also pave the way to new insights into the physics in interstellar clouds or combustion engines [464].

5.3. Decay energy spectroscopy

CLTDs were already applied for decay spectroscopy since the early nineties of the last century. An excellent review on the motivation, the various detection methods, and the results is presented in [22].

With respect to α-spectroscopy, the advantages of the application of CLTDs as compared to conventional detection techniques are:

- the excellent energy resolution which allows to separate α-lines for neighboring isotopes with a high discrimination power;
- the flexibility in the absorber material which allows to have the radioisotopes embedded in the absorber of a composite CLTD. Besides the low detection threshold and the higher detection efficiency (4π solid angle) this enables to measure the full energy released by a decay event, including the nuclear recoils, and without energy degradation due to entrance windows and dead layers of the detector. Therefore, direct Q-value measurements can be easily performed without the need for additional corrections, as well as the detection of very rare events, i.e. very low activity measurements due to an improved background suppression.

A variety of applications were proposed, and impressive results have already been obtained. They reach from nuclear physics (Q-value measurements [103,107,465]) to material analysis [110], radiopurity investigations on very rare contaminants [11,103,106,107,109,120,466,467], α-lifetime measurements [107,109], as well as forensic and environmental monitoring [111,468], and medical purposes [469] (see also [22] and references therein). Besides these topics, CLTDs were also developed and used for ion beam analysis [54] and Rutherford backscattering [470].

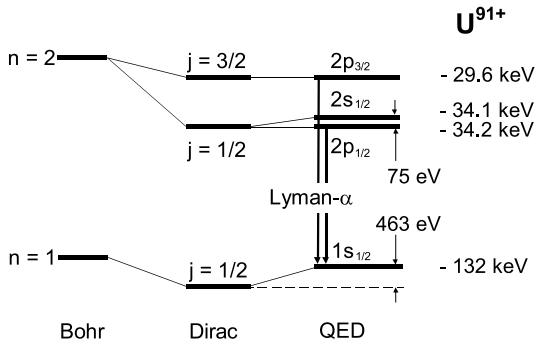

Fig. 6.1. Level scheme for hydrogen-like U^{91+} according to various atomic models. The numbers on the right indicate the electronic binding energies. The 1s Lamb shift is the deviation of the energy of the $1s_{1/2}$ level from the Dirac prediction. For U^{91+}, it amounts to about 463 eV.
Source: Adapted from [15].

Decay energy spectroscopy with CLTDs with respect to x-ray and γ-ray spectroscopy plays also an important role [19,22,60,103,105,108,112,113,115,119,466,469,471]. This subject is briefly discussed in Section 6.

An extensive discussion of the very rich field of β-spectroscopy including neutrino-mass experiments (neutrino-less double β-decay, beta endpoint measurements), etc. would go by far beyond the scope of this article. Here the reader may be referred to some review articles covering this field [3,4,6,7,11,22,42,85–102].

6. CLTDs for high-resolution spectroscopy of hard x-rays and their application in atomic physics

High-resolution x-ray spectroscopy has been one of the driving moments for the development of CLTDs (see Section 1). A key focus hereby was the detection of *soft* x-rays in the energy range below 10 keV which is of prime importance for astrophysics [18–21,49,50,61–73]. It would go beyond the scope of this article to give even a short overview on the rich physics program that has been performed related to ground-based as well as space-borne astrophysics. For a recent overview on this topic, the reader may be referred to [4,19,21,22,67,70]. Instead, we will restrict the last section of this review to high-resolution x-ray spectroscopy for *hard* x-rays, focusing on research related to atomic heavy ion physics questions. This selection is adjusted to the present topic discussed, and does by no means neglect the excellent physics program that has been conducted in the other fields.

6.1. Motivation: tests of quantum electrodynamics in strong electromagnetic fields

Quantum **E**lectro**D**ynamics (QED) is by far the most stringently tested theory in physics. One of its effects is that it leads to a small deviation of the binding energies of the electrons from the values calculated by the relativistic Dirac theory, which is referred to as the *Lamb shift* [472] (see Fig. 6.1). Experimentally, the Lamb shift is determined by measuring the transition energies for electron transitions from the $2p$ to the $1s$ state. For hydrogen, the $2p - 1s$ transitions – commonly referred to as Lyman-α transitions – are known with a relative accuracy of 10^{-15} [473]. However, these transitions lie in the range of microwaves and are accessible with high-frequency laser spectroscopy. If hydrogen-like uranium is considered, the same transitions have a transition energy of around 100 keV and are, therefore, located in the x-ray regime. Whereas in hydrogen and other light systems the QED predictions were confirmed with high accuracy [473], and because higher order contributions are negligible there, the evaluation of QED for such heavy ions poses particular opportunities, because the perturbation variable $Z\alpha$ becomes of the order of one (α being the fine structure constant) [474]. Accordingly, the comparison between theory and experiment is of particular interest for such heavy, hydrogen-like ions. One particular focus has been the determination of the Lamb shift of the $1s$ state in hydrogen-like heavy ions, which is an effect of relativistic QED and offers a particularly sensitive test for theoretical predictions of QED in the domain of very strong electromagnetic fields of the heavy nucleus [168,474–478], especially for higher-order terms which increase strongly with higher Z. On the other hand, these investigations still fall behind the excellent accuracy obtained for hydrogen, both in theory [474] and, even more severely, in experiments [168,479–481]. The most precise measurement of the Lamb shift for heavy ions was performed for hydrogen-like uranium by A. Gumberidze et al. with a relative experimental accuracy of 1% [482]. A recent extensive survey on the status of theory and experiments for QED tests with highly charged ions has been given by P. Indelicato in [475]. According to this survey, experiments need to gain at least one order of magnitude in accuracy before the current state-of-the-art calculations, which meanwhile include second and higher order QED contributions, can be sensitively tested.

Hydrogen-like heavy ions have only one electron which offers the possibility to test QED in the most direct way. When more than one electron is involved, interactions between electrons come into play in addition. These interactions need to be included into the already complicated perturbation theory. At present, transition energies for two-electron and

three-electron systems, i.e. helium-like and lithium-like ions, can be calculated with high accuracy. These calculations demand for experimental data to scrutinize them, but for helium-like heavy ions, experimental data are scarce. Extensive studies have been performed by P. Beiersdorfer et al. only for uranium ions [479,480].

One of the limitations of experiments aiming for a precise determination of the Lamb shift in heavy ions by determining the center of gravity of the relevant x-ray transition energies is the limited energy resolution of germanium x-ray detectors on the one hand (the better the energy resolution the more precise is the determination of the center of gravity of a Gaussian line), and the limited detection efficiency of crystal spectrometers [211] on the other hand. The application of CLTDs for this purpose provides a good compromise between energy resolution and detection efficiency and was, therefore, proposed for measurements at EBIT facilities [483] and at heavy ion storage rings [148] (see next section).

6.2. Experimental conditions for the detection of hard x-rays: electron beam ion traps and heavy ion storage rings

The aforementioned QED experiments have become possible only after heavy ions in high ionic charge states became available in sufficient quantities under well controlled experimental conditions. In fact, the first **E**lectron **B**eam **I**on **T**rap (EBIT-I) [172] at the Lawrence Livermore National Laboratory (LLNL), USA [144], was primarily designed as an X-ray source for spectroscopy. In an EBIT, a highly focused beam of electrons is accelerated to high kinetic energies. It then interacts with axially trapped ions, thereby further ionizing them. The maximum ionic charge state which can be obtained depends, among other factors, on the maximum kinetic energy of the electrons. The EBIT-I at LLNL, and its successors EBIT-II and SuperEBIT have produced a wealth of data for astrophysics, atomic physics, nuclear fusion and other fields [172,484,485]. Thereby, the SuperEBIT has obtained highest charge states also for very heavy ions up to helium-like uranium [486]. The most precise determination of electron transition energies for lithium-like uranium was performed at the SuperEBIT by P. Beiersdorfer et al. with an accuracy of 5×10^{-5} [487]. Another example is the EBIT at the National Institute of Standards and Technologies (NIST), Gaithersburg, USA, which has focused its research on ions of medium Z [488].

However, if hydrogen-like heavy ions are considered, even the SuperEBIT can only provide very small quantities [489, 490]. Accordingly, experiments on hydrogen-like very heavy ions are currently mostly performed at heavy ion accelerators. Among them, heavy ion storage rings offer the unique possibility of accumulating and cooling the ions. In particular, the Experimental Storage Ring (ESR) [231,491] at the GSI, Darmstadt, Germany, is presently the only storage ring worldwide which provides all ions and charge states up to bare uranium in a wide energy range from 500 MeV/u down to about 4 MeV/u. To realize the high ionic charge states requested for hydrogen-like ions, e.g. U^{91+}, it is mandatory to accelerate moderately charged ions to energies of up to 560 MeV/u. When the ions pass through a stripper foil, they loose most or all of their electrons. After injection, the highly charged ions need to be decelerated in the storage ring to the lowest energies for reducing experimental uncertainties due to the Doppler shift. Furthermore, the interaction with an electron beam allows cooling the ion beam to a momentum spread of $\Delta p/p \leq 10^{-4}$ [231]. Recently, the experimental storage facilities at GSI were extended by the installation of the CRYRING, a second storage ring which operates at energies even down to $\leq$300 keV/u [492], and the installation of the HITRAP facility where the ions will be captured in a Penning trap and cooled to ion temperatures of about 4 K [493]. These three facilities will be connected by beamlines, thus providing a versatile experimental area, not only for stable ions, but – in connection with the fragment separator FRS [494] – also for unstable nuclides. The CRYRING is already operational as a part of the **F**acility for **A**ntiproton and **I**on **R**esearch (FAIR) [130] which is currently under construction at Darmstadt. Other storage ring facilities are in operation or currently under construction worldwide. M. Steck and Y. A. Litvinov have given a detailed description of the different facilities existing and under construction, as well as of the prominent techniques for ion cooling in [231]. The last section of their review also gives a concise overview on the different physics programs pursued at these facilities.

As compared to the direct detection of heavy ions which was discussed in Sections 3–5 of the present review, the detection of hard x-rays at EBITs or at heavy ion storage rings is performed under rather different experimental conditions:

- For highly charged ions, the transition energies of the x-rays lie in the range of around 10 keV up to 100 keV, which is about 3–5 orders of magnitude lower than the energies of the ions discussed in Sections 3–5. In addition, x-rays deposit their energy by indirectly ionizing processes, mostly by the photo effect, thus creating electrons which in turn interact with the absorber of the CLTD and induce a temperature change. Therefore, absorbers should be high-Z materials to obtain high absorption efficiency in combination with small absorber thicknesses for obtaining small heat capacity [180].
- The smaller incident energies also put more stringent limits on the volume of the absorber and the thermometer, as well as on the operating temperature to keep the heat capacity small for a sufficiently high thermal signal (see Table 2.2 in Section 2). Accordingly, x-ray detectors are usually operated at temperatures well below 100 mK. These low operating temperatures put a higher demand on cryogenic techniques, meaning that usually either ^{3}He/^{4}He dilution refrigerators or adiabatic demagnetization refrigerators are used. In addition, single detectors are usually combined into detector arrays in order to obtain a reasonable active detector area.
- On the other hand, x-rays even with an energy of down to 10 keV can pass through thin foils of low-Z material without substantial losses of intensity. Therefore, x-ray detectors do not necessarily have to be coupled directly to the vacuum system of the accelerators where the x-rays are produced. Direct coupling is in many cases also prohibited because storage rings and EBITs demand for an ultra-high vacuum with pressures of $\leq 10^{-11}$ mbar [231] which cannot be easily realized in a system as complicated as a cryostat.

- The x-ray emitting ions have velocities ranging from a few permille of $\beta = v/c$ up to 90% of $\beta = v/c$, depending on the storage ring facility. Thus, dependent on the observation angle of the detector, the emitted x-rays are Doppler-shifted. To precisely determine the energy in the rest frame of the ion, the ion velocity and the relative position of the interaction zone with respect to the detector has to be known with sufficient precision to correct for this Doppler-shift. In addition, the interaction zone usually cannot be considered as a point source, but it covers a certain volume. The resulting range of emission angles is associated with a range of Doppler-shifts. This means that a single x-ray energy in the emitter frame is observed as a distribution of x-ray energies in the laboratory frame. This in turn results in a broadening of the observed x-ray lines which is independent of the detector performance [158]. For the particular case of experiments at storage rings for which the highly-charged ions are best produced at high ion energies (see above), the highly-charged ions need to be decelerated to lower kinetic energies, which are required to reduce the uncertainties in the Doppler shift [24,158,492,495].

These conditions demand for a completely different detector design as compared to heavy ion detectors. Several research groups have developed and applied different CLTD concepts at EBITs and at the ESR storage ring. These will be described in the next section. Examples of applications will be discussed in Section 6.4.

6.3. Detector design and detector performance

6.3.1. X-ray detectors based on semiconductor detectors

As discussed in Section 2.2 and Section 3.2.2.1, the concept of CLTDs based on semiconductor thermistors is the oldest and accordingly most mature detector technology [12,179]. One advantage is their large dynamic range, which is not limited by the width of a superconducting transition. In particular, CLTDs based on silicon thermistors are among the oldest CLTDs used for x-ray detection [179]. One driving force behind these developments has been balloon and satellite borne x-ray astrophysics [63,496], but such detectors were soon also applied at the LLNL EBIT in first experiments [483], and at the **E**xperimental **S**torage **R**ing (ESR) at GSI [148,158,497].

6.3.1.1. CLTDs for experiments at the ESR storage ring and the CRYRING

Detector design:

The CLTDs with silicon semiconductor thermistors which were used at the LLNL EBIT and at the ESR are both based on a detector design which was developed by D. McCammon et al. and C. Stahle et al. [63,496] for balloon and satellite missions motivated by astrophysics. Detector arrays with 36 pixels are micro-machined from bulk silicon, and contain implanted leads and implanted thermistors. These thermistors are compensated-doped with phosphorus and boron to obtain a value of $\alpha \approx 6$ for the sensitivity (see Section 2.2) at an operating temperature of about 50 mK. However, compared to the detection of soft x-rays with $E \leq 10$ keV, which is discussed in [70], the detector setup was modified in order to meet the conditions of the Lamb shift experiments.

The detector array for ESR experiments consists of two rows of 18 single thermistors each. For the Lamb shift experiments at the ESR, the silicon thermistors were equipped with absorbers of lead (thickness 50 μm) or tin (thickness 100 μm) which were glued on top of the thermistors by means of an epoxy varnish [157,191]. Both, lead and tin, fulfill the requirements of low heat capacity, as well as of rapid and complete thermalization [157]. Thus the photo peak efficiency obtained for 100 keV X-rays is around 20%. The active area per pixel is around 0.35 mm^2. For a fully equipped detector array with 32 pixels, this amounts to an active detector area of 11 mm^2. The thermal decay constant of around 1 ms at the operating temperature of 50 mK permits count rates of around 100 Hz without the need for a pile-up correction. Fig. 6.2(b and c) displays the layout of one pixel [63], one of the detector arrays used in the ESR experiments [157,158], and a close-up where the individual absorbers are visible.

At an operating temperature of 50 mK, the silicon thermistors have a typical operating resistance of 30 MΩ. To minimize the noise when coupling these high resistances to the readout cables with around 100 Ω resistance, cooled **J**unction **F**ield **E**ffect **T**ransistor**s** (JFETs) are used as impedance adapters [157,178]. These JFETs are kept in a special housing and heated to an operating temperature of 120 K. At room temperature, the voltage signals of the CLTDs are fed into specially adapted preamplifiers which were developed by D. McCammon et al. [52] particularly for these thermistors. The signals are digitized by means of Flash-ADCs. Offline, they are analyzed by means of digital filtering [198] to obtain the optimal energy resolution.

Cryogenic setup:

To maintain an operating temperature of around 50 mK during the limited beamtimes at the ESR with minimal intervals of interruption, and to allow for an optimized solid angle covered by the CLTD, a $^3He/^4He$ dilution refrigerator with a large storage of liquid helium and liquid nitrogen was designed with a special side arm which fits to the geometry of the internal gas-jet target at the ESR. The principle of experiments at the ESR storage ring to determine the 1s Lamb shift is displayed in Fig. 6.3 on the left-hand side: A beam of bare U^{92+} ions is injected, stored, decelerated and cooled in the ESR, and interacts with an internal gas-jet target [231,498] which provides high target densities. This may lead to the capture of one electron and to the population of a 2p state, which promptly decays to the 1s state. The emitted Lyman-α x-rays are detected by x-ray detectors surrounding the internal target in coincidence with the charge exchanged U^{91+} ions which are detected in a dedicated particle detector. To place the CLTDs as close as possible to the interaction zone,

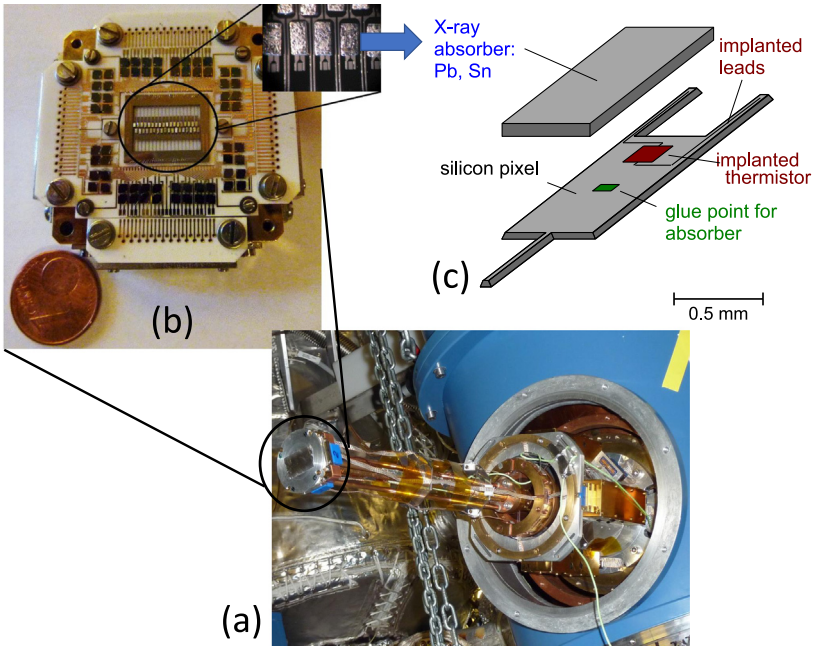

Fig. 6.2. (a) The lower right photograph shows the side arm of the cryostat with the detector array mounted at its end (the array is protected by an aluminum cover with a thin aluminum foil). (b) The upper left photograph shows the detector array equipped with Sn absorbers. The close-up shows individual pixels on an enlarged scale. (c) Next to it, a schematics of one single detector pixel is displayed [63,70,157,158,496].
Source: Reproduced from [24] with kind permission of IOP.

the gas-jet target chamber is equipped with several ports where detectors can be inserted into *vacuum pockets*. The side arm was designed to fit into one of these pockets, which allows bringing the detectors to a distance of about 300 mm to the interaction zone [158]. The layout of this side arm is displayed in Fig. 6.3, right-hand side. It was specially designed for the present Lamb shift experiments [148,157,191] and constructed by Oxford Instruments[20]. A picture is shown in Fig. 6.2. The detectors are mounted at the top of the side arm, which has a length of about 600 mm [191], at the end of a copper rod which in turn is connected to the coldest point of the cryostat at 10 mK. Due to the finite thermal coupling, the detectors themselves are operated at around 50 mK. The CLTDs can be irradiated through a system of aluminum-coated mylar windows. In order to suppress low-frequency microphonics, the first amplifier stage is positioned close to the detectors inside the side arm of the cryostat. The cryostat is prepared to read out a total of 100 detector channels. A detailed description can be found in [15,157,191].

While this cryogenic setup has worked very well in the first experiments at the ESR gas-jet target, it poses also limitations concerning the flexibility of experiments because the need to refill the cryostat with liquid nitrogen and liquid helium demands the interruption of the beam time. In addition, the use of liquid ^{4}He increases the operational costs. Therefore, for the next generation of experiments with CLTDs, a ^{3}He/^{4}He dilution refrigerator with a pulse tube cooler for the outer temperature shields was designed and commissioned [192,499]. It features a side arm which is kept at an operating temperature of 10 mK and fits into the ESR gas-jet target like the previous setup [157], but the system does not need any maintenance during beam times. In addition, the design of the inner geometry allows for vertical mounting of the side arm alternatively to the horizontal setting. This makes the new cryogenic setup much more flexible and adaptable to different experimental needs.

Detector performance:

Three different detector arrays were prepared for different experiments at the ESR. The first prototype array had eight operating pixels equipped with tin and lead absorbers. Lead has a higher photo peak efficiency due to its larger nuclear charge Z, but it was found that the energy resolution of the tin pixels was considerably better. Therefore, the second detector array with sixteen working pixels was entirely equipped with tin absorbers. These two detector arrays were operated in the liquid-helium based ^{3}He/^{4}He dilution refrigerator which was described above. They were extensively tested in the laboratory using a ^{241}Am source with a γ-line at about 59.5 keV. An excellent energy resolution of the order of 45–65 eV was obtained for all pixels [157,158]. Fig. 6.4 shows one example of an energy spectrum with an energy resolution of $\Delta E(\mathrm{FWHM}) = 46$ eV, collected with a tin absorber. These results may be compared to the theoretical limit of the energy resolution for a conventional semiconductor detector which is about $\Delta E \approx 380$ eV for 60 keV photons.

20 Oxford Instruments plc, UK, Tubney Woods, Abingdon, Oxfordshire, OX13 5QX, UK

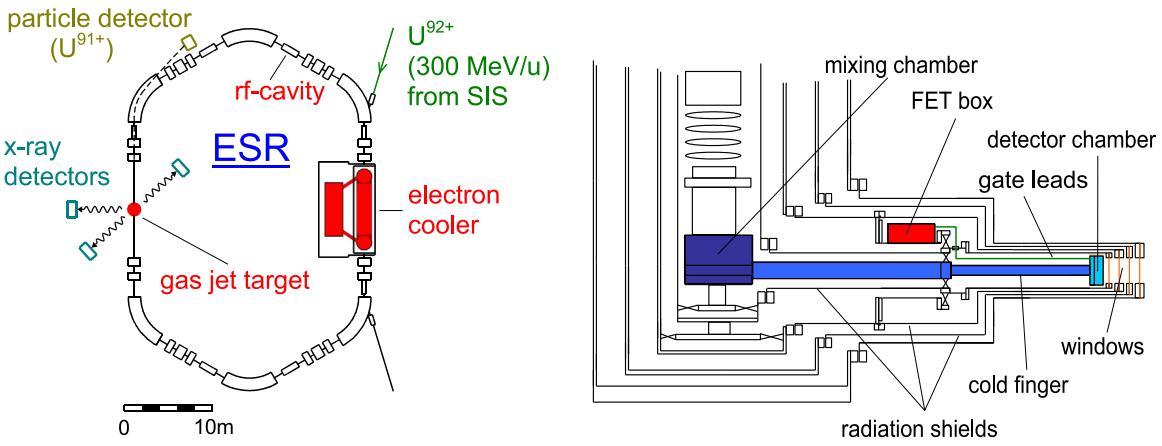

Fig. 6.3. Left-hand side: Experimental setup for Lamb shift measurements on hydrogen-like heavy ions at the internal gas-jet target of the ESR storage ring. Bare U^{92+} ions, which are injected from the synchrotron SIS18, interact with the gas-jet target which is introduced perpendicular to the beam axis and may capture an electron, thereby emitting x-rays which are detected in x-ray detectors surrounding the interaction zone. Right-hand side: Layout of the detector side arm of the $^3He/^4He$ dilution refrigerator which was especially designed for the Lamb shift experiments at the ESR. The side arm allows to bring the CLTD array as close as possible to the interaction zone of the ion beam and the gas-jet (For details see [157,158,191]).
Source: Adapted from [15].

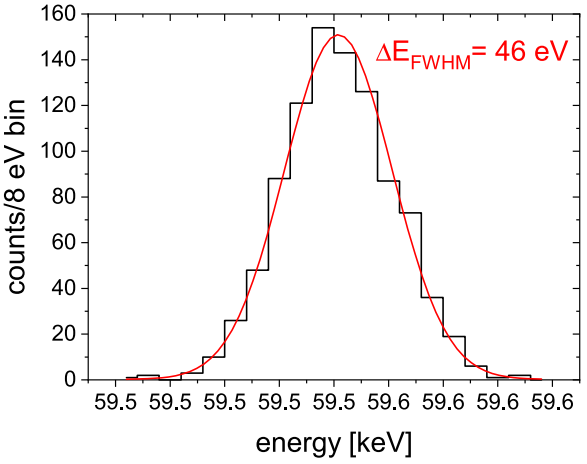

Fig. 6.4. Energy spectrum obtained with a CLTD with a tin absorber for 59.5 keV photons from a ^{241}Am source. The solid line (red) represents a Gaussian fit to the data. For the photo peak, an energy resolution of $\Delta E_{FWHM} = 46$ eV is obtained.
Source: Reproduced from [158] with kind permission of IOP.

To extend the active detector area, a prototype of a more compact detector array was designed for the pulse-tube-cooler-based dry $^3He/^4He$ dilution refrigerator [192,499]. The new design is displayed in Fig. 6.5. Since the first test, improvements in the production procedure have led to an energy resolution of 120 eV for an x-ray energy of 60 keV. The energy resolution is currently limited by vibrational noise from the pulse-tube and may be improved by installing effective vibration damping.

6.3.1.2. CLTDs for experiments at the LLNL EBIT

When the first CLTD was installed at the LLNL EBIT, its primary goal was to provide calibration data for the Astro-E/Astro-H x-ray spectrometers which were supposed to fly on x-ray satellites [483]. Therefore, this first CLTD array was a twin of the going-to-fly Astro-H array, optimized for energies below 10 keV. The thermometers are similar to the ones described in the previous section for the ESR experiments, because both array types were developed and fabricated by the NASA Goddard Space Flight Center [483,496]. The main difference is the detector geometry: The Astro-H array was designed for the imaging of x-ray sources. Accordingly, it is shaped in a geometry of 6×6 thermistors with a total active area of 13 mm^2 [500]. As the target of such measurements were x-ray lines below 10 keV, the CLTD array is equipped with 8 μm thick HgTe absorbers which provide a photo peak efficiency of 95% in the energy range of interest. In an extended measurement campaign it was shown that the combination of a CLTD with an EBIT provides a well suited

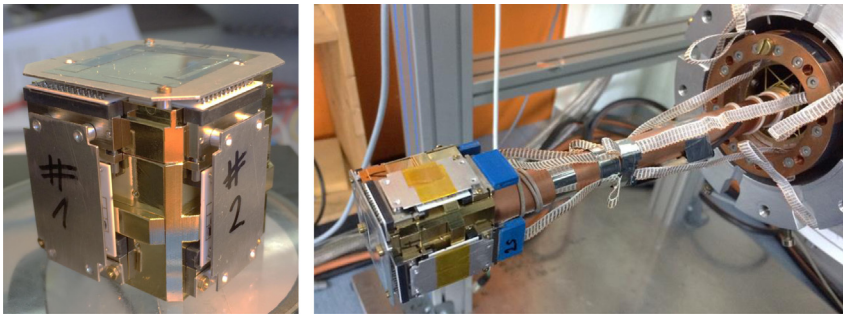

Fig. 6.5. Pictures of a prototype of a more compact design of a CLTD detector for Lamb shift experiments. It features one array with 32 pixels, mounted at the front of the side arm of the cryostat (right-hand side). Pictures courtesy of P. Scholz.
Source: Reproduced from [24].

instrument to investigate ionization cross sections and high-resolution x-ray energies [170]. In particular, because the detection efficiency is considerably larger than the detection efficiency of a crystal spectrometer, absolute excitation cross sections for neon-like to lithium-like iron ions could be determined for the first time [483].

Based on this story of success, a dedicated CLTD array was deployed at the LLNL EBIT in 2008. It is called the **E**BIT **C**alorimeter **S**pectrometer (ECS) [501], and is specially adapted to the operation at an EBIT. The detector geometry is the same as the one of its predecessor, an array of 6 x 6 CLTDs on the basis of silicon thermistors. The absorbers are made of superconducting HgTe, part of them 2 μm thick. However, to increase its energy range, half of the pixels are equipped with thicker absorbers of 100 μm, which provide a higher photo peak efficiency for x-ray energies up to 100 keV. According to [502], an energy resolution of $\Delta E = 4.5$ eV was obtained for x-rays of 6 keV, while an energy resolution of $\Delta E = 33$ eV for x-rays of 60 keV was achieved.

The cryogenic setup has been described in detail in [501,502]. It is based on an *adiabatic demagnetization refrigerator* (ADR) which uses the demagnetization of a magnetic salt pill to cool the detector to 60 mK. The outer cryostat is pre-cooled by a ^{3}He/^{4}He sorption cooler.

6.3.2. X-ray detectors based on metallic magnetic calorimeters for experiments at the ESR storage ring and the CRYRING

The readout principle of magnetic calorimeters is entirely different from the ones for resistance-based thermometers which have been discussed up to now. They make use of the Curie-like temperature dependence of the magnetization of a paramagnetic material in a weak magnetic field to precisely determine the temperature change of the detector after the absorption of an x-ray photon [181,503,504]. The resulting change of magnetization is proportional to the incident energy according to [181]

$$\delta M = \frac{\partial M}{\partial T}\Delta T = \frac{\partial M}{\partial T}\frac{E}{C} \tag{6.1}$$

E is the energy of the x-ray photon, C is the total heat capacity of the detector (see also Section 2.1). The change of the magnetization M is read out by a highly sensitive low-noise SQUID[21] magnetometer as shown in Fig. 6.6. The depicted detector layout makes use of two single pixels that are read out in parallel. This gradiometric setup minimizes the effect of temperature fluctuations of the heat bath and allows the preparation of a superconducting persistent current in the pick-up coil that generates the magnetic field that is required for the temperature sensor.

Detector design:

For the magnetic sensor, two actually conflicting demands need to be met: On the one hand, the heat capacity C of the sensor should be low to obtain a large thermal signal. This would favor dielectric materials where no contribution to the heat capacity from conducting electrons is expected. However, the coupling of magnetic moments to phonons is small for these materials [181], so metallic materials are chosen. Accordingly, these thermistors are referred to as **M**etallic **M**agnetic **C**alorimeter**s** (MMCs). The excellent energy resolution obtained justifies the compromise between magnetic coupling and electronic heat capacity. Accordingly, the material of choice for the sensors is gold, doped with several hundred ppm of the rare-earth element erbium. The group of C. Enss et al. at the University of Heidelberg, Germany, has developed this concept to full maturity and is still leading in producing MMCs [181], although other groups and institutions have meanwhile started [506–508]. An extensive description of the detection concept is given in [181].

In the following sections, we shall restrict ourselves to the x-ray detectors called *maXs (magnetic calorimeters for X-ray spectroscopy)*, namely maXs-20, maXs-30, maXs-100 and maXs-200, which were developed for x-ray spectroscopy at the ESR and the CRYRING storage rings [24,190,505,509]. If gold is doped with a few hundred ppm of erbium, both alloys

21 Superconducting Quantum Interference Device.

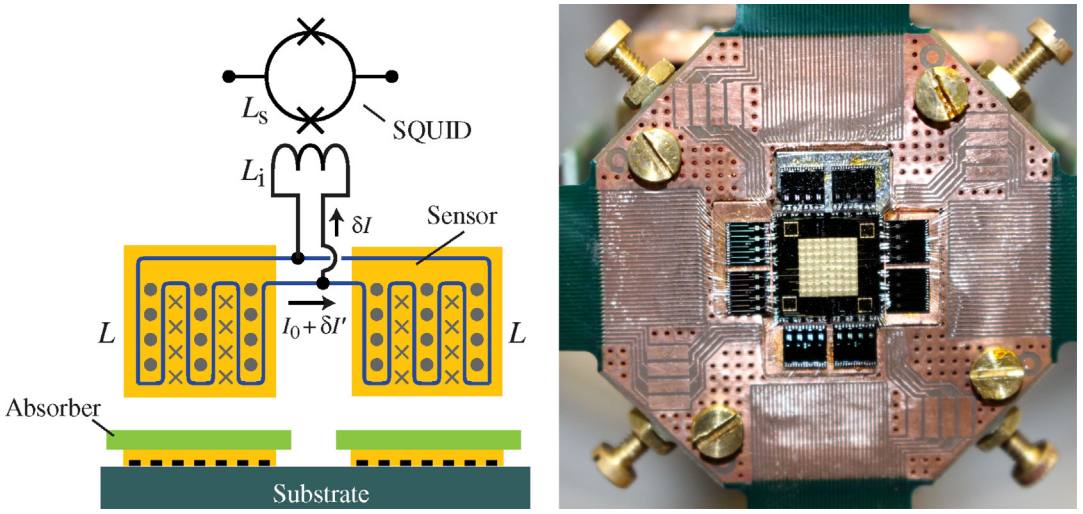

Fig. 6.6. Left-hand side: Schematic drawing of a gradiometric detector consisting of two single metallic magnetic calorimeters. A persistent current I_0 in the superconducting coil can be used to generate the weak magnetic field that is needed to operate the paramagnetic temperature sensor. A SQUID magnetometer is used to monitor any additional current δI that arises from a temperature change of one of the detectors after the absorption of a photon. On the right-hand side, a picture of the maXs-30 MMC detector developed by D. Hengstler et al. is shown [24,190,505].
Source: Reproduced from [24].

form a solid solution where Er^{3+} ions substitute ions of the host material at regular lattice sites [190]. The 4f electrons of the erbium in the gold effectively form a two-level system with an effective spin of 1/2 and an isotropic g-factor of 6.8. In a small external magnetic field, the spins of the erbium ions align at low temperatures. The energy deposition of a photon increases the temperature which in turn causes a decrease in the alignment, thus leading to a temperature-dependent magnetization as explained above. The external magnetic field is created by the pickup coils as shown in Fig. 6.6, left-hand side. Using two pickup coils with different polarity, one readout SQUID can be used for both sensors (see below).

All maXs detectors use gold absorbers to obtain high photo peak efficiency. Because the simultaneous use of the sensors as absorbers leads to a decrease in energy resolution, absorbers of pure gold are electroplated on top of the temperature sensors. This ensures a fast thermalization which in turn results in a very short signal rise time of 90 ns [24, and references therein]. The different types of detector arrays differ mainly in the shape and thickness of the absorbers. The maXs-20 [510] consists of eight pixels in a linear array, each with a size of $250 \times 250\,\mu m^2$. The actual sensor beneath the absorber has a size of $160 \times 160 \times 1.5\,\mu m^3$. The thermal connection is made by twenty-four gold posts with a height of 5 μm and a diameter of 10 μm each. The absorber thickness of the maXs-20 array is 5 μm which provides a photo peak efficiency of 45% at 20 keV. The maXs-200 array was designed to provide high photo peak efficiency for x-ray energies up to 200 keV, which results in an absorber thickness of 200 μm, an absorber area of 500 μm × 2 mm and a slightly thicker sensor. With this design, a single pixel obtains a photo peak efficiency of 45% at 100 keV, and of 12% at 200 keV [510]. Based on these two linear arrays, a two-dimensional detector array with 8 × 8 pixels, named maXs-30, was developed [24,190,505]. A picture is shown in Fig. 6.6 (right-hand side). With a nominal absorber thickness of 30 μm, each pixel reaches a photo peak efficiency of above 30% for x-ray energies up to 90 keV. The total array provides an active detector area of $16\,mm^2$, which is advantageous for the small event rates of experiments at the ESR and the CRYRING.

Detector readout:

Dc-SQUIDs are the most sensitive devices for detecting the change in magnetization of a paramagnetic sensor. They can be operated with small power dissipation at very low temperatures and, therefore, be used as a sensitive flux-to-voltage converter below 4 K. A dc-SQUID [511] consists of a superconducting loop interrupted by two Josephson junctions. Due to the Josephson effect, the voltage across the device depends periodically on the magnetic flux through it. Operated at a steep point in this flux-voltage characteristics in a flux-locked-loop, the device transfers a change in magnetic flux into a change in voltage. As can be seen in Fig. 6.6 (left-hand side), the paramagnetic sensors are placed on top of a meander-shaped pickup coil which in turn is coupled by the inductance L_i to the readout SQUID. This geometry has two advantages: First, the persistent current for the magnetic field of the paramagnetic sensor does not have to flow through the SQUID which reduces the SQUID noise. Second, this configuration allows for reading out two MMCs with one SQUID, thus reducing the number of SQUIDs for a detector array.

Detector performance:

Fig. 6.7 shows two examples of energy spectra, taken in the laboratory with x-rays or γ-ray sources, with the maXs-20, and the maXs-30 detector arrays, respectively. The maXs-20 array which is optimized for energies below 20 keV reaches

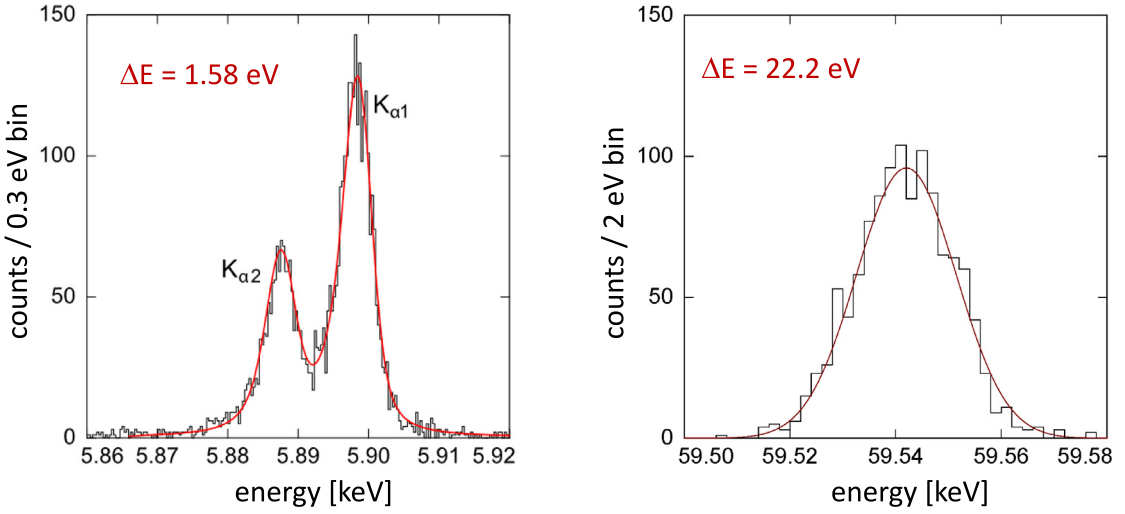

Fig. 6.7. The left-hand side displays an energy spectrum obtained with the maXs-20 detector array for the Mn lines of a ^{55}Fe source. The energy resolution of the lines is $\Delta E_{FWHM} = 1.58$ eV (reproduced from [510]). The panel on the right-hand side displays an energy spectrum of x-rays from an ^{241}Am source obtained with the maXs-30 detector. In this case, the energy resolution is $\Delta E_{FWHM} = 22.2$ eV [24,190,505, and references therein]. *Source:* Reproduced from [24].

an energy resolution of $\Delta E_{FWHM} = 1.58$ eV for x-rays of 5.9 keV [510]. This is among the best results obtained with CLTDs for x-rays and very close to the energy resolution of state-of-the-art crystal spectrometers [211,512]. However, the MMC combines this excellent energy resolution with a much larger dynamic range. The two-dimensional maXs-30 detector array was optimized for the application at the ESR and the CRYRING to detect x-rays from highly-charged heavy ions. Its energy resolution of $\Delta E_{FWHM} = 22.2$ eV for 60 keV x-rays is also among the best results obtained in this energy range worldwide. For comparison, the crystal spectrometer FOCAL reaches an energy resolution of around 60 eV [211,513], but with lower detection efficiency and a very limited bandwidth.

6.4. Application of CLTDs for the detection of hard x-rays

6.4.1. The determination of the 1s Lamb shift in hydrogen-like heavy ions

As discussed in Section 6.1, the determination of the 1s Lamb shift in hydrogen-like heavy ions is one of the most stringent tests of quantum electrodynamics. The ions are decelerated in the ESR to the desired energy, cooled and stored for seconds to several hours. In the experiments presented in this section, the ions interact with the internal gas-jet target of the ESR (see Fig. 6.3) [15,158,498]. With a certain probability, a bare ion captures an electron and promptly emits Lyman-α x-rays. The CLTDs, as well as the two detectors of the crystal spectrometer FOCAL [211] were mounted under different observation angles at flanges with pockets provided at the gas-jet interaction chamber. The CLTDs were mounted under an observation angle of about 135°.

Fig. 6.8 displays the energy spectrum obtained for hydrogen-like uranium ions at an ion energy of 89 MeV/u, taken at the ESR with the CLTDs as a proof of principle for the Lamb shift experiments which are discussed in the next section [158,168,497]. The energy resolution of $\Delta E = 115$ eV is mostly limited by the Doppler broadening. The finite diameter of the ion beam, as well as of the gas-jet of the target lead to a finite size of the interaction region of which the x-rays are emitted. The resulting observation under a range of emission angles is associated with a range of Doppler shifts. This means that a single x-ray energy in the emitter frame is observed as a distribution of x-ray energies in the laboratory frame. This, in turn, results in a broadening of the observed x-ray lines which is independent of the detector performance [158]. Nevertheless, the already very promising result of this experiment, where CLTDs were used for the first time at a heavy ion storage ring for the investigation of Lyman-α transitions of hydrogen-like heavy ions, proved that the application of CLTDs in this field of physics may provide substantial advantages as compared to the application of conventional germanium x-ray detectors or crystal spectrometers.

Determination of the 1s Lamb shift on hydrogen-like lead and gold ions:

Two CLTD detector arrays with effective areas of 1.5 mm^2 and 4.2 mm^2 were applied at the ESR in two experiments to determine the 1s Lamb shift in hydrogen-like lead and gold [158,166,167,169,497]. Fig. 6.9 (upper part) shows example spectra of Lyman-α x-rays from lead and gold ions together with calibration lines [158]. Even though the detector performance under the experimental conditions at the ESR was sightly worse than in the uranium experiment with an average energy resolution of around 200 eV, the statistical error concerning the Lamb shift was small compared to

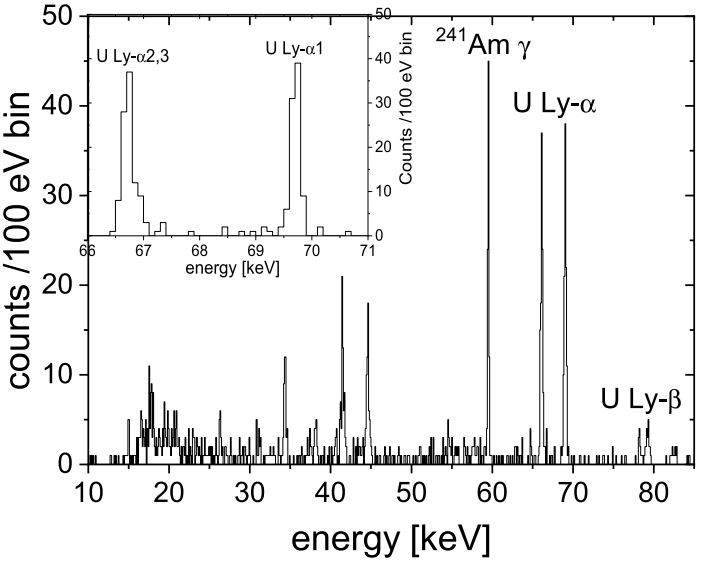

Fig. 6.8. This energy spectrum displays the Lyman-α transitions of hydrogen-like uranium U^{91+}, observed at the ESR with a CLTD in a first proof-of-principle experiment. The insert shows the region of the Lyman-α transitons in an expanded scale. In this spectrum, the energy resolution for the Lyman-$\alpha 1$ transition was $\Delta E_{FWHM} = 115$ eV, limited by the so-called Doppler broadening [158,497].
Source: Reproduced from [158] with kind permission of IOP.

the systematic uncertainties in both cases. As compared to measurements with a germanium detector or a crystal spectrometer, x-ray background is negligible because the single detector volumes are rather small. Accordingly, coincidence measurements with an additional particle detector, which are mandatory for experiments with germanium detectors and crystal spectrometers, can be omitted in the case of CLTDs, a fact that clearly simplifies the experimental demands and increases the overall statistics.

The non-linear energy response function of the silicon thermistors was modeled by a third order polynomial using several calibration lines from different x-ray and $\gamma-$ray sources (see [158] for a detailed discussion). Its contribution to the systematic uncertainty was 15%. The systematic uncertainties were dominated by the correction of the Doppler shift. In comparison to an ion trap, where the ions are brought almost to rest, the ions in a storage ring have, at least for the first series of experiments, relatively high ion energies up to several hundred MeV/u. As a consequence, the emitted X-ray lines are Doppler shifted and Doppler broadened according to the formulas

$$E_{lab} = E_{emit} \cdot \frac{\sqrt{1-\beta^2}}{1-\beta\cos(\theta_{lab})} \tag{6.2}$$

$$\Delta E_{lab,Doppler} = \Delta\cos(\theta_{lab}) \cdot \frac{\beta}{1-\beta\cos(\theta_{lab})} \cdot E_{lab} \tag{6.3}$$

where $\beta = \frac{v}{c}$ contains the ion velocity and θ_{lab} is the angle of observation, E_{emit} is the x-ray energy in the emitter frame, and $\Delta E_{lab,Doppler}$ is the additional contribution to the FWHM due to the Doppler shift. It is obvious that the precision with which these variables are known ultimately will limit the accuracy in the determination of the x-ray energy.

Fig. 6.9 (lower part) shows the results for each pixel as a function of the pixel position relative to the center of the detector array. The Doppler shift has been corrected for. The mean values of $E_{Ly-\alpha 1} = (77919 \pm 10)$ eV for lead, and of $E_{Ly-\alpha 1} = (71565 \pm 9)$ eV for gold, respectively agree within the uncertainties with the theory predictions of V. A. Yerokin and V. M. Shabaev, $E_{Ly-\alpha 1} = 77934.4(5)$ eV for lead, and of $E_{Ly-\alpha 1} = 71569.7(5)$ eV for gold, respectively [474]. In the present experiments, the main systematic limitation was introduced by the determination of θ_{lab} [158]. This limited the overall accuracy of the determined Lamb shift to about 25%. Within these error bars, the results for the 1s Lamb shift of (260 ± 53) eV for lead, and (211 ± 42) eV for gold, respectively, are in good agreement with predictions from quantum electrodynamics [158]. For lead, the measurement even represents the most precise measurement of the 1s Lamb shift up to date to our knowledge.

Metallic magnetic calorimeters were also applied in commissioning experiments at the ESR [24,505] and the CRYRING [509]. These first test experiments were quite successful, but the application in a real Lamb shift experiment is still pending. The improved energy resolution and the lower energies in the CRYRING will certainly open the door to a higher precision, finally allowing for a real scrutinizing test of the QED in hydrogen-like heavy ions.

It should also be mentioned that the first attempt to investigate the 2s Lamb Shift in the Balmer transition series of Au^{78+} [176] failed due to the low detection efficiency at high x-ray energies and the limited solid angle of the CLTD used.

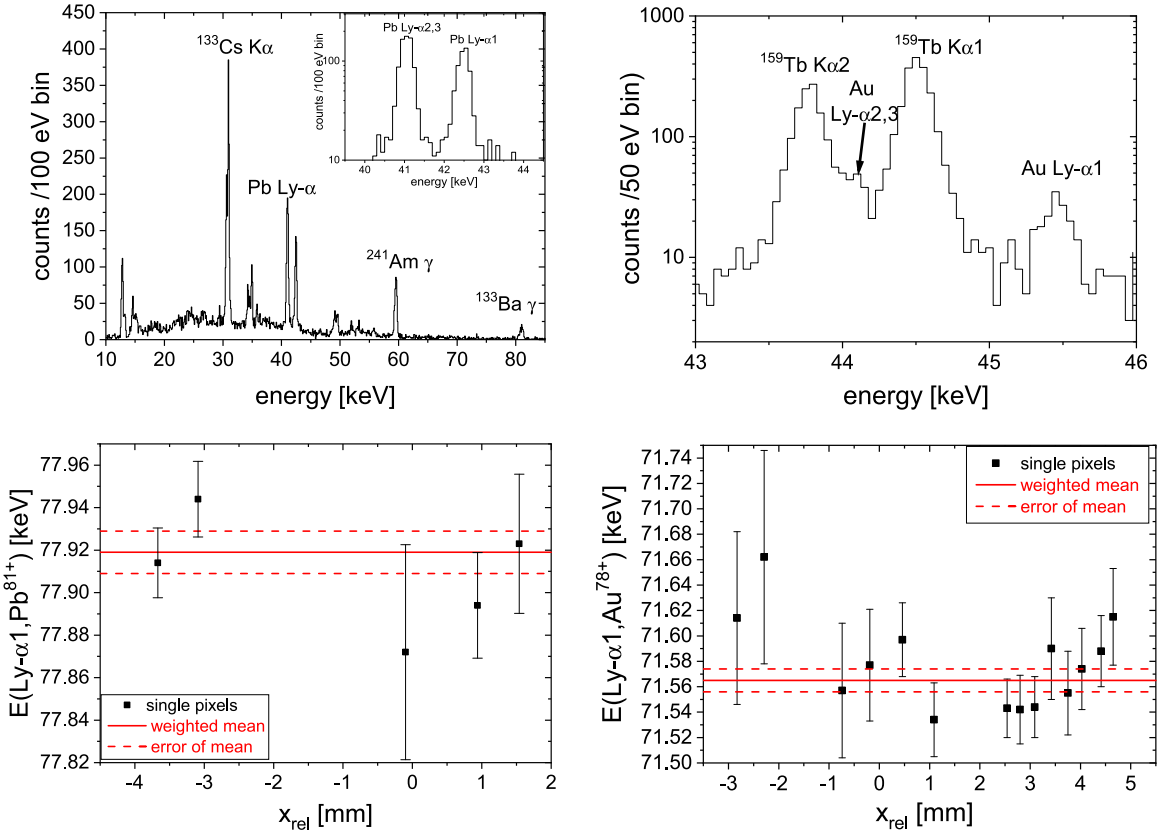

Fig. 6.9. Upper part: Two example spectra of Lyman-α x-rays from hydrogen-like lead and gold ions together with calibration lines from ^{241}Am and ^{159}Tb sources, are displayed [158]. Both spectra were obtained with CLTDs at the ESR storage ring with lead ions of 218.6 MeV/u and gold ions of 124.7 MeV/u. The spectra are not yet corrected for the Doppler shift. Lower part: the results for the Lyman-α energies obtained for the single pixels are displayed as a function of the position of the pixels x_{rel} relative to the center of the array. The energies are corrected for the Doppler shift which in turn is dependent on the pixel position. The red lines denote the weighted mean of $E_{Ly-\alpha 1} = (77919 \pm 10)$ eV for lead, and of $E_{Ly-\alpha 1} = (71565 \pm 9)$ eV for gold, respectively. The average values agree within the uncertainties with the theory predictions of V. A. Yerokin and V. M. Shabaev, $E_{Ly-\alpha 1} = 77934.4(5)$ eV for lead, and of $E_{Ly-\alpha 1} = 71569.7(5)$ eV for gold, respectively [474].
Source: Adapted from [158] with kind permission of IOP.

6.4.2. Application of CLTDs at EBITs

As stated above, one of the first applications of a CLTD at an EBIT had mainly astrophysical purposes [18,483,500]. However, these astrophysics questions were closely related to questions of atomic structure. Among the first experiments performed at the LLNL-EBIT with a CLTD was the investigation of absolute cross sections of electron excitation in different ionic charge states of iron by precisely determining the transition energy and the line intensity of different transitions [483]. These cross sections play an important role in the interpretation of stellar spectra, but they also influence theoretical models of electronic interactions in few-electron systems. The investigation of these cross sections with crystal spectrometers is not possible because the line intensities are too small as compared to other background processes. Precise measurements of the K-shell transition energies in L-shell Si and S ions [514] provided not only important input for the interpretation of astrophysical x-ray spectra. They also check benchmark calculations of correlation effects in few-electron systems. The influence of these correlation effects was also investigated in a series of measurements on neon-like ions from argon (Ar^{8+}) up to molybdenum (Mo^{32+}) [515]. Whereas a considerable difference between theory and experiment was observed for light ions, a better agreement is obtained for molybdenum. Further measurements with even heavier ions are mandatory to confirm this trend.

One heavy ion of particular interest for plasma physics is tungsten, because it is foreseen to be used as a coating material in fusion reactors [516]. As a consequence, it will be present in many fusion plasmas. The accurate knowledge of the transition energies and emission cross sections will be mandatory to use x-ray spectroscopy on tungsten as a diagnostic tool for, e.g. the temperature inside a reactor. Therefore, the transition energies and line intensities were investigated at the LLNL EBIT for W^{64+} to W^{71+}. The results were compared to state-of-the-art atomic plasma calculations and pave the way to use tungsten spectroscopy as a diagnostic tool in fusion plasmas in the future [517]. These investigations make use of the advantage that by tuning the energy of the electron beam, a particular charge state of the ions in the EBIT can

be prepared. On the other hand, the application of a CLTD at the NIST EBIT was used to study the ion–electron interaction in the EBIT itself and to investigate the overlap of ion beam and electron beam [518].

All experiments described above have a close relation to astrophysical questions, and therefore investigated x-ray energies below 10 keV. However, some investigations have also been performed at higher x-ray energies. Gold *hohlraums*[22] are often employed as targets for inertial confinement of fusion material [516]. When the fusion process is initiated, the gold evaporates and is ionized, but its average ionic charge stage(s) is not well known. The LLNL EBIT can produce well-defined high ionic charge states also for very heavy ions, thus allowing to determine the correlation between charge state and x-ray emission lines for a given configuration. In the experiment of E. Träbert et al. charge states up to Au^{69+} were produced and the x-ray emission spectra were recorded with the ECS spectrometer [516,519]. The excellent energy resolution of the CLTD array in combination with the well-defined charge states from the EBIT gave an unambiguous identification of all x-ray lines belonging to a particular charge state. In the future, these lines can be used to identify different gold charge states after the inertial fusion has started.

Concerning the K-shell spectra of hydrogen-like heavy ions, EBITs are dealing with their limited production rate for very heavy highly charged ions (see discussion in Section 6.2). However, in the range of medium Z, hydrogen-like ions can be produced in quantities high enough to allow for high-precision spectroscopy. One example that has been studied at the LLNL EBIT is x-ray spectroscopy on helium-like through beryllium-like praseodymium ($Z = 59$) [171]. To increase the detection efficiency for x-ray energies around 35 keV, four HgTe absorbers of the XRS/EBIT CLTD [500] were replaced by bismuth absorbers with a thickness of 30 μm. The results of the measurements agree within error bars with calculations using different computer codes [171]. The uncertainty is dominated by statistics. Also x-ray spectroscopy on hydrogen-like and helium-like xenon was performed with the ECS CLTD array after its commissioning at the LLNL EBIT [174]. In particular, the Lyman-α transition of hydrogen-like xenon was determined to be $(31\,284.9 \pm 1.8)$ eV (sum of statistical and systematic uncertainties). From that value, a 1s Lamb shift of (46.0 ± 1.8) eV is derived [474]. This value agrees within error bars with the theory value which is calculated with an accuracy of ± 0.02 eV in the same reference. For this measurement, the uncertainty is dominated by the statistical uncertainty of ± 1.45 eV.

6.4.3. Perspectives for future applications

- Further improvement of the accuracy of the 1s Lamb shift:
  Currently, the accuracy is limited by the correction of the Doppler shift which was necessary due to the relatively high ion energies at the ESR. Reducing the ion velocity will also minimize the contribution of this factor to the overall uncertainty. Therefore, the next experiments on the 1s Lamb shift in hydrogen-like heavy ions will be performed at the CRYRING [231,492], where the ions can be slowed down to velocities of below 1 MeV/u. A first commissioning experiment with MMCs was already performed (see above). In the heavy ion trap facility HITRAP [493], which is currently under commissioning, the highly charged ions will be slowed down practically to rest, thus eliminating the need for a correction of the Doppler shift entirely. These facilities with negligible Doppler broadening in combination with the excellent energy resolution of CLTDs will allow Doppler-free x-ray spectroscopy with ultra-high precision and will provide a new regime of sensitivity. Another approach is independent of alterations of the experimental setup. It makes use of the large dynamic range of CLTDs. Next to the Lyman x-ray lines, also Balmer lines at energies of 15–25 keV in the emitter frame are emitted [520]. The QED corrections on these lines are negligibly small. Therefore, if they are detected in parallel to the Lyman lines, their energy can be used to determine the Doppler correction factor without detailed knowledge about the detection angle and the ion velocity.
- Investigation of unstable nuclides:
  The future research facility FAIR [130] will provide high-intensity beams of unstable nuclides, for which high-precision x-ray spectroscopy will be an interesting subject in itself. Prominent physics questions to be addressed are, next to fundamental interactions and tests of the QED, decay spectroscopy of highly-charged radionuclides and the determination of their nuclear ground state properties such as nuclear charge radii. For example, the determination of the 1s Lamb Shift at rest will be possible not only in stable but also in highly-charged radioactive ions. For such radioactive nuclides, the determination of nuclear charge radii from precision x-ray spectroscopy will be a particularly interesting subject [15,521,522]. The determination of nuclear charge radii by means of the 1s Lamb shift is possible because, besides the QED contributions of self energy ($\approx$80%) and vacuum polarization ($\approx -$ 20%), the effect of finite nuclear size ($\approx$40%) also contributes considerably to the 1s Lamb shift [474]. Therefore, apart from the experimental uncertainties, the accuracy on the QED test will be finally limited by the uncertainties on the finite nuclear size effects, estimated for ^{238}U to be about 0.1 eV [474,491]. On the other hand, this provides the Lamb shift experiments also with the potential to deduce nuclear charge radii by testing QED in one isotope with a well known nuclear structure, and by investigating the Lamb shift for the corresponding chain of isotopes, which may in the future also be extended to unstable isotopes. Due to the substantial contribution of the effect of the finite nuclear size to the 1s Lamb shift [168], a sensitive test of QED by using a stable isotope with known **R**oot **M**ean **S**quare (RMS) radius, such measurements will allow to systematically determine charge radii for chains of exotic isotopes with high accuracy.

22 Small golden spheres which contain hydrogen gas under high pressure.

- Investigation of electron–electron interactions in few-electron systems:
  Highly charged heavy ions with two or three electrons have become accessible for computation in recent years [475]. In these systems, in addition to the QED effects for one electron, the interaction between the electrons plays an important role. Except for helium-like uranium [523–525], practically no experimental data exist for heavy systems. On the other hand, such experimental data are very much needed to validate the computations.
- Determining the transition energy in ^{229}Th for a nuclear clock:
  The current international system of units (SI) is based on a hyperfine transition in ^{133}Cs which is used to define the unit of a *second*. This *cesium atomic clock* has a relative precision of 5×10^{-13}, limited by the natural line width of the hyperfine transition. An even higher precision could be obtained with a *nuclear γ transition* which has a much smaller natural line width [526,527]. One particularly interesting candidate is ^{229}Th, for which nuclear structure theory predicts a transition of around 3.5 eV [528]. Several groups have used CLTDs or MMCs to indirectly measure this transition energy by measuring the different x-ray transition energies for transitions during the decay of the nucleus [175,529,530]. Currently, the best value is (8.10 ± 0.17) eV [530], in agreement with the value determined based on internal conversion electrons [531]. However, to realize a nuclear clock it is necessary to access the transition with laser excitation. The uncertainty of ± 0.17 eV is still too large for the small bandwidth of a UV laser. Therefore, it is mandatory to increase the precision of the CLTD or MMC measurements by at least a factor of ten [526].
- Nuclear safeguard:
  Next to the above-mentioned fundamental research topics, x-ray and $\gamma-$ray spectroscopy has also some importance for potential practical applications. One example is the identification of plutonium isotopes, in particular the abundance of ^{240}Pu and ^{242}Pu, in material samples for the control of non-proliferation [467,532,533]. One method is the use of the characteristic γ- and x-ray lines from the different Pu isotopes and their respective daughters [532]. For these investigations, high-resolving x-ray detectors for energies between 100 keV and 200 keV are beneficial, because line overlap limits the reliability of such investigations [112]. A feasibility study has been performed by C. Bates et al. with MMCs [112,534] which showed that the isotope identification is possible with an energy resolution of below 200 eV at 200 keV. W. Doriese et al. have developed a dedicated 14-pixel multiplexed array of CLTDs and have obtained an energy resolution of 47 eV at 103 keV [535]. This detector array used transition-edge sensors based on a thin bilayer of Mo and Cu with a transition temperature of around 100 mK. To increase the photo peak efficiency, polycrystalline Sn absorbers were used. First tests revealed a large number of transition lines for the different Pu isotopes which had to be identified by a complicated Bayesian analysis [532]. To distinguish between ^{235}U and ^{226}Ra is not only needed for nuclear waste management, but also to avoid false alarms at border controls [19]. These two nuclides can be identified by separating their closely spaced γ-lines at around 186 keV. A. S. Hower and coworkers demonstrated that the two lines can be separated with CLTDs [19], but for practical application at airports or state borders, further development work is mandatory.
- Material analysis:
  For material analysis in dilute or solid samples, the main challenge is to distinguish the signal of a particular element from the background coming from the rest of the sample. One method is to use a bright, broad-band x-ray source in combination with a high-resolving x-ray detector [113,536]. In this *time-resolved x-ray absorption spectroscopy*, the broadband x-ray source shines through a thin sample and onto the x-ray spectrometer. The resulting absorption spectrum is obtained by comparing measurements without and with the sample, recording all absorption edges and the corresponding elements simultaneously [60,113]. Another option is to use the x-ray fluorescence lines after initial broad-band excitation of the diluted elements.
  In both cases, next to a good energy resolution, count rate capability is an important issue. Therefore, STJs are usually favored, but W. Doriese et al. have also developed a TES array which has been applied successfully in several laboratories for such investigations [113].
- Metrology:
  CLTDs offer the advantage of using a source embedded in the absorber (see Section 5.3). The aim of decay energy measurements is to determine, among others, total decay cross sections for $\alpha-$ and $\beta-$decay and the consecutive $\gamma-$ and x-rays [22,466,469,471]. Embedding the source in the absorber allows for a detection efficiency close to 100% which minimizes systematic uncertainties. While many activities have been focused on γ- and x-rays at energies below 10 keV [471], MMCs with large gold absorbers for the determination of absolute photo emission line intensities of actinides have been developed and tested [537].
- CLTD x-ray detectors based on transition-edge sensors:
  For a rather long time, TES-based x-ray detectors were restricted to low x-ray energies below 10 keV, because the coupling of thick absorbers to thin superconducting films turned out to be a challenging task [180]. However, nowadays TES for x-rays with energies above 10 keV have become available.
  For the typical operating temperatures of x-ray detectors, namely around 50 to 100 mK, different TES concepts are available. Among the mostly used are bi- or multilayers of the superconductor molybdenum in combination with gold [64] or copper [113,535,538]. By choosing the number and/or thickness of the layers, the transition temperature of the TES can be adjusted very precisely to the desired value. For example, the TES array of W.B. Doriese et al. features layers of Mo of 60 nm alternating with layers of Cu with a thickness of 200 nm [113]. As absorber material,

polycrystalline bismuth is used for energies up to 10 keV, while polycrystalline tin is used for higher energies [535]. The absorbers are connected to the TES's via a lithographically patterned epoxy post.

The big advantage of the application of TES is that mature multiplexing schemes are established for large detector arrays [535]. However, it should be stated that such schemes are also being developed for MMCs [24,190]. Accordingly, both technologies (MMCs and TES's) have great potential for x-ray spectroscopy with large detector arrays of even several thousand pixels which will be a true alternative to germanium detectors with large detector solid angle.

7. Conclusions and outlook

Calorimetric **L**ow **T**emperature **D**etector**s** (CLTDs) are operated by reading out the temperature rise of an absorber after the thermalization of the energy which is deposited by an incident particle or photon. Due to the Debye law, these detectors reach their highest sensitivity at low operating temperatures. Their detection concept, which is essentially different from that of conventional energy detectors, opens new and promising perspectives for radiation detectors. In particular, substantial advantage over ionization detectors, based on charge collection, with respect to basic properties like energy resolution, linearity of the energy response, detection threshold, radiation hardness, and others are obtained.

In the present review article we made an attempt to discuss the development, construction, and application of CLTDs in the field of heavy ion physics with a focus on nuclear and atomic physics. The excellent performance of CLTDs already obtained for the detection of heavy ions with relative energy resolutions down to one to a few times 10^{-3} for a wide range of ions (^{4}He to ^{238}U) and incident energies (0.05–360 MeV/u), and a perfect energy linearity with the absence of pulse height defects represents a considerable improvement as compared to conventional detection schemes. This performance allowed already the successful application in experiments, such as the determination of isotopic yield distributions of fission fragments in the light, the symmetry and the heavy mass region, the determination of electronic stopping powers of heavy ions in matter down to energies far below the Bragg peak, and trace analysis of rare isotopes in accelerator mass spectrometry. In the future, these activities may be continued and a couple of interesting further applications are proposed. For example, the already obtained mass resolution close to 1 amu for very heavy ions like ^{238}U, obtained with a ToF/CLTD spectrometer, may allow the in-flight mass identification of reaction products in experiments concerning nuclear structure and nuclear astrophysics with radioactive beams in inverse kinematics, trace analysis in accelerator mass spectroscopy, or the improved identification of superheavy elements, and other species. Besides, applications in high resolution nuclear spectroscopy, decay energy spectroscopy, and applied physics investigations are also topics of interest.

In the field of atomic heavy ion physics, CLTDs are applied in many research activities word wide. The excellent energy resolution down to $\Delta E = 22$ keV recently obtained for 60 keV x-rays, which is superior as compared to any conventional x-ray detector, has already allowed to investigate x-ray transitions in highly charged heavy ions. An improvement in accuracy of QED tests in extreme electromagnetic fields by means of a precise determination of the 1s Lamb shift represents, beside others, one of the highlight activities in this field.

In summary we conclude that we are convinced that CLTDs bear a large potential to be or become an important tool for applications in heavy ion physics within the years to come, and that the potential applications point to an exciting future.

Declaration of competing interest

The authors declare that they have no known competing financial interests or personal relationships that could have appeared to influence the work reported in this paper.

Acknowledgments

Part of the results presented in this review have been obtained in close collaboration with researchers from allover the world. We appreciated very much the good cooperation in the experiments with all of them, as well as many fruitful discussions of the results. Moreover, we particularly thank D. McCammon, F. von Feilitzsch, F. Gönnenwein, W. Henning, H. J. Kluge, C. A. Kilbourne, O. Kiselev, W. Kutschera, U. Köster, M. Mutterer, G. Münzenberg, C. Scheidenberger, K. W. Shepard, T. Stöhlker and W. H. Trzaska for many enlightening discussions, helpful advice and support. For the support in the preparation of this manuscript we thank S. Dubey, A. Echler, P. Grabitz and U. Köster. Last but not least, we acknowledge the funding of various funding agencies, among them the German Federal Ministry of Education and Research (BMBF), as well as the German Research Council (DFG).

References

[1] G.F. Knoll, Radiation, Detection and Measurement, fourth ed., Wiley, 2010.
[2] W.R. Leo, Techniques for Nuclear and Particle Physics Experiments, second ed., Springer, New York, Berlin, Heidelberg, 1994.
[3] N.E. Booth, B. Cabrera, E. Fiorini, Annu. Rev. Nucl. Part. Sci. 46 (1996) 471, http://dx.doi.org/10.1146/annurev.nucl.46.1.471.
[4] K. Pretzl, in: C. Fabian, H. Schopper (Eds.), Particle Reference Library Vol. 2: Detectors for Particles and Radiation, Springer, Heidelberg, New York, 2020, p. 871.

[5] A. Barone (Ed.), Proceedings of the Workshop on Superconducing Particle Detectors, Torino, 1987, World Scientific Press, 1988.
[6] L. Stodolsky, Phys. Today 44 (1991) 24, http://dx.doi.org/10.1063/1.881266.
[7] E. Fiorini, Phys. B 169 (1) (1991) 388, http://dx.doi.org/10.1016/0921-4526(91)90256-E.
[8] G. Waysand, G. Chardin (Eds.), Superconducting and Low-Temperature Particle Detectors, in: Europ. Materials Res. Soc. Symp., Elsevier, North Holland, 1989, http://dx.doi.org/10.1016/C2009-0-09801-8.
[9] A. Barone, Nucl. Phys. B (Proc. Suppl.) 44 (1995) 645, http://dx.doi.org/10.1016/S0920-5632(95)80099-9.
[10] N.E. Booth, D.J. Goldie, Supercond. Sci. Technol. 9 (1996) 493, http://dx.doi.org/10.1088/0953-2048/9/7/001.
[11] E. Fiorini, Nucl. Phys. B (Proc. Suppl.) 48 (1996) 41, http://dx.doi.org/10.1016/0920-5632(96)00201-0.
[12] D. Twerenbold, Rep. Progr. Phys. 59 (1996) 349, http://dx.doi.org/10.1088/0034-4885/59/3/002.
[13] H. Kraus, Supercond. Sci. Technol. 9 (1996) 827, http://dx.doi.org/10.1088/0953-2048/9/10/001.
[14] K. Pretzl, Nucl. Instrum. Methods A 454 (2000) 114, http://dx.doi.org/10.1016/S0168-9002(00)00812-3.
[15] P. Egelhof, S. Kraft-Bermuth, in: C. Enss (Ed.), Cryogenic Particle Detection, in: Top. Appl. Phys., vol. 99, Springer, Berlin, Heidelberg, New York, 2005, p. 469, http://dx.doi.org/10.1007/10933596_11.
[16] B. Sadoulet, in: B. Young, B. Cabrera, A. Miller (Eds.), AIP Conf. Proc., vol. 1185, 2009, p. 785, http://dx.doi.org/10.1063/1.3292455.
[17] K.M. Morgan, Phys. Today 71 (2018) 28, http://dx.doi.org/10.1063/PT.3.3995.
[18] S.R. Bandler, et al., J. Astron. Telesc. Instrum. Syst. 5 (2) (2019) 021017, http://dx.doi.org/10.1117/1.JATIS.5.2.021017.
[19] J.N. Ullom, D.A. Bennet, Supercond. Sci. Technol. 28 (2015) 084003, http://dx.doi.org/10.1088/0953-2048/28/8/084003.
[20] C. Kilbourne Stahle, D. McCammon, K.D. Irwin, Phys. Today 52 (8) (1999) 32, http://dx.doi.org/10.1063/1.882776.
[21] L. Gottardi, K. Nagayashi, Appl. Sci. 11 (9) (2021) 3793, http://dx.doi.org/10.3390/app11093793.
[22] K.E. Koehler, Appl. Sci. 11 (9) (2021) 4044, URL https://www.mdpi.com/2076-3417/11/9/4044.
[23] P. Egelhof, Adv. Solid State Phys. 39 (1999) 61, http://dx.doi.org/10.1007/BFb0107465.
[24] S. Kraft-Bermuth, et al., Atoms 6 (2018) 59, http://dx.doi.org/10.3390/atoms6040059.
[25] J. Uhlig, et al., J. Synchrotron Radiat. 22 (3) (2015) 766, http://dx.doi.org/10.1107/S1600577515004312.
[26] D.A. Bennett, et al., Rev. Sci. Instrum. 83 (9) (2012) 093113, http://dx.doi.org/10.1063/1.4754630.
[27] C. Kittel, Introduction to Solid State Physics, Wiley, ISBN: 978-1-119-45416-8, 2018.
[28] S.P. Langley, Proc. Am. Acad. Arts Sci. 16 (1881) 342.
[29] P. Curie, A. Laborde, C. R. Hebd. Seances Acad. Sci. 136 (1903) 673.
[30] F. Simon, Nature 135 (1935) 763, http://dx.doi.org/10.1038/135763a0.
[31] A. Goetz, Phys. Rev. 55 (1939) 1270, http://dx.doi.org/10.1103/PhysRev.55.1270.2.
[32] D.H. Andrews, R.D. Fowler, M.C. Williams, Phys. Rev. 86 (1949) 154, http://dx.doi.org/10.1103/PhysRev.76.154.2.
[33] G.H. Wood, B.L. White, Appl. Phys. Lett. 15 (1969) 237, http://dx.doi.org/10.1063/1.1652983.
[34] G.H. Wood, B.L. White, Can. J. Phys. 51 (1973) 2032, http://dx.doi.org/10.1139/p73-267.
[35] K.W. Shepard, W.Y. Lai, J.E. Mercereau, J. Appl. Phys. 46 (1975) 4664, http://dx.doi.org/10.1063/1.321527.
[36] H.H. Andersen, et al., Phys. Rev. A 16 (1977) 1929, http://dx.doi.org/10.1103/PhysRevA.16.1929.
[37] N. Coron, et al., Nature 314 (1985) 75, http://dx.doi.org/10.1038/314075a0.
[38] B. Neuhauser, et al., Jap. J. Appl. Phys. 26 (1987) 1671, http://dx.doi.org/10.7567/JJAPS.26S3.1671.
[39] F.v. Feilitzsch, et al., Nucl. Instrum. Methods A 271 (1988) 332, http://dx.doi.org/10.1016/0168-9002(88)90181-7.
[40] A. Alessandrello, et al., Phys. Lett. B 202 (4) (1988) 611, http://dx.doi.org/10.1016/0370-2693(88)91873-4.
[41] T.O. Niinikoski, F. Udo, Tech. Rep. 74–6, CERN, 1974.
[42] E. Fiorini, T.O. Niinikoski, Nucl. Instrum. Methods 224 (1984) 83, http://dx.doi.org/10.1016/0167-5087(84)90449-6.
[43] D. McCammon, et al., Jap. J. Appl. Phys. 26 (1987) 2084, http://dx.doi.org/10.7567/JJAPS.26S3.2084.
[44] B. Cabrera, L.M. Krauss, F. Wilczek, Phys. Rev. Lett. 55 (1985) 25, http://dx.doi.org/10.1103/PhysRevLett.55.25.
[45] B. Sadoulet, IEEE Trans. Nucl. Sci. 35 (1988) 47, http://dx.doi.org/10.1109/23.12671.
[46] J.R. Primack, D. Seckel, B. Sadoulet, Annu. Rev. Nucl. Part. Sci. 38 (1988) 751, http://dx.doi.org/10.1146/annurev.ns.38.120188.003535.
[47] F. v. Feilitzsch, Proceedings of the 9th Moriond Workshop, Moriond, France, 1989, p. 435.
[48] K. Pretzl, N. Schmitz, L. Stodolsky (Eds.), Proceedings of the Workshop on Low Temperature Physics for Neutrinos and Dark Matter, LTD1, Ringberg Castle, Germany, Springer, 1987.
[49] D. McCammon, et al., Nuclear Phys. A 527 (1991) 821c, http://dx.doi.org/10.1016/0375-9474(91)90238-2.
[50] D. McCammon, et al., Nucl. Instrum. Methods A 326 (1993) 157, http://dx.doi.org/10.1016/0168-9002(93)90346-J.
[51] S.H. Moseley, J.C. Mather, D. McCammon, J. Appl. Phys. 56 (1984) 1257, http://dx.doi.org/10.1063/1.334129.
[52] D. McCammon, et al., J. Appl. Phys. 56 (1984) 1263, http://dx.doi.org/10.1063/1.334130.
[53] H.H. Andersen, Nucl. Instrum. Methods Phys. Res. B 12 (1985) 437, http://dx.doi.org/10.1016/0168-583X(85)90046-1.
[54] H.H. Andersen, Nucl. Instrum. Methods Phys. Res. B 15 (1986) 722, http://dx.doi.org/10.1016/0168-583X(86)90399-X.
[55] J. Ullom, et al. (Eds.), Proceedings of the 19th Workshop on Low Temperature Detectors, in: J. Low Temp. Phys., 209, 2022.
[56] K. Mitsuda, et al. (Eds.), Proceedings of the 17th Workshop on Low Temperature Detectors, in: J. Low Temp. Phys., 193 - 194, 2019.
[57] M. Faverzani, et al. (Eds.), Proceedings of the 18th Workshop on Low Temperature Detectors, in: J. Low Temp. Phys., 199 (2020).
[58] C. Enss (Ed.), Cryogenic Particle Detection, in: Top. Appl. Phys., vol. 99, Springer, Berlin, Heidelberg, New York, 2005.
[59] P. Egelhof, S. Kraft-Bermuth, AIP Conf. Proc. 1185 (2009) 761, http://dx.doi.org/10.1063/1.3292450.
[60] S. Yamada, et al., Rev. Sci. Instrum. 92 (1) (2021) 013103, http://dx.doi.org/10.1063/5.0020642.
[61] N. Rando, et al., Nucl. Instrum. Methods A 444 (2000) 441, http://dx.doi.org/10.1016/S0168-9002(99)01433-3.
[62] N. Rando, et al., Nucl. Instrum. Methods A 522 (2004) 62, http://dx.doi.org/10.1016/j.nima.2004.01.019.
[63] D. McCammon, et al., Astrophys. J. 576 (2002) 188, http://dx.doi.org/10.1086/341727.
[64] C. Kilbourne Stahle, et al., Nucl. Instrum. Methods A 520 (2004) 466, http://dx.doi.org/10.1016/j.nima.2003.11.374.
[65] B. Cabrera, et al., Appl. Phys. Lett. 73 (1998) 735, http://dx.doi.org/10.1063/1.121984.
[66] D.D.E. Martin, et al., in: I.S. McClean, I. Masanori (Eds.), SPIE Proc., vol. 6269, 2006, p. 62690O, http://dx.doi.org/10.1117/12.671213.
[67] B. Cabrera, R.W. Romani, in: C. Enss (Ed.), Cryogenic Particle Detection, in: Top. Appl. Phys., vol. 99, Springer, Berlin, Heidelberg, New York, 2005, p. 417, http://dx.doi.org/10.1007/10933596_9.
[68] P. Verhoeve, J. Low Temp. Phys. 151 (2008) 675, http://dx.doi.org/10.1007/s10909-008-9730-9.
[69] R. Adam, et al., Astron. Astrophys. 586 (2016) A133, http://dx.doi.org/10.1051/0004-6361/201425034.
[70] F.S. Porter, G.V. Brown, J. Cottam, in: C. Enss (Ed.), Cryogenic Particle Detection, in: Top. Appl. Phys., vol. 99, Springer, Berlin, Heidelberg, New York, 2005, p. 359, http://dx.doi.org/10.1007/10933596_8.
[71] D. Wulf, et al., Astrophys. J. 884 (2) (2019) 120, http://dx.doi.org/10.3847/1538-4357/ab41f8.
[72] S.S. Holt, Astrophys. Lett. Commun. 26 (1987) 61.
[73] S.J. Smith, et al., J. Astron. Telesc. Instrum. Syst. 5 (2) (2019) 021008, http://dx.doi.org/10.1117/1.JATIS.5.2.021008.

[74] G. Chardin, in: C. Enss (Ed.), Cryogenic Particle Detection, in: Top. Appl. Phys., vol. 99, Springer, Berlin, Heidelberg, New York, 2005, p. 313, http://dx.doi.org/10.1007/10933596_7.
[75] G. Angloher, et al., Astropart. Phys. 23 (3) (2005) 325, http://dx.doi.org/10.1016/j.astropartphys.2005.01.006.
[76] D.S. Akerib, et al., Phys. Rev. D 72 (2005) 052009, http://dx.doi.org/10.1103/PhysRevD.72.052009.
[77] R. Agnese, et al., Phys. Rev. Lett. 116 (2016) 071301, http://dx.doi.org/10.1103/PhysRevLett.116.071301.
[78] V. Sanglard, et al., Phys. Rev. D 71 (2005) 122002, http://dx.doi.org/10.1103/PhysRevD.71.122002.
[79] E. Armengaud, et al., Phys. Lett. B 702 (2011) 329, http://dx.doi.org/10.1016/j.physletb.2011.07.034.
[80] G. Angloher, et al., Astropart. Phys. 31 (4) (2009) 270, http://dx.doi.org/10.1016/j.astropartphys.2009.02.007.
[81] G. Angloher, et al., Phys. Dark Univ. 3 (2014) 41, http://dx.doi.org/10.1016/j.dark.2014.03.004.
[82] G. Angloher, et al., Eur. Phys. J. C 76 (2016) 25, http://dx.doi.org/10.1140/epjc/s10052-016-3877-3.
[83] R. Agnese, et al., Phys. Rev. D 95 (2017) 082002, http://dx.doi.org/10.1103/PhysRevD.95.082002.
[84] R. Strauss, et al., Eur. Phys. J. C 77 (2017) 506, http://dx.doi.org/10.1140/epjc/s10052-017-5068-2.
[85] F. Fontanelli, et al., Nucl. Instrum. Methods A 370 (1996) 247, http://dx.doi.org/10.1016/0168-9002(95)01100-5.
[86] E. Fiorini, in: C. Enss (Ed.), Cryogenic Particle Detection, in: Top. Appl. Phys., vol. 99, Springer, Berlin, Heidelberg, New York, 2005, p. 453, http://dx.doi.org/10.1007/10933596_10.
[87] C. Arnaboldi, et al., Nucl. Instrum. Methods A 518 (2004) 775, http://dx.doi.org/10.1016/j.nima.2003.07.067.
[88] C. Arnaboldi, et al., Phys. Rev. Lett. 95 (2005) 142501, http://dx.doi.org/10.1103/PhysRevLett.95.142501.
[89] K. Alfonso, et al., Phys. Rev. Lett. 115 (2015) 102502, http://dx.doi.org/10.1103/PhysRevLett.115.102502.
[90] M. Biassoni, O. Cremonesi, Nucl. Phys. News 26 (1) (2016) 12, http://dx.doi.org/10.1080/10619127.2016.1140971.
[91] G. Wang, et al., 2015, arXiv:1504.03599, phys. ins.-det. accessed 9. May. 2023.
[92] E. Armengaud, et al., Eur. Phys. J. C 77 (2017) 785, http://dx.doi.org/10.1140/epjc/s10052-017-5343-2.
[93] E. Cosulich, et al., Nuclear Phys. A 592 (1) (1995) 59, http://dx.doi.org/10.1016/0375-9474(95)00307-M.
[94] F. Gatti, Nucl. Phys. B - Proc. Suppl. 91 (1) (2001) 293, http://dx.doi.org/10.1016/S0920-5632(00)00954-3.
[95] M. Sisti, et al., Nucl. Instrum. Methods A 520 (1) (2004) 125, http://dx.doi.org/10.1016/j.nima.2003.11.273.
[96] L. Gastaldo, et al., Eur. Phys. J. Spec. Top. 226 (2017) 1623, http://dx.doi.org/10.1140/epjst/e2017-70071-y.
[97] A. Nucciotti, et al., Nucl. Instrum. Methods A 824 (2016) 182, http://dx.doi.org/10.1016/j.nima.2015.09.066.
[98] M.P. Croce, et al., J. Low Temp. Phys. 184 (2016) 958, http://dx.doi.org/10.1007/s10909-015-1451-2.
[99] A. De Rújula, M. Lusignoli, Phys. Lett. B 118 (4) (1982) 429, http://dx.doi.org/10.1016/0370-2693(82)90218-0.
[100] A. Nucciotti, J. Low Temp. Phys. 151 (2008) 597, http://dx.doi.org/10.1007/s10909-008-9718-5.
[101] A. Nucciotti, the MARE collaboration, Nucl. Phys. B - Proc. Suppl. 229–232 (2012) 155, http://dx.doi.org/10.1016/j.nuclphysbps.2012.09.025.
[102] F. Gatti, in: F.S. Porter, D. McCammon, M. Galeazzi, C.K. Stahle (Eds.), AIP Conf. Proc., vol. 605, 2002, p. 429, http://dx.doi.org/10.1063/1.1457679.
[103] A. Alessandrello, et al., Nucl. Instrum. Methods A 320 (1992) 388, http://dx.doi.org/10.1016/0168-9002(92)90799-A.
[104] L. Lesyna, et al., J. Low Temp. Phys. 93 (1993) 779, http://dx.doi.org/10.1007/BF00693512.
[105] M. LeGros, et al., Nucl. Instrum. Methods A 357 (1995) 110, http://dx.doi.org/10.1016/0168-9002(94)01469-8.
[106] R. Ladbury, Phys. Today 51 (1998) 19, http://dx.doi.org/10.1063/1.2805869.
[107] P. de Marcillac, et al., Nature 422 (2003) 876, http://dx.doi.org/10.1038/nature01541.
[108] D.E. Newbury, et al., in: C. Enss (Ed.), Cryogenic Particle Detection, in: Top. Appl. Phys., vol. 99, Springer, Berlin, Heidelberg, New York, 2005, p. 267, http://dx.doi.org/10.1007/10933596_6.
[109] S. Cebrián, et al., Phys. Lett. B 556 (1) (2003) 14, http://dx.doi.org/10.1016/S0370-2693(03)00123-0.
[110] J.N. Ullom, J. Low Temp. Phys. 151 (2008) 746, http://dx.doi.org/10.1007/s10909-008-9749-y.
[111] M. Croce, et al., J. Low Temp. Phys. 167 (2012) 955, http://dx.doi.org/10.1007/s10909-011-0419-0.
[112] C. Bates, et al., J. Low Temp. Phys. 184 (2016) 351, http://dx.doi.org/10.1007/s10909-015-1348-0.
[113] W.B. Doriese, et al., Rev. Sci. Instrum. 88 (5) (2017) 053108, http://dx.doi.org/10.1063/1.4983316.
[114] D. Twerenbold, Nucl. Instrum. Methods A 370 (1996) 253, http://dx.doi.org/10.1016/0168-9002(95)01102-1.
[115] S.E. Labov, et al., in: S. Cooper (Ed.), Proceedings of the 7th International Workshop on Low Temperature Detectors, 1997, p. 82, ISBN 3-00-002266-x, URL https://www.osti.gov/biblio/645067.
[116] G.C. Hilton, et al., Nature 391 (1998) 672, http://dx.doi.org/10.1038/35582.
[117] M. Frank, et al., Mass Spectrom. Rev. 18 (1999) 155, http://dx.doi.org/10.1002/(SICI)1098-2787(1999)18:3/4<155::AID-MAS1>3.0.CO;2-W.
[118] O. Novotný, et al., J. Appl. Phys. 118 (10) (2015) 104503, http://dx.doi.org/10.1063/1.4930036.
[119] D. Wollman, et al., Nucl. Instrum. Methods A 444 (1) (2000) 145, http://dx.doi.org/10.1016/S0168-9002(99)01351-0.
[120] A. Alessandrello, et al., Nucl. Instrum. Methods Phys. Res. B 142 (1998) 163, http://dx.doi.org/10.1016/S0168-583X(98)00279-1.
[121] J.N. Ullom, et al., Nucl. Instrum. Methods A 444 (1) (2000) 385–388, http://dx.doi.org/10.1016/S0168-9002(99)01411-4.
[122] S. Rutzinger, et al., Nucl. Instrum. Methods A 520 (1) (2004) 625–627, http://dx.doi.org/10.1016/j.nima.2003.11.360.
[123] S.J. Smith, et al., J. Low Temp. Phys. 167 (2012) 168, http://dx.doi.org/10.1007/s10909-012-0574-y.
[124] https://www.gsi.de, accessed 09-05-2023, 2022.
[125] https://ganil-spiral2.eu, accessed 01-10-2022, 2022.
[126] https://www.anl.gov, accessed 09-05-2023, 2022.
[127] https://www.riken.jp/en/research/labs/rnc/, accessed 09-05-2023, 2023.
[128] H.H. Gutbrod, et al. (Eds.), FAIR Baseline Technical Report, 2006, ISBN-3-9811298-0-6.
[129] K. Gross, J. Eschke, Nucl. Phys. News 16 (1) (2006) 5–8, http://dx.doi.org/10.1080/10506890600579835.
[130] https://fair-center.eu, accessed 09-05-2023, 2023.
[131] https://frib.msu.edu, accessed 09-05-2023, 2023.
[132] J.C. Yang, et al., Nucl. Instrum. Methods Phys. Res. B 317 (2013) 263, http://dx.doi.org/10.1016/j.nimb.2013.08.046.
[133] S. Jeong, Nucl. Phys. News 26 (4) (2016) 42, http://dx.doi.org/10.1080/10619127.2016.1246033.
[134] C. Vockenhuber, et al., Int. J. Mass Spectr. 223–224 (2003) 713, http://dx.doi.org/10.1016/S1387-3806(02)00944-2.
[135] R. Golser, W. Kutschera, Nucl. Phys. News 27 (3) (2017) 29, http://dx.doi.org/10.1080/10619127.2017.1351183.
[136] A. Dewald, Nucl. Phys. News 27 (3) (2017) 20, http://dx.doi.org/10.1080/10619127.2017.1317177.
[137] P.A. Mandó, Nucl. Phys. News 19 (1) (2009) 5, http://dx.doi.org/10.1080/10506890902740101.
[138] M. De Cesare, et al., Nucl. Instrum. Methods Phys. Res. B 268 (7) (2010) 779, http://dx.doi.org/10.1016/j.nimb.2009.10.029.
[139] D.P. Child, M.A.C. Hotchkis, M.L. Williams, J. Anal. At. Spectrom. 23 (2008) 765, http://dx.doi.org/10.1039/b715788f.
[140] M. López-Lora, et al., Talanta 178 (2018) 202, http://dx.doi.org/10.1016/j.talanta.2017.09.026.
[141] M. Stocker, et al., Nucl. Instrum. Methods Phys. Res. B 240 (2005) 483, http://dx.doi.org/10.1016/j.nimb.2005.06.224.
[142] https://www.jyu.fi/science/en/physics/research, accessed 09-05-2023, 2023.
[143] https://www.mpi-hd.mpg.de/blaum/storage-rings/index.en.html, accessed 06-05-2023, 2023.
[144] https://ebit.llnl.gov, accessed 09-05-2023, 2023.

[145] https://www.ill.eu, accessed 09-05-2023, 2023.
[146] K.W. Shepard, private communicaton, Argonne National Lab., USA, 1988.
[147] W. Henning, private communication, GSI Darmstadt, Germany, Univ. Mainz, Germany, and Argonne National Lab., USA, 1988.
[148] P. Egelhof, et al., Nucl. Instrum. Methods A 370 (1996) 263, http://dx.doi.org/10.1016/0168-9002(95)01105-6.
[149] P. Egelhof, et al., in: L. Brogiato, D.v. Camin, E. Fiorini (Eds.), Proceedings of the 3rd International Workshop on Low Temperature Detectors for Neutrinos and Dark Matter, 1990, p. 289, Edition Frontières, Gif-sur-Yvette Cedex.
[150] J. Meier, et al., in: N.E. Booth, G.L. Salmon (Eds.), Proceedings of the 4th International Workshop on Low Temperature Detectors for Neutrinos and Dark Matter, 1992, p. 173, Edition Frontières, Gif-sur-Yvette Cedex.
[151] A.v. Kienlin, et al., in: N.E. Booth, G.L. Salmon (Eds.), Proceedings of the 4th International Workshop on Low Temperature Detectors for Neutrinos and Dark Matter, 1992, p. 377, Edition Frontières, Gif-sur-Yvette Cedex.
[152] A.v. Kienlin, et al., Nucl. Instrum. Methods A 368 (1996) 815, http://dx.doi.org/10.1016/0168-9002(95)00562-5.
[153] H.J. Meier, et al., Nucl. Instrum. Methods A 370 (1996) 259, http://dx.doi.org/10.1016/0168-9002(95)01104-8.
[154] S. Kraft-Bermuth, et al., Rev. Sci. Instrum. 80 (2009) 103304, http://dx.doi.org/10.1063/1.3213622.
[155] A. Echler, et al., J. Low Temp. Phys. 167 (2012) 949, http://dx.doi.org/10.1007/s10909-012-0485-y.
[156] J.F. Ziegler, Nucl. Instrum. Methods Phys. Res. B (1998) 141, http://dx.doi.org/10.1016/S0168-583X(97)00664-2.
[157] A. Bleile, et al., AIP Conf. Proc. 605 (2002) 409, http://dx.doi.org/10.1063/1.1457674.
[158] S. Kraft-Bermuth, et al., J. Phys. B 50 (2017) 055603, http://dx.doi.org/10.1088/1361-6455/50/5/055603.
[159] S. Dubey, et al., Phys. Rev. C 102 (2020) 044602, http://dx.doi.org/10.1103/PhysRevC.102.044602.
[160] S. Dubey, et al., Phys. Rev. C 104 (2021) 034621, http://dx.doi.org/10.1103/PhysRevC.104.034621.
[161] S. Dubey, et al., to be published, 2023.
[162] A. Echler, et al., Nucl. Instrum. Methods Phys. Res. B 391 (2017) 38, http://dx.doi.org/10.1016/j.nimb.2016.10.011.
[163] W. Kutschera, Int. J. Mass Spectr. 242 (2) (2005) 145, http://dx.doi.org/10.1016/j.ijms.2004.10.029.
[164] S. Kraft-Bermuth, Ph.D. thesis, Johannes Gutenberg Universität Mainz, 2004. http://dx.doi.org/10.25358/openscience-3434.
[165] S. Kraft, et al., Nucl. Instrum. Methods A 520 (2004) 63, http://dx.doi.org/10.1016/j.nima.2003.11.221.
[166] S. Kraft-Bermuth, et al., Phys. Scr. T 166 (2015) 014028, http://dx.doi.org/10.1088/0031-8949/2015/T166/014028.
[167] S. Kraft-Bermuth, et al., J. Low Temp. Phys. 176 (2014) 1002, http://dx.doi.org/10.1007/s10909-013-1002-7.
[168] T. Stöhlker, et al., Lecture Notes in Phys. 745 (2008) 157, http://dx.doi.org/10.1007/978-3-540-75479-4_9.
[169] V. Andrianov, et al., AIP Conf. Proc. 1185 (2009) 99, http://dx.doi.org/10.1063/1.3292459.
[170] F.S. Porter, et al., Can. J. Phys. 86 (2008) 231, http://dx.doi.org/10.1139/p07-147.
[171] D.B. Thorn, et al., Can. J. Phys. 86 (2008) 241, http://dx.doi.org/10.1139/p07-134.
[172] P. Beiersdorfer, Can. J. Phys. 86 (2008) 1, http://dx.doi.org/10.1139/p07-135.
[173] C.K. Stahle, et al., Nucl. Instrum. Methods A 319 (1) (1992) 393, http://dx.doi.org/10.1016/0168-9002(92)90584-Q.
[174] D.B. Thorn, et al., Phys. Rev. Lett. 103 (2009) 163001, http://dx.doi.org/10.1103/PhysRevLett.103.163001.
[175] B.R. Beck, et al., Phys. Rev. Lett. 98 (2007) 142501, http://dx.doi.org/10.1103/PhysRevLett.98.142501.
[176] E. Silver, et al., Nucl. Instrum. Methods A 520 (2004) 60, http://dx.doi.org/10.1016/j.nima.2003.11.220.
[177] G. Weber, et al., Annual Report, Helmholtz-Institut Jena, 2021, p. 47.
[178] D. McCammon, in: C. Enss (Ed.), Cryogenic Particle Detection, in: Top. Appl. Phys., vol. 99, Springer, Berlin, Heidelberg, New York, 2005, p. 1, http://dx.doi.org/10.1007/10933596_1.
[179] D. McCammon, in: C. Enss (Ed.), Cryogenic Particle Detection, in: Top. Appl. Phys., vol. 99, Springer, Berlin, Heidelberg, New York, 2005, p. 35, http://dx.doi.org/10.1007/10933596_2.
[180] K.D. Irwin, G.C. Hilton, in: C. Enss (Ed.), Cryogenic Particle Detection, in: Top. Appl. Phys., vol. 99, Springer, Berlin, Heidelberg, New York, 2005, p. 63, http://dx.doi.org/10.1007/10933596_3.
[181] A. Fleischmann, C. Enss, G.M. Seidel, in: C. Enss (Ed.), Cryogenic Particle Detection, in: Top. Appl. Phys., vol. 99, Springer, Berlin, Heidelberg, New York, 2005, p. 151, http://dx.doi.org/10.1007/10933596_4.
[182] P. Lerch, A. Zehnder, in: C. Enss (Ed.), Cryogenic Particle Detection, in: Top. Appl. Phys., vol. 99, Springer, Berlin, Heidelberg, New York, 2005, p. 217, http://dx.doi.org/10.1007/10933596_5.
[183] P. Sigmund, Nucl. Instrum. Methods Phys. Res. B 135 (1) (1998) 1, http://dx.doi.org/10.1016/S0168-583X(97)00638-1.
[184] A. Echler, Ph.D. thesis, Johannes Gutenberg Universität Mainz, 2013. http://dx.doi.org/10.25358/openscience-3653.
[185] W. Shockley, W.T. Read, Phys. Rev. 87 (1952) 835, http://dx.doi.org/10.1103/PhysRev.87.835.
[186] R.N. Hall, Phys. Rev. 87 (1952) 387, http://dx.doi.org/10.1103/PhysRev.87.387.
[187] M. Toulemonde, et al., Nucl. Instrum. Methods Phys. Res. B 116 (1996) 37, http://dx.doi.org/10.1016/0168-583X(96)00007-9.
[188] L. Pitaevskii, in: K.H. Bennemann, J.B. Ketterson (Eds.), Superconductivity: Conventional and Unconventional Superconductors, Springer Heidelberg Berlin, 2008, p. 27.
[189] R.L. Kelley, et al., J. Low Temp. Phys. 93 (1993) 225, http://dx.doi.org/10.1007/BF00693424.
[190] S. Kempf, et al., J. Low Temp. Phys. 193 (2018) 365, http://dx.doi.org/10.1007/s10909-018-1891-6.
[191] A. Bleile, et al., Nucl. Instrum. Methods A 444 (2000) 488, http://dx.doi.org/10.1016/S0168-9002(99)01429-1.
[192] P.A. Scholz, et al., Nucl. Instrum. Methods Phys. Res. B 408 (2017) 323, http://dx.doi.org/10.1016/j.nimb.2017.04.078.
[193] E. Steinbauer, et al., Nucl. Instrum. Methods Phys. Res. B 85 (1) (1994) 642, http://dx.doi.org/10.1016/0168-583X(94)95898-X.
[194] J. Zhang, et al., Phys. Rev. B 48 (1993) 2312, http://dx.doi.org/10.1103/PhysRevB.48.2312.
[195] N. Wang, et al., Phys. Rev. B 41 (1990) 3761, http://dx.doi.org/10.1103/PhysRevB.41.3761.
[196] B.I. Shklovskii, A.L. Efros, Electronic Properties of Doped Semiconductors, Springer Berlin Heidelberg, 1984.
[197] W. Shockley, Solid-State Electron. 2 (1) (1961) 35, http://dx.doi.org/10.1016/0038-1101(61)90054-5.
[198] J.C. Mather, Appl. Opt. 21 (1982) 1125, http://dx.doi.org/10.1364/AO.21.001125.
[199] C.A. Hamilton, Cryogenics 20 (5) (1980) 235, http://dx.doi.org/10.1016/0011-2275(80)90046-6.
[200] J. Lindhard, et al., Mat. Fys. Medd. Dan. Vid. Selsk. 33 (1963) 1.
[201] W. Bolse, Mater. Sci. Eng. R 12 (1994) 53, http://dx.doi.org/10.1016/0927-796X(94)90001-9.
[202] J. Amaré, et al., J. Phys.: Conf. Ser. 39 (2006) 200, http://dx.doi.org/10.1088/1742-6596/39/1/051.
[203] D. McCammon, et al., IEEE Trans. Nucl. Sci. 33 (1) (1986) 235, http://dx.doi.org/10.1109/TNS.1986.4337089.
[204] D. McCammon, et al., in: L. Brogiato, D. v. Camin, E. Fiorine (Eds.), Proceedings of the 3rd International Workshop on Low Temperature Detectors for Neutrinos and Dark Matter, 1990, p. 213, Edition Frontières, Gif-sur-Yvette Cedex.
[205] M. Toulemonde, et al., Nucl. Instrum. Methods Phys. Res. B 46 (1990) 64, http://dx.doi.org/10.1016/0168-583X(90)90670-P.
[206] D. Liu, et al., AIP Conf. Proc. 605 (2002) 87, http://dx.doi.org/10.1063/1.1457602.
[207] J.B. Moulton, et al., Nucl. Instrum. Methods 157 (2) (1978) 325, http://dx.doi.org/10.1016/0029-554X(78)90309-9.
[208] W.H. Trzaska, et al., Nucl. Instrum. Methods Phys. Res. B 267 (2009) 3403, http://dx.doi.org/10.1016/j.nimb.2009.08.006.
[209] W.H. Trzaska, et al., Nucl. Instrum. Methods Phys. Res. B 195 (2002) 147, http://dx.doi.org/10.1016/S0168-583X(02)01255-7.

[210] M. Ogihara, et al., Nucl. Instrum. Methods A 251 (2) (1986) 313, http://dx.doi.org/10.1016/0168-9002(86)90796-5.
[211] H.F. Beyer, et al., J. Phys. B 48 (2015) 144010, http://dx.doi.org/10.1088/0953-4075/48/14/144010.
[212] A. Bracco, et al. (Eds.), NuPECC Long Range Plan 2017 Perspectives in Nuclear Physics, European Science Foundation and ELI-NP, 2017, accessed 18-02-2023. URL http://www.nupecc.org/pub/lrp17/lrp2017.pdf.
[213] J.F. Ziegler, M.D. Ziegler, J.P. Biersack, Nucl. Instrum. Methods Phys. Res. B 268 (2010) 1818, http://dx.doi.org/10.1016/j.nimb.2010.02.091.
[214] W. de Boer, et al., Phys. Status Solidi A 204 (2007) 3004, http://dx.doi.org/10.1002/pssa.200776327.
[215] H.B.G. Casimir, Physica 5 (6) (1938) 495, http://dx.doi.org/10.1016/S0031-8914(38)80162-2.
[216] B. Canut, et al., Phys. Rev. B 51 (1995) 12194, http://dx.doi.org/10.1103/PhysRevB.51.12194.
[217] A.v. Kienlin, Ph.D. thesis, Johannes Gutenberg Universität Mainz, 1993.
[218] H.J. Meier, Ph.D. thesis, Johannes Gutenberg Universität Mainz, 1994.
[219] K. Djotni, Master's thesis, Johannes Gutenberg Universität Mainz, 1991.
[220] H.J. Meier, Master's thesis, Johannes Gutenberg Universität Mainz, 1990.
[221] A. Echler, Master's thesis, Johannes Gutenberg Universität Mainz, 2007.
[222] J. Meier, et al., J. Low Temp. Phys. 93 (1993) 231, http://dx.doi.org/10.1007/BF00693425.
[223] P. Grabitz, Ph.D. thesis, Johannes Gutenberg Universität Mainz, 2019. http://dx.doi.org/10.25358/openscience-2343.
[224] S. Dubey, Ph.D. thesis, Johannes Gutenberg Universität Mainz, 2019. http://dx.doi.org/10.25358/openscience-3764.
[225] A.E. Szymkowiak, et al., J. Low Temp. Phys. 93 (3/4) (1993) 281, http://dx.doi.org/10.1007/BF00693433.
[226] W.E. Gifford, in: K.D. Timmerhaus (Ed.), Advances in Cryogenic Engineering, Springer US, Boston, MA, 1966, p. 152.
[227] A.E. Weinbach, Master's thesis, Johannes Gutenberg Universität Mainz, 1995.
[228] H.J. Meier, et al., Nuclear Phys. A 626 (1997) 451c, http://dx.doi.org/10.1016/S0375-9474(97)00569-1.
[229] P. Grabitz, Master's thesis, Johannes Gutenberg Universität Mainz, Staatsexamensarbeit, 2012.
[230] W. Lauterfeld, Master's thesis, Johannes Gutenberg Universität Mainz, 2016.
[231] M. Steck, Y.A. Litvinov, Prog. Part. Nucl. Phys. 115 (2020) 103811, http://dx.doi.org/10.1016/j.ppnp.2020.103811.
[232] W. Böhmer, Master's thesis, Johannes Gutenberg Universität Mainz, 1991.
[233] O. Hahn, F. Strassmann, Naturwissenschaften 27 (1939) 11, http://dx.doi.org/10.1007/BF01488241.
[234] O. Hahn, F. Strassmann, Naturwissenschaften 27 (1939) 89, http://dx.doi.org/10.1007/BF01488988.
[235] L. Meitner, O.R. Frisch, Nature 143 (1939) 471, http://dx.doi.org/10.1038/143471a0.
[236] R. Vandenbosch, J.R. Huizenga, Nuclear Fission, New York Academic, 1973, URL https://www.osti.gov/biblio/4359815.
[237] A.C. Wahl, At. Data Nucl. Data Tables 39 (1) (1988) 1, http://dx.doi.org/10.1016/0092-640x(88)90016-2.
[238] C. Wagemans (Ed.), The Nuclear Fission Process, CRC Press, Boca Raton, Ann Arbor, Boston, London, 1991.
[239] H.G. Börner, F. Gönnenwein, The Neutron: A Tool and an Object in Nuclear and Particle Physics, World Scientific, Singapore, 2012, http://dx.doi.org/10.1142/7283.
[240] B.D. Wilkins, E.P. Steinberg, R.R. Chasman, Phys. Rev. C 14 (1976) 1832, http://dx.doi.org/10.1103/PhysRevC.14.1832.
[241] U. Brosa, S. Grossmann, A. Müller, Phys. Rep. 197 (4) (1990) 167, http://dx.doi.org/10.1016/0370-1573(90)90114-H.
[242] P. Möller, et al., Nature 409 (2001) 785, http://dx.doi.org/10.1038/35057204.
[243] H. Goutte, et al., Phys. Rev. C 71 (2005) 024316, http://dx.doi.org/10.1103/PhysRevC.71.024316.
[244] A. Bail, et al., Phys. Rev. C 84 (2011) 034605, http://dx.doi.org/10.1103/PhysRevC.84.034605.
[245] T. Ichikawa, et al., Phys. Rev. C 86 (2012) 024610, http://dx.doi.org/10.1103/PhysRevC.86.024610.
[246] K.-H. Schmidt, et al., Nucl. Data Sheets 131 (2016) 107, http://dx.doi.org/10.1016/j.nds.2015.12.009.
[247] N. Schunck, L.M. Robledo, Rep. Progr. Phys. 79 (11) (2016) 116301, http://dx.doi.org/10.1088/0034-4885/79/11/116301.
[248] A.N. Andreyev, K. Nishio, K.-H. Schmidt, Rep. Progr. Phys. 81 (1) (2018) 016301, http://dx.doi.org/10.1088/1361-6633/aa82eb.
[249] K.-H. Schmidt, B. Jurado, Rep. Progr. Phys. 81 (10) (2018) 106301, http://dx.doi.org/10.1088/1361-6633/aacfa7.
[250] H. Naik, R.J. Singh, R.H. Iyer, J. Phys. G: Nucl. Part. Phys. 30 (2) (2004) 107, http://dx.doi.org/10.1088/0954-3899/30/2/010.
[251] N. Bohr, J.A. Wheeler, Phys. Rev. 56 (1939) 426, http://dx.doi.org/10.1103/PhysRev.56.426.
[252] M. Goeppert-Mayer, Phys. Rev. 74 (1948) 235, http://dx.doi.org/10.1103/PhysRev.74.235.
[253] O. Haxel, J.H.D. Jensen, H.E. Suess, Phys. Rev. 75 (1949) 1766, http://dx.doi.org/10.1103/PhysRev.75.1766.2.
[254] A.J.M. Plompen, et al., Eur. Phys. J. A 56 (2020) 181, http://dx.doi.org/10.1140/epja/s10050-020-00141-9.
[255] D.A. Brown, et al., Nucl. Data Sheets 148 (2018) 1, http://dx.doi.org/10.1016/j.nds.2018.02.001.
[256] K. Shibata, et al., J. Nucl. Sci. Technol. 48 (1) (2011) 1, http://dx.doi.org/10.1080/18811248.2011.9711675.
[257] P. Dimitriou, F.J. Hambsch, S. Pomp, INDC, no. INDC(NDS)-0713, IAEA, 2016, URL https://www-nds.iaea.org/publications/indc/indc-nds-0713/.
[258] P. Armbruster, et al., Z. Phys. A 355 (1996) 191, http://dx.doi.org/10.1007/bf02769684.
[259] P. Armbruster, et al., Phys. Rev. Lett. 93 (2004) 212701, http://dx.doi.org/10.1103/PhysRevLett.93.212701.
[260] M. Bernas, et al., Nuclear Phys. A 725 (2003) 213, http://dx.doi.org/10.1016/S0375-9474(03)01576-8.
[261] M. Bernas, et al., Nuclear Phys. A 765 (1) (2006) 197, http://dx.doi.org/10.1016/j.nuclphysa.2005.10.009.
[262] S. Steinhäuser, et al., Nuclear Phys. A 634 (1–2) (1998) 89–111, http://dx.doi.org/10.1016/S0375-9474(98)00148-1.
[263] C. Donzaud, et al., Eur. Phys. J. A 1 (1998) 407, http://dx.doi.org/10.1007/s100500050076.
[264] K.-H. Schmidt, et al., Nuclear Phys. A 665 (3–4) (2000) 221, http://dx.doi.org/10.1016/S0375-9474(99)00384-X.
[265] J.L. Rodríguez-Sánchez, et al., Phys. Rev. C 94 (2016) 034605, http://dx.doi.org/10.1103/PhysRevC.94.034605.
[266] E. Pellereau, et al., Phys. Rev. C 95 (2017) 054603, http://dx.doi.org/10.1103/PhysRevC.95.054603.
[267] A. Chatillon, et al., Phys. Rev. C 99 (2019) 054628, http://dx.doi.org/10.1103/PhysRevC.99.054628.
[268] M. Caamaño, et al., Phys. Rev. C 88 (2013) 024605, http://dx.doi.org/10.1103/PhysRevC.88.024605.
[269] H.L. Anderson, E. Fermi, A.V. Grosse, Phys. Rev. 59 (1) (1941) 52, http://dx.doi.org/10.1103/physrev.59.52.
[270] J.K. Dickens, Nucl. Sci. Eng. 70 (2) (1979) 177, http://dx.doi.org/10.13182/nse79-a19650.
[271] H. Thierens, et al., Phys. Rev. C 29 (1984) 498, http://dx.doi.org/10.1103/PhysRevC.29.498.
[272] P. Schillebeeckx, et al., Nuclear Phys. A 580 (1) (1994) 15, http://dx.doi.org/10.1016/0375-9474(94)90812-5.
[273] D.F. da Cruz, D. Rochman, A. Koning, Nucl. Data Sheets 118 (2014) 531–534, http://dx.doi.org/10.1016/j.nds.2014.04.126.
[274] E. Moll, et al., Nucl. Instrum. Methods 123 (3) (1975) 615, http://dx.doi.org/10.1016/0029-554x(75)90219-0.
[275] P. Armbruster, et al., Nucl. Instrum. Methods 139 (1976) 213, http://dx.doi.org/10.1016/0029-554x(76)90677-7.
[276] H.-G. Clerc, et al., Z. Phys. A 274 (1975) 203, http://dx.doi.org/10.1007/BF01437731.
[277] C. Schmitt, et al., Nuclear Phys. A 430 (1) (1984) 21, http://dx.doi.org/10.1016/0375-9474(84)90191-X.
[278] H.-G. Clerc, et al., Nuclear Phys. A 452 (2) (1986) 277, http://dx.doi.org/10.1016/0375-9474(86)90310-6.
[279] M. Djebara, et al., Nuclear Phys. A 496 (2) (1989) 346, http://dx.doi.org/10.1016/0375-9474(89)90179-6.
[280] W. Schwab, et al., Nuclear Phys. A 577 (3–4) (1994) 674, http://dx.doi.org/10.1016/0375-9474(94)90939-3.
[281] O. Serot, et al., Nucl. Data Sheets 119 (2014) 320, http://dx.doi.org/10.1016/j.nds.2014.08.088.
[282] I. Tsekhanovich, et al., Nuclear Phys. A 688 (3–4) (2001) 633, http://dx.doi.org/10.1016/S0375-9474(00)00586-8.

[283] H.O. Denschlag, in: D.N. Poenaru, W. Greiner (Eds.), Experimental Techniques in Nuclear Physics, De Gruyter, 1997, p. 535, http://dx.doi.org/10.1515/9783110809824.535.
[284] H.O. Denschlag, Nucl. Sci. Eng. 94 (4) (1986) 337, http://dx.doi.org/10.13182/NSE86-A18345.
[285] H.O. Denschlag, J. Radioanal. Nucl. Chem. 243 (2000) 69, http://dx.doi.org/10.1023/A:1006711112593.
[286] M. Bresesti, et al., J. Inorg. Nucl. Chem. 29 (5) (1967) 1189, http://dx.doi.org/10.1016/0022-1902(67)80356-7.
[287] E.A.C. Crouch, At. Data Nucl. Data Tables 19 (5) (1977) 417, http://dx.doi.org/10.1016/0092-640X(77)90023-7.
[288] G. Rudstam, et al., Radiochim. Acta 49 (4) (1990) 155, http://dx.doi.org/10.1524/ract.1990.49.4.155.
[289] J. Galy, et al., Eur. Phys. J. A 8 (2000) 331, http://dx.doi.org/10.1007/s100500070086.
[290] S. Julien-Laferrière, et al., Phys. Rev. C 102 (3) (2020) 034602, http://dx.doi.org/10.1103/PhysRevC.102.034602.
[291] U. Quade, et al., Nuclear Phys. A 487 (1) (1988) 1, http://dx.doi.org/10.1016/0375-9474(88)90127-3.
[292] W. Lang, et al., Nuclear Phys. A 345 (1980) 34, http://dx.doi.org/10.1016/0375-9474(80)90411-X.
[293] U. Quade, K. Rudolph, G. Siegert, Nucl. Instrum. Methods 164 (3) (1979) 435, http://dx.doi.org/10.1016/0029-554x(79)90075-2.
[294] J.P. Bocquet, R. Brissot, H.R. Faust, Nucl. Instrum. Methods A 267 (2–3) (1988) 466, http://dx.doi.org/10.1016/0168-9002(88)90487-1.
[295] J.P. Bocquet, R. Brissot, Nuclear Phys. A 502 (1989) 213c, http://dx.doi.org/10.1016/0375-9474(89)90663-5.
[296] N. Bohr, Mat. Fys. Medd. Dan. Vid. Selsk 18 (8) (1948).
[297] P. Sigmund, Stopping of Heavy Ions: A Theoretical Approach, Springer Tracts in Modern Physics, 204, Springer, Berlin, Heidelberg, New York, 2004, http://dx.doi.org/10.1007/b98483.
[298] H. Geissel, et al., Nucl. Instrum. Methods Phys. Res. B 195 (2002) 3, http://dx.doi.org/10.1016/S0168-583X(02)01311-3.
[299] H. Bethe, Ann. Phys. 397 (1930) 325, http://dx.doi.org/10.1002/andp.19303970303.
[300] J.S. Forster, et al., Nucl. Instrum. Methods 136 (2) (1976) 349, http://dx.doi.org/10.1016/0029-554x(76)90218-4.
[301] L.C. Northcliffe, R.F. Schilling, At. Data Nucl. Data Tables 7 (3–4) (1970) 233, http://dx.doi.org/10.1016/s0092-640x(70)80016-x.
[302] N. Bohr, Lond. Edinb. Dublin Philos. Mag. J. Sci. 30 (178) (1915) 581, http://dx.doi.org/10.1080/14786441008635432.
[303] U. Köster, et al., Nucl. Instrum. Methods A 613 (2010) 363, http://dx.doi.org/10.1016/j.nima.2009.09.078.
[304] S. Dubey, et al., J. Low Temp. Phys. 193 (2018) 1257, http://dx.doi.org/10.1007/s10909-018-1988-y.
[305] P. Grabitz, et al., J. Low Temp. Phys. 184 (3–4) (2016) 944–951, http://dx.doi.org/10.1007/s10909-016-1566-0.
[306] S. Kraft-Bermuth, et al., to be published, 2023.
[307] http://www.bl.physik.uni-muenchen.de/tandem/besucherinfo/besucherinfo.pdf, accessed: 09-05-2023, 2023.
[308] N.S. Wu, M. Hu, Chromatographia 28 (7–8) (1989) 415, http://dx.doi.org/10.1007/bf02261025.
[309] G.N. Knyadzeva, et al., Nucl. Instrum. Methods Phys. Res. B 248 (2006) 7, http://dx.doi.org/10.1016/j.nimb.2006.04.071.
[310] M.J. Cubison, J.L. Jimenez, Atmos. Meas. Tech. 8 (6) (2015) 2333, http://dx.doi.org/10.5194/amt-8-2333-2015.
[311] Y.K. Gupta, et al., Phys. Rev. C 96 (2017) 014608, http://dx.doi.org/10.1103/PhysRevC.96.014608.
[312] H. Wohlfarth, et al., Z. Phys. A 287 (2) (1978) 153, http://dx.doi.org/10.1007/bf01408085.
[313] B.Q. Lee, Ph.D. thesis, Australian National University, 2017.
[314] G. Mention, et al., Phys. Rev. D 83 (7) (2011) 073006, http://dx.doi.org/10.1103/physrevd.83.073006.
[315] A.A. Sonzogni, T.D. Johnson, E.A. McCutchan, Phys. Rev. C 91 (1) (2015) 011301, http://dx.doi.org/10.1103/physrevc.91.011301.
[316] K. Schreckenbach, et al., Phys. Lett. B 99 (3) (1981) 251, http://dx.doi.org/10.1016/0370-2693(81)91120-5.
[317] F. von Feilitzsch, A.A. Hahn, K. Schreckenbach, Phys. Lett. B 118 (1) (1982) 162, http://dx.doi.org/10.1016/0370-2693(82)90622-0.
[318] K. Schreckenbach, et al., Phys. Lett. B 160 (4) (1985) 325, http://dx.doi.org/10.1016/0370-2693(85)91337-1.
[319] A. Hahn, et al., Phys. Lett. B 218 (3) (1989) 365, http://dx.doi.org/10.1016/0370-2693(89)91598-0.
[320] J.H. Choi, et al., Phys. Rev. Lett. 116 (2016) 211801, http://dx.doi.org/10.1103/PhysRevLett.116.211801.
[321] F.P. An, et al., Phys. Rev. Lett. 116 (2016) 061801, http://dx.doi.org/10.1103/PhysRevLett.116.061801.
[322] Y. Abe, et al., J. High Energy Phys. 2016 (01) (2016) 163, http://dx.doi.org/10.1007/JHEP01(2016)163.
[323] B.R. Davis, et al., Phys. Rev. C 19 (1979) 2259, http://dx.doi.org/10.1103/PhysRevC.19.2259.
[324] M. Fallot, et al., Phys. Rev. Lett. 109 (20) (2012) 202504, http://dx.doi.org/10.1103/physrevlett.109.202504.
[325] D.A. Dwyer, T.J. Langford, Phys. Rev. Lett. 114 (1) (2015) 012502, http://dx.doi.org/10.1103/physrevlett.114.012502.
[326] H. Almazán, et al., Phys. Rev. Lett. 121 (2018) 161801, http://dx.doi.org/10.1103/PhysRevLett.121.161801.
[327] J. Ashenfelter, et al., Phys. Rev. Lett. 121 (2018) 251802, http://dx.doi.org/10.1103/PhysRevLett.121.251802.
[328] G. Bak, et al., Phys. Rev. Lett. 121 (2018) 201801, http://dx.doi.org/10.1103/PhysRevLett.121.201801.
[329] D. Adey, et al., Phys. Rev. Lett. 121 (2018) 241805, http://dx.doi.org/10.1103/PhysRevLett.121.241805.
[330] Y.J. Ko, et al., Phys. Rev. Lett. 118 (2017) 121802, http://dx.doi.org/10.1103/PhysRevLett.118.121802.
[331] A.-A. Zakari-Issoufou, et al., Phys. Rev. Lett. 115 (2015) 102503, http://dx.doi.org/10.1103/PhysRevLett.115.102503.
[332] B.C. Rasco, et al., Phys. Rev. Lett. 117 (2016) 092501, http://dx.doi.org/10.1103/PhysRevLett.117.092501.
[333] A. Fijałkowska, et al., Phys. Rev. Lett. 119 (2017) 052503, http://dx.doi.org/10.1103/PhysRevLett.119.052503.
[334] S.V. Tipnis, et al., Phys. Rev. C 58 (2) (1998) 905, http://dx.doi.org/10.1103/physrevc.58.905.
[335] A.A. Sonzogni, et al., Phys. Rev. Lett. 116 (2016) 132502, http://dx.doi.org/10.1103/PhysRevLett.116.132502.
[336] Y. Abe, et al., Phys. Rev. Lett. 108 (2012) 131801, http://dx.doi.org/10.1103/PhysRevLett.108.131801.
[337] P. Egelhof, et al., Application of Calorimetric Low Temperature Detectors for Investigation of Z-Distributions of Fission Fragments, Institut Laue-Langevin (ILL), 2015, http://dx.doi.org/10.5291/ILL-DATA.3-01-637.
[338] P. Egelhof, et al., Application of Calorimetric Low Temperature Detectors for Investigation of Z-Distributions of Fission Fragments, Institut Laue-Langevin (ILL), 2016, http://dx.doi.org/10.5291/ILL-DATA.3-01-646.
[339] F.L. Lisman, et al., Nucl. Sci. Eng. 42 (1970) 191, http://dx.doi.org/10.13182/NSE70-A19500.
[340] G. Siegert, et al., Phys. Lett. B 53 (1) (1974) 45, http://dx.doi.org/10.1016/0370-2693(74)90339-6.
[341] G. Siegert, et al., Phys. Rev. C 14 (1976) 1864, http://dx.doi.org/10.1103/PhysRevC.14.1864.
[342] http://www.khschmidts-nuclear-web.eu/GEF-2018-1-1.html, accessed 06-05-2023, 2023.
[343] A.E. Norris, A.C. Wahl, Phys. Rev. 146 (1966) 926, http://dx.doi.org/10.1103/PhysRev.146.926.
[344] R.B. Strittmatter, Ph.D. thesis, University of Illinois, 1978.
[345] J.K. Dickens, J.W. McConnell, Nucl. Sci. Eng. 73 (1) (1980) 42, http://dx.doi.org/10.13182/NSE80-A18707.
[346] J.F. Berger, M. Girod, D. Gogny, Nuclear Phys. A 428 (1984) 23, http://dx.doi.org/10.1016/0375-9474(84)90240-9.
[347] J.-F. Lemaître, et al., Phys. Rev. C 99 (2019) 034612, http://dx.doi.org/10.1103/PhysRevC.99.034612.
[348] S. Julien-Laferriére, Ph.D. thesis, Université Grenoble-Alpes, 2018.
[349] S. Julien-Laferriére, et al., to be published.
[350] A. Göök, F.-J. Hambsch, S. Oberstedt, EPJ Web Conf. 239 (2020) 05009, http://dx.doi.org/10.1051/epjconf/202023905009.
[351] B.L. Tracy, et al., Phys. Rev. C 5 (1) (1972) 222, http://dx.doi.org/10.1103/physrevc.5.222.
[352] A.C. Wahl, J. Radioanal. Chem. 55 (1) (1980) 111, http://dx.doi.org/10.1007/bf02514543.
[353] H. Nifenecker, et al., Z. Phys. A 308 (1) (1982) 39, http://dx.doi.org/10.1007/BF01415847.

[354] F. Rejmund, et al., Nuclear Phys. A 678 (3) (2000) 215, http://dx.doi.org/10.1016/S0375-9474(00)00322-5.
[355] B. Jurado, K.-H. Schmidt, J. Phys. G 42 (5) (2015) 055101, http://dx.doi.org/10.1088/0954-3899/42/5/055101.
[356] G. Simon, et al., Nucl. Instrum. Methods A 286 (1) (1990) 220, http://dx.doi.org/10.1016/0168-9002(90)90224-T.
[357] A. Wambersie, et al., J. ICRU 5 (1) (2005) iii, http://dx.doi.org/10.1093/jicru_ndi002.
[358] H. Paul, Nucl. Instrum. Methods Phys. Res. B 261 (1) (2007) 1176, http://dx.doi.org/10.1016/j.nimb.2007.04.113.
[359] H. Geissel, G. Münzenberg, K. Riisager, Annu. Rev. Nucl. Part. Sci. 45 (1) (1995) 163, http://dx.doi.org/10.1146/annurev.ns.45.120195.001115.
[360] G. Kraft, Progr. Part. Nucl. Phys. 45 (2000) S473, http://dx.doi.org/10.1016/S0146-6410(00)00112-5.
[361] G. Maynard, et al., in: C. Labaune, W.J. Hogan, K.A. Tanaka (Eds.), Inertial Fusion Sciences and Applications 99, Editions Scientifiques et Medicales Elsevier SAS, France, 2000, p. 495.
[362] D.S. Gemmell, Rev. Modern Phys. 46 (1) (1974) 129, http://dx.doi.org/10.1103/RevModPhys.46.129.
[363] G. Lulli, et al., Nucl. Instrum. Methods Phys. Res. B 193 (1) (2002) 103, http://dx.doi.org/10.1016/S0168-583X(02)00734-6.
[364] P. Sigmund, A. Schinner, Nucl. Instrum. Methods Phys. Res. B 195 (2002) 64, http://dx.doi.org/10.1016/S0168-583X(01)01162-4.
[365] P. Sigmund, 2017, private communication.
[366] P.L. Grande, G. Schiwietz, Nucl. Instrum. Methods Phys. Res. B 267 (6) (2009) 859, http://dx.doi.org/10.1016/j.nimb.2009.02.017.
[367] P.L. Grande, G. Schiwietz, 2012, www.casp-program.org.
[368] J.F. Ziegler, 2023, www.srim.org, accessed 01-05-2023.
[369] S.P. Ahlen, Rev. Modern Phys. 52 (1980) 121, http://dx.doi.org/10.1103/RevModPhys.52.121.
[370] J. Lindhard, A.H. Sörensen, Phys. Rev. A 53 (1996) 2443, http://dx.doi.org/10.1103/PhysRevA.53.2443.
[371] Y. Zhang, Nucl. Instrum. Methods Phys. Res. B 196 (2002) 1, http://dx.doi.org/10.1016/S0168-583X(02)01246-6.
[372] W.H. Trzaska, et al., Nucl. Instrum. Methods Phys. Res. B 183 (2001) 203, http://dx.doi.org/10.1016/S0168-583X(01)00728-5.
[373] A. Javanainen, et al., IEEE Trans. Nucl. Sci. 54 (4) (2007) 1158, http://dx.doi.org/10.1109/TNS.2007.895121.
[374] H. Paul, Electronic stopping power of stopping for ions, 2023, https://www-nds.iaea.org/stopping/, accessed: 09-05-2023.
[375] H.H. Andersen, et al., Kgl. Danske Videnskab. Selsk. Mat.-Fys. Medd 35 (4) (1966).
[376] H.H. Andersen, et al., Phys. Rev. 153 (1967) 338, http://dx.doi.org/10.1103/PhysRev.153.338.
[377] A. Echler, et al., J. Low Temp. Phys. 176 (2014) 1033, http://dx.doi.org/10.1007/s10909-013-1043-y.
[378] F. Busch, et al., Nucl. Instrum. Methods 171 (1980) 71, http://dx.doi.org/10.1016/0029-554X(80)90011-7.
[379] M. Rossi, et al., Nucl. Instrum. Methods Phys. Res. B 347 (2015) 39, http://dx.doi.org/10.1016/j.nimb.2015.01.055.
[380] H. Geissel, et al., Various datasets summarized in the electronic library of H. Paul [374], 2022.
[381] H. Geissel, et al., Nucl. Instrum. Methods 194 (1982) 21, http://dx.doi.org/10.1016/0029-554X(82)90483-9.
[382] R. Bimbot, et al., Nucl. Instrum. Methods 174 (1) (1980) 231, http://dx.doi.org/10.1016/0029-554X(80)90436-X.
[383] H. Pape, H.G. Clerc, K.H. Schmidt, Z. Phys. A 286 (1978) 159, http://dx.doi.org/10.1007/BF01408970.
[384] M.D. Brown, C.D. Moak, Phys. Rev. B 6 (1972) 90, http://dx.doi.org/10.1103/PhysRevB.6.90.
[385] S. Datz, T.S. Noggle, C.D. Moak, Nucl. Instrum. Methods 38 (1965) 221, http://dx.doi.org/10.1016/0029-554X(65)90142-4.
[386] G. Schiwietz, P.L. Grande, Nucl. Instrum. Methods Phys. Res. B 273 (2012) 1, http://dx.doi.org/10.1016/j.nimb.2011.07.023.
[387] H. Paul, Nucl. Instrum. Methods Phys. Res. B 273 (2012) 15, http://dx.doi.org/10.1016/j.nimb.2011.07.026.
[388] H. Geissel, 2017, private communication.
[389] https://www.klinikum.uni-heidelberg.de/interdisziplinaere-zentren/heidelberger-ionenstrahl-therapiezentrum-hit/, accessed: 09-05-2023, 2023.
[390] https://www.ukgm.de/ugm_2/deu/umr_ptz/index.html, accessed: 09-05-2023, 2023.
[391] U. Amaldi, G. Kraft, Rep. Progr. Phys. 68 (8) (2005) 1861, http://dx.doi.org/10.1088/0034-4885/68/8/r04.
[392] J.R. Castro, et al., Int. J. Rad. Oncol. Biol. Phys. 8 (1982) 2191, http://dx.doi.org/10.1016/0360-3016(82)90569-7.
[393] M. Durante, et al., Phys. Rep. 800 (2019) 1, http://dx.doi.org/10.1016/j.physrep.2019.01.004.
[394] W. Gonzalez, Y. Prezado, Med. Phys. 45 (2018) 2620, http://dx.doi.org/10.1002/mp.12902.
[395] T. Friedrich, 2020, private communication.
[396] W. Kutschera, Int. J. Mass Spectr. 349–350 (2013) 203, http://dx.doi.org/10.1016/j.ijms.2013.05.023.
[397] S. Richter, et al., Int. J. Mass Spectr. 193 (1) (1999) 9, http://dx.doi.org/10.1016/S1387-3806(99)00102-5.
[398] G.A. Cowen, Sc. Am. 235 (1976) 36.
[399] P. Steier, et al., Nucl. Instrum. Methods Phys. Res. B 188 (2002) 283, http://dx.doi.org/10.1016/S0168-583X(01)01114-4.
[400] P. Steier, et al., Nucl. Instrum. Methods Phys. Res. B 266 (2008) 2246, http://dx.doi.org/10.1016/j.nimb.2008.03.002.
[401] H.-A. Synal, Int. J. Mass Spectr. 349–350 (2013) 192, http://dx.doi.org/10.1016/j.ijms.2013.05.008.
[402] A. Sakaguchi, et al., Geochem. J. 46 (2012) 355, http://dx.doi.org/10.2343/geochemj.2.0216.
[403] A. Sakaguchi, et al., Earth Planetary Sci. Lett. 333 (2012) 165, http://dx.doi.org/10.1016/j.epsl.2012.04.004.
[404] K.M. Wilcken, et al., Nucl. Instrum. Methods Phys. Res. B 259 (2007) 727, http://dx.doi.org/10.1016/j.nimb.2007.01.210.
[405] T. Shinonaga, et al., Geochem. J. 55 (2021) 33, http://dx.doi.org/10.2343/geochemj.2.0615.
[406] M. Paul, et al., Nucl. Instrum. Methods Phys. Res. B 172 (1) (2000) 688, http://dx.doi.org/10.1016/S0168-583X(00)00279-2.
[407] https://www.anl.gov/phy/accelerator-mass-spectrometry-ams, accessed 09-05-2023, 2023.
[408] A. Dewald, J. Jolie, A. Zilges, Nucl. Phys. News 18 (3) (2008) 26, http://dx.doi.org/10.1080/10506890802336232.
[409] B.-A. Dittmann, et al., Nucl. Instrum. Methods Phys. Res. B 438 (2019) 189, http://dx.doi.org/10.1016/j.nimb.2018.04.032.
[410] M. Suter, Nucl. Instrum. Methods Phys. Res. B 223 - 224 (2004) 139, http://dx.doi.org/10.1016/j.nimb.2004.04.030.
[411] P. Steier, et al., Nucl. Instrum. Methods Phys. Res. B 458 (2019) 82, http://dx.doi.org/10.1016/j.nimb.2019.07.031.
[412] A. Navin, et al., J. Phys. G 38 (2) (2011) 024004, http://dx.doi.org/10.1088/0954-3899/38/2/024004.
[413] T. Aumann, P.F. Bortignon, H. Emling, Annu. Rev. Nucl. Part. Sci. 48 (1) (1998) 351, http://dx.doi.org/10.1146/annurev.nucl.48.1.351.
[414] M.N. Harakeh, A. van der Woude, Giant Resonances, Claredon Press, Oxford, 2001.
[415] J. Speth (Ed.), Electric and Magnetic Giant Resonances in Nuclei, in: Int. Rev. Nucl. Phys., vol. 7, World Scientific Singapore, 1991, http://dx.doi.org/10.1142/1126.
[416] H. Emling, Prog. Part. Nucl. Phys. 33 (1994) 729, http://dx.doi.org/10.1016/0146-6410(94)90052-3.
[417] C.A. Bertulani, 1994, private communication.
[418] R. Liguori Neto, et al., Nuclear Phys. A 560 (2) (1993) 733, http://dx.doi.org/10.1016/0375-9474(93)90043-W.
[419] T. Aumann, Nuclear Phys. A 805 (1) (2008) 198c, http://dx.doi.org/10.1016/j.nuclphysa.2008.02.248.
[420] T. Suda, H. Simon, Progr. Part. Nucl. Phys. 96 (2017) 1, http://dx.doi.org/10.1016/j.ppnp.2017.04.002.
[421] S.E. van Bramer, An Introduction to Mass Spectrometry, Widener University, Chester PA, 1998, https://science.widener.edu/svb/massspec/massspec.pdf, accessed 08-05-2023.
[422] V.K. Liechtenstein, et al., Nucl. Instrum. Methods A 480 (1) (2002) 185, http://dx.doi.org/10.1016/S0168-9002(01)02089-7.
[423] R. Lozeva, et al., Nucl. Instrum. Methods Phys. Res. B 204 (2003) 678, http://dx.doi.org/10.1016/S0168-583X(02)02150-X.
[424] Z. Podolyák, Nucl. Instrum. Methods Phys. Res. B 266 (19) (2008) 4589, http://dx.doi.org/10.1016/j.nimb.2008.05.106.

[425] M.J. Taylor, et al., Nucl. Instrum. Methods A 606 (3) (2009) 589, http://dx.doi.org/10.1016/j.nima.2009.05.003.
[426] P. Golubev, et al., Nucl. Instrum. Methods A 723 (2013) 55, http://dx.doi.org/10.1016/j.nima.2013.04.058.
[427] F. Gönnenwein, Nuclear Phys. A 502 (1989) 159, http://dx.doi.org/10.1016/0375-9474(89)90660-X.
[428] A. Oed, et al., Nucl. Instrum. Methods 219 (3) (1984) 569, http://dx.doi.org/10.1016/0167-5087(84)90232-1.
[429] M. Mutterer, et al., Nucl. Instrum. Methods A 608 (2) (2009) 275, http://dx.doi.org/10.1016/j.nima.2009.06.060.
[430] S. Kraft, et al., AIP Conf. Proc. 605 (2002) 405, http://dx.doi.org/10.1063/1.1457673.
[431] G. Münzenberg, Acta Phys. Pol. B 43 (2012) 139, http://dx.doi.org/10.5506/APhysPolB.43.139.
[432] G. Münzenberg, Nuclear Phys. A 944 (2015) 5, http://dx.doi.org/10.1016/j.nuclphysa.2015.06.008.
[433] P. Armbruster, Annu. Rev. Nucl. Part. Sc. 35 (1) (1985) 135, http://dx.doi.org/10.1146/annurev.ns.35.120185.001031.
[434] G. Münzenberg, Rep. Progr. Phys. 51 (1) (1988) 57, http://dx.doi.org/10.1088/0034-4885/51/1/002.
[435] S. Hofmann, Rep. Progr. Phys. 61 (6) (1998) 639, http://dx.doi.org/10.1088/0034-4885/61/6/002.
[436] S. Hofmann, G. Münzenberg, Rev. Modern Phys. 72 (2000) 733, http://dx.doi.org/10.1103/RevModPhys.72.733.
[437] P. Schury, et al., Nucl. Instrum. Methods Phys. Res. B 376 (2016) 425, http://dx.doi.org/10.1016/j.nimb.2016.02.061.
[438] Y.T. Oganessian, et al., Phys. Rev. C 87 (2013) 014302, http://dx.doi.org/10.1103/PhysRevC.87.014302.
[439] T.-H. Huang, et al., J. Phys.: Conf. Ser. 420 (2013) 012005, http://dx.doi.org/10.1088/1742-6596/420/1/012005.
[440] A. Herlert, EPJ Web Conf. 71 (2014) 00064, http://dx.doi.org/10.1051/epjconf/20147100064.
[441] S. Minaev, et al., Phys. Rev. ST Accel. Beams 12 (2009) 120101, http://dx.doi.org/10.1103/PhysRevSTAB.12.120101.
[442] W. Barth, et al., EPJ Web Conf. 138 (2017) 01026, http://dx.doi.org/10.1051/epjconf/201713801026.
[443] C.E. Düllmann, Nucl. Instrum. Methods Phys. Res. B 266 (19) (2008) 4123, http://dx.doi.org/10.1016/j.nimb.2008.05.022.
[444] A. Türler, R. Eichler, A. Yakushev, Nuclear Phys. A 944 (2015) 640, http://dx.doi.org/10.1016/j.nuclphysa.2015.09.012.
[445] R. Eichler, Nucl. Phys. News 29 (1) (2019) 11, http://dx.doi.org/10.1080/10619127.2019.1571803.
[446] Y. Oganessian, Nucl. Phys. News 29 (1) (2019) 5, http://dx.doi.org/10.1080/10619127.2019.1571799.
[447] J.M. Gates, et al., Phys. Rev. C 92 (2015) 021301, http://dx.doi.org/10.1103/PhysRevC.92.021301.
[448] T. Aumann, Progr. Part. Nucl. Phys. 59 (1) (2007) 3, http://dx.doi.org/10.1016/j.ppnp.2006.12.018.
[449] A. Chakrabarti, Nucl. Instrum. Methods Phys. Res. B 261 (1) (2007) 1018, http://dx.doi.org/10.1016/j.nimb.2007.04.145.
[450] B. Rubio, T. Nilsson, Nucl. Phys. News 16 (1) (2006) 9, http://dx.doi.org/10.1080/10506890600579843.
[451] R. Krücken, the NuSTAR collaboration, J. Phys. G 31 (10) (2005) 1807, http://dx.doi.org/10.1088/0954-3899/31/10/077.
[452] H.-J. Wollersheim, Acta Phys. Pol. B 42 (2011) 705, http://dx.doi.org/10.5506/APhysPolB.42.705.
[453] D. Rudolph, et al., Technical Report, 2008, https://www.nuclear.lu.se/fileadmin/nuclear/Grundlaeggande/lycca-TDR.pdf.
[454] N. Boucheneb, et al., Nuclear Phys. A 502 (1989) 261, http://dx.doi.org/10.1016/0375-9474(89)90666-0.
[455] M.O. Frégeau, et al., Nucl. Instrum. Methods A 817 (2016) 35, http://dx.doi.org/10.1016/j.nima.2016.02.011.
[456] D. Gerber, et al., in: S. Cooper (Ed.), Proceedings of the 7th International Workshop on Low Temperature Detectors, Max-Planck-Institut München, 1997, p. 73.
[457] G. Westmacott, et al., Rapid Commun. Mass Spectrom. 14 (2000) 600, http://dx.doi.org/10.1002/(SICI)1097-0231(20000415)14:7<600::AID-RCM915>3.0.CO;2-0.
[458] G. Westmacott, et al., Rapid Commun. Mass Spectrom. 14 (2000) 1854, http://dx.doi.org/10.1002/1097-0231(20001015)14:19<1854::AID-RCM102>3.0.CO;2-M.
[459] R.J. Wenzel, et al., Anal. Chem. 77 (2005) 4329, http://dx.doi.org/10.1021/ac0482054.
[460] L.D. Plath, et al., Anal. Chem. 87 (2015) 8985, http://dx.doi.org/10.1021/acs.analchem.5b02180.
[461] D.M. Sipe, et al., ACS Nano 12 (2018) 2591, http://dx.doi.org/10.1021/acsnano.7b08541.
[462] M. Ohkubo, et al., Nucl. Instrum. Methods A 559 (2006) 779, http://dx.doi.org/10.1016/j.nima.2005.12.137.
[463] M. Ohkubo, et al., Int. J. Mass Spectrom. 299 (2011) 94, http://dx.doi.org/10.1016/j.ijms.2010.09.027.
[464] D.Z. Keifer, M.F. Jarrold, Mass Spectr. Rev. 36 (2017) 715, http://dx.doi.org/10.1002/mas.21495.
[465] W.S. Yoon, et al., Nucl. Instrum. Methods A 784 (2015) 143, http://dx.doi.org/10.1016/j.nima.2014.09.037.
[466] N. Coursol, et al., Nucl. Instrum. Methods A 312 (1) (1992) 24, http://dx.doi.org/10.1016/0168-9002(92)90121-J.
[467] R.D. Horansky, et al., Appl. Phys. Lett. 93 (12) (2008) 123504, http://dx.doi.org/10.1063/1.2978204.
[468] S.-J. Lee, et al., J. Phys. G 37 (5) (2010) 055103, http://dx.doi.org/10.1088/0954-3899/37/5/055103.
[469] A.D. Tollefson, et al., Appl. Radiat. Isot. 172 (2021) 109693, http://dx.doi.org/10.1016/j.apradiso.2021.109693.
[470] A. Benoit, M. Martin, B. Pannetier, J. Low Temp. Phys. 93 (1993) 727, http://dx.doi.org/10.1007/BF00693503.
[471] M. Loidl, et al., J. Low Temp. Phys. 151 (2008) 1055, http://dx.doi.org/10.1007/s10909-008-9793-7.
[472] W.E. Lamb, R.C. Retherford, Phys. Rev. 72 (1947) 241, http://dx.doi.org/10.1103/PhysRev.72.241.
[473] M. Niering, et al., Phys. Rev. Lett. 84 (2000) 5496, http://dx.doi.org/10.1103/PhysRevLett.84.5496.
[474] V.A. Yerokhin, V.M. Shabaev, J. Phys. Chem. Ref. Data 44 (2015) 033103, http://dx.doi.org/10.1063/1.4927487.
[475] P. Indelicato, J. Phys. B: At. Mol. Opt. Phys. 52 (2019) 232001, http://dx.doi.org/10.1088/1361-6455/ab42c9.
[476] V.M. Shabaev, et al., Proc. of Science 353 FFK2019 (2019) 052, http://dx.doi.org/10.22323/1.353.0052.
[477] H.F. Beyer, in: D. Liesen (Ed.), Physics with Multiply Charged Ions, Plenum Press, New York, 1995, p. 31.
[478] H.F. Beyer, T. Stöhlker, in: E. Zavattini, D. Bakalov, C. Rizzo (Eds.), Frontier Tests of QED and Physics of the Vacuum, Heron Press, Sofia, 1998, p. 356.
[479] P. Beiersdorfer, Can. J. Phys. 87 (2009) 9, http://dx.doi.org/10.1139/p08-071.
[480] P. Beiersdorfer, J. Phys. B 43 (2010) 074032, http://dx.doi.org/10.1088/0953-4075/43/7/074032.
[481] K. Kubicek, et al., Phys. Rev. A 90 (2014) 032508, http://dx.doi.org/10.1103/PhysRevA.90.032508.
[482] A. Gumberidze, et al., Phys. Rev. Lett. 94 (2005) 223001, http://dx.doi.org/10.1103/PhysRevLett.94.223001.
[483] G.V. Brown, et al., in: F.S. Porter, et al. (Eds.), AIP Conf. Proc., vol. 605, 2002, p. 413, http://dx.doi.org/10.1063/1.1457675.
[484] P. Beiersdorfer, et al., Phys. Scr. T 92 (2001) 268, http://dx.doi.org/10.1238/Physica.Topical.092a00268.
[485] P. Beiersdorfer, J. Phys. B 48 (2015) 144017, http://dx.doi.org/10.1088/0953-4075/48/14/144017.
[486] J.W. McDonald, R.W. Bauer, D.H.G. Schneider, Rev. Sci. Instrum. 73 (2002) 30, http://dx.doi.org/10.1063/1.1419216.
[487] P. Beiersdorfer, et al., Phys. Rev. Lett. 95 (2005) 233003, http://dx.doi.org/10.1103/PhysRevLett.95.233003.
[488] J.D. Gillaspy, Phys. Scr. 89 (2014) 114004, http://dx.doi.org/10.1088/0031-8949/89/11/114004.
[489] L. Schweikhard, et al., Nucl. Instrum. Methods Phys. Res. B 142 (1998) 245, http://dx.doi.org/10.1016/S0168-583X(98)00281-X.
[490] R.E. Marrs, S.R. Elliott, D.A. Knapp, Phys. Rev. Lett. 72 (1994) 4082, http://dx.doi.org/10.1103/PhysRevLett.72.4082.
[491] T. Stöhlker, et al., Phys. Rev. Lett. 85 (2000) 3109, http://dx.doi.org/10.1103/PhysRevLett.85.3109.
[492] M. Lestinsky, Y. Litvinov, T.S. (Eds.), Eur. Phys. J. Spec. Top. 225 (2016) 797, http://dx.doi.org/10.1140/epjst/e2016-02643-6.
[493] F. Herfurth, et al., Phys. Scr. T 166 (2015) 014065, http://dx.doi.org/10.1088/0031-8949/2015/T166/014065.
[494] H. Geissel, et al., Nucl. Instrum. Methods Phys. Res. B 70 (1) (1992) 286, http://dx.doi.org/10.1016/0168-583X(92)95944-M.
[495] S. Kraft-Bermuth, et al., J. Low Temp. Phys. 167 (2012) 765, http://dx.doi.org/10.1007/s10909-012-0520-z.

[496] C.K. Stahle, et al., Nucl. Instrum. Methods A 370 (1996) 173, http://dx.doi.org/10.1016/0168-9002(95)01096-3.
[497] V. Andrianov, et al., J. Low Temp. Phys. 151 (2008) 1049, http://dx.doi.org/10.1007/s10909-008-9792-8.
[498] M. Kühnel, et al., Nucl. Instrum. Methods A 602 (2009) 311, http://dx.doi.org/10.1016/j.nima.2008.12.212.
[499] P.A. Scholz, S. Kraft-Bermuth, V. Andrianov, J. Low Temp. Phys. 184 (2016) 576, http://dx.doi.org/10.1007/s10909-015-1438-z.
[500] F.S. Porter, et al., in: F.S. Porter, D. McCammon, M. Galeazzi, C.K. Stahle (Eds.), AIP Conf. Proc., vol. 605, 2002, p. 421, http://dx.doi.org/10.1063/1.1457677.
[501] F.S. Porter, et al., J. Low Temp. Phys. 151 (2008) 1061, http://dx.doi.org/10.1007/s10909-008-9788-4.
[502] F.S. Porter, et al., in: B. Cabrera, A. Miller, B. Young (Eds.), AIP Conf. Proc., vol. 1185, 2009, p. 454, http://dx.doi.org/10.1063/1.3292376.
[503] M. Bühler, E. Umlauf, Europhys. Lett. 5 (4) (1988) 297, http://dx.doi.org/10.1209/0295-5075/5/4/003.
[504] C. Enss, et al., J. Low Temp. Phys. 121 (2000) 137, http://dx.doi.org/10.1023/A:1004863823166.
[505] D. Hengstler, Ph.D. thesis, Heidelberg University, 2017, https://katalog.ub.uni-heidelberg.de/titel/68211116.
[506] W.S. Yoon, et al., J. Low Temp. Phys. 176 (2014) 644, http://dx.doi.org/10.1007/s10909-013-1067-3.
[507] S.T.P. Boyd, et al., J. Low Temp. Phys. 199 (2020) 681, http://dx.doi.org/10.1007/s10909-020-02406-5.
[508] W. Yoon, et al., J. Low Temp. Phys. 199 (2020) 916, http://dx.doi.org/10.1007/s10909-019-02311-6.
[509] P. Pfäfflein, et al., Phys. Scr. 97 (2022) 114005, http://dx.doi.org/10.1088/1402-4896/ac93be.
[510] C. Pies, et al., J. Low Temp. Phys. 167 (2012) 269, http://dx.doi.org/10.1007/s10909-012-0557-z.
[511] S. Pitaevskii, J. Ketterson, in: K.H. Bennemann, J.B. Ketterson (Eds.), Superconductivity: Conventional and Unconventional Superconductors, Springer-Verlag Heidelberg Berlin, 2008, p. 316.
[512] S. Chatterjee, et al., Nucl. Instrum. Methods Phys. Res. B 245 (1) (2006) 67, http://dx.doi.org/10.1016/j.nimb.2005.11.074.
[513] T. Gassner, et al., New J. Phys. 20 (7) (2018) 073033, http://dx.doi.org/10.1088/1367-2630/aad01d.
[514] N. Hell, et al., Astrophys. J. 830 (2016) 26, http://dx.doi.org/10.3847/0004-637X/830/1/26.
[515] D. Panchenko, et al., Phys. Rev. A 95 (2017) 062503, http://dx.doi.org/10.1103/PhysRevA.95.062503.
[516] G.V. Brown, et al., in: B. Cabrera, A. Miller, B. Young (Eds.), AIP Conf. Proc., vol. 1185, 2009, p. 446, http://dx.doi.org/10.1063/1.3292374.
[517] J. Clementson, et al., Can. J. Phys. 89 (2011) 571, http://dx.doi.org/10.1139/P11-028.
[518] M. Matranga, et al., Nucl. Instrum. Methods Phys. Res. B 205 (2003) 244, http://dx.doi.org/10.1016/S0168-583X(03)00943-1.
[519] E. Träbert, et al., J. Phys.: Conf. Ser. 163 (2009) 012010, http://dx.doi.org/10.1088/1742-6596/163/1/012010.
[520] R. Reuschl, et al., Radiat. Phys. Chem. 75 (2006) 1740, http://dx.doi.org/10.1016/j.radphyschem.2006.05.006.
[521] T. Stöhlker, et al., on behalf of the APPA collaboration, Nucl. Instrum. Methods Phys. Res. B 365 (2015) 680, http://dx.doi.org/10.1016/j.nimb.2015.07.077.
[522] T. Stöhlker, Y.A. Litvinov, for the SPARC Collaboration, Phys. Scr. T 166 (2015) 014025, http://dx.doi.org/10.1088/0031-8949/2015/T166/014025.
[523] A. Gumberidze, et al., J. Phys.: Conf. Ser. 58 (2007) 87, http://dx.doi.org/10.1088/1742-6596/58/1/013.
[524] A. Gumberidze, et al., Phys. Rev. A 84 (2011) 042710, http://dx.doi.org/10.1103/PhysRevA.84.042710.
[525] A. Gumberidze, et al., Phys. Rev. A 99 (2019) 032706, http://dx.doi.org/10.1103/PhysRevA.99.032706.
[526] L. von der Wense, C. Zhang, Eur. Phys. J. D 74 (2020) 146, http://dx.doi.org/10.1140/epjd/e2020-100582-5.
[527] T. Kotthaus, et al., Phys. Lett. B 718 (2012) 460, http://dx.doi.org/10.1016/j.physletb.2012.10.083.
[528] R.G. Helmer, C.W. Reich, Phys. Rev. C 49 (1994) 1845, http://dx.doi.org/10.1103/PhysRevC.49.1845.
[529] A. Yamaguchi, et al., Phys. Rev. Lett. 123 (2019) 222501, http://dx.doi.org/10.1103/PhysRevLett.123.222501.
[530] T. Sikorsky, et al., Phys. Rev. Lett. 125 (2020) 142503, http://dx.doi.org/10.1103/PhysRevLett.125.142503.
[531] B. Seiferle, et al., Nature 573 (2019) 243, http://dx.doi.org/10.1038/s41586-019-1533-4.
[532] T. Burr, et al., Nucl. Data Sheets 123 (2015) 140, http://dx.doi.org/10.1016/j.nds.2014.12.025.
[533] A.S. Hoover, et al., Anal. Chem. 87 (2015) 3996, http://dx.doi.org/10.1021/acs.analchem.5b00195.
[534] G.B. Kim, et al., J. Low Temp. Phys. 193 (2018) 1236, http://dx.doi.org/10.1007/s10909-018-1978-0.
[535] W.B. Doriese, et al., Appl. Phys. Lett. 90 (2007) 193508, http://dx.doi.org/10.1063/1.2738371.
[536] C.A. Kilbourne, in: B. Cabrera, A. Miller, B. Young (Eds.), AIP Conf. Proc., vol. 1185, 2009, p. 419, http://dx.doi.org/10.1063/1.3292367.
[537] R. Mariam, M. Rodrigues, M. Loidl, J. Low Temp. Phys. 193 (2018) 1269, http://dx.doi.org/10.1007/s10909-018-2001-5.
[538] P. Szypryt, et al., Rev. Sci. Instrum. 90 (2019) 123107, http://dx.doi.org/10.1063/1.5116717.